

# Calibration and Analysis of the GCT Camera for the Cherenkov Telescope Array

Jason J. Watson

Brasenose College  
University of Oxford

*A thesis submitted for the degree of  
Doctor of Philosophy*

Trinity 2018

## Abstract

10 Lorem ipsum dolor sit amet, consectetur adipiscing elit. Pellentesque sit amet  
11 nibh volutpat, scelerisque nibh a, vehicula neque. Integer placerat nulla massa,  
12 et vestibulum velit dignissim id. Ut eget nisi elementum, consectetur nibh in,  
13 condimentum velit. Quisque sodales dui ut tempus mattis. Duis malesuada arcu  
14 at ligula egestas egestas. Phasellus interdum odio at sapien fringilla scelerisque.  
15 Mauris sagittis eleifend sapien, sit amet laoreet felis mollis quis. Pellentesque  
16 dui ante, finibus eget blandit sit amet, tincidunt eu neque. Vivamus rutrum  
17 dapibus ligula, ut imperdiet lectus tincidunt ac. Pellentesque ac lorem sed  
18 diam egestas lobortis.

Suspendisse leo purus, efficitur mattis urna a, maximus molestie nisl. Aenean porta semper tortor a vestibulum. Suspendisse viverra facilisis lorem, non pretium erat lacinia a. Vestibulum tempus, quam vitae placerat porta, magna risus euismod purus, in viverra lorem dui at metus. Sed ac sollicitudin nunc. In maximus ipsum nunc, placerat maximus tortor gravida varius. Suspendisse pretium, lorem at porttitor rhoncus, nulla urna condimentum tortor, sed suscipit nisi metus ac risus.

Aenean sit amet enim quis lorem tristique commodo vitae ut lorem. Duis vel tincidunt lacus. Sed massa velit, lacinia sed posuere vitae, malesuada vel ante. Praesent a rhoncus leo. Etiam sed rutrum enim. Pellentesque lobortis elementum augue, at suscipit justo malesuada at. Lorem ipsum dolor sit amet, consectetur adipiscing elit. Praesent rhoncus convallis ex. Etiam commodo nunc ex, non consequat diam consectetur ut. Pellentesque vitae est nec enim interdum dapibus. Donec dapibus purus ipsum, eget tincidunt ex gravida eget. Donec luctus nisi eu fringilla mollis. Donec eget lobortis diam.

<sup>34</sup> Suspendisse finibus placerat dolor. Etiam ornare elementum ex ut vehicula.  
<sup>35</sup> Donec accumsan mattis erat. Quisque cursus fringilla diam, eget placerat neque  
<sup>36</sup> bibendum eu. Ut faucibus dui vitae dolor porta, at elementum ipsum semper.  
<sup>37</sup> Sed ultrices dui non arcu pellentesque placerat. Etiam posuere malesuada turpis,  
<sup>38</sup> nec malesuada tellus malesuada.

39      **Calibration and Analysis of the GCT**  
40      **Camera for the Cherenkov Telescope**  
41      **Array**



43      Jason J. Watson  
44      Brasenose College  
45      University of Oxford

46      A thesis submitted for the degree of  
47      *Doctor of Philosophy*  
48      Trinity 2018

# Acknowledgements

## 50 Personal

51 Lorem ipsum dolor sit amet, consectetur adipiscing elit. Vestibulum feugiat et est at  
52 accumsan. Praesent sed elit mattis, congue mi sed, porta ipsum. In non ullamcorper  
53 lacus. Quisque volutpat tempus ligula ac ultricies. Nam sed erat feugiat, elementum  
54 dolor sed, elementum neque. Aliquam eu iaculis est, a sollicitudin augue. Cras  
55 id lorem vel purus posuere tempor. Proin tincidunt, sapien non dictum aliquam,  
56 ex odio ornare mauris, ultrices viverra nisi magna in lacus. Fusce aliquet molestie  
57 massa, ut fringilla purus rutrum consectetur. Nam non nunc tincidunt, rutrum dui  
58 sit amet, ornare nunc. Donec cursus tortor vel odio molestie dignissim. Vivamus  
59 id mi erat. Duis porttitor diam tempor rutrum porttitor. Lorem ipsum dolor sit  
60 amet, consectetur adipiscing elit. Sed condimentum venenatis consectetur. Lorem  
61 ipsum dolor sit amet, consectetur adipiscing elit.

62 Aenean sit amet lectus nec tellus viverra ultrices vitae commodo nunc. Mauris  
63 at maximus arcu. Aliquam varius congue orci et ultrices. In non ipsum vel est  
64 scelerisque efficitur in at augue. Nullam rhoncus orci velit. Duis ultrices accumsan  
65 feugiat. Etiam consectetur ornare velit et eleifend.

66 Suspendisse sed enim lacinia, pharetra neque ac, ultricies urna. Phasellus sit  
67 amet cursus purus. Quisque non odio libero. Etiam iaculis odio a ex volutpat,  
68 eget pulvinar augue mollis. Mauris nibh lorem, mollis quis semper quis, consequat  
69 nec metus. Etiam dolor mi, cursus a ipsum aliquam, eleifend venenatis ipsum.  
70 Maecenas tempus, nibh eget scelerisque feugiat, leo nibh lobortis diam, id laoreet  
71 purus dolor eu mauris. Pellentesque habitant morbi tristique senectus et netus  
72 et malesuada fames ac turpis egestas. Nulla eget tortor eu arcu sagittis euismod  
73 fermentum id neque. In sit amet justo ligula. Donec rutrum ex a aliquet egestas.

## 74 Institutional

75 Lorem ipsum dolor sit amet, consectetur adipiscing elit. Ut luctus tempor ex at  
76 pretium. Sed varius, mauris at dapibus lobortis, elit purus tempor neque, facilisis  
77 sollicitudin felis nunc a urna. Morbi mattis ante non augue blandit pulvinar.  
78 Quisque nec euismod mauris. Nulla et tellus eu nibh auctor malesuada quis  
79 imperdiet quam. Sed eget tincidunt velit. Cras molestie sem ipsum, at faucibus  
80 quam mattis vel. Quisque vel placerat orci, id tempor urna. Vivamus mollis, neque  
81 in aliquam consequat, dui sem volutpat lorem, sit amet tempor ipsum felis eget ante.  
82 Integer lacinia nulla vitae felis vulputate, at tincidunt ligula maximus. Aenean

<sup>83</sup> venenatis dolor ante, euismod ultrices nibh mollis ac. Ut malesuada aliquam urna,  
<sup>84</sup> ac interdum magna malesuada posuere.

<sup>85</sup> **CTA**

<sup>86</sup> ctapipe, target, chec.....

# Abstract

87

88 Lorem ipsum dolor sit amet, consectetur adipiscing elit. Pellentesque sit amet  
89 nibh volutpat, scelerisque nibh a, vehicula neque. Integer placerat nulla massa,  
90 et vestibulum velit dignissim id. Ut eget nisi elementum, consectetur nibh in,  
91 condimentum velit. Quisque sodales dui ut tempus mattis. Duis malesuada arcu at  
92 ligula egestas egestas. Phasellus interdum odio at sapien fringilla scelerisque. Mauris  
93 sagittis eleifend sapien, sit amet laoreet felis mollis quis. Pellentesque dui ante,  
94 finibus eget blandit sit amet, tincidunt eu neque. Vivamus rutrum dapibus ligula,  
95 ut imperdiet lectus tincidunt ac. Pellentesque ac lorem sed diam egestas lobortis.

96 Suspendisse leo purus, efficitur mattis urna a, maximus molestie nisl. Aenean  
97 porta semper tortor a vestibulum. Suspendisse viverra facilisis lorem, non pretium  
98 erat lacinia a. Vestibulum tempus, quam vitae placerat porta, magna risus euismod  
99 purus, in viverra lorem dui at metus. Sed ac sollicitudin nunc. In maximus ipsum  
100 nunc, placerat maximus tortor gravida varius. Suspendisse pretium, lorem at  
101 porttitor rhoncus, nulla urna condimentum tortor, sed suscipit nisi metus ac risus.

102 Aenean sit amet enim quis lorem tristique commodo vitae ut lorem. Duis vel  
103 tincidunt lacus. Sed massa velit, lacinia sed posuere vitae, malesuada vel ante.  
104 Praesent a rhoncus leo. Etiam sed rutrum enim. Pellentesque lobortis elementum  
105 augue, at suscipit justo malesuada at. Lorem ipsum dolor sit amet, consectetur  
106 adipiscing elit. Praesent rhoncus convallis ex. Etiam commodo nunc ex, non  
107 consequat diam consectetur ut. Pellentesque vitae est nec enim interdum dapibus.  
108 Donec dapibus purus ipsum, eget tincidunt ex gravida eget. Donec luctus nisi  
109 eu fringilla mollis. Donec eget lobortis diam.

110 Suspendisse finibus placerat dolor. Etiam ornare elementum ex ut vehicula.  
111 Donec accumsan mattis erat. Quisque cursus fringilla diam, eget placerat neque  
112 bibendum eu. Ut faucibus dui vitae dolor porta, at elementum ipsum semper.  
113 Sed ultrices dui non arcu pellentesque placerat. Etiam posuere malesuada turpis,  
114 nec malesuada tellus malesuada.

---

# Contents

115

116	<b>List of Figures</b>	x
117	<b>Abbreviations</b>	xiii
118	<b>Glossary</b>	xvi
119	<b>1 Introduction</b>	1
120	1.1 Plan . . . . .	2
121	1.1.1 Topics . . . . .	2
122	1.1.2 Questions . . . . .	2
123	1.2 Atmospheric Cherenkov Showers . . . . .	3
124	1.3 Imaging Atmospheric Cherenkov Technique . . . . .	3
125	1.3.1 Cherenkov Shower Characteristics . . . . .	3
126	1.3.2 Photon Arrival Time . . . . .	3
127	1.4 The Cherenkov Telescope Array . . . . .	3
128	1.5 Small Sized Telescopes . . . . .	3
129	1.6 Science with the Small Sized Telescopes . . . . .	3
130	<b>2 The Compact High Energy Camera</b>	4
131	2.1 Introduction . . . . .	4
132	2.2 Photosensors . . . . .	5
133	2.2.1 Photomultiplier Tubes . . . . .	6
134	2.2.2 Multi-Anode Photomultiplier Tubes . . . . .	8
135	2.2.3 Silicon Photomultipliers . . . . .	9
136	2.2.4 Performance Parameters of SiPMs . . . . .	11
137	2.2.5 Excess Noise Factor (ENF) . . . . .	14
138	2.2.6 Future . . . . .	16
139	2.3 Camera Electronics . . . . .	17
140	2.3.1 Front-End Electronics (FEE) . . . . .	17
141	2.3.2 Back-End Electronics (BEE) . . . . .	20
142	2.3.3 LED Flashers . . . . .	21
143	2.4 Signal Digitisation . . . . .	21
144	2.4.1 Sampling . . . . .	21
145	2.4.2 Triggering . . . . .	22
146	2.4.3 Digitisation and Readout . . . . .	23

147	<b>3 The CTA System Architecture</b>	<b>24</b>
148	3.1 Introduction . . . . .	24
149	3.2 Requirements . . . . .	25
150	3.2.1 B-TEL-1010 Charge Resolution . . . . .	27
151	3.2.2 B-TEL-1030 Time Resolution . . . . .	30
152	3.2.3 B-TEL-1295 Pixel Availability . . . . .	31
153	3.3 Data Level and Flow Model . . . . .	31
154	<b>4 Software</b>	<b>35</b>
155	4.1 Introduction . . . . .	35
156	4.2 TARGET Libraries . . . . .	36
157	4.2.1 TargetDriver . . . . .	36
158	4.2.2 TargetIO . . . . .	36
159	4.2.3 TargetCalib . . . . .	38
160	4.3 Monte Carlo Software . . . . .	39
161	4.3.1 CORSIKA . . . . .	40
162	4.3.2 sim_telarray . . . . .	41
163	4.4 Reduction Tools . . . . .	41
164	4.4.1 ctapipe . . . . .	42
165	4.4.2 CHECLabPy . . . . .	47
166	4.5 Science Tools . . . . .	48
167	4.5.1 Gammapy . . . . .	49
168	4.5.2 ctools . . . . .	49
169	<b>5 Calibration</b>	<b>51</b>
170	5.1 Introduction . . . . .	51
171	5.2 TARGET Calibration . . . . .	52
172	5.2.1 Electronic Pedestal Subtraction . . . . .	53
173	5.2.2 Transfer Function . . . . .	56
174	5.3 Photosensor Calibration . . . . .	61
175	5.3.1 Gain Matching . . . . .	62
176	5.3.2 SPE Fitting . . . . .	64
177	5.3.3 Flat-Field Coefficients . . . . .	65
178	5.3.4 Dead Pixels . . . . .	68
179	5.4 Saturation Recovery . . . . .	69
180	5.5 Timing Corrections . . . . .	69
181	5.6 Future . . . . .	70

---

182	<b>6 Waveform Processing</b>	<b>72</b>
183	6.1 Introduction . . . . .	72
184	6.2 Charge Extraction Methods . . . . .	73
185	6.2.1 Peak Finding . . . . .	74
186	6.2.2 Integration . . . . .	76
187	6.2.3 Approaches Adopted by Other IACTs . . . . .	78
188	6.2.4 Performance Assessment . . . . .	80
189	6.3 Shower Reconstruction . . . . .	80
190	6.3.1 Image Parametrisation . . . . .	81
191	6.3.2 Direction Reconstruction . . . . .	82
192	6.3.3 Energy Reconstruction . . . . .	83
193	6.3.4 $\gamma$ -Hadron Discrimination . . . . .	83
194	<b>7 Camera Performance</b>	<b>85</b>
195	7.1 Introduction . . . . .	85
196	7.2 CHEC-S Monte Carlo Model . . . . .	86
197	7.3 CHEC-S Charge Resolution . . . . .	88
198	7.3.1 Procedure and Datasets . . . . .	88
199	7.3.2 Lab Results . . . . .	92
200	7.3.3 Lab versus Monte Carlo . . . . .	92
201	7.3.4 Night Sky Background . . . . .	95
202	7.3.5 Optical Crosstalk . . . . .	97
203	7.3.6 Analytical Description . . . . .	99
204	7.3.7 Conclusion . . . . .	101
205	7.4 CHEC-S Pulse Shape . . . . .	101
206	7.5 CHEC-S Time Resolution . . . . .	102
207	7.6 CHEC-M . . . . .	104
208	<b>8 On-Sky Observations</b>	<b>107</b>
209	8.1 Introduction . . . . .	107
210	8.2 Cherenkov Shower Images . . . . .	108
211	8.3 Jupiter Observations . . . . .	112
212	8.4 Conclusion . . . . .	114
213	8.5 Future . . . . .	114
214	<b>9 Summary</b>	<b>115</b>
215	<b>Appendices</b>	

216	<b>A The Silicon Photomultiplier</b>	117
217	A.1 Introduction . . . . .	117
218	A.2 The P-N Junction . . . . .	117
219	A.3 Avalanche PhotoDiode (APD) . . . . .	120
220	A.4 Geiger-mode Avalanche PhotoDiode (G-APD) . . . . .	120
221	A.5 Silicon Photomultiplier (SiPM) . . . . .	121
222	<b>B Laboratory Characterisation</b>	123
223	B.1 Introduction . . . . .	123
224	B.2 Filter Wheel . . . . .	125
225	B.2.1 Reference SiPMT . . . . .	125
226	B.2.2 Camera Correction . . . . .	126
227	B.3 Illumination Profile . . . . .	126
228	B.3.1 Laser Profile . . . . .	127
229	B.3.2 Camera Geometry . . . . .	127
230	B.3.3 Total Correction . . . . .	129
231	B.4 Absolute Illumination . . . . .	130
232	B.5 Average Expected Charge . . . . .	131
233	B.6 Consideration of Errors and Uncertainty . . . . .	132
234	<b>C SPE Fitting</b>	133
235	<b>D Transfer Function Investigations</b>	134
236	D.1 Plan . . . . .	134
237	D.1.1 Topics . . . . .	134
238	D.1.2 Questions . . . . .	134
239	D.2 Introduction . . . . .	134
240	D.3 TF Approaches . . . . .	135
241	D.3.1 No TF - Pedestal Subtraction Only . . . . .	135
242	D.3.2 Raw TF Lookup with pedestal . . . . .	135
243	D.3.3 PCHIP Interpolation . . . . .	135
244	D.3.4 Polynomial Fit . . . . .	135
245	D.4 “Per Sampling Cell” or “Per Storage Cell” . . . . .	135
246	D.5 Approach Comparison . . . . .	135
247	D.5.1 SPE Distribution . . . . .	135
248	D.5.2 Charge Resolution . . . . .	135

249	<b>E Charge Extractor Investigations</b>	<b>136</b>
250	E.1 Introduction . . . . .	136
251	E.2 Integration Window . . . . .	136
252	E.2.1 Optimal Integration Window Parameters . . . . .	137
253	E.2.2 Comparison with <i>Cross Correlation</i> . . . . .	139
254	E.2.3 Conclusion . . . . .	141
255	<b>References</b>	<b>143</b>

---

# List of Figures

256

257	2.1	Diagram of a Photomultiplier Tube. . . . .	6
258	2.2	Photomultiplier Tube timing characteristics. . . . .	7
259	2.3	Internals of a Multi-anode Photomultiplier Tube. . . . .	8
260	2.4	Multi-Anode Photomultiplier Tube crosstalk. . . . .	9
261	2.5	Performance characteristics for the SiPMs used in CHEC-S. . . . .	11
262	2.6	Example of the SiPM's PDE dependence on overvoltage. . . . .	12
263	2.7	Illustration of the possible ways optical crosstalk is produced. . . . .	13
264	2.8	Comparison of the single photoelectron multiplication response between CHEC-M and CHEC-S. . . . .	15
265	2.9	Characteristic performance of future CHEC-S SiPMs. . . . .	16
266	2.10	Image of the CHEC-M focal surface. . . . .	17
268	2.11	Image of the CHEC-S focal surface. . . . .	18
269	2.12	Image of the MAPMT and FEE for CHEC-M. . . . .	19
270	2.13	Image of the SiPM and FEE for CHEC-S. . . . .	19
271	2.14	Functional block diagram of the TARGET 5 ASIC. . . . .	22
272	3.1	Charge resolution requirement. . . . .	27
273	3.2	High-level data model hierarchy. . . . .	32
274	3.3	Simplified camera data flow. . . . .	33
275	4.1	Data-flow overview for waveform samples within the TARGET libraries	37
276	4.2	CORSIKA extensive air shower simulations. . . . .	40
277	4.3	Contents of the DataContainer object. . . . .	44
278	4.4	Functional block diagram of the EventSource class. . . . .	45
279	4.5	Functional block diagram of the EventSourceFactory class. . . . .	45
280	4.6	Functional block diagram of the <code>ctapipe</code> low-level calibration classes.	47
281	5.1	Raw waveform . . . . .	52
282	5.2	Comparison of pedestal-subtracted waveform with raw waveform . .	52
283	5.3	Comparison of calibration stages with a Cherenkov shower image. .	53
284	5.4	Storage-cell-amplitude dependence on position in the waveform. .	54
285	5.5	Spread of electronic-pedestal values before and after the pedestal subtraction. . . . .	56
287	5.6	Transfer Function generation waveforms. . . . .	57
288	5.7	Transfer Function lookup tables. . . . .	58

---

289	5.8	Fit of the waveform in order to extract samples to generate the Alternating Current (AC) Transfer Function. . . . .	59
290	5.9	Gain-Matching Residuals . . . . .	62
291	5.10	Comparison of SPE spectra between CHEC-M and CHEC-S. . . . .	64
292	5.11	Flat-field calibration . . . . .	65
293	5.12	Flat-field Coefficients . . . . .	66
294	5.13	Flat-field residuals. . . . .	67
295	5.14	Flat-field residuals at other illuminations. . . . .	67
296	5.15	Saturation Recovery. . . . .	69
297	5.16	Pulse timing correction for each pixel. . . . .	70
298	6.1	Annotated waveform. . . . .	74
299	6.2	Cross correlation stages. . . . .	77
300	6.3	Hillas Parametrisation Schematic. . . . .	81
301	6.4	Shower source location reconstruction. . . . .	82
302	6.5	Shower core location reconstruction. . . . .	82
303	6.6	Discriminating between images of gamma-ray and hadron induced showers. . . . .	84
304	6.7	Hillas width and length from CHEC-S simulations. . . . .	84
305	7.1	Comparison of the SPE spectra between lab measurements and simulations. . . . .	87
306	7.2	CHEC-S measured charge versus average expected charge. . . . .	90
307	7.3	CHEC-S average measured charge versus average expected charge. .	90
308	7.4	<i>Charge Resolution</i> of the Lab dataset in default units. . . . .	91
309	7.5	<i>Charge Resolution</i> of the Lab dataset with respect to the requirement.	91
310	7.6	Comparison of the different <i>Charge Resolution</i> procedures. . . . .	93
311	7.7	Comparison of the <i>Charge Resolution</i> at different NSBs. . . . .	95
312	7.8	Comparison of the <i>Charge Resolution</i> at different NSBs using the <i>MCLabTrue</i> procedure. . . . .	96
313	7.9	Comparison of the <i>Charge Resolution</i> at two different NSBs when observing Cherenkov showers (via the <i>MConsky</i> procedure). . . . .	96
314	7.10	Comparison of the <i>Charge Resolution</i> at different values of optical crosstalk. . . . .	97
315	7.11	Comparison of the <i>Lab Charge Resolution</i> with different bias voltages applied to the SiPM pixel. . . . .	98
316	7.12	Analytical fit of the <i>Lab Charge Resolution</i> . . . . .	100
317	7.13	Pulse shape versus average expected charge for CHEC-S. . . . .	102
318	7.14	Pulse shape versus average expected charge for a CHEC-S simulation.	103
319	7.15	CHEC-S <i>Time Resolution</i> . . . . .	104

---

327	7.16	CHEC-M average measured charge versus average expected charge.	105
328	7.17	<i>Charge Resolution</i> of CHEC-M. . . . .	106
329	8.1	Photo of CHEC-M installed on the GCT telescope structure. . . . .	108
330	8.2	Photo of the reflection of CHEC-M in the secondary mirror. . . . .	109
331	8.3	<i>Hillas</i> length versus width for an on-sky observation run with CHEC-M.110	
332	8.4	Selection of on-sky images. . . . .	111
333	8.5	Camera image of the excess baseline RMS for observations of Jupiter.112	
334	8.6	Camera slices of the Jupiter observations. . . . .	113
335	8.7	Zoom of the Jupiter camera image. . . . .	113
336	A.1	A typical illustration of a P-N Junction. . . . .	118
337	A.2	Illustration of the silicon bandgap. . . . .	119
338	A.3	Diagram of an Avalanche PhotoDiode. . . . .	119
339	A.4	G-APD reverse bias voltage cycle. . . . .	121
340	A.5	Simplified equivalent circuit of an SiPM detector. . . . .	122
341	B.1	Filter-wheel Position Calibration . . . . .	124
342	B.2	Measured charge versus transmission . . . . .	125
343	B.3	Secondary filter-wheel calibration . . . . .	126
344	B.4	Camera geometry correction schematic . . . . .	128
345	B.5	Illumination profile correction images. . . . .	129
346	B.6	Obtaining relationship between filter-wheel transmission and average illumination. . . . .	130
347	B.7	Calibration from filter-wheel transmission to expected charge . . . . .	131
349	E.1	Definition of integration window on a waveform. . . . .	137
350	E.2	Optimal integration-window parameters. . . . .	138
351	E.3	<i>Charge Resolution</i> comparison between <i>Cross Correlation</i> and <i>Window Integration</i> for <i>Lab</i> data. . . . .	139
353	E.4	<i>Charge Resolution</i> comparison between <i>Cross Correlation</i> and <i>Window Integration</i> for <i>MCLab</i> data with an optical crosstalk of 40 %. .	140
355	E.5	<i>Charge Resolution</i> comparison between <i>Cross Correlation</i> and <i>Window Integration</i> for <i>MCLab</i> data with an optical crosstalk of 20 %. .	140
357	E.6	<i>Charge Resolution</i> comparison between <i>Cross Correlation</i> and <i>Window Integration</i> for <i>MCLab</i> data with a high amount of electronic noise. . . . .	141

---

## Abbreviations

<sup>361</sup> **AC** Alternating Current

<sup>362</sup> **ADC** Analogue-to-Digital Converter

<sup>363</sup> **AERIE** Analysis and Event Reconstruction Integrated Environment

<sup>364</sup> **AGN** Active Galactic Nuclei

<sup>365</sup> **APD** Avalanche PhotoDiode

<sup>366</sup> **ASIC** Application-Specific-Integrated Circuit

<sup>367</sup> **ASTRI** Astrofisica con Specchi a Tecnologia Replicante Italiana

<sup>368</sup> **BEE** Back-End Electronics

<sup>369</sup> **CHEC** Compact High Energy Camera

<sup>370</sup> **CITIROC** Cherenkov Imaging Telescope Integrated Read Out Chip

<sup>371</sup> **CORSIKA** COsmic Ray SImulations for KAscade

<sup>372</sup> **CTA** Cherenkov Telescope Array

<sup>373</sup> **DAC** Digital-to-Analogue Converter

<sup>374</sup> **DACQ** Data-Acquisition

<sup>375</sup> **DC** Direct Current

<sup>376</sup> **DCR** Dark-Count Rate

<sup>377</sup> **DPPS** Data Processing and Preservation System

<sup>378</sup> **ENF** Excess Noise Factor

<sup>379</sup> **FACT** First G-APD Cherenkov Telescope

<sup>380</sup> **FEE** Front-End Electronics

<sup>381</sup> **FITS** Flexible Image Transport System

- <sup>382</sup> **FoV** Field of View
- <sup>383</sup> **FPGA** Field-Programmable Gate Array
- <sup>384</sup> **G-APD** Geiger-mode Avalanche PhotoDiode
- <sup>385</sup> **GCT** Gamma-ray Cherenkov Telescope
- <sup>386</sup> **H.E.S.S.** High Energy Stereoscopic System
- <sup>387</sup> **HAWC** High-Altitude Water Cherenkov observatory
- <sup>388</sup> **HV** High Voltage
- <sup>389</sup> **IACT** Imaging Atmospheric Cherenkov Telescope
- <sup>390</sup> **IRF** Instrument Response Function
- <sup>391</sup> **KASCADE** KArlsruhe Shower Core and Array DEtector
- <sup>392</sup> **MAGIC** Major Atmospheric Gamma Imaging Cherenkov Telescopes
- <sup>393</sup> **MAPMT** Multi-Anode Photomultiplier Tube
- <sup>394</sup> **NSB** Night-Sky Background
- <sup>395</sup> **OES** Observation Execution System
- <sup>396</sup> **PDE** Photon Detection Efficiency
- <sup>397</sup> **PMT** Photomultiplier Tube
- <sup>398</sup> **PSF** Point Spread Function
- <sup>399</sup> **QE** Quantum Efficiency
- <sup>400</sup> **RMS** Root-Mean-Square
- <sup>401</sup> **SCT** Schwarzschild-Couder Telescope
- <sup>402</sup> **SiPM** Silicon Photomultiplier
- <sup>403</sup> **SPE** Single PhotoElectron
- <sup>404</sup> **SST** Small Size Telescope

<sup>405</sup> **SUSS** Science User Support System

<sup>406</sup> **SWIG** Simplified Wrapper and Interface Generator

<sup>407</sup> **TARGET** TeV Array Readout with GSa/s sampling and Event Trigger

<sup>408</sup> **UDP** User Datagram Protocol

<sup>409</sup> **VERITAS** Very Energetic Radiation Imaging Telescope Array System

<sup>410</sup> **VHE** Very High Energy

---

## Glossary

<sup>412</sup> **CHEC-M** CHEC utilising MAPMTs as the photosensor.

<sup>413</sup> **CHEC-S** CHEC utilising SiPMs as the photosensor.

<sup>414</sup> **FWHM** The full width of a pulse (or distribution) at half of its maximum.

<sup>415</sup> **T5TEA** ASIC chip used alongside TARGET-C for the trigger handling.

<sup>416</sup> **TARGET-5** Version 5 of the TARGET ASIC.

<sup>417</sup> **TARGET-C** Version C of the TARGET ASIC.

<sup>418</sup> **TIO** Custom FITS file format defined by TargetIO used for storing waveform data  
<sup>419</sup> from TARGET-based cameras

<sup>420</sup> **V<sub>ped</sub>** Reference pedestal voltage input into the TARGET ASIC to provide a  
<sup>421</sup> modest amount of common-mode noise rejection.

---

# 1

422

423

## Introduction

424

### Contents

---

425

426	<b>1.1 Plan</b> . . . . .	<b>2</b>
427	1.1.1 Topics . . . . .	2
428	1.1.2 Questions . . . . .	2
429	<b>1.2 Atmospheric Cherenkov Showers</b> . . . . .	<b>3</b>
430	<b>1.3 Imaging Atmospheric Cherenkov Technique</b> . . . . .	<b>3</b>
431	1.3.1 Cherenkov Shower Characteristics . . . . .	3
432	1.3.2 Photon Arrival Time . . . . .	3
433	<b>1.4 The Cherenkov Telescope Array</b> . . . . .	<b>3</b>
434	<b>1.5 Small Sized Telescopes</b> . . . . .	<b>3</b>
435	<b>1.6 Science with the Small Sized Telescopes</b> . . . . .	<b>3</b>

---

436

438

## 1.1 Plan

### 1.1.1 Topics

- High Energy Astrophysics
  - Fermi
  - Fermi Bubbles
  - HAWC
- IACTs
- CTA
- CTA Science
  - Science Cases
  - Use "Science with CTA" paper
- SSTs
- SST Science
  - What do we contribute?
  - What can't be done without us?
- GCT
- CHEC
  - What makes us better?
  - Advantages of Schwarzschild-Couder
    - \* Increased FoV
    - \* Size
    - \* Cost
  - Advantages of full waveform readout
  - Other Advantages?
    - \* Trigger
    - \* Energy/power/voltage Requirements
    - \* Commonalities (SCT)

### 1.1.2 Questions

- ?

439

Shower properties, photons from bottom of shower are received before those at the top as the particle travels faster than light.  
Good figure in [1]

440

Gamma/Hadron/Lepton

441

Terminology note: charge not used in terms of columns, it refers to counts of photoelectrons, for which mV and ADC are a proxy of. Do a ctrl-f at end to check how charge is used

442

<sup>443</sup> **1.2 Atmospheric Cherenkov Showers**

<sup>444</sup> **1.3 Imaging Atmospheric Cherenkov Technique**

<sup>445</sup> **1.3.1 Cherenkov Shower Characteristics**

<sup>446</sup> **1.3.2 Photon Arrival Time**

<sup>447</sup> Quoted from Holder2005: The longitudinal development of an air shower is reflected in the long axis of the elliptical image recorded in the camera. The photon arrival time profile along this axis is largely a result of geometrical path length differences, and hence the shower core distance. As the shower particles move faster than the speed of light in air, when the shower has a small core distance Cherenkov light emitted from lower in the atmosphere is received at the telescope first. At large core distances, this situation is reversed, as the Cherenkov light travel time from the shower to the telescope dominates. The effect of this is to produce a timing gradient along the long axis of the image, the size and sign of which depend upon the core distance. For gamma-ray showers from a point source at the centre of the field of view, the shower core distance is directly related to the angular distance in the camera of the image from the source position. Figure

<sup>448</sup> **1.4 The Cherenkov Telescope Array**

<sup>449</sup> CTA will be, for the first time in VHE gamma-ray astronomy, operated as an  
<sup>450</sup> open observatory.

<sup>451</sup> **1.5 Small Sized Telescopes**

<sup>452</sup> **1.6 Science with the Small Sized Telescopes**

---

# 2

453

454

## The Compact High Energy Camera

455

### Contents

---

456

457	<b>2.1 Introduction</b>	4
458	<b>2.2 Photosensors</b>	5
459	2.2.1 Photomultiplier Tubes	6
460	2.2.2 Multi-Anode Photomultiplier Tubes	8
461	2.2.3 Silicon Photomultipliers	9
462	2.2.4 Performance Parameters of SiPMs	11
463	2.2.5 Excess Noise Factor (ENF)	14
464	2.2.6 Future	16
465	<b>2.3 Camera Electronics</b>	17
466	2.3.1 Front-End Electronics (FEE)	17
467	2.3.2 Back-End Electronics (BEE)	20
468	2.3.3 LED Flashers	21
469	<b>2.4 Signal Digitisation</b>	21
470	2.4.1 Sampling	21
471	2.4.2 Triggering	22
472	2.4.3 Digitisation and Readout	23

473

475

---

476

### 2.1 Introduction

477 Due to the design of Gamma-ray Cherenkov Telescope (GCT) as a dual-mirror  
478 Schwarzschild-Couder telescope, it is capable of a 9° Field of View (FoV) while  
479 simultaneously reducing the plate scale by a factor of  $\sim 3$  compared to single-  
480 telescope designs. The resulting plate scale value for the GCT design is  $\sim 39.6 \text{ mm}/^\circ$   
481 [2]. This large reduction in plate scale allows for a much more compact camera,  
482 for which novel opportunities in photosensor technology exist [3]. The appropriate  
483 photosensor angular pixel size for an Imaging Atmospheric Cherenkov Telescope

intro: talk  
about  
benefit of  
high FoV

<sup>484</sup> (IACT), in order to be less than the FWHM of a typical 1 TeV gamma-ray image,  
<sup>485</sup> is  $\sim 0.2^\circ$ . Correspondingly, the GCT camera requires a pixel less than  $\sim 8$  mm. The  
<sup>486</sup> camera that has been developed for GCT is appropriately known as the Compact  
<sup>487</sup> High Energy Camera (CHEC).

<sup>488</sup> Two designs have been implemented for CHEC, each featuring a different multi-  
<sup>489</sup> pixel photon-counting sensor technology. A Multi-Anode Photomultiplier Tube  
<sup>490</sup> (MAPMT) based camera known as CHEC-M was the first to be commissioned,  
<sup>491</sup> and received its inauguration on the GCT telescope structure at the Observatoire  
<sup>492</sup> de Paris-Meudon in November 2015 [4]. A second camera, known as CHEC-S, is  
<sup>493</sup> currently undergoing commissioning at the Max-Planck-Institut für Kernphysik in  
<sup>494</sup> Heidelberg, Germany. This camera utilises Silicon Photomultipliers (SiPMs) as  
<sup>495</sup> a photosensor. CHEC-S also features upgrades the digitisation chain that were  
<sup>496</sup> developed since the commissioning of CHEC-M.

<sup>497</sup> This chapter will describe the components of the Compact High Energy Camera  
<sup>498</sup> (CHEC), covering the photosensor, Front-End Electronics (FEE) and Back-End  
<sup>499</sup> Electronics (BEE). These descriptions will be focussed on the factors contributed  
<sup>500</sup> by the components that have a significant influence on the low-level calibration  
<sup>501</sup> and performance investigations covered in this thesis. Furthermore, the external  
<sup>502</sup> components and laboratory set-up will be described. Finally, the data output of  
<sup>503</sup> the camera is described, with specific focus on the characteristics of the waveform  
<sup>504</sup> readout. The calibration and analysis of these waveforms obtained from the full  
<sup>505</sup> camera electronics chain is the primary focus of this thesis.

## <sup>506</sup> 2.2 Photosensors

<sup>507</sup> For a photosensor to be useful to IACTs, it must be:

- <sup>508</sup> 1. Sensitive to Cherenkov (blue) light.
- <sup>509</sup> 2. Fast in its response to a signal, which is required to detect the prompt  
<sup>510</sup> Cherenkov shower flashes.
- <sup>511</sup> 3. Cheap, allowing large arrays of them to be combined to fill the full plate scale  
<sup>512</sup> of the telescope and provide high spatial resolution of the shower.

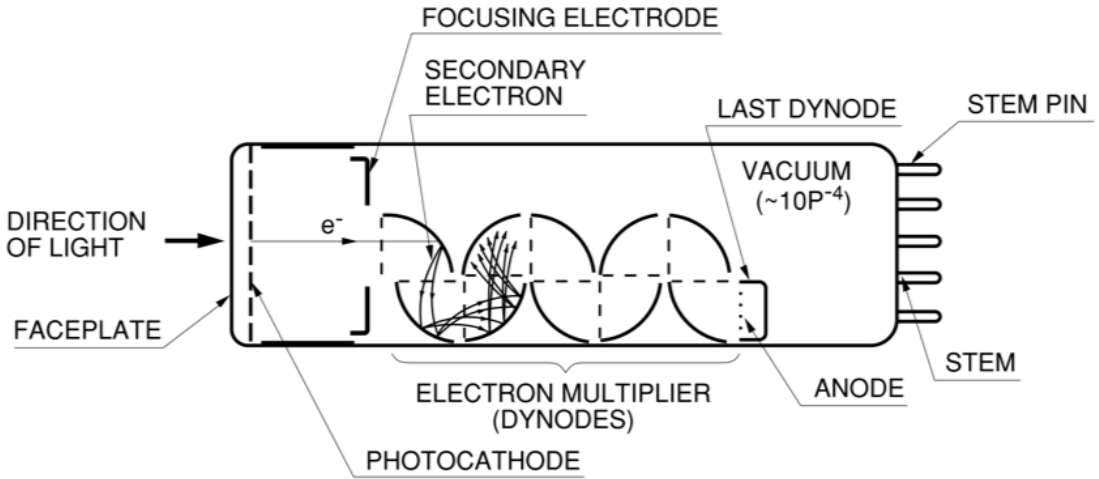


**Figure 2.1:** Common diagram of a Photomultiplier Tube (box-and-grid type) [5].

### 513 2.2.1 Photomultiplier Tubes

514 Since the inception of the Imaging Atmospheric Cherenkov Technique, the photo-  
 515 sensors used for IACT cameras have almost exclusively been Photomultiplier Tubes  
 516 (PMTs) [6]. These detectors operate as photon counting devices, where the charge  
 517 produced by a single photon is amplified into a large current signal that can be  
 518 read out. The components of a PMT are as follows (using Figure 2.1 for reference):

519 **Photocathode** Produces electrons from incident photons via the photoelectric  
 520 effect. These electrons are often referred to as “photoelectrons”. Associated  
 521 with a photocathode is its wavelength-dependant probability that photon will  
 522 be converted into a photoelectron. This is known as its Quantum Efficiency  
 523 (QE), and is determined by the compound it is made of. The photocathodes  
 524 in PMTs are typically sensitive to visible light, with a QE that peaks at  $\sim 30\%$   
 525 for  $\sim 400$  nm (for the best photocathodes) [5].

526 **Focusing Electrode** Ensures that photoelectrons produced at the edges of the  
 527 photocathode are focussed onto the first dynode.

528 **Electron Multiplier** The High Voltage (HV) across the PMT accelerates the  
 529 photoelectrons to the first dynode. Upon the impact, the dynode will release  
 530 a further amount of electrons, the number of which is proportional to the  
 531 kinetic energy of the incident electron. These secondary electrons are then  
 532 accelerated to the next dynode, which has a higher voltage than the previous  
 533 dynode. where  $A$

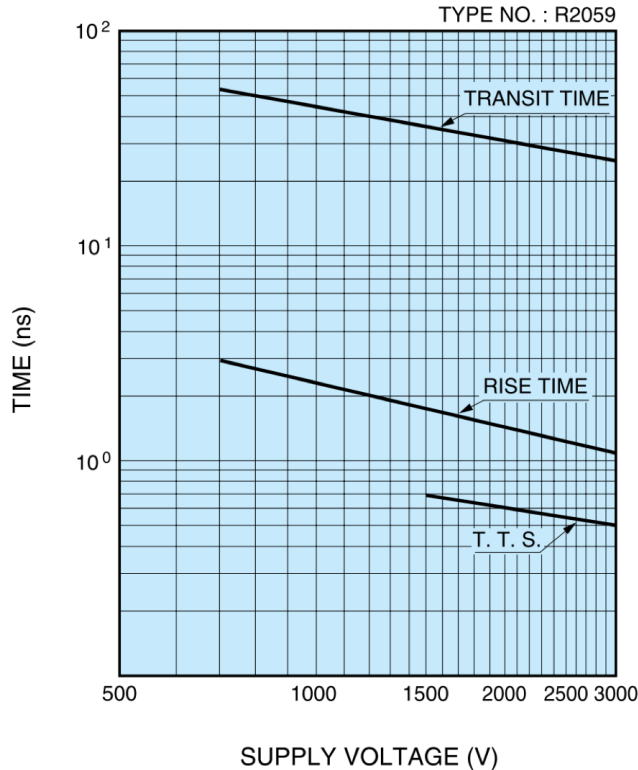


**Figure 2.2:** Typical values for the timing response of a Photomultiplier Tube [5].

534   **Anode** The total result of the dynode chain is a proportional amplification from  
 535   the initial photocathode current  $I_c$  to the output anode current  $I_a$ . The  
 536   proportionality factor is known as the gain of the photomultiplier. The gain  
 537    $G$  depends on the number of dynode stages  $n$ , and the value of high voltage  
 538   applied  $V$  [5]:

$$G = \frac{I_a}{I_c} = kV^{\alpha n}, \quad (2.1)$$

539   where  $k$  is a constant that depends on the photomultiplier design, and  $\alpha$   
 540   is a coefficient determined by the dynode material and geometric structure  
 541   (typically has values around 0.7 to 0.8).

542   Due to their wide usage across many fields, PMTs are available at a very  
 543   reasonable cost. The timing response of PMTs faithfully reproduce the incident  
 544   light pulse, however the anode's pulse rise time property does modify the response  
 545   slightly [5]. Additionally, there is a delay in signal due to the electron transit time  
 546   along the dynode chain. This transit time has an associated "transit time spread"  
 547   due to the different paths the electrons may take in the dynode chain. These time  
 548   response characteristics are dependant on the dynode structure and applied voltage.  
 549   Examples of the typical timing response values are shown in Figure 2.2.

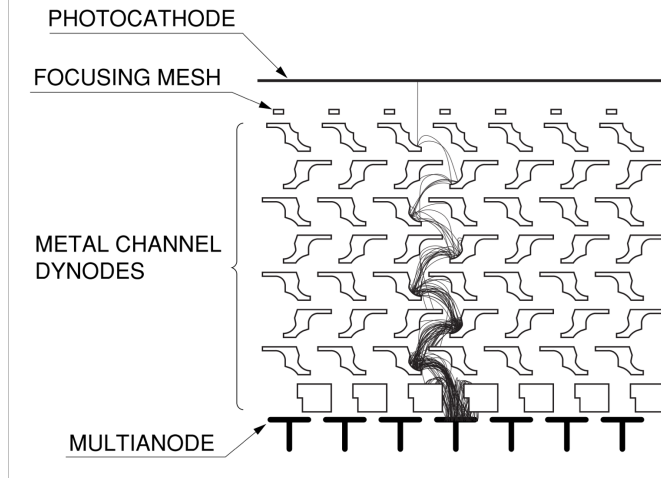


**Figure 2.3:** Electrode structure of a Multi-anode Photomultiplier Tube, demonstrating an example electron multiplication trajectory [7].

550 Beyond their low QE, a second disadvantage of a PMT is its high voltage  
 551 requirement [6]. Furthermore, since PMTs generally have  $\sim 10$  dynode stages,  
 552 Equation 2.1 dictates that a small change in voltage will result in a large variation  
 553 in gain. The high voltage supply therefore needs to be extremely stable [5]. This  
 554 is particularly unfavourable for the application of PMTs in IACTs, due to the  
 555 typical remoteness of the telescopes. A third disadvantage is the robustness of  
 556 a PMT, as they are very sensitive to light and can be permanently damaged if  
 557 exposed to bright sources. This limits the amount of observation time that is  
 558 safe for IACTs, and considerations such as the moon's location in the sky need  
 559 to be considered [Knoetig2013].

### 560 2.2.2 Multi-Anode Photomultiplier Tubes

561 In order to be compatible with the reduced plate scale of the telescope, more  
 562 compact options than PMTs must be found. An extension to the PMT technology  
 563 is the Multi-Anode Photomultiplier Tube (MAPMT). This photosensor consists  
 564 of many PMTs arranged in a compact grid to provide position-sensitive detection  
 565 of light. A diagram of the internal dynode structure for MAPMTs is shown in  
 566 Figure 2.3. The chosen MAPMT model for CHEC-M is the Hamamatsu H10966B .  
 567 This flat panel type MAPMT features an  $8 \times 8$  multianode, resulting in 64 pixels per  
 568 MAPMT. The entire module's diameter is 49 mm, while each pixel has a diameter of  
 569  $\sim 6$  mm. It provides a QE of  $\sim 30\%$  at 400 nm wavelength, a typical gain of  $3.3 \times 10^5$ ,  
 570 and a typical anode rise time and transit time of 0.4 ns and 4 ns, respectively [8].

571 An important concern when using an MAPMT is the crosstalk. This is the  
 572 measure of how accurately the signal readout retains its positional information.

	P1	P2	P3	P4	P5	P6	P7	P8	
P1	100	1.3	—	—	—	—	—	—	P8
P9	1.4	0.3	—	—	—	—	—	—	P16
P17	—	—	0.1	0.8	0.2	—	0.2	1.2	P24
P25	—	—	0.5	100	0.7	—	0.7	100	P32
P33	—	—	0.1	0.9	0.2	—	0.2	1.2	P40
P41	—	—	—	—	—	—	—	—	P48
P49	—	—	—	0.3	1.3	0.3	—	—	P56
P57	—	—	—	2.0	100	2.0	—	—	P64
	P57	P58	P59	P60	P61	P62	P63	P64	

**Figure 2.4:** Example of the crosstalk present in an MAPMT, measured by using a fibre [8].

573 It is hampered by the broadening of the electron flow in the photocathode and  
 574 dynode chain. The crosstalk characteristics presented in the technical document  
 575 for Hamamatsu H10966B are shown in Figure 2.4.

### 576 2.2.3 Silicon Photomultipliers

577 For a photosensor to be considered as a replacement for the tried-and-trusted PMT  
 578 technology within IACT astronomy, it must deliver a higher QE for a comparable  
 579 cost. SiPMs, or its solid state single photon detector precursors, have been actively  
 580 developed since the 1960s [9]. They have recently matured into a feasible replacement  
 581 for traditional PMT technology, causing a transitioning trend in the majority of  
 582 fields that previously relied on PMTs. The physics behind SiPM technology is  
 583 more complicated than that of PMTs, therefore a full description of their inner  
 584 workings is reserved for Appendix A.

585 As a short summary, an SiPMs microcell consists of a single Avalanche Photo-  
 586 toDiode (APD), operated in Geiger mode (i.e. with a reverse bias voltage past  
 587 the breakdown voltage). The breakdown voltage is the voltage beyond which  
 588 the gain of an APD tends to infinity. Therefore, an incident photon (or thermal  
 589 excitation, i.e. “dark count”) which produces an electron-hole pair in the silicon  
 590 will consequently cause an avalanche of excess charge carriers, turning the silicon  
 591 conductive and producing a macroscopic current. As the charge produced in this  
 592 avalanche is essentially limited by the quenching resistor, the same charge is read

593 out irrespective of the number of incident photons. The APD operated in Geiger  
 594 mode is therefore referred to as a binary device. By arranging an array of up to  
 595 10,000 of these microcells per mm<sup>2</sup> to form an SiPM pixel, a high resolution photon  
 596 counting sensor can be produced with a large dynamic range.

597 The major factors that contribute to the appeal of modern iterations of SiPM  
 598 technology as a replacement for PMTs are outlined by Ghassemi, Sato, and  
 599 Kobayashi [10]:

- 600 • The transition probability of a photoelectron from a silicon crystal's valence  
   601 band to its conduction band is higher than the emission probability achievable  
   602 in an alkali-based photocathode. This factor results in a higher attainable  
   603 QE.
- 604 • The semiconductor properties of silicon enable a high collection efficiency  
   605 of photoelectron charge, resulting in a reduced spread in the amplification  
   606 of a single photoelectron in comparison to PMTs (in the absence of optical  
   607 crosstalk considerations, see Section 2.2.5)
- 608 • The high electrical conductance of doped silicon enables the low-voltage (of  
   609 the order of 10-100 V) operation of an SiPM.
- 610 • The high fill factor of SiPM pixels and the compactness of the tiles allow a  
   611 reduced dead space.
- 612 • The mechanical reliability in terms of its ageing/warm-up considerations is  
   613 much better than in PMTs, as well as its performance in magnetic fields.

614 Additionally, as there is no photocathode to degrade, nor possibility chance  
 615 for a damaging current to be reached (due to the quenching by the resistor),  
 616 SiPMs are very robust to excess illuminations of light. This provides IACTs the  
 617 opportunity to continue observing under bright night sky conditions, such as intense  
 618 moonlight [**Knoetig2013, Heller2017**].

619 The first, and only to date, IACT telescope to adopt SiPMs as the photosensor  
 620 is FACT (First G-APD Cherenkov Telescope). Operational since 2011, and built  
 621 on the refurbished HEGRA IACT on the Canary Island La Palma, the 1440  
 622 pixel SiPM camera is installed in combination with a 9.5 m<sup>2</sup> single mirror. As  
 623 reported by Biland et al. [11], FACT has proved SiPM technology is a viable  
 624 alternative to PMTs for future IACTs. This conclusion was reached even with  
 625 the first generation of commercially available SiPMs. SiPMs have gone through  
 626 considerable improvements since the construction of FACT.

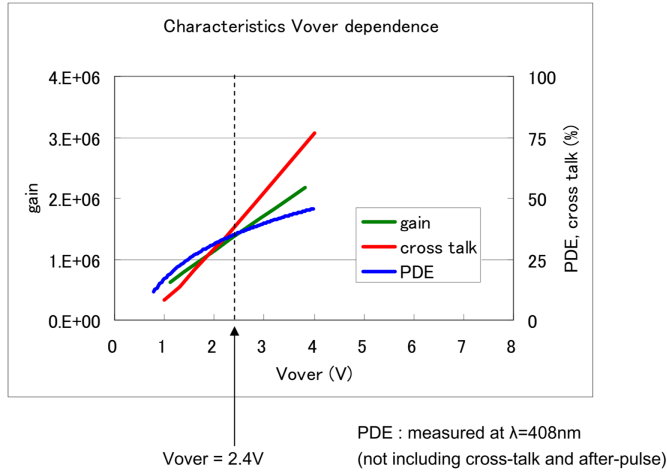


**Figure 2.5:** Performance characteristics (gain, PDE, optical crosstalk) for the SiPMs used in CHEC-S, copied from the datasheet provided by Hamamatsu [12].

The SiPMs currently used in the CHEC-S prototype are the Hamamatsu S12642-1616PA-50 tiles. These tiles have 256 pixels of size  $3 \times 3 \text{ mm}^2$ . These are combined to provide 64 camera pixels of  $\sim 6 \times 6 \text{ mm}^2$ . The performance parameters of this SiPM tile (which will be introduced in Section ??), as measured by Hamamatsu, are displayed in Figure 2.5.

#### 2.2.4 Performance Parameters of SiPMs

For a complete investigation into the performance obtained from the CHEC-S camera, it is important to understand the influence of the characteristic parameters of an SiPM.

##### Gain

As the charge read out from a SiPM microcell is quantised by the quenching resistor, the gain of an SiPM is characterised with the following simple relation between the capacitance of microcell diode  $C$  and the overvoltage  $\Delta V$  applied [13]:

$$G = \frac{C\Delta V}{e}, \quad (2.2)$$

$$\Delta V = V_{bias} - V_{br}, \quad (2.3)$$

where  $e$  is the electron charge,  $V_{bias}$  is the bias voltage, and  $V_{br}$  is the breakdown voltage. Consequently, the total charge  $Q$  output from SiPM pixel is proportional to the number of fired microcells  $N_{fired}$ :

$$Q = N_{fired}Gq. \quad (2.4)$$

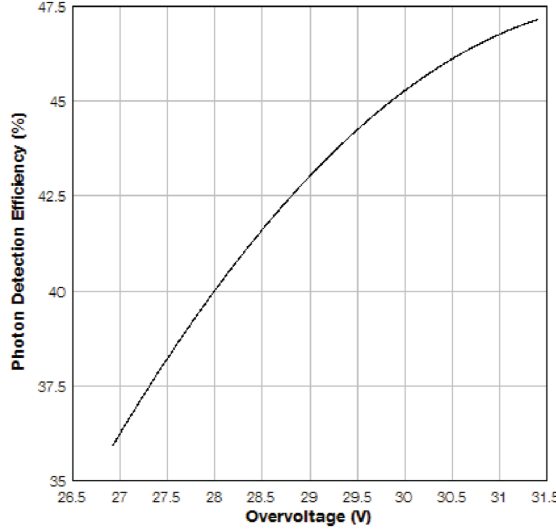


**Figure 2.6:** Example of the SiPM's PDE dependence on overvoltage [13].

644 This well-described quantisation of the charge is the reason for the high photon  
 645 counting resolution of SiPMs.

#### 646 Photon Detection Efficiency (PDE)

647 The Photon Detection Efficiency (PDE) of an SiPM is the measure of its wavelength-  
 648 dependant sensitivity to photons. Due to the microcell structure, this property  
 649 differs slightly to the QE of a PMT. Qualitatively, it is the statistical probability  
 650 that an incident photon produces an avalanche. Quantitatively, as shown in the  
 651 SensL SiPM technical note [13], it is defined as the product between the silicon's:

- 652     • Quantum Efficiency  $\eta(\lambda)$  - Likelihood of a photon producing an electron-hole  
       pair.
- 654     • Avalanche Initiation Probability  $\epsilon(V)$  - Probability of a produced excess charge  
       carrier initiating an avalanche.
- 656     • Fill Factor  $F$  - Ratio of active to inactive area.

657 Resulting in the equation:

$$PDE(\lambda, V) = \eta(\lambda) \cdot \epsilon(V) \cdot F. \quad (2.5)$$

658 The dependence of the PDE on its overvoltage is indicated in Equation 2.5  
 659 and Figure 2.6. As the overvoltage is increased,  $\epsilon(V)$  approaches 1, and the  
 660 PDE saturates.

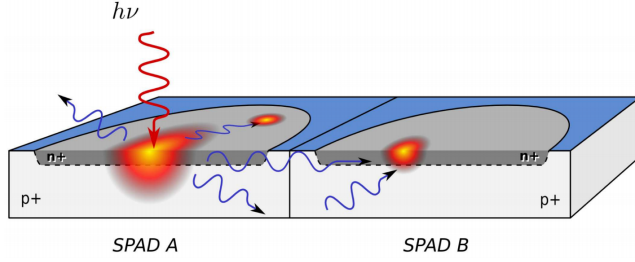


**Figure 2.7:** Illustration showing the different routes for secondary photon to produce optical crosstalk in adjacent microcells [14].

### 661 Dark Counts

662 As mentioned in the description of the behaviour of an SiPM microcell, an excess  
 663 charge carrier can be released from a semiconductor atom through thermal excitation,  
 664 which then produces an avalanche. This is commonly referred to as a “dark  
 665 count” (as there was no photon to cause the avalanche), and produces a single  
 666 photoelectron signal in the SiPM pixel. The Dark-Count Rate (DCR) is the  
 667 associated measure of this phenomena, quoted in Hz. It is a function of active  
 668 area, overvoltage and temperature. Although dark counts are also present in PMTs,  
 669 they are much more prominent in SiPMs.

### 670 Optical Crosstalk

671 During the avalanche process, it is possible for the accelerated charge carriers to  
 672 produce secondary photons. These photons are able to travel significant distances  
 673 through the silicon, and could create an electron-hole pair in adjacent microcells. The  
 674 electron-hole pair for each cell will create an additional avalanche, and possibly create  
 675 further secondary photons. In Figure 2.7 the various routes a secondary photon can  
 676 travel to a neighbouring microcell are shown. Not only can secondary photons travel  
 677 directly to the neighbouring cell, they can possibly be reflected on the boundaries of  
 678 the silicon, returning to produce an electron-hole pair in the avalanche region [14].

679 This process happens instantaneously. Therefore, according to Equation 2.4,  
 680 a single photoelectron/dark-count signal can result in a measured charge  $N_{\text{fired}}$   
 681 times greater than the expected charge of  $Gq$ . I.e. a single photon may generate  
 682 a signal equivalent to 2 or 3 photons [13]. The value associated with optical  
 683 crosstalk is its probability that an avalanching microcell will cause an avalanche in  
 684 a second cell. As with the other parameters discussed so far, the optical crosstalk  
 685 increases with overvoltage.

686 **Afterpulsing**

687 Another phenomena that can occur as a result of the avalanche is the afterpulsing.  
 688 This is where an excess charge carrier becomes temporarily trapped in a defect of  
 689 the silicon, before being released and continuing on their avalanche. The afterpulse  
 690 probability also increases with overvoltage, however modern SiPMs have severely  
 691 diminished this probability [10, 13].

692 **Temperature Dependence**

693 Aside from the dark counts, none of the SiPM parameters described in this section  
 694 have a direct dependence on temperature. However, they do all have a dependence  
 695 on overvoltage, and consequently, the breakdown voltage. The primary influence  
 696 of an increase in temperature on an SiPM is a linear increase in the breakdown  
 697 voltage. The proportionality coefficient for the SiPMs used by CHEC-S is reasonably  
 698 small, at  $60\text{ mV/C}^\circ$ . Nevertheless, a large variation in temperature would result  
 699 in a change in the SiPM performance parameters.

700 To keep the temperature controlled and low (to minimise the DCR), the  
 701 SiPMs in CHEC-S are thermally bonded to a liquid cooled faceplate (Figure 2.11).  
 702 Furthermore, by changing the bias voltage in response to a change in temperature,  
 703 the same overvoltage can be maintained, therefore minimising dependence on  
 704 temperature for the parameters. This process is known as “bias compensation”,  
 705 and is mentioned again in Section 5.3.

706 **2.2.5 Excess Noise Factor (ENF)**

707 A common expression for the variation in photosensor response to a single photoelec-  
 708 tron is its Excess Noise Factor (ENF). This factor encompasses the multiplicative  
 709 errors in the amplification process for both the MAPMT and SiPM.

710 The dominating contributions to the ENF in a PMT are the fluctuations in the  
 711 secondary multiplication factor at each dynode. This is a statistical fluctuation  
 712 due to cascade multiplication. The multiplication factor can also differ across a  
 713 dynode, therefore the trajectory of the electron can change the read out amplitude  
 714 [7]. Conversely, the multiplication of charge in an SiPM is very quantised, due to  
 715 the microcells being operated in Geiger mode, and therefore functioning as binary  
 716 device. This would suggest the ENF of an SiPM is very close to 1. However, due to  
 717 the statistical fluctuations caused by the optical crosstalk and afterpulsing of the  
 718 device, the ENF is not perfect. Therefore, the ENF of an SiPM has the potential

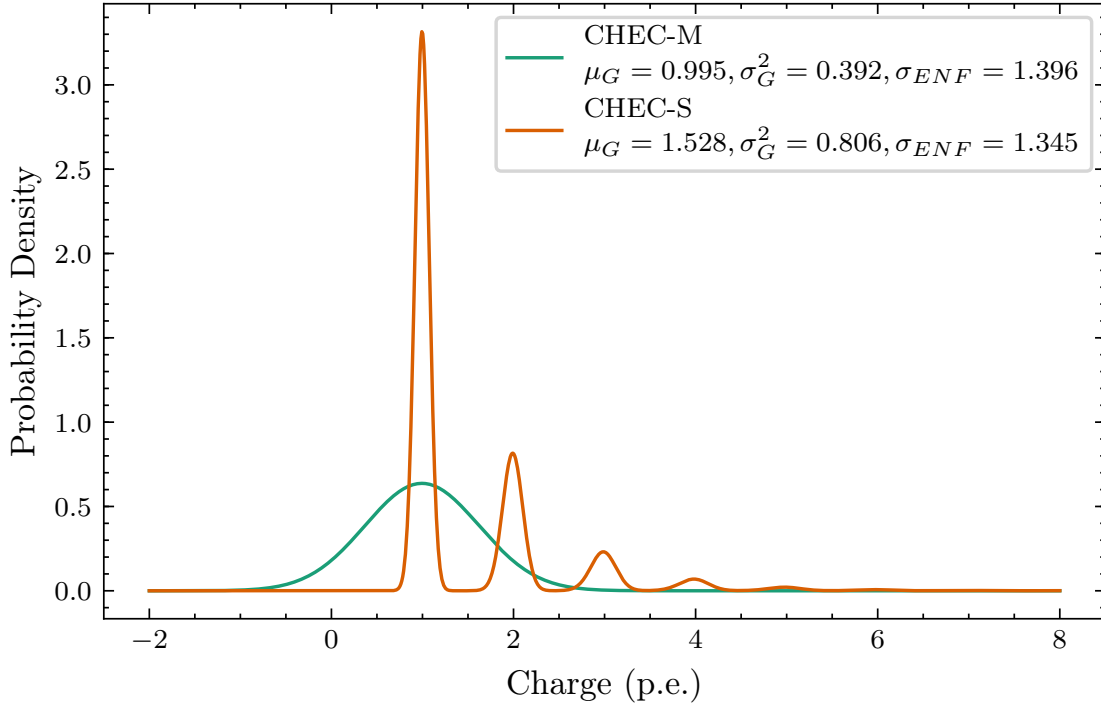


**Figure 2.8:** Comparison of the single photoelectron multiplication response between CHEC-M and CHEC-S, demonstrating the difference in ENF between the two detector types. The characteristic parameters for the photosensors, used to create this plot, are obtained from the fits described in Appendix ??.

of being worse than that of a PMT, despite the extremely high photoelectron counting resolution [15].

As described by Teich, Matsuo, and Saleh [16], the ENF  $\sigma_{ENF}$  can be expressed in terms of the photomultiplier's average gain  $\mu_G$  and the gain variance  $\sigma_G^2$ :

$$\sigma_{ENF} = 1 + \frac{\sigma_G^2}{\mu_G^2}. \quad (2.6)$$

As suggested by Equation 2.6, a perfect photomultiplier with zero multiplication variance would have an ENF of 1. This representation of the ENF can be visualised in terms of the multiplication response/probability of a single photoelectron in the photomultiplier. Figure 2.8 demonstrates this response for the MAPMTs of CHEC-M and the SiPMs of CHEC-S.

Using Equation 2.6,  $\sigma_{ENF}$  is calculated from the mean and variance of the single photoelectron multiplication response for each camera, and displayed in the legend of Figure 2.8. The ENF of the SiPMs is quite large and almost comparable to the ENF of the MAPMTs. The reason for this, as demonstrated in Chapter 7, is the high optical crosstalk (35-40 %) present in this iteration of SiPMs.

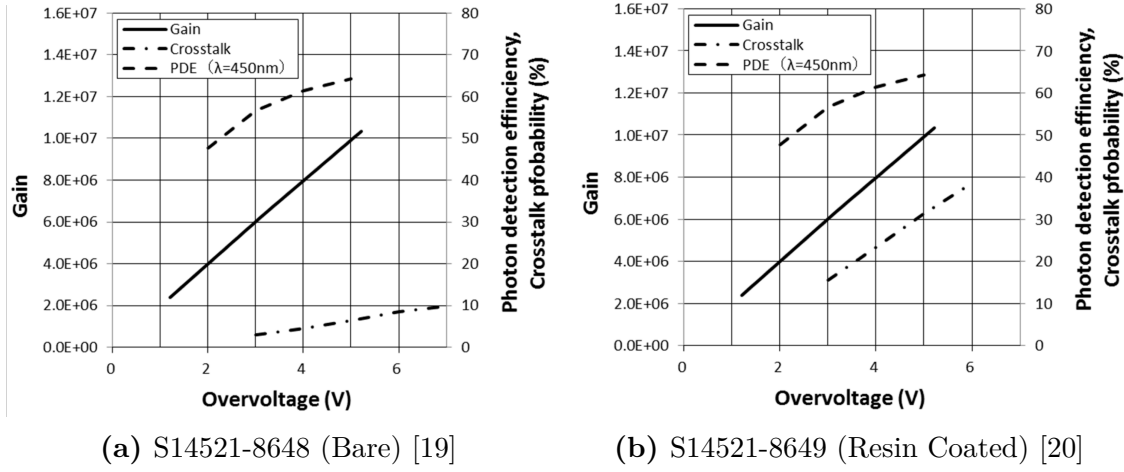


**Figure 2.9:** Characteristic performance of two potential SiPM productions for the use in future CHEC-S prototypes.

The ENF is a key ingredient to the *Charge Resolution Cherenkov Telescope Array* (CTA) Requirement introduced in Section 3.2.1, and will be further explored in the performance results of the camera in Chapter 7.

## 2.2.6 Future

It is clear from Figure 2.8 that the main area of improvement to be made in the SiPM chosen for the final design of CHEC is in the optical crosstalk. Producers of SiPMs are actively developing techniques to achieve this with minimal impedance of other characteristics such as the PDE. One simple approach to reduce the optical crosstalk is the inclusion of “trenches” between the cells [17, 18]. This is a form of optical isolation achieved by creating trenches around each cell and filling them with oxide and metal to absorb secondary photons. However, this addition can reduce the fill factor of the SiPM, thereby reducing the PDE via Equation 2.5. Although these trenches stop the majority of secondary photons, which have a direct path to the neighbouring microcell (Figure 2.7), they do not affect the photons that take an indirect route via reflection. The trenches therefore reduce optical crosstalk, but does not eliminate it completely.

Two SiPM productions by Hamamatsu are being considered for the next CHEC-S prototype. S14521-8648 exhibits a greatly reduced optical crosstalk, down to  $<10\%$  (shown in Figure 2.9a). S14521-8649 is the same silicon design, but has a protective resin coating to reduce the chance of damage to the pixels. The optical crosstalk of this second silicon is slightly higher (shown in Figure 2.9b) as the coating allows another surface for secondary photons to reflect into neighbouring

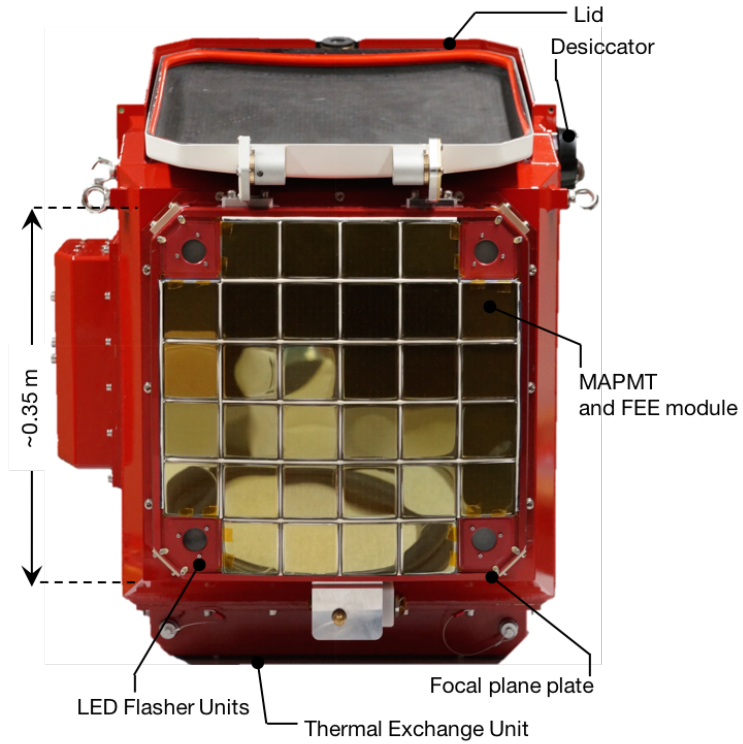


**Figure 2.10:** Focal surface of the CHEC-M prototype, annotated with key components. Adapted from Zorn et al. [21].

microcells. If it is deemed that the protective coating is unnecessary, the former SiPM will be chosen to maximise performance.

## 2.3 Camera Electronics

The fully built prototypes of CHEC-M and CHEC-S, including the fitted photosensors, are shown in Figures 2.10 and 2.11. This section will discuss the internal electronics belonging to each of the prototype cameras.

The internal electronics of CHEC can be categorised as either FEE or BEE. The distinction is made in their position in the camera, and the number of photosensors that are handled by them. A single FEE module is required per photosensor, whereas the BEE handle entire camera, obtaining the data from each of the FEE modules.

### 2.3.1 Front-End Electronics (FEE)

The Front-End Electronics (FEE) of the camera handle the recording of the signal from the photosensors into a digital data stream for storage, calibration, and subsequently the analysis. Images of the FEE modules for the two CHEC prototypes are shown in Figures 2.12 and 2.13.

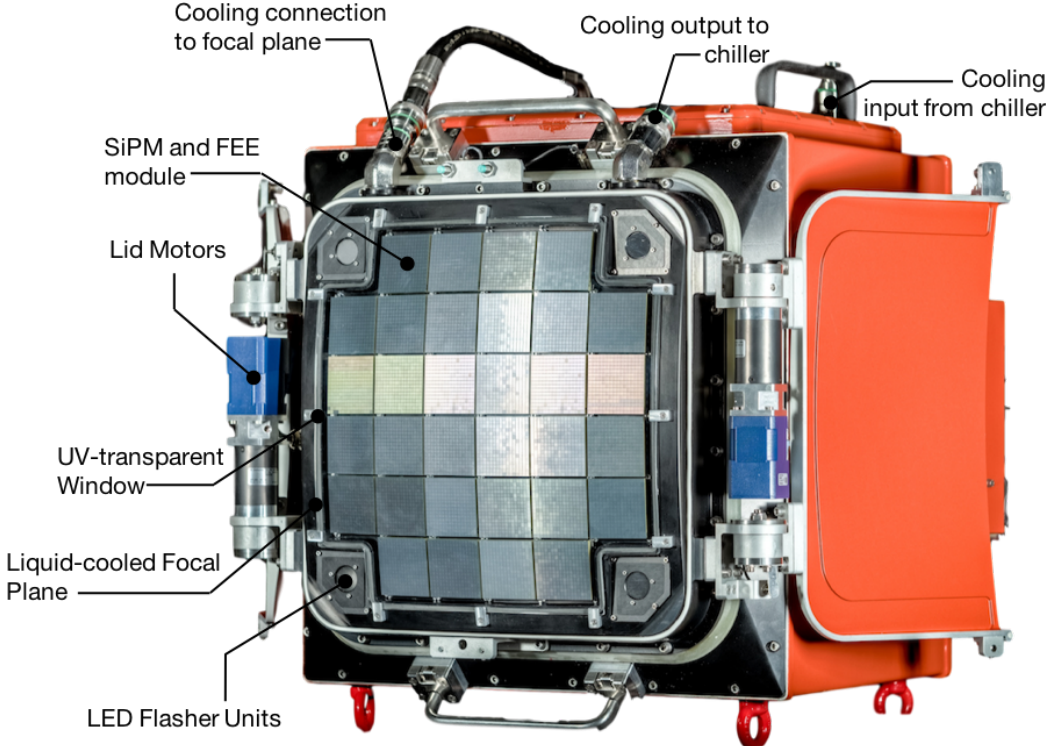


**Figure 2.11:** Focal surface of the CHEC-S prototype, annotated with key components.

770      The first stage in extracting the signal from the photosensors is the amplification  
 771      and shaping of the analogue signal. The primary reason this is performed is to  
 772      ensure the signal pulses have the optimal shape for triggering. The optimal pulse is  
 773      dictated from Monte Carlo simulations to be around 5-10 ns FWHM and a 10-90 %  
 774      rise time of 2-6 ns [21]. If the pulse shape is faster than this specification, the pulses  
 775      from individual Cherenkov photons are unable to pile up to produce a trigger due  
 776      to their time gradient (Section ?? ). Conversely, if the pulse is slower, Night-Sky  
 777      Background (NSB) photons are able to produce a trigger. The amplification and  
 778      shaping is achieved with either the external preamplifier (CHEC-M) or the amplifier  
 779      and shaper circuits built into the TARGET-C module (CHEC-S).

780      The second component of the FEE is the TARGET (TeV Array Readout with  
 781      GSa/s sampling and Event Trigger) module. These modules are composed of [24]:

- 782      • the sampling ASIC (Application-Specific-Integrated Circuit),
- 783      • the Analogue-to-Digital Converters (ADCs) for digitising,
- 784      • the triggering ASIC

ref time  
gradient

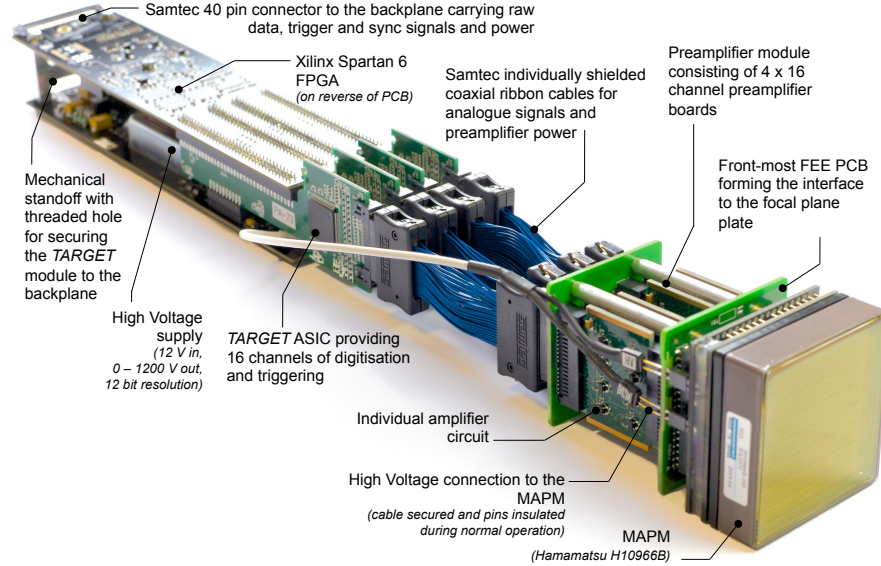


**Figure 2.12:** Image of the MAPMT connected to the CHEC-M FEE with the components labelled [21, 22].

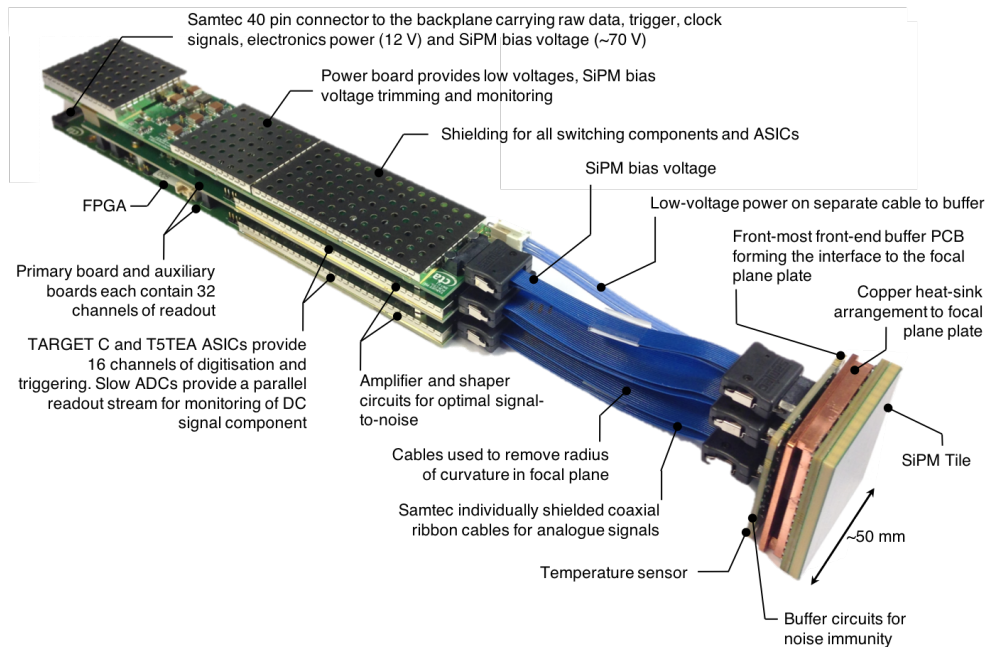


**Figure 2.13:** Image of the SiPM connected to the CHEC-S FEE with the components labelled [23].

- 
- 785     • the Field-Programmable Gate Array (FPGA) to initiate and handle the  
786       readout,
- 787     • and the internal Digital-to-Analogue Converter (DAC) for setting the opera-  
788       tional values for the components.

789 By keeping the TARGET modules limited to this small list of components, they are  
790 kept affordable and reliable. Two TARGET modules versions have been integrated  
791 into CHEC prototype cameras so far. CHEC-M utilised the TARGET-5 modules  
792 (Figure 2.12), named as such due the TARGET-5 ASIC housed in the module.  
793 The TARGET-5 ASIC is responsible for both the sampling and the triggering [25].  
794 Meanwhile, CHEC-S uses the latest TARGET module design, often referred to  
795 as TARGET-C. This version of the module has split the sampling and triggering  
796 between two ASICs to reduce the interference between the two functionalities  
797 (thereby improving trigger performance [24]). The sampling and trigger ASICs are  
798 known as TARGET-C (hence the module’s name) and T5TEA, respectively.

799 Each ASIC has 16 input channels, associated with 16 photosensor pixels.  
800 Therefore, each TARGET module contains four of each ASIC to accommodate all  
801 64 pixels on the photosensors. Both cameras contain a total of 32 FEE modules  
802 arranged in a grid, producing the curved focal surface of the camera. This 1 m  
803 radius of curvature is required by the Schwarzschild-Couder optics to ensure that  
804 the focus of the optics is constant over the field of view. The flexibility of the  
805 ribbon cables installed between the photosensor and TARGET module allow for  
806 this curved alignment, while keeping the module drawers in the camera enclosure  
807 simple. The combination of these 32 FEE results in a camera with 2,048 pixels.  
808 The focal surfaces of each camera are shown in Figures .

add chec  
camera  
figures

809 Aside from the photosensor, the version of TARGET used in the camera is  
810 the only other major differing components between CHEC-M and CHEC-S related  
811 to the waveform readout.

### 812 2.3.2 Back-End Electronics (BEE)

813 The BEE also consists of two components [21]:

814 **Backplane** Responsible for providing the power, clock and trigger to the FEE  
815 modules. It is also responsible for routing the raw waveform data from the  
816 FEE to the Data-Acquisition (DACQ) boards.

**DACQ Boards** Provides a communication link between the camera server PC and the FEE modules. This link is also used for the transfer of raw waveform data. Two boards are used, each connected to 16 FEE modules via 1 Gbps Ethernet links. The connection between a single board and the PC is via two 1 Gbps fibre-optic links. One fibre-optic link is for the downlink, the other for the uplink, ensuring communication with the camera can be maintained during data taking. Data is sent to and from the FEE modules via a custom format over UDP (User Datagram Protocol). To ensure the 1 Gbps uplink is not saturated by the traffic from the 32 1 Gbps links to the FEE, controlled delays between packet sending are utilised.

### 2.3.3 LED Flashers

An additional component of the camera electronics relevant to this thesis are the LED flashers. Located in each corner of the camera focal surface (Figures 2.10 and 2.11), these units will provide uniform illumination of the camera via reflection in the secondary mirror. The illumination provided by the LED flashes is configurable, and will allow in situ calibration of the camera’s photosensors [26].

## 2.4 Signal Digitisation

This section will detail the steps of processing the analogue signal received from each photosensor pixel. The description given here is applicable to both CHEC-M and CHEC-M.

### 2.4.1 Sampling

Designed specifically for the readout of short Cherenkov signal observed with IACT cameras, the TARGET ASIC provides high sampling rates of 1 GSa/s ( $10^9$  samples per second) per channel [24]. The sampling of the ASIC is performed by an array of “sampling cells” and “storage cells”. Each cell physically corresponds to an individual switched capacitor. The sampling array consists of two blocks of 32 cells, corresponding to 64 ns of readout in total. By operating these blocks in a “ping pong” mode, the signal from a photosensor pixel can be sampled by one block while the other block is buffered to the storage array. The storage array contains a maximum of  $2^{14} = 16,384$  cells, enabling a buffer depth of up to  $\sim 16 \mu\text{s}$  [24]. This process is performed in parallel for each of the ASIC channels, and each channel has its own sampling array and storage array. A schematic of the arrays is shown in Figure 2.14.

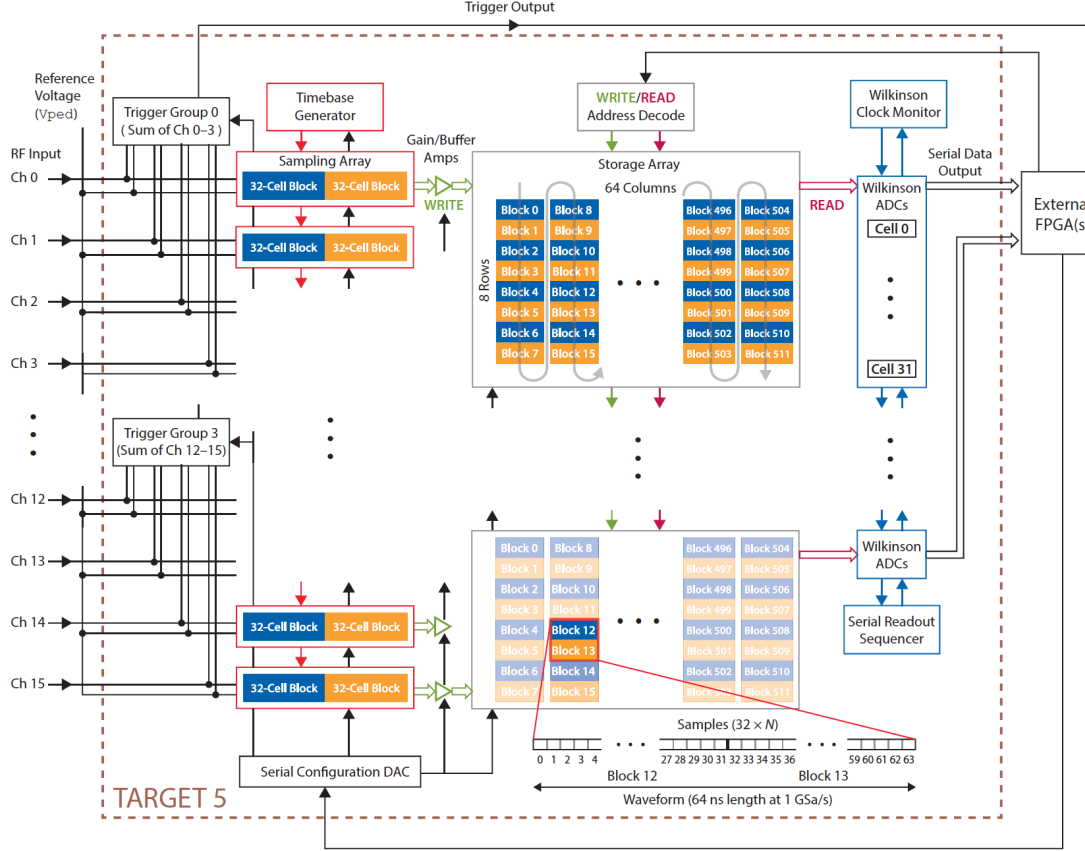


**Figure 2.14:** Functional block diagram of the TARGET 5 ASIC, demonstrating the sampling, digitisation, and read out processes [25].

#### 2.4.2 Triggering

The camera can be either externally triggered (e.g. by using a pulse generator), or internally triggered based on a signal generated by the trigger-responsible TARGET ASIC (TARGET-5 or T5TEA). As the trigger relies on a two-way communication between the FEE and BEE, it is described after introducing them both. The internal trigger operates as follows [21]:

1. The camera pixels are split into square groups of 4 neighbouring pixels. These are hereafter referred to as a superpixel. A CHEC camera therefore has 512 superpixels.
2. The TARGET ASIC responsible for the trigger continuously generates an analogue sum of the photosensor signal on a per superpixel basis.
3. If the analogue sum in a superpixel is greater than the threshold, then a digital signal is produced with a (configurable) coincidence time length. A

check  
other  
usages of  
superpixel

862 signal is produced per superpixel over the threshold, and sent to the trigger  
 863 FPGA on the backplane.

- 864 4. If there is a coincidence in digital signal between any two neighbouring  
 865 superpixels then a readout request is sent from the backplane trigger FPGA  
 866 to all of the TARGET modules.

867 **2.4.3 Digitisation and Readout**

868 Included inside the trigger request sent from the backplane is a 64-bit nanosecond  
 869 counter, known as a TACK. The value of this counter is compared to the counter  
 870 in the FPGA onboard the TARGET module to determine the look-back time in  
 871 the ASIC buffer [21]. Starting from the buffer look-back time, the analogue signals  
 872 stored in the storage capacitors are digitised with the Wilkinson ADC for the  
 873 user-specified number of cells [24]. The output of this digitisation is a list of 12-bit  
 874 samples collectively known as the waveform. The number of samples in a waveform  
 875 corresponds to the number of cells digitised, and must be a multiple of 32. Typically,  
 876 the number of samples is usually configured to be either 96 or 128 samples per  
 877 channel. The units of these raw digitised samples is referred to as “ADC” or analogue-  
 878 to-digital counts. In addition to the signal from the photosensors, the samples  
 879 contain electronic noise from the sampling and digitisation chain. Techniques to  
 880 extract the Cherenkov signal in the presence of this noise, and other noise sources  
 881 (such as NSB photons and dark counts) are discussed in Chapters 5 and 6.

882 The waveforms per channel are delivered to the TARGET FPGA, where they are  
 883 packaged into a UDP packet, and sent to the DACQ boards. The packets from each  
 884 pixel are then combined, before they are sent to the camera server PC for storage.

---

# 3

885

886

## The CTA System Architecture

887

### Contents

---

888

889	<b>3.1 Introduction</b>	24
890	<b>3.2 Requirements</b>	25
891	3.2.1 B-TEL-1010 Charge Resolution	27
892	3.2.2 B-TEL-1030 Time Resolution	30
893	3.2.3 B-TEL-1295 Pixel Availability	31
894	<b>3.3 Data Level and Flow Model</b>	31

895

897

---

898

### 3.1 Introduction

899 Due to the large scope of CTA, in both its construction and operation, a formal  
900 approach towards a system architecture was adopted [27]. One important aspect  
901 within this architecture is the distinction between the CTA Consortium and the  
902 CTA Observatory. The CTA Consortium is a group of scientists responsible for  
903 directing the science goals of the observatory, and for developing software and  
904 hardware (including cameras), which are supplied to the observatory as in-kind  
905 contributions. The consortium consists of 200 institutes across 31 countries [28].  
906 Conversely, the CTA Observatory is the major astronomical facility that acquires  
907 the science data and delivers them to a wide user community as an open observatory.  
908 The CTA Observatory gGmbH is the legal entity for CTA in the preparation for  
909 the implementation of the CTA Observatory, and works in close cooperation with  
910 the consortium during this process [29].

911 The purpose of the CTA Architecture is to ensure a coherent view of the  
912 functionality and capabilities of CTA. The CTA Architecture can then drive the  
913 pre-construction phase to guarantee:

- 
- 914     • a coherent development process,
- 915     • the seamless integration of the developed units into the final array,
- 916     • and that the performance of the final array is capable of meeting its science  
917        goals.

918   During this chapter I will describe two concepts that are connected to the CTA  
919   Architecture that are important in the context of this thesis. Firstly, the CTA  
920   requirements which all cameras, including CHEC, must meet. Secondly, the  
921   descriptions of how data are handled in CTA, including the data flow and data  
922   level definitions.

## 923   3.2 Requirements

924   In order to ensure the science goals of CTA are achievable, and that the observatory  
925   remains operational for the full 30 year life-time, certain standards must be upheld  
926   by all components of the observatory; this is the purpose of the CTA requirements.  
927   The requirements cover every aspect of the observatory, including: the survival  
928   and operation under different environmental conditions (e.g. **B-ENV-1120 Earth-**  
929   **quake collapse prevention (South)**, **B-ENV-0320 Survival humidity**), the  
930   time allowed by the analysis pipeline for processing (e.g. **A-OBS-0810 Data**  
931   **Processing Efficiency**), the reliability of telescope components (e.g. **B-TEL-**  
932   **0520 Structure Lifetime**), and the ability to meet the expected performance  
933   under different observation conditions (e.g. **PROG-0025 Differential Sensitivity**  
934   **under Low Moonlight - North**). In order for an in-kind contribution to  
935   be accepted, it must meet the requirements defined by the observatory. These  
936   requirements are therefore the standards against which we compare the performance  
937   of CHEC, and are the primary drivers in my development of the low-level calibration  
938   and analysis. However, there exists more than 60 requirements specifically tailored  
939   for the cameras. Consequently, the full review of the camera is a large undertaking  
940   that extends beyond the scope of this thesis. Instead, only the requirements that  
941   have relevance to the topics of this thesis are discussed.

942   It is important to note that the requirements, located on the CTA Jama  
943   website [30], are currently under review and therefore subject to change. A major  
944   change that is currently under way at the time of this writing is the redefinition from  
945   units of photoelectrons to photons. Originally, a common consolidated PMT was  
946   envisioned to be used for all cameras in CTA, motivating the relevant requirements

947 to be expressed in terms of photoelectrons. However, due to the advances in sensor  
948 technology and the adoption of SiPMs by cameras such as CHEC-S, this assumption  
949 has led to problems with such a definition [31]. While one camera would measure  
950 X photoelectrons for a particular number of photons, a different camera (with a  
951 different Photon Detection Efficiency (PDE)) would measure Y photoelectrons.  
952 Additionally, the definition of the requirements in photoelectrons encourages the  
953 cameras to be optimised in terms of their Excess Noise Factor (ENF), potentially at  
954 the cost of its PDE. The measurement in photons is therefore a much more coherent  
955 expression of signal for the array, which ensures requirements are stated in terms of  
956 the cameras ability to detect the Cherenkov-shower photons, instead of the cameras  
957 ability to resolve the number of photoelectrons produced at the photocathode.

958 As the procedure of converting the requirements from photoelectrons to photons  
959 is ongoing, this thesis will contain reference to the photoelectron definition of  
960 the requirements. A copy of the requirements relevant to this thesis, in the  
961 form they exist in Jama at the time of this writing, are included alongside the  
962 discussion in this section. This is to ensure clarity about which version of the  
963 requirement definition is being referred to. Future investigations should check  
964 the latest requirement definition.

965 **3.2.1 B-TEL-1010 Charge Resolution**

**Jama Excerpt**

The required fractional charge resolution for Cherenkov signals in each Camera pixel for a specified background level of 0.125 photoelectrons/ns is given in the Figure below and Table attached. Charge measurements must be possible for 0-1000 photoelectron signals. The average charge resolution should be calculated for the reference Gamma-Ray Spectrum.

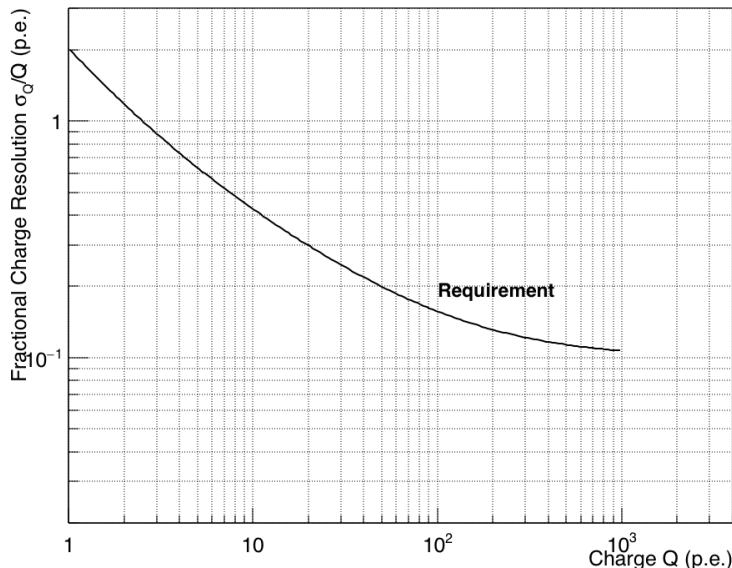


**Figure 3.1:** Fractional rms charge resolution  $\sigma_Q/Q$  per pixel for different Cherenkov light signal amplitudes, expressed in units of photoelectrons (p.e.). All sources of fluctuations, including Poisson fluctuations in photoelectron number, must be included. The true pixel charge  $Q$  is that measured in an ideal detector with the same photon-detection efficiency.

Notes: It is expected that this requirement is verified with reference to:

- Monte Carlo simulation of Cherenkov light from gamma-ray initiated showers (using a verified telescope model),
- Level-C Specification on Laboratory Measured *Charge Resolution*,
- Monte Carlo simulation of the laboratory test set-up (as a means of telescope model verification).

Note that between 1000 p.e. and 2000 p.e., some sensitivity to increasing input signal must exist.

This requirement applies to post-calibration (DL1) data.

Note that this requirement will likely need to be expanded to cover performance at higher NSB levels.

---

## 967 Definition

968 The standard criterion for the low-level camera performance used in CTA is the  
 969 *Charge Resolution*. It encompasses both the bias and the standard deviation of the  
 970 extracted charge versus the expected charge to provide a measure of the waveform,  
 971 calibration, and charge reconstruction quality. Analogous to the Root-Mean-Square  
 972 Error, the fractional *Charge Resolution*  $\frac{\sigma_Q}{Q_T}$  for a particular “true charge”  $Q_T$  (the  
 973 number of photoelectrons that would be measured directly after the photocathode  
 974 of the sensor) is defined as:

$$\frac{\sigma_Q}{Q_T} = \frac{1}{Q_T} \sqrt{\frac{\sum_{i=0}^N (Q_{M_i} - Q_T)^2}{N}}, \quad (3.1)$$

975 where  $N$  is the total number of measured charges,  $Q_{M_i}$ , with that value of  $Q_T$ .  
 976 The associated CTA requirement defines the maximum allowed values of  $\frac{\sigma_Q}{Q_T}$  for  
 977 values of  $Q_T$  between 1-1000 p.e., which must be adhered to when resolving the  
 978 signal for any camera in CTA.

## 979 Requirement Derivation

980 The uncertainty in charge reconstruction can be expressed in the form:

$$\frac{\sigma_Q}{Q} = \frac{1}{Q} \sqrt{\sigma_0^2 + \sigma_{ENF}^2 Q + \sigma_g^2 Q^2}, \quad (3.2)$$

981 where  $\sigma_0$  encapsulates noise contributions (electronic and NSB),  $\sigma_{ENF}$  is the *Excess*  
 982 *Noise Factor* (a measure of fluctuations in charge amplification, see Section 2.2.5),  
 983 and  $\sigma_g$  is the multiplicative errors in the calibration (i.e. the miscalibration)  
 984 of the gain [31][32].  $\sigma_0$  can be further expanded in terms of the two primary  
 985 noise contributions:

$$\sigma_0 = \sqrt{NSB \times t_w + n_e^2}, \quad (3.3)$$

986 i.e. the *NSB* rate (which includes the DCR for the purpose of this discussion) is  
 987 coupled with the effective signal readout window size,  $t_w = 15$  ns, and summed  
 988 with the electronic noise,  $n_e$ . A contribution from electronic noise of  $n_e = 0.87$  p.e.  
 989 is assumed, combined with a value of  $NSB = 0.125$  p.e./ns as defined in the  
 990 requirement. A value of  $\sigma_g = 0.1$  and  $\sigma_{ENF} = 1.2$  is also assumed [31]. The  
 991 resulting combination of miscalibration and noise factors in Equation 3.2 gives the  
 992 *Charge Resolution* requirement illustrated in Figure 3.1.

---

993 **Approach**

994 As it is impossible to know the “true charge” generated by a Cherenkov signal in  
 995 the field, Monte Carlo simulations must be relied upon in order to prove a camera  
 996 meets this requirement. The process for achieving this is outlined in the notes to  
 997 the requirement. It is expected that this requirement is validated in three ways:

- 998 1. With lab measurements where the camera is uniformly illuminated with a  
 999 calibrated light source.
- 1000 2. With simulations of the previous approach, in order to verify the simulation  
 1001 model of the camera.
- 1002 3. With Monte Carlo simulations of Cherenkov signal incident on the full telescope  
 1003 model.

1004 The final item is the most important in confirming the requirements are met, as  
 1005 temporally-uniform illuminations do not sufficiently test the ability to find the  
 1006 signal pulse in the waveforms for the case of a Cherenkov-shower illumination. The  
 1007 prior items are important to verify that the *Charge Resolution* result obtained  
 1008 in the final item is applicable to the real camera, i.e. the simulation model of  
 1009 the camera is accurate.

1010 The software package `sim_telarray` (Chapter 4) stores the “true charge”  
 1011 generated at the photocathode for each shower event into the output file. Therefore,  
 1012 with an accurate simulation model of the camera, it is an appropriate package  
 1013 for investigating a camera’s performance against this requirement. However, in  
 1014 order to ensure Poisson fluctuations in photoelectron number are included, as per  
 1015 the requirement, when using the “true charge” stored in the simulation file, the  
 1016 corrected form of Equation 3.1 is

$$\frac{\sigma_Q}{Q_T} = \frac{1}{Q_T} \sqrt{\frac{\sum_{i=0}^N (Q_{M_i} - Q_T)^2}{N} + Q_T}. \quad (3.4)$$

1017 With the form in Equation 3.4, a perfect detector that consistently reads-out a  
 1018 “measured charge” with an equal value to the “true charge” would hit the Poisson  
 1019 limit. This limit ensures realistic conclusions can be reached from the Monte Carlo  
 1020 simulations, as it is not physically possible to know the the “true charge” generated  
 1021 by the photocathode without fluctuations.

1022 **3.2.2 B-TEL-1030 Time Resolution**

**Jama Excerpt**

The rms difference in the reconstructed signal arrival time for any two simultaneously illuminated pixels in the Camera with amplitudes of five photoelectrons must not exceed 2 ns. This is for a specified background level of 0.125 photoelectrons/ns.

Notes: This requirement should be verified based on laboratory testing of a prototype at the specified background level.

1023

1024 A second important requirement concerning the signal inside the waveforms is  
1025 the *Time Resolution* requirement. While the capability to accurately locate the  
1026 signal is already assessed by the *Charge Resolution*, the purpose of this requirement  
1027 is to instead ensure that the physical camera exhibits sensible behaviour with regards  
1028 to the relative location of the signal between pixels, per event. One interpretation  
1029 of the *Time Resolution*  $\sigma_T$  is the standard deviation of the difference in pulse time  
1030 between every pixel in the camera, per event. This can be expressed as:

$$\sigma_T = \sqrt{\frac{\sum_{i=0}^N (\sum_{j=i+1}^N (T_{i-j} - \bar{T}_{i-j})^2)}{\binom{N}{2} - 1}}, \quad (3.5)$$

1031

$$\bar{T}_{i-j} = \frac{\sum_{i=0}^N (\sum_{j=i+1}^N T_{i-j})}{\binom{N}{2}}, \quad (3.6)$$

1032 where  $T_{i-j} = T_i - T_j$ , i.e. the difference between the extracted pulse time  $T_i$  for  
1033 pixel  $i$ , and extracted pulse time  $T_j$  for pixel  $j$ .  $\binom{N}{2}$  is the binomial coefficient of the  
1034 number of pixels  $N$  “choose” 2, i.e. the total number of unique pixel combinations.

1035 In this definition of *Time Resolution*,  $\sigma_T$  is calculated per event. However, the  
1036 camera is better characterised by the mean and standard deviation of  $\sigma_T$  over  
1037 multiple events. In order to meet the requirement, the *Time Resolution* should  
1038 be under 2 ns for pixels with measured charges above 5 p.e., in an environment  
1039 containing an NSB photon rate of at least 0.125 p.e./ns. Any pixel timing corrections  
1040 (described later in Section 5.5) that are required should be applied to the pulse  
1041 time extracted from the waveform. Furthermore, the *Time Resolution* does not  
1042 need to be extracted with the same approach as used in the charge extraction,  
1043 as long as the approach is justifiable.

---

<sup>1044</sup> **3.2.3 B-TEL-1295 Pixel Availability**

**Jama Excerpt**

During observations, at least 95% of all camera pixels must be available and usable for data analysis. In addition, continuous regions of non-functioning pixels must not exceed 2% of all camera pixels. Pixels excluded due to NSB levels beyond those required are not included in this budget.

<sup>1045</sup>      This requirement sets a limit on the amount of “dead” pixels that a camera  
<sup>1046</sup> is allowed to have before the entire camera is considered to be unavailable. For  
<sup>1047</sup> CHEC, which contains 2048 pixels, this imposes the following possible limitations:

- <sup>1049</sup>      • The camera may only have a maximum of 102 dead pixels. This allows 3 dead  
<sup>1050</sup> pixels per module.
- <sup>1051</sup>      • The amount of continuous pixels that are allowed to be dead is 41, therefore  
<sup>1052</sup> if an entire TARGET module dies (each module containing 64 pixels), the  
<sup>1053</sup> camera’s capabilities become insufficient for the CTA requirements. However,  
<sup>1054</sup> a maximum of two TARGET ASICs (each ASIC containing 16 pixels) are  
<sup>1055</sup> allowed to die.

<sup>1056</sup> **3.3 Data Level and Flow Model**

<sup>1057</sup> Further aspects of the CTA Architecture that are relevant to this work are the *Data*  
<sup>1058</sup> *Processing Level* definitions, and the flow between them. These definitions dictate  
<sup>1059</sup> how the data obtained from the telescopes are handled within the observatory,  
<sup>1060</sup> and are important in ensuring each telescope adopts a similar processing chain to  
<sup>1061</sup> guarantee compatibility between themselves and the pipeline framework software.  
<sup>1062</sup> Figure 3.2 shows the full hierarchy for data specification in the observatory. The *Data*  
<sup>1063</sup> *Processing Level* indicates the progression of the data along the processing chain,  
<sup>1064</sup> the *multiplicity* indicates the scope of the data, and the *classification* designates the  
<sup>1065</sup> type of the data [33]. The levels are also split according to the system responsible  
<sup>1066</sup> for them (Figure 3.3). The Observation Execution System (OES) is responsible  
<sup>1067</sup> for the control and monitoring of the CTA array components, the scheduling of  
<sup>1068</sup> observations, and the online data acquisition and processing. The responsibilities  
<sup>1069</sup> of the Data Processing and Preservation System (DPPS) include processing the  
<sup>1070</sup> observational data into science data products, producing and analysing simulation  
<sup>1071</sup> data, and the long-term preservation of data products. Finally, the Science User  
<sup>1072</sup> Support System (SUSS) will provide access to the high-level CTA data products,

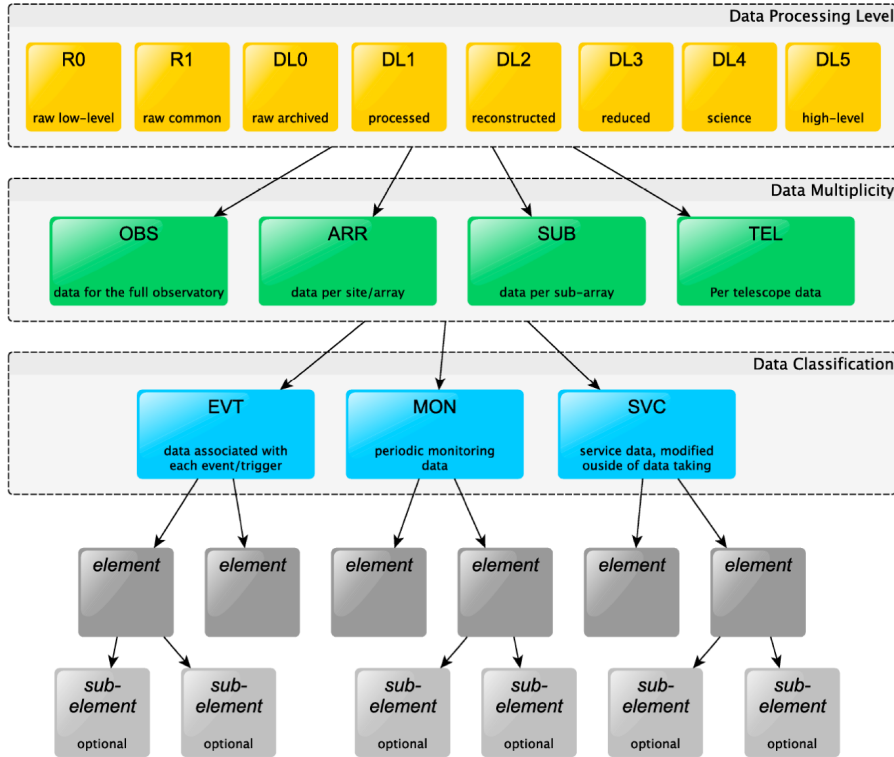


**Figure 3.2:** Hierarchy of data element names including the data level, the classifications of data (based on their rate), and data elements/groups and sub-elements/groups [33].

1073 along with the corresponding CTA software to analyse them. It also provides a  
 1074 point of access for proposal submission.

1075 As the primary focus of this thesis is on the waveform data from a single  
 1076 telescope, the rest of this section will be focussed on describing the data levels  
 1077 relevant to the *EVT classification* (Figure 3.2), and the processes used to transition  
 1078 between them. These definitions are still undergoing development within CTA,  
 1079 but the foundations are generally agreed upon.

1080 **R0 (raw low-level):** Raw waveform data, internal to the “Camera Functional  
 1081 Unit” (the official term given to an individual camera).

1082 **R1 (raw common):** Waveform data with *R1 Calibration* applied. This low-level  
 1083 calibration is unique to the camera; the calibration’s purpose is to remove the  
 1084 dependence on the behaviour of its specific electronics, such that *R1* data is in  
 1085 a common format for all telescopes. The CHEC *R1 Calibration* is described in  
 1086 Chapter 5. A selection of gain-channel is also performed for cameras with two  
 1087 channels. The data at this level are serialised to a wire format, i.e. a block  
 1088 of data sent over a network in a common way between the telescopes. This  
 1089 data level is processed by the *Online Analysis* pipeline in order to produce

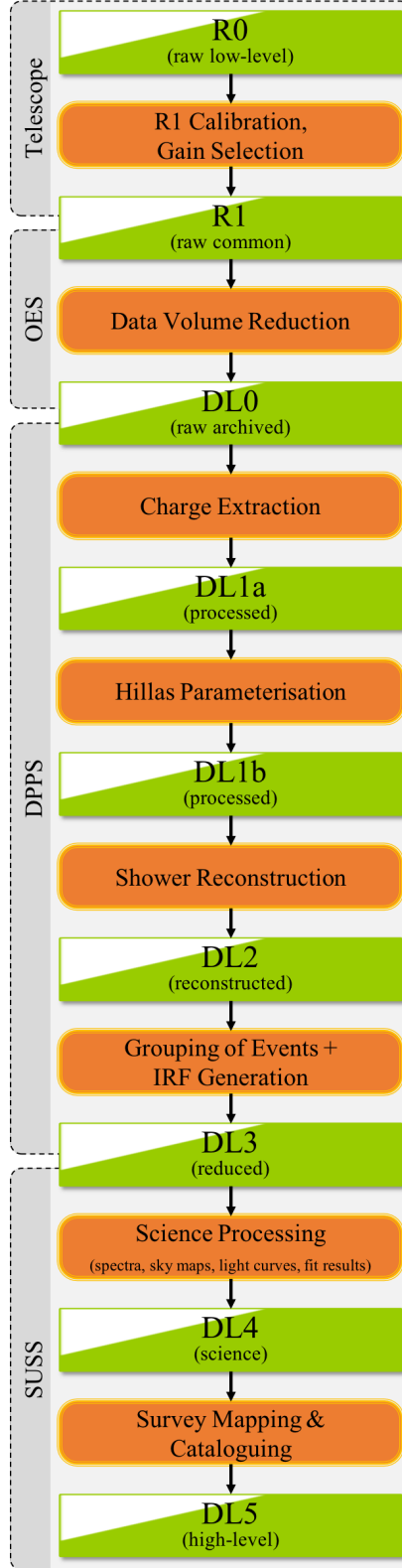


**Figure 3.3:** Simplified camera data flow, showing the *EVT*-classified data streams (in green) and the processing steps between them (orange). The levels are grouped by the systems responsible for them.

immediate science alerts. The *R1* level therefore has its own set of (relaxed) requirements to adhere to (including its own *Charge Resolution* requirement), ensuring that the minimum standard required for the *Online Analysis* and *Data Volume Reduction* is met. Further (potentially slower) calibration may be applied at a later stage (between *DL0* and *DL1a*) such that the results of the offline pipeline are of optimum quality.

**DL0 (*raw archived*):** Similar data to the *R1* level, except serialised into files and stored for long-term archival. In order to achieve this with the excessively large data volume produced by CTA, *Data Volume Reduction* must be performed to achieve two orders of magnitude reduction. The simplest form of reduction is known as zero-suppression, where only waveforms of pixels deemed to have signal are kept. This is one of the responsibilities of the OES.

**DL1 (*processed*):** The signal charge per pixel is extracted from the *DL0* waveform data, and characterised in terms of its *Hillas Parameters*. This process is handled by the DPPS offline data processing pipeline, of which `ctapipe` is a prototype. Further information about `ctapipe` can be found in Chapter 4, and details about the processes involved in this stage are described in Chapter 6.

**DL2 (*reconstructed*):** The *DL1* products (pixel charges and *Hillas Parameters*) are used to reconstruct shower parameters including energy, direction, and source particle. At this point, the *TEL multiplicity* is dropped, as the information from each telescope has been combined to perform the reconstruction, and the individual telescopes are no longer relevant. The operations involved in this stage are also performed by the DPPS offline pipeline, and are described in Chapter 6.

**DL3 (*reduced*):** Events are sorted into sets according to their type (e.g. gamma-ray candidates, electron candidates, selected hadron candidates, etc.) alongside their reconstruction parameters. Associated instrumental response characterizations and any technical data needed for science analysis are also included in this level.

**DL4 (*science*):** The *DL3* data are read into one of the CTA tools within the SUSS designed to support science data analysis. Two prototype tools developed for this purpose are `Gammapy` and `ctools` (Chapter 4). These tools enable the construction of binned data products like spectra, sky maps, or light curves, enabling the analysis of astrophysical sources.

**DL5 (*high-level*):** *DL4* data is accumulated to generate legacy datasets such as the CTA survey sky maps or the CTA source catalogue.

---

# 4

1126

1127

## Software

1128

### Contents

---

1129

1130	<b>4.1</b>	<b>Introduction</b>	.	.	.	.	.	<b>35</b>
1131	<b>4.2</b>	<b>TARGET Libraries</b>	.	.	.	.	.	<b>36</b>
1132	4.2.1	TargetDriver	.	.	.	.	.	36
1133	4.2.2	TargetIO	.	.	.	.	.	36
1134	4.2.3	TargetCalib	.	.	.	.	.	38
1135	<b>4.3</b>	<b>Monte Carlo Software</b>	.	.	.	.	.	<b>39</b>
1136	4.3.1	CORSIKA	.	.	.	.	.	40
1137	4.3.2	sim_telarray	.	.	.	.	.	41
1138	<b>4.4</b>	<b>Reduction Tools</b>	.	.	.	.	.	<b>41</b>
1139	4.4.1	ctapipe	.	.	.	.	.	42
1140	4.4.2	CHECLabPy	.	.	.	.	.	47
1141	<b>4.5</b>	<b>Science Tools</b>	.	.	.	.	.	<b>48</b>
1142	4.5.1	Gammapy	.	.	.	.	.	49
1143	4.5.2	ctools	.	.	.	.	.	49

1144

1146

---

1147

## 4.1 Introduction

1148 Arguably, software is one of the most important aspects of modern-day astronomy.  
1149 This is especially so for the Imaging Atmospheric Cherenkov Technique, due to  
1150 its reliance on high-speed digitisers, the dependence of its sensitivity on how well  
1151 one can reconstruct the shower, and the contrast between the rates of Very High  
1152 Energy (VHE) gamma rays versus the hadron shower background.

1153 In Chapter 3, the data processing steps required to transition from the digitised  
1154 waveform data obtain from the cameras to the science data released to the scientific  
1155 community are described. In order transition through this chain, a number of  
1156 software packages were developed, and are to be offered to the CTA Observatory as

in-kind contributions. This chapter provides an outline of the software packages involved in the processing pipeline for CTA and the camera commissioning for CHEC. In cases where I have been involved in the development of the software, my contributions are also mentioned.

## 4.2 TARGET Libraries

A collection of libraries have been created to operate, read-out, and calibrate the cameras containing TARGET modules (i.e. CHEC and the Schwarzschild-Couder Telescope (SCT) camera). Naturally, these are often referred to as the “TARGET Libraries”. These low-level libraries were written in C++ as they prioritise efficiency over flexibility. To enable the use of these libraries from the Python packages used in waveform reduction (described later in this chapter), a Python wrapper for these libraries is automatically generated during compilation through the utilisation of SWIG (Simplified Wrapper and Interface Generator)<sup>1</sup>.

check  
spaces after  
cpp macro

These libraries are presently stored on the CTA-SVN version control server, and installation instructions can be found at [https://forge.in2p3.fr/projects/gct/wiki/Installing\\_CHEC\\_Software](https://forge.in2p3.fr/projects/gct/wiki/Installing_CHEC_Software), provided you have permissions to the GCT Redmine.

### 4.2.1 TargetDriver

URL: [svn.in2p3.fr/cta/COM/CCC/TargetDriver/trunk](http://svn.in2p3.fr/cta/COM/CCC/TargetDriver/trunk)  
SVN revision: 32311

In order to operate the TARGET modules, the `TargetDriver` library is required. This C++ library configures the TARGET modules, and listens for the UDP packets containing the waveform data.

### 4.2.2 TargetIO

URL: [svn.in2p3.fr/cta/COM/CCC/TargetIO/trunk](http://svn.in2p3.fr/cta/COM/CCC/TargetIO/trunk)  
SVN revision: 33028

The file format used to store waveforms from the TARGET modules is the FITS (Flexible Image Transport System) format. A customised binary table, defined by `TargetIO`, is used to store the waveform data inside of the FITS file. Files containing this `TargetIO`-defined bin table are hereby referred to as TIO files. This file format was created as a temporary solution as the official CTA format is yet to be defined. FITS was chosen for two reasons:

- It is a well known file format, and uses a convenient library with extensive compatibilities with other programming frameworks/languages.

<sup>1</sup><http://www.swig.org/>

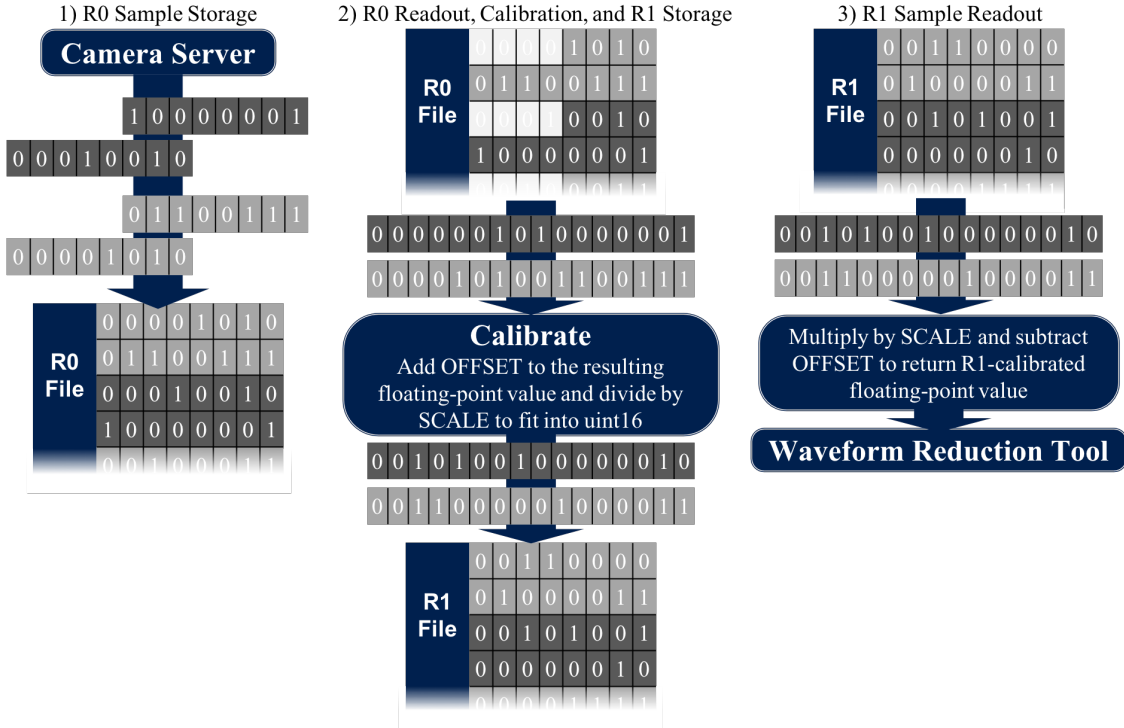


**Figure 4.1:** Overview of the data-flow for waveform samples within the TARGET libraries. Although only the samples are shown here, all other waveform data is also sent along this stream, including ASIC and Channel number, indicating the start of a new waveform.

- 1191     • As we wished to store the UDP packets with minimal data arranging, the  
1192        capability to deposit our custom-defined binary table inside the FITS file is  
1193        pragmatic.

1194     The custom binary table format is complicated to read directly with typical FITS  
1195        readers, therefore the TargetIO library is always used to read and write waveform  
1196        and header (information such as observation time) data to and from the TIO file.  
1197        TIO files can either contain *R0* (uncalibrated) or *R1* (low-level calibrated) waveform  
1198        data. Each sample in a waveform is stored to file as an unsigned 16-bit integer.  
1199        The procedure of storing the samples is demonstrated by Figure 4.1:

- 1200     1) 8-bit/char packets are sent from the TARGET FPGA and stored directly to  
1201        file. The raw waveform digital counts measured by the camera are serialised  
1202        in an unsigned 12-bit integer format, therefore the first four bits of the first  
1203        8-bit sample packet are used to indicate sample order.
- 1204     2) When reading a sample from the R0 TIO file, the first four bits are ignored, and  
1205        the remaining twelve bits are combined into an unsigned 16-bit sample. The

1206 samples are passed to `TargetCalib` for calibration. The resulting calibrated  
 1207 floating-point sample is scaled and offset to fit into an unsigned 16-bit integer  
 1208 for storage. The `OFFSET` and `SCALE` are stored in the header of the FITS  
 1209 file.

1210 3) When reading a sample from a R1 TIO file, the entirety of the two 8-bit  
 1211 packets are kept and combined. The value is returned to floating-point format  
 1212 using the `OFFSET` and `SCALE` stored in the file header.

1213 To ensure the full efficiency of the C++ library is exploited via the Python  
 1214 wrapper, I contributed the `WaveformArrayReader` C++ class, which, when passed a  
 1215 contiguous block of memory (such as a `numpy.ndarray`), promptly fills the array  
 1216 with the entire camera's waveform data for that event. For example, to read an  
 1217 *R1* TIO file from Python using `TargetIO` directly:

```
1218 1 import numpy as np
1219 2 from target_io import WaveformArrayReader
1220 3
1221 4 # Create the reader and get the number of pixels and number of
1222 5 # samples from the header
1223 6 reader = WaveformArrayReader("/path/to/file/Run17473_r1.tio")
1224 7 n_pixels = reader.fNPixels
1225 8 n_samples = reader.fNSamples
1226 9
1227 10 # Generate the memory to be filled in-place
1228 11 waveforms = np.zeros((n_pixels, n_samples), dtype=np.float32)
1229 12
1230 13 # Storage cell id for the first sample of the event per pixel
1231 14 first_cell_ids = np.zeros(n_pixels, dtype=np.uint16)
1232 15
1233 16 # Fill the arrays
1234 17 event_index = 20
1235 18 reader.GetR1Event(event_index, waveforms, first_cell_ids)
1236 19 # 'waveforms' array is now filled with entire event's waveform data
```

### 1239 4.2.3 TargetCalib

1240 URL: [svn.in2p3.fr/cta/COM/CCC/TargetCalib/trunk](http://svn.in2p3.fr/cta/COM/CCC/TargetCalib/trunk)  
 1241 SVN revision: 33028

1242 To correct for the effects of the TARGET electronics on the waveforms, `TargetCalib`  
 1243 was built. I have been responsible for the development of this package for the  
 1244 majority of its lifetime. The calibrations performed by this library are detailed  
 1245 in Chapter 5. This package has also been adopted by SCT recently. The main  
 1246 classes in the library include:

1247 **PedestalMaker** Generates the Pedestal calibration file.

1248 **TfMaker** Generates the Transfer Function calibration file.

1249 **Calibrator** Applies the Pedestal and Transfer Function calibration files to the  
1250 waveform samples.

1251 **Mapping** Handles the files containing the camera's pixel mapping, and provides an  
1252 interface to the information. This class is necessary due to the non-intuitive  
1253 mapping between physical pixel position, and order of pixel readout (Figure ).  
1254 Most commonly, this class is utilised for the plotting of camera images. The  
1255 class is compatible with the mapping of any square-pixel telescope, and  
1256 customisable to provide the mapping of the pixels in a single module, the  
1257 mapping of the superpixels, the mapping of the modules, or the neighbours  
1258 to a pixel/superpixel/module. This class will be deprecated once the central  
1259 CTA database of telescope configurations exists.

figure  
showing  
the pixel  
positions,  
camera or  
module?

1260 **CameraConfiguration** Provides an interface to certain camera-version dependant  
1261 variables. Currently the variables that might change with camera-version  
1262 (stored in the TIO file header) include number of storage cells, pixel mapping,  
1263 and reference pulse shape. The correct version of the parameter is returned  
1264 according to the camera-version provided, allowing for the automated process-  
1265 ing of the data of different camera versions. This class will also be replaced  
1266 by the central CTA database.

1267 Efforts are being made to improve the **TargetCalib**'s (more specifically the  
1268 **Calibrator** class's) efficiency in terms of both memory and processing time, as  
1269 it will need to meet the CTA Requirements for *Online Analysis* (Chapter 3). It  
1270 is possible that in the future there will be two separate **Calibrator** classes for  
1271 the *Online* and *Offline Analyses* respectively.

### 1272 4.3 Monte Carlo Software

1273 An important aspect in modern IACT analysis is the utilisation of Monte Carlo  
1274 simulations. Within CTA they are paramount in both the design of the array, to  
1275 find the most cost-effective solution that enables the attainment of its scientific  
1276 goals , and as a complement to observational data in order to reconstruct Cherenkov  
1277 showers from IACT images. Two packages are typically used for the generation  
1278 of the files containing simulated Cherenkov shower images: **CORSIKA** (C0smic Ray  
1279 SImulations for KAscade) and **sim\_telarray**. While I had no involvement in  
1280 the development of these packages, I had to learn how to use them in order to  
1281 obtain simulations containing a model of the CHEC camera.

add  
reference?

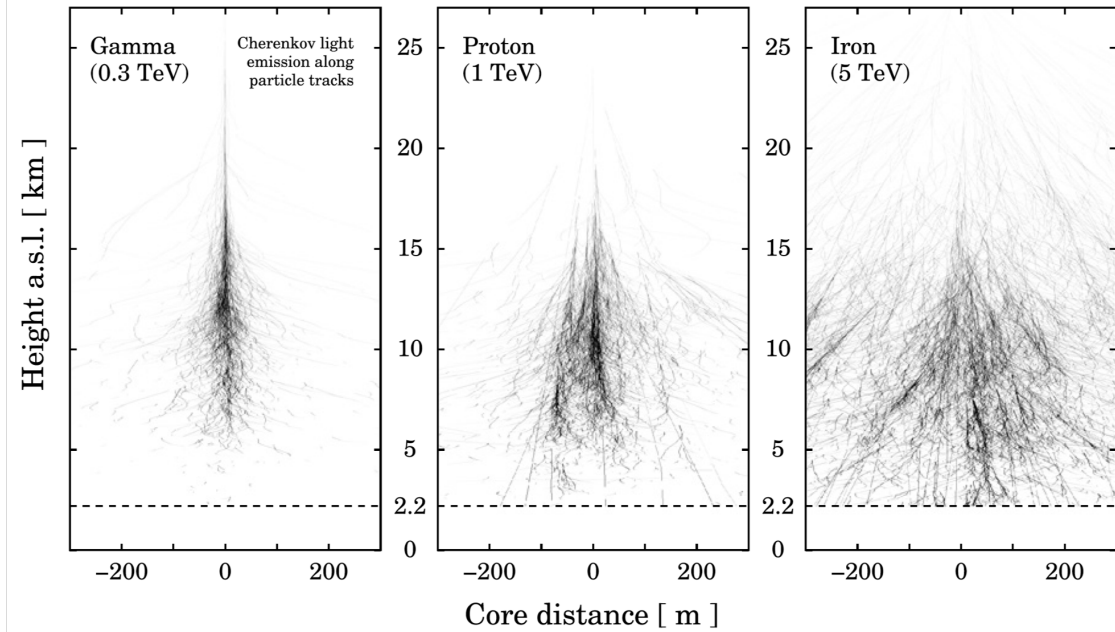


**Figure 4.2:** Cherenkov light production simulation from extensive air showers simulated by CORSIKA, for different primary particles for a site at 2200 m altitude. Darkness of the particle tracks shown increases with increasing emission of Cherenkov light [34].

#### 4.3.1 CORSIKA

URL: <https://www.ikp.kit.edu/corsika/>  
Version: 6.99

Originally developed for the KASCADE (KARlsruhe Shower Core and Array DEtector) cosmic-ray experiment, the CORSIKA package is “a program for detailed simulation of extensive air showers initiated by high energy cosmic ray particles” [35, p. i]. Given a specified astrophysical primary particle (protons, light nuclei, photons), the simulation tracks the particle, its interaction products, and its secondary decay products through the atmosphere, using the latest hadronic and leptonic interaction models. It can also simulate the Cherenkov photon production produced by the superluminal products. In combination with the IACT extension package written by Bernlöhr [34], these Cherenkov photons are tracked to a “fiducial sphere” surrounding the telescope, while including atmospheric refraction and absorption effects (Figure 4.2). Photons emitted at angles away from the telescope can be ignored to reduce the computational cost of this tracking. Photons are also simulated in bunches as opposed to individually to aid efficiency. The philosophy behind the development of CORSIKA is to provide an evolving package which accumulates the expertise from various experiments with connections to high energy and air shower physics. Due to the complexity involved in simulating extensive air showers, this is an attractive approach to minimise effort and errors, and ease the comparison of simulation results between experiments. As a result, CORSIKA is the most extensively

1303 used air shower simulation package in VHE astrophysics. Experiments other than  
 1304 CTA that utilise **CORSIKA** include (but are not limited to) H.E.S.S. (High Energy  
 1305 Stereoscopic System), VERITAS (Very Energetic Radiation Imaging Telescope Array  
 1306 System), MAGIC (Major Atmospheric Gamma Imaging Cherenkov Telescopes),  
 1307 and HAWC (High-Altitude Water Cherenkov observatory).

### 1308    4.3.2 **sim\_telarray**

1309    URL: <https://www.mpi-hd.mpg.de/hfm/CTA/MC/Software/>  
 1310    Version: 2018-06-12\_testing

1311 The second component in simulating the CTA observations of air showers is the  
 1312 simulation of the instrument’s response to the Cherenkov photons resulting from  
 1313 the **CORSIKA** output. This includes the optical ray-tracing of the Cherenkov photons  
 1314 from where they impacted the “fiducial sphere” in **COSIKA** through the telescope’s  
 1315 optics, the conversion of the photon into an electron by the sensors photocathode,  
 1316 the activation of the camera’s trigger, and the digitisation of the resulting signal.  
 1317 The **sim\_telarray** package, developed by Bernlöhr [34] for H.E.S.S., has been  
 1318 adopted and developed to reproduce the CTA telescopes response to Cherenkov  
 1319 light in the Monte Carlo simulation chain.

1320    Also included within the **sim\_telarray** package is the **light\_emission** package.  
 1321 This simple simulator produces **CORSIKA** output files for simple illumination cases.  
 1322 For example, one can simulate the uniform illumination of the camera focal plane.  
 1323 Therefore, using this **CORSIKA** output file as input to **sim\_telarray** will reproduce  
 1324 the illumination profiles often used in lab tests during the camera commissioning  
 1325 phase. This is especially useful in the Monte Carlo verification and validation  
 1326 process, discussed in Chapter 7.

## 1327    4.4 Reduction Tools

1328 Tools used to process the waveforms in order to either characterise the camera or  
 1329 progress down the data-level chain (Figure 3.3) are often referred to as “reduction  
 1330 tools”. Within the CHEC group we utilise Python for all of our waveform reduction.  
 1331 We made this choice due to its high popularity for data science and signal processing  
 1332 and its extensive library of statistical and numerical packages. The most important  
 1333 examples of these packages include:

1334    **NumPy**<sup>2</sup> Enables the efficient processing of numerical data. This is accomplished  
 1335    using their powerful N-dimensional array object known as a `numpy.ndarray`

---

<sup>2</sup><http://www.numpy.org/>

---

1336 [36]. At the lowest level, a `numpy.ndarray` is a contiguous block of memory  
 1337 much like an array in C. However, NumPy defines many methods which utilise  
 1338 optimised low-level C and Fortran operations to process the contained data  
 1339 in the most efficient way possible, often performing better than handwritten  
 1340 C or Fortran.

1341 **SciPy**<sup>3</sup> Expands on the operations one can perform on the `numpy.ndarray` object,  
 1342 providing an extensive amount of functionality useful for scientific computing,  
 1343 including statistical operations, interpolation, and signal processing.

1344 **Astropy**<sup>4</sup> Developed by the astronomy community to consolidate various common  
 1345 astronomy procedures into a single package.

1346 **Pandas**<sup>5</sup> Provides high-performance, easy-to-use, table-like data structures known  
 1347 as a `pandas.DataFrame`. Each column in the table can be processed as a  
 1348 `numpy.ndarray`.

1349 **Matplotlib**<sup>6</sup> Supplies extensive 2D plotting capabilities for Python, and is com-  
 1350 patible with `numpy.ndarray` objects.

1351 Different reduction packages may be designed with different purposes, but each  
 1352 can potentially import methods from another, which is especially simple to do when  
 1353 developing in Python. Although many other CTA groups have also adopted Python  
 1354 for their waveform reduction software, it is not a standard across CTA.

#### 1355 4.4.1 `ctapipe`

1356 URL: <https://github.com/cta-observatory/ctapipe>  
 1357 Version: 0.6.0

1358 Waveform data from each CTA telescope must be processed and the results combined  
 1359 using standardised approaches, such that the data at each processing stage is  
 1360 compatible with the next, and the resulting reduced data and shower reconstruction  
 1361 is of optimum quality. This was the motivation behind the design of the *Data*  
 1362 *Processing Level* architecture (Section 3.3). The most reliable way to ensure this  
 1363 architecture is adhered to was to create a single data processing pipeline with  
 1364 the capability to transform *DL0* waveforms into *DL2* reduced shower parameters.  
 1365 The prototype that has been developed among members of the CTA Consortium  
 1366 for this purpose is `ctapipe`.

---

<sup>3</sup><https://www.scipy.org/>

<sup>4</sup><http://www.astropy.org/>

<sup>5</sup><https://pandas.pydata.org/>

<sup>6</sup><https://matplotlib.org/>

1367 The majority of pipeline frameworks in VHE astronomy utilise what we refer to  
1368 as a “bottom-up” approach, where the algorithms are written in low-level languages  
1369 such as C or C++, and perhaps interfaced with a high-level language such as Python.  
1370 Examples of this include the software written for H.E.S.S. (including their Data  
1371 Acquisition system [37]), and the AERIE (Analysis and Event Reconstruction  
1372 Integrated Environment) framework written for HAWC [38]. Contrary to this,  
1373 the `ctapipe` framework utilises a “top-down” approach, where algorithms are first  
1374 written in Python. Through the utilisation of `NumPy`, the majority of these Python  
1375 algorithms will process data efficiently, removing the need to write complex low-level  
1376 code. Additionally, as mentioned previously, there exists a wide scientific-computing  
1377 community in the world of Python, contributing their collective knowledge into  
1378 open-source packages. Within `ctapipe` we utilise this rich resource and benefit from  
1379 the open-source model: reducing time wasted to re-implement existing methods, and  
1380 limiting the potential for bugs to go undiscovered. However, in some complicated  
1381 applications which perform very specific tasks, it is not possible to implement an  
1382 algorithm with `NumPy` expressions efficiently. As `ctapipe` utilises `numpy.ndarray`  
1383 for the storage of data wherever it is possible or logical (including the camera  
1384 waveforms and images), the following additional options are available for processing  
1385 the data efficiently:

1386 **Numba** A Python compiler, either prior to runtime, or “just-in-time”. Allows for  
1387 the optimisation of array-oriented and maths-heavy Python code without the  
1388 need to switch to a different language.

1389 **Cython** Converts Python code into C code, which can then be compiled for easy  
1390 optimisation. Also enables the easy importing of external C or C++ code into  
1391 Python.

1392 **C/C++** The algorithm could instead be completely written in C or C++. The  
1393 code can be included into Python in a variety of ways. One way is the use of  
1394 **Cython**. A second possibility is the utilisation of **SWIG**, as we have done for  
1395 the TARGET libraries.

1396 In the remainder of this subsection, I will describe the most important areas  
1397 of `ctapipe` to which I have contributed.

---

```
ctapipe.io.containers.DataContainer:
    r0.*: Raw Data
    r1.*: R1 Calibrated Data
    dl0.*: DL0 Data Volume Reduced Data
    dl1.*: DL1 Calibrated image
    dl2.*: Reconstructed Shower Information
    mc.*: Monte-Carlo data
    mcheader.*: Monte-Carlo run header data
    trig.*: Central trigger information
    count: Number of events processed
    inst.*: Instrumental information (deprecated)
    pointing[*]: Telescope pointing positions
```

**Figure 4.3:** Print result of a `ctapipe.io.containers.DataContainer` object, showing its contents.

## 1398    **DataContainer**

1399    As `ctapipe` must be capable of processing the data from any camera indiscriminately,  
 1400    one of the most important classes in `ctapipe` is the `ctapipe.io.containers.`  
 1401    `DataContainer`. This class can be filled from any data source, thereby allowing  
 1402    the same operations to be performed on the data irrespective of camera type. One  
 1403    of my contributions to `ctapipe` was to suggest that it would be logical for the  
 1404    contents of this class to closely follow the CTA data-level definitions (Section 3.3),  
 1405    as demonstrated in Figure 4.3. Therefore, in each stage of the data processing, the  
 1406    correct data level is read, and the following data level is filled. This also easily  
 1407    allows for different data levels to be saved to file, and to be read at a later time  
 1408    for further processing along the chain.

## 1409    **EventSource**

1410    Presently in the development of CTA, a common file format has not yet been defined.  
 1411    Therefore, each camera currently uses their own data format for camera prototyping,  
 1412    such as the TIO format within CHEC. Additionally, `sim_telarray` stores the  
 1413    telescope simulation files in its own compressed data format, called HESSIO (for  
 1414    legacy reasons). In order for `ctapipe` to be fully prototyped, it must therefore be  
 1415    capable of reading in each of these file formats. One of my major contributions to  
 1416    `ctapipe` was the development of the `ctapipe.io.eventsource.EventSource` class.  
 1417    This class provides a base from which a new `EventSource` class can be created  
 1418    in order to add a file format to `ctapipe`'s compatibility list. For example, I also  
 1419    created the `ctapipe.io.hessioeventsources.HESSIOEventSource` and `ctapipe.io`  
 1420    `.targetioeventsources.TargetIOEventSource`. To create a new `EventSource` class,

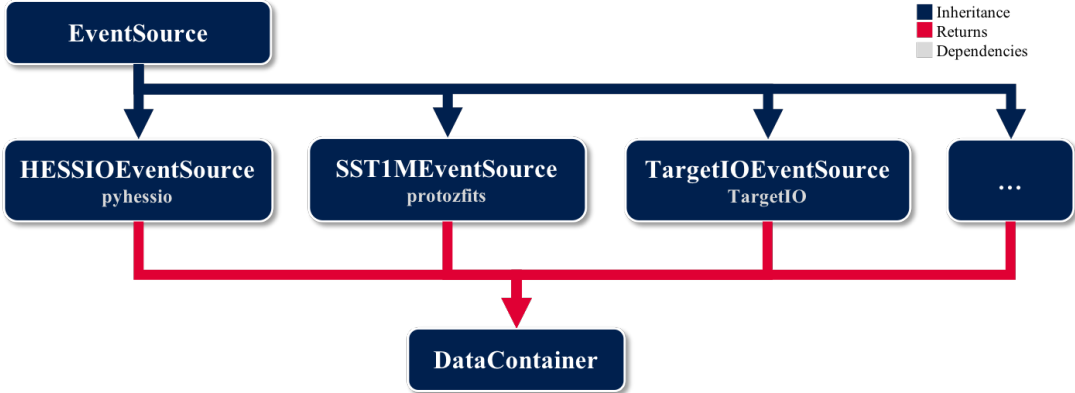


**Figure 4.4:** Functional block diagram of the `ctapipe.io.eventsource.EventSource` class, showing the inheritance, dependencies, and object returned for a selection of the existing `EventSource` classes.

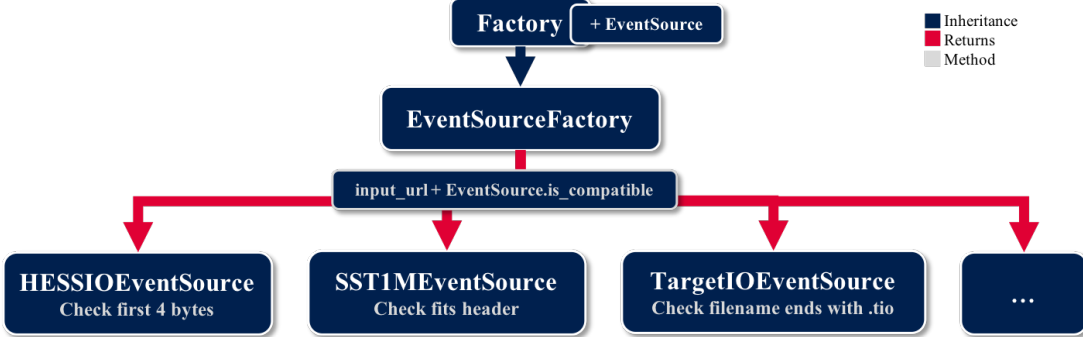


**Figure 4.5:** Functional block diagram of the `ctapipe.io.eventsourcefactory`. `EventSourceFactory` class, showing the inheritance, the potential `EventSource` classes that could be returned, and the methods used to assess the compatibility of the input URL with the `EventSource`.

one simply has to define how the data is read from the file, into the `ctapipe.io`.  
`containers`.`DataContainer`. A dependency on the external custom camera software  
may exist for the reading of the file format. One must also create an `is_compatible`  
method for checking if the file supplied is compatible with the `EventSource`. The  
functional block diagram for the `EventSource` class is shown in Figure 4.4.

## 1426    **Factory**

Alongside the variety of file formats, there also exists a variety among IACT analysis  
techniques that are applicable to CTA, such as different charge extraction techniques  
or shower parametrisation approaches (Chapter 6). Early in my involvement with

1430 `ctapipe` I identified the need for a design pattern that could enable the configuration  
 1431 of the processing chain at runtime, depending on user and file inputs. This approach  
 1432 needed to be clean and modular, otherwise such approaches can get very confusing  
 1433 and hard to maintain. As Python is a very flexible language, this problem was  
 1434 potentially easier to solve than if `ctapipe` was designed in a different language.  
 1435 The accepted solution, which I proposed and implemented, was to generate the  
 1436 `ctapipe.core.factory.Factory` class, which operates according to the “factory  
 1437 method pattern” [39]. By inheriting from the `Factory` class, one can design a  
 1438 factory that, when given a particular input, returns the corresponding class. The  
 1439 input can be designed to be anything, from a file path to a user’s input on the  
 1440 command line. One example of a `Factory` is the `ctapipe.io.eventsourcefactory`  
 1441 `.EventSourceFactory` class (Figure 4.5). Given an input URL, every `EventSource`  
 1442 is looped through, and the corresponding `is_compatible` static method is called.  
 1443 When `is_compatible` returns `True`, that `EventSource` is returned and used to  
 1444 read the file into the `DataContainer`. This functionality design makes reading  
 1445 any compatible file format into `ctapipe` extremely simple. The code snippet  
 1446 below demonstrates how to read a file and print the `event_id` for each event. It  
 1447 uses the helper function `ctapipe.io.eventsourcefactory.event_source` which  
 1448 internally handles the creation of an `EventSourceFactory` object. This snippet also  
 1449 demonstrates the simple functionality provided by the `EventSource` to easily loop  
 1450 through the events inside the file, irrespective of the file format.

```

1451
1452 1 from ctaapipe.io.eventsourcefactory import event_source
1453 2 with event_source(url) as source:
1454 3     for event in source:
1455 4         print(event.r0.event_id)
  
```

## 1457 Calibration and Waveform Reduction in `ctapipe`

1458 Another major contribution of mine has been the development and maintenance  
 1459 of the calibration and waveform reduction pipeline within `ctapipe`. As with the  
 1460 `DataContainer`, each stage is split according to the data levels. Although the *R1*  
 1461 *Calibration* is a responsibility of the Camera Functional Unit (Section 3.3) and not  
 1462 the DPPS, it was concluded that it may be useful to be able to call *R1 Calibration*  
 1463 methods from `ctapipe` during the prototyping phase. As shown in Figure 4.6, the  
 1464 `ctapipe.image.charge_extractors.ChargeExtractor` classes are included within  
 1465 this scheme. The different charge extraction methods (Chapter 6) are each selectable  
 1466 via the `ctapipe.image.charge_extractors.ChargeExtractorFactory`. An exam-  
 1467 ple of importing C code via Cython can be found for the `NeighbourPeakIntegrator`,

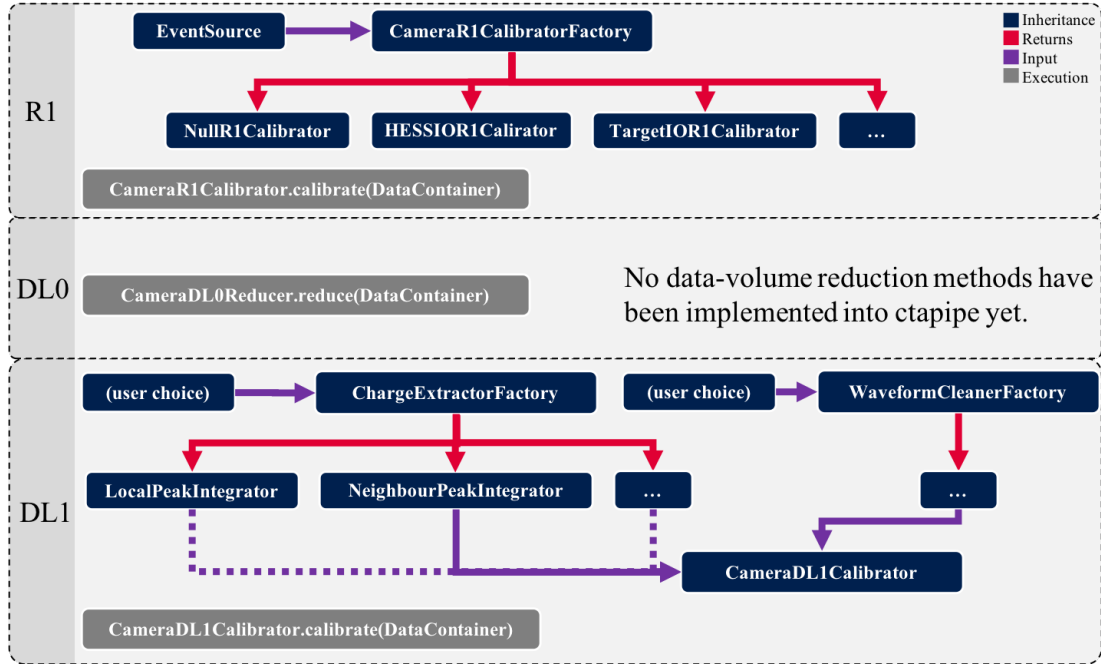


**Figure 4.6:** Functional block diagram of the `ctapipe` low-level calibration and waveform reduction classes (*R1*, *DL0*, and *DL1*).

as the loop over neighbouring pixels within a camera was too complex to optimally execute using NumPy.

The development of `ctapipe` is ongoing, but it now contains implementations of many of the common procedures used in the Imaging Atmospheric Cherenkov Technique, described in Chapter 6. It also contains some of the more complex procedures, such as the latest version of the ImPACT shower reconstruction technique developed by [40]. `ctapipe` has reached a level of maturity where people are able to utilise it for the processing of the waveform data from their prototype cameras. I have used `ctapipe` extensively for this purpose during my DPhil to analyse waveform and image data from CHEC, especially for the Cherenkov showers images obtained during the GCT on-telescope campaigns (Chapter 8). Additionally, CTA members have began to produce their own Instrument Response Functions (IRFs) using `ctapipe`. An official implementation of IRF production is intended to be included in `ctapipe` soon.

#### 4.4.2 CHECLabPy

URL: <https://github.com/cta-chec/CHECLabPy>  
 Version: ??

add version

It was decided within CHEC that we need our own waveform reduction pipeline for camera commissioning and algorithm prototyping. The purpose of creating this package was to unify the analysis code in CHEC, and supply a common

1488 method for file IO, thereby simplifying the reading of TIO files. A second primary  
 1489 motivation for this package was to provide an executable that would reduce the  
 1490 waveforms from TIO files into its signal, noise, and timing parameters, and store  
 1491 it into an accessible data format with no dependencies on the TARGET libraries  
 1492 or `ctapipe`. This therefore allows anyone within CHEC to easily and immediately  
 1493 perform investigations on a dataset.

1494 To meet these needs, I created the `CHECLabPy` Python package. `CHECLabPy`  
 1495 has been designed with a similar coding style to `ctapipe`. It operates on the  
 1496 same principle of a “top-down” approach, and utilises common scientific computing  
 1497 Python packages. Due to this similarity, algorithms that are deemed useful to  
 1498 transfer to `ctapipe`, such as the charge extraction approach we choose to use for  
 1499 CHEC, can easily be integrated into `ctapipe` in the future. The primary executable  
 1500 for reducing waveform data from TIO files is called `extract_d11.py`, which allows  
 1501 a selection of `WaveformReducer` from the command-line using a similar factory  
 1502 method to the one I designed for `ctapipe`. The reduced parameters from the  
 1503 waveforms are then stored into a `pandas.DataFrame` object, which is then saved  
 1504 to disk in the HDF5<sup>7</sup> file format.

## 1505 4.5 Science Tools

1506 Although not used in within this thesis, the science tools are important components  
 1507 to the CTA processing pipeline that are worthy of mention in this chapter. They  
 1508 will be provided to the scientific community, along with the *DL3* data, by the  
 1509 SUSS to support the science data analysis. This is an important aspect of the  
 1510 “open-observatory” operation of CTA. The purpose of the science tools is to perform  
 1511 the following tasks (as described by Deil et al. [41, p. 4]):

- 1512 • selection of a data cube (energy and positions) around a sky position from all  
   1513 event lists,
- 1514 • computation of the corresponding exposure,
- 1515 • estimation the background directly from the data (e.g. with a ring background  
   1516 model [42]) or from a model (e.g. templates built from real data beforehand),
- 1517 • creation of sky images (signal, background, significance, etc) and morphology  
   1518 fitting,

---

<sup>7</sup><https://support.hdfgroup.org/HDF5/>

- 
- 1519     • spectrum measurement with a 1D analysis or with a 3D analysis by adjusting  
 1520       both spectral and spatial shape of gamma-ray sources,  
  
 1521     • computation of light-curves and phasograms, search for transient signals,  
  
 1522     • derivation of a catalog of excess peaks (or a source catalog).

1523     As previous IACT experiments all built their own internal analysis tools,  
 1524     no common tools exist within the gamma-ray astronomy field. Therefore, two  
 1525     independently-developed tools have been proposed for this purpose: **Gammapy** and  
 1526     **ctools**. Both packages intend to improve on the sharing-of-tools aspect of gamma-  
 1527     ray astronomy, through enabling the analysis of observational data from other  
 1528     experiments, and encouraging the standardisation of the data format used (FITS).  
 1529     Although the tools were developed to perform very similar operations, such as  
 1530     the construction of binned data products (including spectra, sky maps, and light  
 1531     curves) they have opposing design philosophies.

#### 1532     4.5.1 **Gammapy**

1533     URL: <https://github.com/gammapy/gammapy>

1534     A package known as PyFACT was developed in 2011/2012 which explored the  
 1535     possibility of using the open-source Python model for VHE data analysis, utilising  
 1536     the common scientific computing packages, NumPy and SciPy [41]. Although PyFACT  
 1537     was never adopted in any official capacity, it did demonstrate that such an approach  
 1538     could be useful in the VHE astronomy field. From the inspiration by PyFACT, and  
 1539     due to the amalgamation of the Python astronomy community to create **Astropy**,  
 1540     it was decided to create **Gammapy** as an **Astropy** affiliated package. This means  
 1541     that wherever possible, it uses functionality from **Astropy**, thereby benefiting from  
 1542     the entire Python astronomy community. This design philosophy is the same  
 1543     approach adopted by **ctapipe**.

#### 1544     4.5.2 **ctools**

1545     URL: <http://cta.irap.omp.eu/ctools/index.html>

1546     Conversely, the design philosophy of **ctools** is to strictly minimise dependencies  
 1547     as much as possible. The only dependency of **ctools** is the adjacently developed  
 1548     **GammaLib** C++ shared library, which contains “all the classes, support functions,  
 1549     and some global variables that are needed to analyse gamma-ray event data” [43,  
 1550     p. 2]. The advantage of this design lies in the complete independence from the  
 1551     maintenance of other libraries. If a dependency is no longer maintained in the future,  
 1552     many problems can arise in the form of incompatibilities, such those regarding  
 1553     operating systems or the updates inside the software package itself. However,

1554 the disadvantage of this design is the larger initial development effort required,  
1555 and necessity to reimplement common methods from scratch. Much like other  
1556 science analysis frameworks in high-energy astronomy (e.g. Fermi Science Tools),  
1557 `ctools` is a collection of tools that each perform a single, well-defined analysis step.  
1558 These tools are written in C++, but can also be called directly from Python via  
1559 the `SWIG`-generated interface. However, no standard interface exists for conversion  
1560 between `numpy.ndarray` and `ctools` objects, forcing the reliance on the `GammaLib`  
1561 library for any efficient analysis.

---

# 5

1562

1563

## Calibration

1564

### Contents

---

1565

1566	<b>5.1 Introduction</b>	51
1567	<b>5.2 TARGET Calibration</b>	52
1568	5.2.1 Electronic Pedestal Subtraction	53
1569	5.2.2 Transfer Function	56
1570	<b>5.3 Photosensor Calibration</b>	61
1571	5.3.1 Gain Matching	62
1572	5.3.2 SPE Fitting	64
1573	5.3.3 Flat-Field Coefficients	65
1574	5.3.4 Dead Pixels	68
1575	<b>5.4 Saturation Recovery</b>	69
1576	<b>5.5 Timing Corrections</b>	69
1577	<b>5.6 Future</b>	70

---

1579

1580

1581

### 5.1 Introduction

1582 In order to obtain meaningful and reliable results from the camera, a number  
1583 of calibrations must be applied to the waveforms read. A primary objective of  
1584 my DPhil was to investigate the most optimal and efficient approaches for these  
1585 calibrations (in accordance with the CTA requirements described in Chapter 3),  
1586 and to determine if additional calibrations are required.

1587 When I joined the CHEC development, the calibration discussion was still in its  
1588 infancy. Some approaches had been tested in a laboratory environment [44], but  
1589 there had been little discussion on how exactly the calibrations could be applied  
1590 efficiently in an analysis pipeline, where one might not be able to use the same  
1591 detailed calibration due to limited resources (such as memory and processing time).

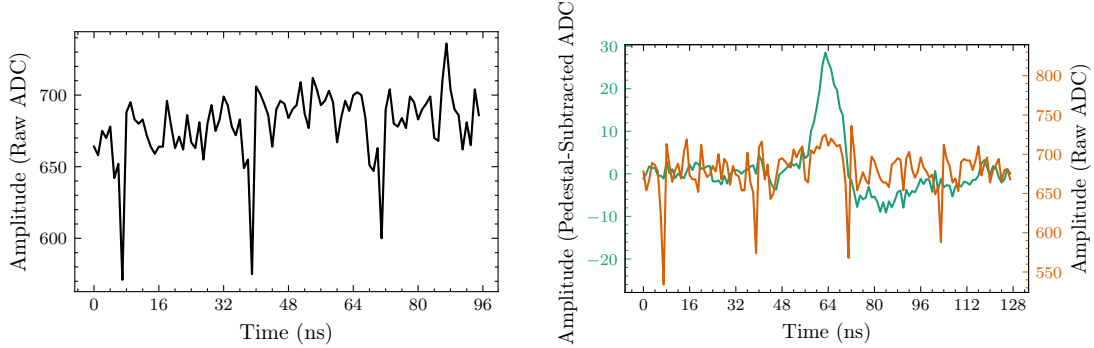


**Figure 5.1:** TARGET-C waveform as read out from CHEC-S, showing the electronic pedestal in the absence of any other input, before any calibration is applied.

**Figure 5.2:** CHEC-S waveform containing a 5 p.e. pulse, before and after pedestal subtraction.

1592 A major contribution of my DPhil was to prototype the calibration procedures,  
 1593 develop an approach for a calibration pipeline, write the software to perform such  
 1594 a pipeline, and finally assess its performance. This was an iterative process, the  
 1595 development of which is still ongoing. However, a procedure now exists that allows  
 1596 us to obtain meaningful results from the waveform data, a capability that is of  
 1597 paramount importance in the commissioning of the camera.

1598 In this chapter I will outline each of the calibration steps that are presently  
 1599 adopted for CHEC. They are introduced in the general order that they are applied,  
 1600 and split into the categories of TARGET ASIC, photosensor, and "other" calibrations.

## 1601 5.2 TARGET Calibration

1602 The calibrations described in this section relate to the TARGET module. As detailed  
 1603 in Chapter 2, the TARGET ASIC is responsible for the sampling, digitisation and  
 1604 readout of the waveform data. As a result, there are two calibrations that are solely  
 1605 related to the TARGET ASIC: electronic pedestal subtraction and the linearity  
 1606 correction via the transfer function.

1607 The functional block diagram of the TARGET ASIC in Figure 2.14 outlines  
 1608 the electronics that require calibration, and can be used as a reference in the  
 1609 following descriptions.

1610 As the calibrations in this section are very low-level, and related to CHEC's  
 1611 specific FEE, they are handled by the TargetCalib library (Chapter 4).

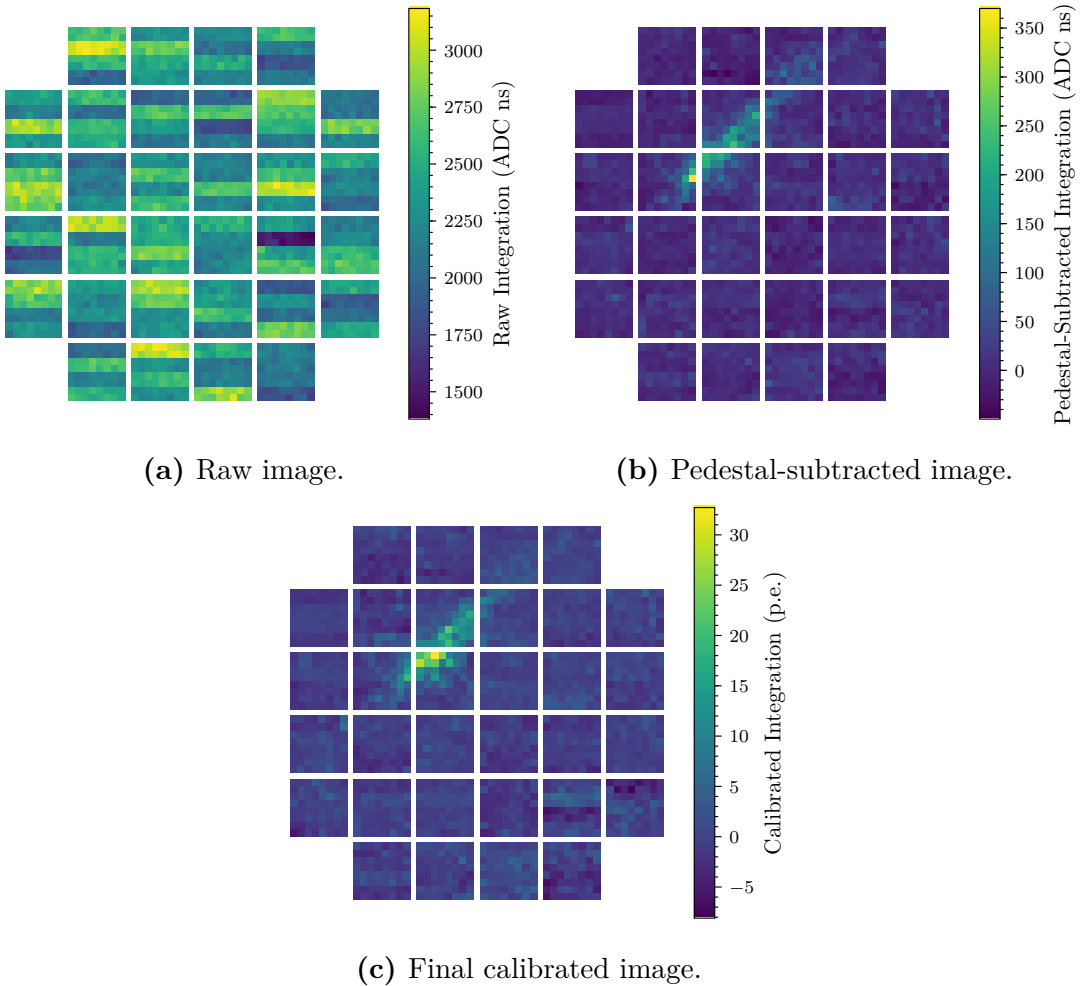


**Figure 5.3:** The same image of a Cherenkov shower taken with CHEC-M, but at different stages of calibration. An integration window was chosen using the *Neighbour Peak Finding* technique (Chapter 6) on the p.e. calibrated waveforms. The same samples were then integrated for each of the calibration stages.

### 5.2.1 Electronic Pedestal Subtraction

The most important, but also the simplest, waveform data calibration to apply is the subtraction of the electronic pedestal. Each cell in the storage array of the ASIC is a unique capacitor. For a specific  $V_{ped}$ , each capacitor has its own resulting electronic pedestal value. As each sample of the waveform corresponds to a single storage cell, each sample therefore has a unique pedestal value to be subtracted. This is apparent in Figures 5.1 and 5.2 where the variation from sample-to-sample is very large in the raw waveform, and the low-amplitude pulses are almost indistinguishable. The fluctuations in the raw waveforms between pixels is also significant, to the point where low-amplitude Cherenkov showers are undetectable in the camera (Figure 5.3a). However, the dominating variations are between ASICs. As a result,

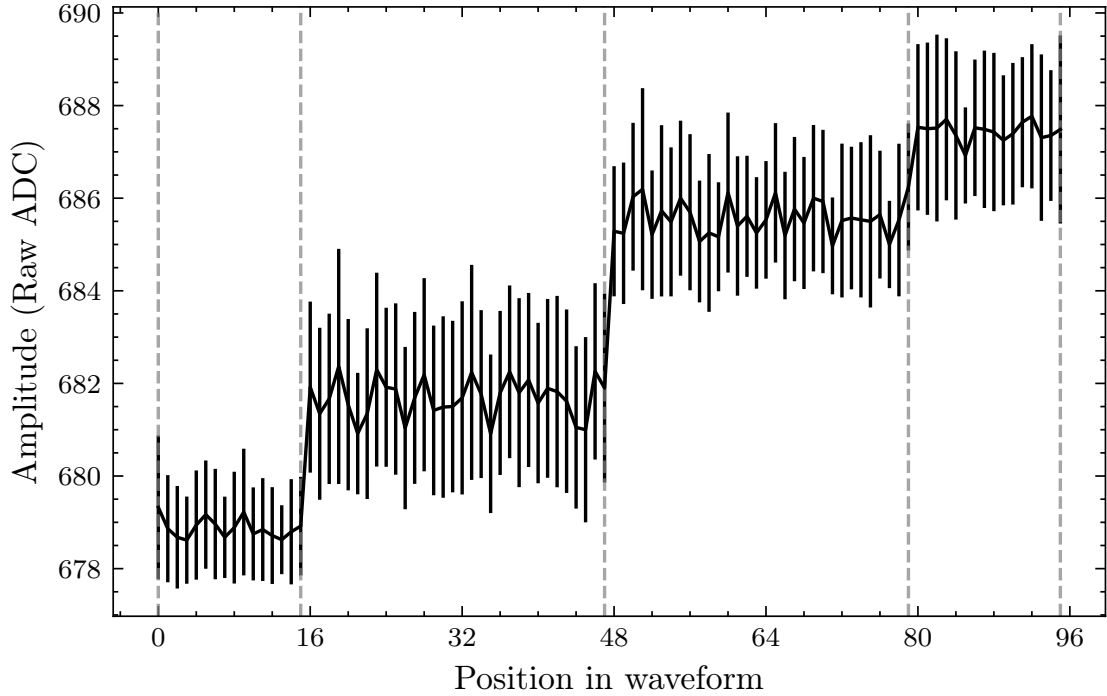


**Figure 5.4:** Average amplitude of the electronic pedestal for a single storage cell in a TARGET-C ASIC, at different positions in the waveform. Error bars indicate the standard deviation of the amplitudes. The grey dashed lines indicate the position of the block edges in the waveform for this cell. The average of the values inside each block segment equals the pedestal value stored in the lookup table for that cell, in each of those block positions.

the outlines of the ASICs are the dominating feature in camera images containing raw samples, such as Figure 5.3a. With a pedestal-subtraction calibration alone, the waveforms are transformed into a state in which a moderate amount of Cherenkov shower assessment can be performed, as demonstrated in Figure 5.3b.

There are  $2^{14} = 16,384$  storage cells per channel (for CHEC-M,  $2^{12} = 4096$  for CHEC-S), therefore one could naively conclude that there are  $32(\text{Modules}) \times 64(\text{Channels}) \times 16,384(\text{Cells})$  pedestal values to keep record of. However, an additional characteristic of the TARGET ASIC is that the pedestal amplitude depends on the position in the waveform. The source of this characteristic is due to the fact that the storage cell blocks are not entirely decoupled from each other; the discharge of one block affects adjacent blocks. This effect is apparent in Figure 5.4, where the pedestal amplitude of a single cell changes depending on the position of its parent block in the waveform. Consequently, an extra dimension of “position in waveform” must be considered in the waveform lookup table.

---

1637 **Generation**

1638 In order to perform the pedestal subtraction, one must first generate a lookup  
 1639 table of pedestal values. This can be easily obtained with a calibration run  
 1640 where the voltages across the photosensor are disabled, and forcing the camera  
 1641 to trigger (with either an external pulse generator, or internally via software)  
 1642 to obtain a large amount of waveform data. Typically around 30,000 events  
 1643 provide enough samples for every storage cell, in every waveform position, to  
 1644 have at least 10 entries. The samples are then collected as a running average  
 1645 with the dimensions [*Module, Channel, StartingBlock, Blockphase + Sample\_i*],  
 1646 where the *StartingBlock* is the storage block that the first sample in the waveform  
 1647 belongs to, *Blockphase* is the cell index within the storage block that the waveform  
 1648 begins on, and *Sample\_i* is the index of each sample in the waveform. This is  
 1649 illustrated in Figure , where for these two readout windows shown, the pedestal  
 1650 running average Pedestal [TM] [CHANNEL] [9][8:103] and Pedestal [TM] [CHANNEL]  
 1651 ] [8][12:107] will be contributed to, respectively.

include  
figure, and  
edit to use  
bp 8 and  
12

1652 The TargetCalib library handles the pedestal lookup table generation, and  
 1653 stores it into a FITS file. A new pedestal file is typically generated at the start  
 1654 of each new dataset, as the dependencies on temperature and evolution with  
 1655 time are still being investigated.

1656 **Application**

1657 To apply the pedestal, the entry within the lookup table that corresponds to each  
 1658 sample is subtracted from the waveform. The result of the subtraction can be  
 1659 seen in Figures 5.2 and 5.3b.

1660 **Performance**

1661 The primary quantification of this calibration's performance is the standard deviation  
 1662 of electronic-pedestal samples that have had separately-created pedestal values  
 1663 subtracted from them. Figure 5.5 demonstrates the performance of the pedestal  
 1664 subtraction for a TARGET-C channel, achieving a residual variation of 1.59 ADC  
 1665 (approximately 0.286 p.e.).

update  
value

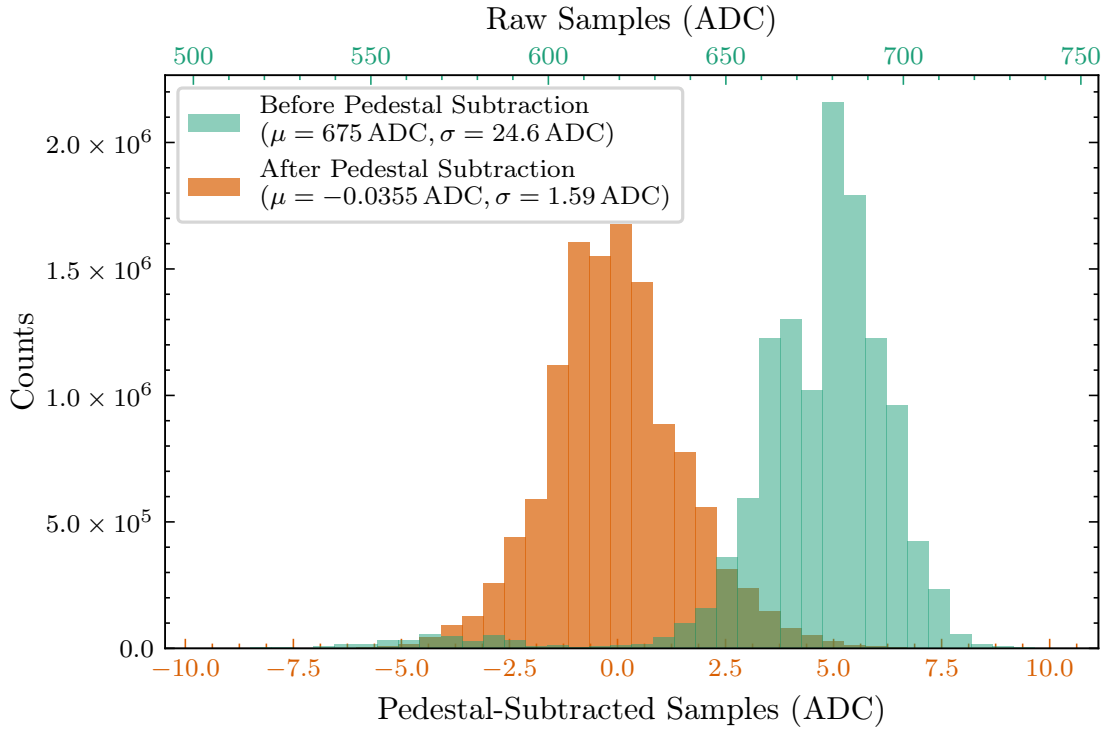


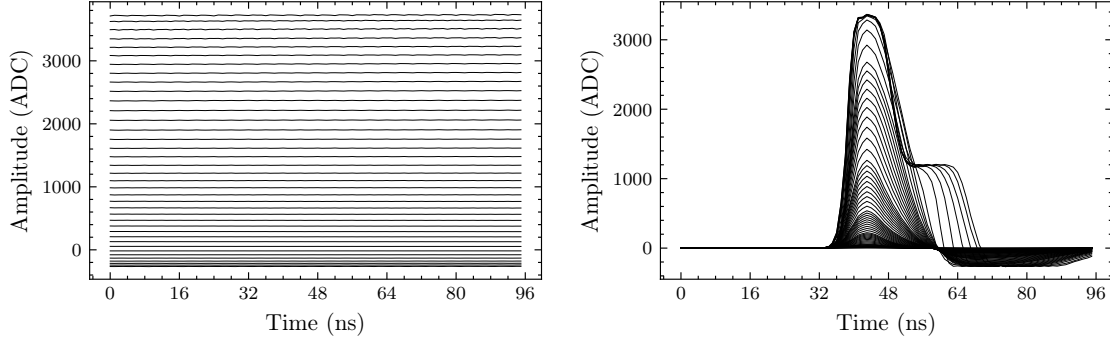
**Figure 5.5:** Spread of electronic-pedestal values before and after the pedestal subtraction for a single TARGET-C channel. The waveforms used to create the pedestal lookup table are from a different dataset to those used in these histograms. The mean  $\mu$  and the standard deviation  $\sigma$  of each distribution are also shown.

### 1666 5.2.2 Transfer Function

1667 The other calibration related to the sampling and digitisation inside the TARGET  
 1668 ASIC is caused by the non-linearities in the storing and reading of the analogue  
 1669 signal, to and from the storage cells (i.e. the charge and discharge of the switched  
 1670 capacitors). With reference to Figure 2.14, this means the non-linearity occurs  
 1671 in the steps between the sampling and storage array, and between the storage  
 1672 array and the Wilkinson ADCs. The non-linearity of these components is propagated  
 1673 to the sample readout - a sample with twice the amplitude input into TARGET  
 1674 will have less than twice the amplitude when readout.

1675 To correct for this non-linearity, a look-up table is generated to convert from  
 1676 the sample amplitude that is read out from the ASIC (in ADC) to the sample  
 1677 amplitude that is input into the ASIC (in mV). This look-up table is known as  
 1678 the Transfer Function. As one might expect, each sampling cell has its own linear  
 1679 response to account for, and therefore a look-up table is typically required at least  
 1680 per channel and per sampling cell, however a noticeably improved performance is  
 1681 observed by considering a Transfer Function per storage cell .

need to show this, maybe in TF Investigations appendix?



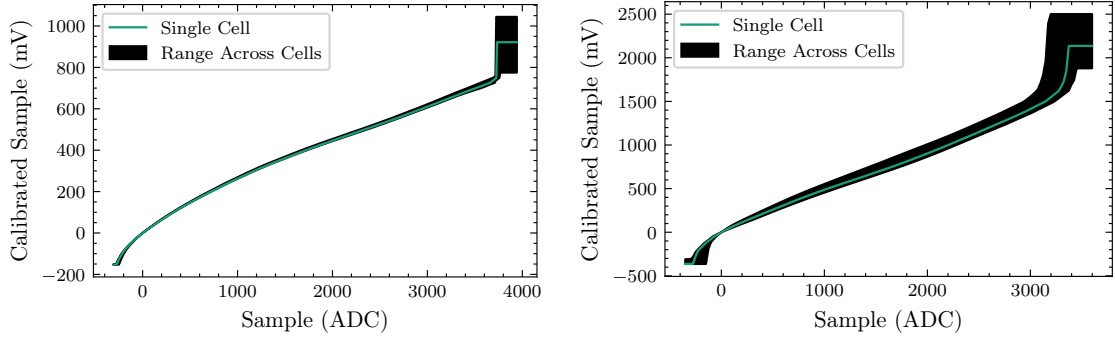
(a) DC Transfer Function input, measured with TARGET-5. (b) AC Transfer Function input, measured with TARGET-C.

**Figure 5.6:** Multiple average waveforms, increasing in amplitude. Each average contains 1000 waveforms from the same single channel. These waveforms cover the full dynamic range of the TARGET ASIC, and are used as inputs to generate the DC and AC Transfer Functions, respectively. The saturation behaviour of the TARGET-C ASIC can be seen in the high amplitude waveforms in (b).

1682 There are two forms of Transfer Function that have been considered for CHEC,  
 1683 distinguished by the type of input used to generate them. A Direct Current (DC)  
 1684 Transfer Function is created by applying a constant DC input of known voltage into  
 1685 the module, and iterating over the full dynamic range by varying the voltage. An  
 1686 AC Transfer Function is generated by inputting a pulse of a known amplitude with a  
 1687 shape expected from the photosensor, and iterating as with the DC approach. During  
 1688 previous investigations of the TARGET module, where sinusoidal signals were input  
 1689 into the module, a dependence on the signal frequency and input amplitude was  
 1690 observed that acts to further reduce the output amplitude [25, 44]. The source of  
 1691 this dependence was deemed to be due to the amplifiers, which cannot slew fast  
 1692 enough to keep up with the input signal if the frequency and amplitude are large.  
 1693 Due to the use of a pulse to generate the AC Transfer Functions, the result inherently  
 1694 includes the correction required for the frequency that the pulses correspond to.

### 1695 Generation (DC Transfer Function)

1696 During the commissioning of CHEC-M, a DC Transfer Function was used with no  
 1697 AC corrections. To generate this Transfer Function, the internal input pedestal  
 1698 voltage ( $V_{ped}$ ) setting is used to apply a DC voltage offset to the sampling ASIC.  
 1699 This pedestal voltage is provided by a commercially obtained DAC, installed on  
 1700 the TARGET-5 module. This DAC has been characterised by the supplier, so the  
 1701 voltage amplitude obtained for each setting is known.



(a) DC Transfer Function lookup table, (b) AC Transfer Function lookup table, measured with TARGET-5. Contains 64 Transfer Functions, one for each Sampling Cell.  
 measured with TARGET-C. Contains 4,096 Transfer Functions, one for each Storage Cell.

**Figure 5.7:** The Transfer Function lookup tables for a single channel.

1702 By repeating the process for Vped values from 500 mV to 1700 mV, in steps  
 1703 of 25 mV, the full dynamic range of the module is explored, covering the range  
 1704 –250 ADC to 3700 ADC (Figure ??). The running averages of the ADC samples are  
 1705 grouped and monitored according to [*Module, Channel, Sampling Cell, Input Amplitude*],  
 1706 utilising every sample in the waveform. Around 1,000 events are required to  
 1707 provide sufficient statistics.

1708 The second step in the generation of the DC Transfer Function is to linearly inter-  
 1709 polate the running averages at the ADC points defined by the user. This provides a  
 1710 lookup table of mV values with dimensions [*Module, Channel, Sampling Cell, ADC Value*]  
 1711 that can be used to provide a calibrated value for a measured ADC value. The  
 1712 lookup table for a single channel is illustrated in Figure 5.7a. This table is saved to  
 1713 a FITS file, ready for application. A fresh DC Transfer Function lookup table  
 1714 was typically created once a day during the CHEC-M commissioning.

### 1715 Generation (AC Transfer Function)

1716 When the upgrade from the TARGET-5 module to TARGET-C was made, the  
 1717 commercially provided DAC for the setting of Vped was removed, and instead  
 1718 T5TEA generates a Vped internally itself. Contrary to the commercial DAC, the  
 1719 Vped provided by T5TEA is uncalibrated. Furthermore, the voltage applied is  
 1720 individual per channel, complicating the procedure to calibrate in. As a result, the  
 1721 approach of using the internal Vped setting to generate a DC Transfer Function  
 1722 was abandoned. Instead, the decision was made to transition to an AC Transfer  
 1723 Function that uses the expected pulse shape as an input. This approach therefore  
 1724 corrects for the AC effect with the appropriate frequency. However, in order

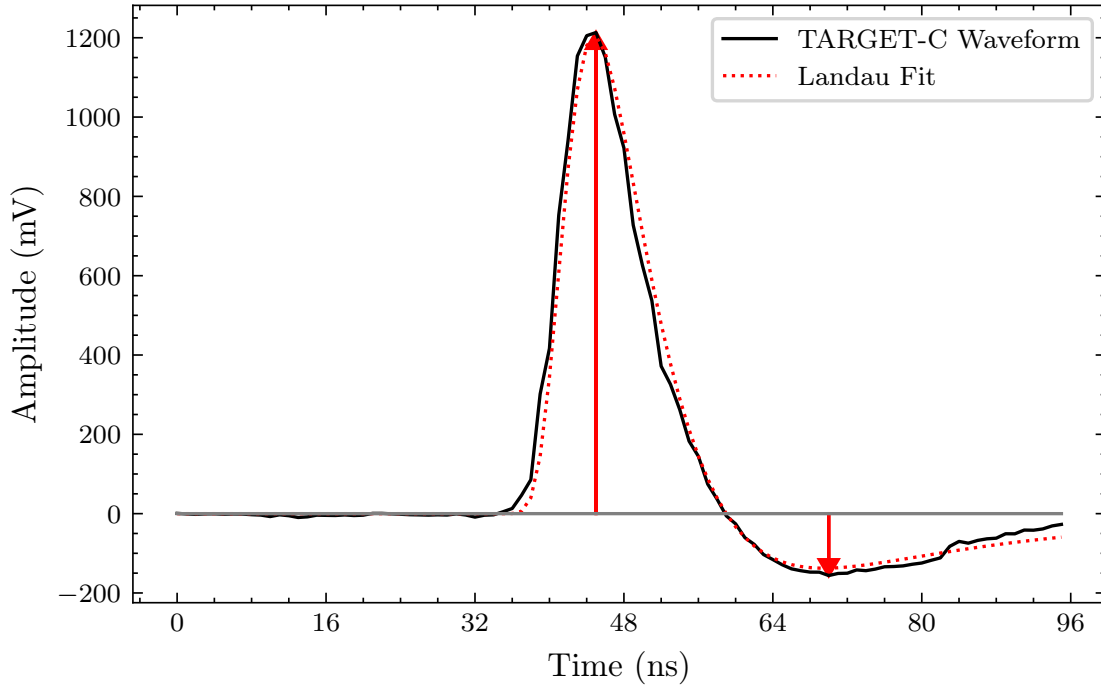


**Figure 5.8:** An example of the amplitude extraction used for generating the AC Transfer Function. The waveform is fit with two Landau functions (red curve). The samples of the waveform that occur at the time of the minimum and maximum of the fit (red arrows) are used as the inputs to the AC Transfer Function.

1725 to externally input pulses from a pulse generator the module must be removed  
 1726 from the camera. Therefore, the AC Transfer Function is only generated once  
 1727 in the present calibration pipeline.

1728 The full dynamic range is once again probed, by injecting pulses of varying  
 1729 amplitude. In order to extract the values that correspond to negative amplitudes  
 1730 in this method, the amplitude of the input undershoot is also monitored. Only  
 1731 the samples that correspond to the maximum of the input pulse (and minimum  
 1732 of the undershoot) has a “true” amplitude of the input amplitude. Therefore, to  
 1733 extract the correct samples, each waveform is fitted with two Landau functions,  
 1734 a fair approximation to the pulse shape (Figure 5.8). Consequently, only two  
 1735 samples are extracted per waveform, requiring a much larger population of events  
 1736 ( $\sim 200,000$ ) in order to generate a reliable running average grouped according to  
 1737 [*Module, Channel, StorageCell, InputAmplitude*]. It is important to note that a  
 1738 Transfer Function per storage cell was adopted for TARGET-C, as it was found to  
 1739 significantly improve the residuals (see Appendix ?? for further discussion).

1740 The second step in the generation of the AC Transfer Function is identical  
 1741 to that in the DC case. The resulting lookup table for a single channel can  
 1742 be seen in Figure 5.7b.

**1743 Application**

**1744** Irrespective of the Transfer Function type, the lookup tables are stored in a format  
**1745** which enables them to be applied identically. When calibrating an ADC sample,  
**1746** the relevant lookup table is obtained according to the channel and cell of the  
**1747** sample, and is linearly interpolated to provide the calibrated mV value for the  
**1748** specified ADC value.

**1749 Performance**

**1750** Due to its complexity and variety of approaches, the Transfer Function is still one  
**1751** of the most actively discussed aspects of the CHEC calibration. Some possibilities  
**1752** for improvement include:

- 1753** • An improved sample extraction method for the AC Transfer Function Wave-  
**1754** form,
- 1755** • The possibility for a DC approach for TARGET-C,
- 1756** • Returning to the approach described in earlier TARGET studies where the  
**1757** pedestal is included inside the Transfer Function [25],
- 1758** • Alternatives to linear interpolation, such as Piecewise Cubic Hermite Interpo-  
**1759** lating Polynomial (PCHIP),
- 1760** • Exchanging the lookup table for a parametrised regression characterisation of  
**1761** the Transfer Function (such as a high-order polynomial),
- 1762** • Deciding between "per storage cell" or "per sampling cell",
- 1763** • Inclusion of temperature corrections.

**1764** Appendix ?? provides some insight into the current progression in these ac-  
**1765** tive investigations.

**1766** Assessing the performance of the Transfer Functions is a more complicated task  
**1767** than for the pedestals. We are no longer comparing to a null signal, and instead  
**1768** comparing to an input amplitude which contains its own uncertainty, and could  
**1769** potentially be incorrect. So while the performance results may indicate that the  
**1770** residuals of the Transfer Function are small, this does not necessarily mean the  
**1771** calibration is accurate. Therefore, the most decisive performance indicator should  
**1772** be one that provides an independent measurement on the “correct” amplitude. The  
**1773** most obvious scheme fitting this requirement is the *Charge Resolution*, described  
**1774** in Chapter 3, the results of which are explored in Appendix ??.

### 1775 5.3 Photosensor Calibration

1776 The other primary component in the detector chain that requires calibration is  
 1777 the photosensor itself. As photosensors are a much more common instrument used  
 1778 in a variety of experiments, the calibration procedures required are already well  
 1779 known in the academic community. It is therefore mostly a simple case of adapting  
 1780 existing approaches to fit our requirements.

1781 The typical procedure in Cherenkov camera waveform analysis includes ex-  
 1782 tracting the signal/charge from the waveform of each pixel. This procedure,  
 1783 and the different methods to achieve it, is described in Chapter 6. The value  
 1784 extracted is typically in digitisation counts (ADC) or units of voltage, multiplied  
 1785 by time if the charge extraction approach is an integral over the waveform. For  
 1786 example, the units of the extracted charge from CHEC-S using the *Cross-Correlation*  
 1787 method (see Section 6.2.2) is mVns. Once extracted, this charge must be corrected  
 1788 for the relative efficiency of its pixel compared to the mean of the camera in  
 1789 order to achieve a uniform response (“flat-fielding”), and then converted into a  
 1790 counting unit that is common among the telescopes in the array (such as photons  
 1791 or photoelectrons), thereby simplifying the processing of array data [45]. This  
 1792 procedure is characterised in the equation:

$$I_i = \frac{A_{Qi} - A_{0i}}{\gamma_Q} \times \gamma_{FFi}, \quad (5.1)$$

1793 where

- 1794 •  $A_{Qi}$  is the charge extracted in units of mVns for pixel  $i$ , proportional to the  
   1795 number of photoelectrons,
- 1796 •  $A_{0i}$  is the baseline in the absence of a signal for pixel  $i$ . It should be obtained  
   1797 using the same charge extraction approach used for the signal,
- 1798 •  $\gamma_Q$  is the nominal conversion value from mVns to photoelectrons/photons for  
   1799 the entire camera,
- 1800 •  $\gamma_{FFi}$  is the flat-field coefficient for the pixel  $i$ ,
- 1801 • and  $I_i$  is the resulting calibrated signal in photoelectrons/photons.

1802 In the final calibration design of CTA,  $A_{0i}$  is intended to be supplied by the  
 1803 telescope alongside the waveforms at regular intervals. The regular updating of  
 1804 this value ensures that any changes to the baseline due to electronic noise, NSB  
 1805 rate, or temperature variations (which can also increase DCR, see Section 2.2.4)

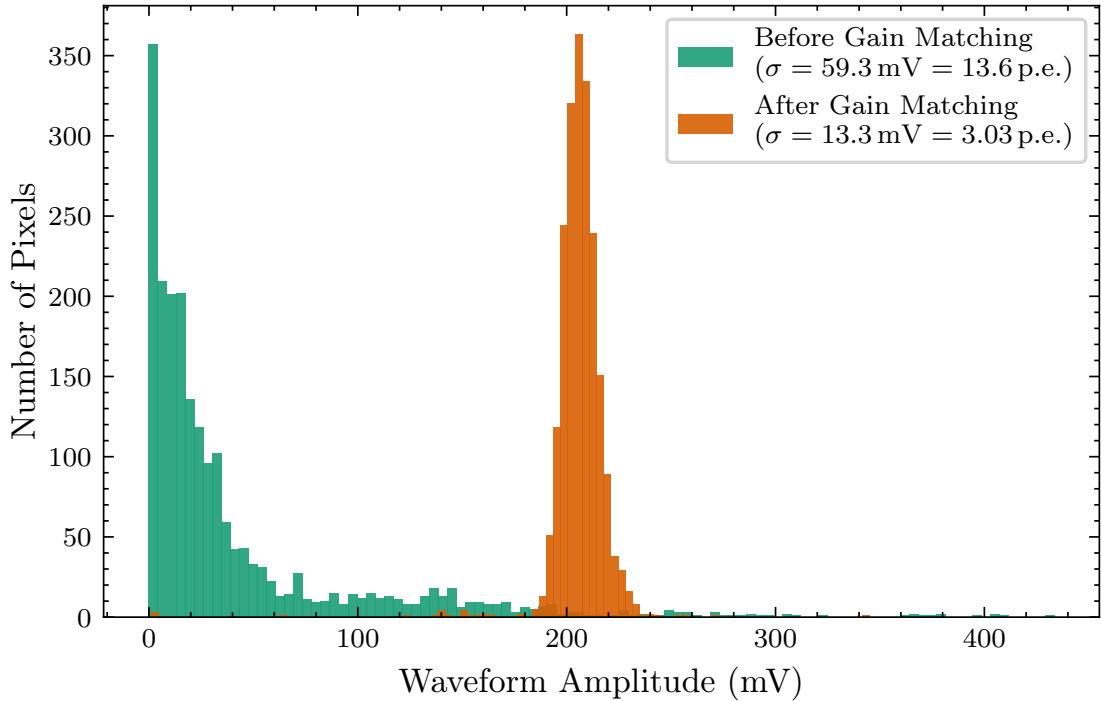


**Figure 5.9:** Comparison between the spread in the average signal amplitude per pixel before and after gain matching with CHEC-S, for a dataset with approximately 50 p.e. average illumination. In the “before” case the DAC value in every superpixel was set to 100. Every pixel in the camera was included in the histogram. The mean  $\mu$  and the standard deviation  $\sigma$  of each distribution are also shown.

1806 are accounted for. However, this parameter was set to zero for the content of  
 1807 this thesis, and was not investigated. Instead, a less effective but simpler baseline  
 1808 subtraction was performed by monitoring the running average of the first 16 samples  
 1809 of the past 50 waveforms for each pixel. This running average was subtracted  
 1810 from each waveform before charge extraction. The remainder of this section will  
 1811 describe how to obtain the other calibration values,  $\gamma_Q$  and  $\gamma_{FF_i}$ , and the other  
 1812 procedures related to the photosensor calibration.

### 1813 5.3.1 Gain Matching

1814 The flat-field coefficients,  $\gamma_{FF_i}$ , provide an offline compensation for the photosensor  
 1815 parameters which alter the signal response in the waveform. While this is typically  
 1816 only the gain in the case of MAPMTs, these parameters are more numerous for  
 1817 SiPMs, and are described in Section 2.2.4. However, these parameters also have a  
 1818 dependence on the voltages across the photosensor, which is a controllable value.  
 1819 The dependence of the CHEC-S SiPM parameters on voltage is shown in Figure 2.5.  
 1820 With the CHEC-M MAPMTs it is only possible to change the voltage value for an

entire module, whereas with the CHEC-S SiPMs the voltages can be configured per superpixel (group of four pixels). Therefore, voltage values can be selected before data-taking which result in a more uniform signal response between photosensor pixels. This is referred as “Gain Matching”, however the name is slightly misleading, as it is the signal that is being matched, not the gain. It is performed by specifying the amplitude (in mV) that every pixel should be matched to, and then performing the following iterative procedure:

1. The camera is uniformly illuminated with approximately 50 p.e..
2. The waveforms are readout, calibrated, and averaged per superpixel/module (excluding any dead pixels).
3. The peak amplitudes of the average waveforms are extracted.
4. Each module/superpixel is categorised as being above or below the requested amplitude.
5. Depending on their category, the voltage setting is increased or reduced by steps of 5 (in arbitrary DAC units), such that it increments closer to the requested amplitude. If the amplitude has been overstepped in the previous measurement, a smaller step value is used. The minimum DAC step value available is 1, which corresponds to  $\frac{10}{256}$  V. If the amplitude is not responding to changes in voltage, the pixel is classified as “dead”, and excluded from the average waveforms.
6. The new voltage settings are applied and the process is repeated.

In the future, this iterative technique will be replaced with a set of lookup tables for different requested amplitudes. These lookup tables will contain the final voltage settings resulting from this iterative technique. Additionally in the future, the requested signal will not be specified in terms of peak amplitude, but in terms of the *Cross Correlation* charge extraction approach. The resulting spread in signal response for CHEC-S as a result of the gain matching is shown in Figure 5.9.

The additional benefit of the gain matching is that it provides a convenient part in the data-taking chain to apply the bias compensation for temperature dependences (introduced in Section 2.2.4). This is achieved using the monitored temperature value per module (included in the data stream from the FEE modules) and a lookup table of the appropriate corrections to the voltages, such that a constant signal response is kept across the camera. This particular in-situ calibration has not yet been implemented, but is intended for the future.

mention  
superpix-  
els in ch3

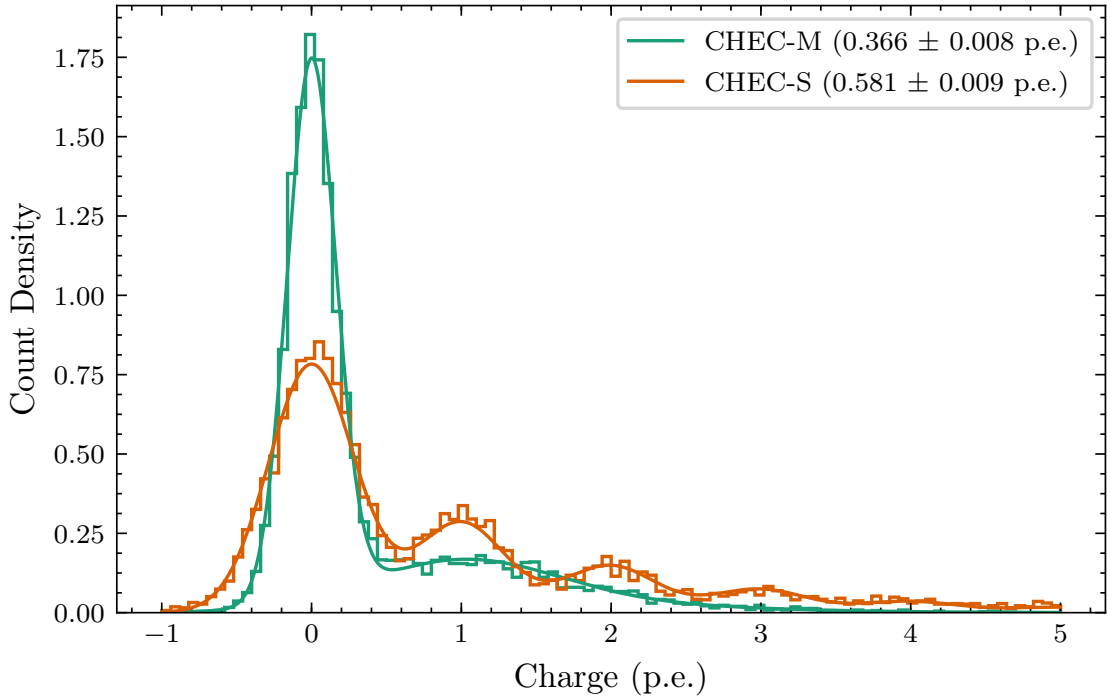


**Figure 5.10:** Comparison of SPE spectra between CHEC-M and CHEC-S for a single pixel, along with their corresponding fit function.

### 1855 5.3.2 SPE Fitting

1856 Due to the photon-counting nature of MAPMTs and SiPMs, when the signal  
 1857 extracted from a pixel, illuminated with a low light-level ( $\sim 1$  p.e.), is accumulated  
 1858 into a histogram, the resulting spectra (Figure 5.10) show peaks at regular intervals  
 1859 corresponding to the baseline (zeroth peak), 1 p.e. (first peak), 2 p.e. (second peak),  
 1860 etc. As explained in Section 2.2.4, the single photoelectron resolution of SiPMs  
 1861 is very high, much higher than is observed with MAPMTs. This accounts for the  
 1862 difference between the two photosensors in Figure 5.10. These spectra are referred  
 1863 to as “Single PhotoElectron (SPE) Spectra”. The physical processes that result in  
 1864 these spectra are well understood for MAPMTs and SiPMs, and therefore analytical  
 1865 formulae exist describing the spectra. When these formulae are fit to the histogram,  
 1866 they can be used to extract certain parameters of the photosensor, including the  
 1867 average incident illumination  $\lambda$ , in units of photoelectrons. As  $\lambda$  provides an absolute  
 1868 illumination value, it allows for the full calibration of average expected charge for  
 1869 each filter-wheel position, for each pixel (Section ??). This is the first step required  
 1870 in obtaining the flat-field coefficients. For more details on this fitting procedure,  
 1871 and the formulae used to describe the SPE spectra, refer to Appendix ??.

check consistency in spelling

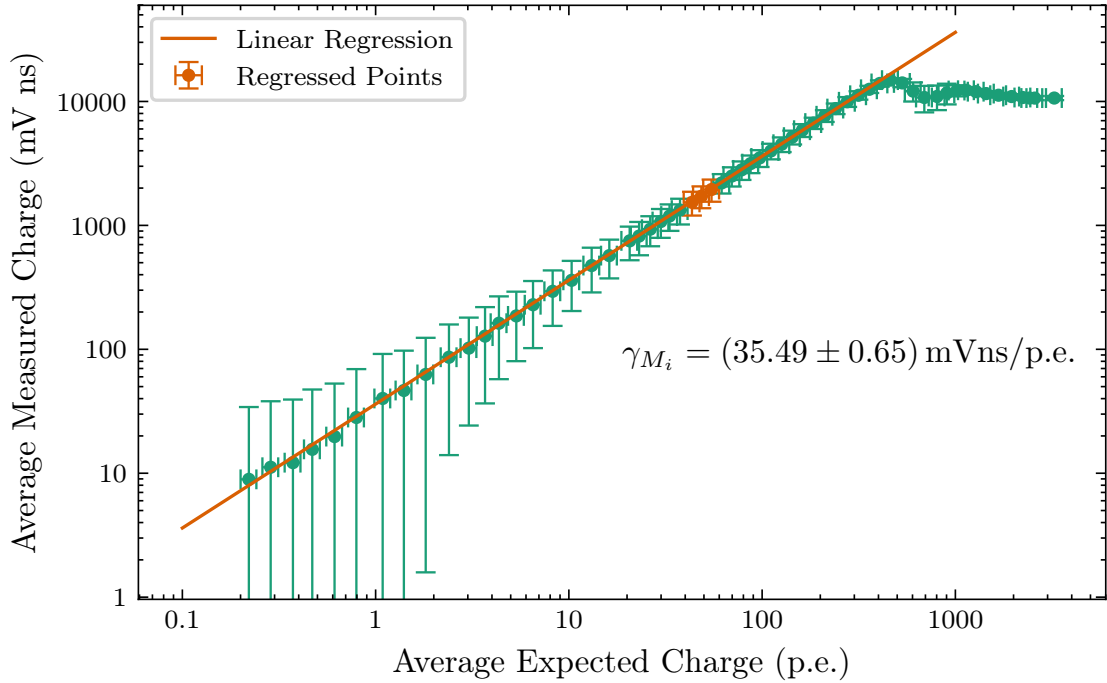


**Figure 5.11:** The average measured charge per illumination for a single pixel. The Y error bars are the standard deviations of the charges for each illumination for a single pixel. The X error bars are the uncertainties on the average expected charge calibration (Section B.6). The orange points were used in a linear regression through the origin to determine the flat-field coefficients for each pixel. The resulting gradient for the pixel ( $\gamma_{M_i}$ ) is annotated.

### 1872 5.3.3 Flat-Field Coefficients

1873 Once the “average expected charge” dependence on filter-wheel position/transmis-  
 1874 sion is characterised (Section ??), we can calculate the coefficients,  $\gamma_{M_i}$ , required  
 1875 to convert the average measured charge (in mVns) into the charge we expect (in  
 1876 photoelectrons/photon). The application of these coefficients to the extracted/mea-  
 1877 sured charge has two effects:

- 1878 • The signal response between pixels is homogenised - the same average amount  
 1879 of charge will be extracted for any pixel illuminated with an average of N  
 1880 photons.
- 1881 • The signal response is converted into the common telescope-array units of  
 1882 photoelectrons or photons.

1883 Therefore:

$$\gamma_{M_i} = \frac{\gamma_Q}{\gamma_{FF_i}}. \quad (5.2)$$

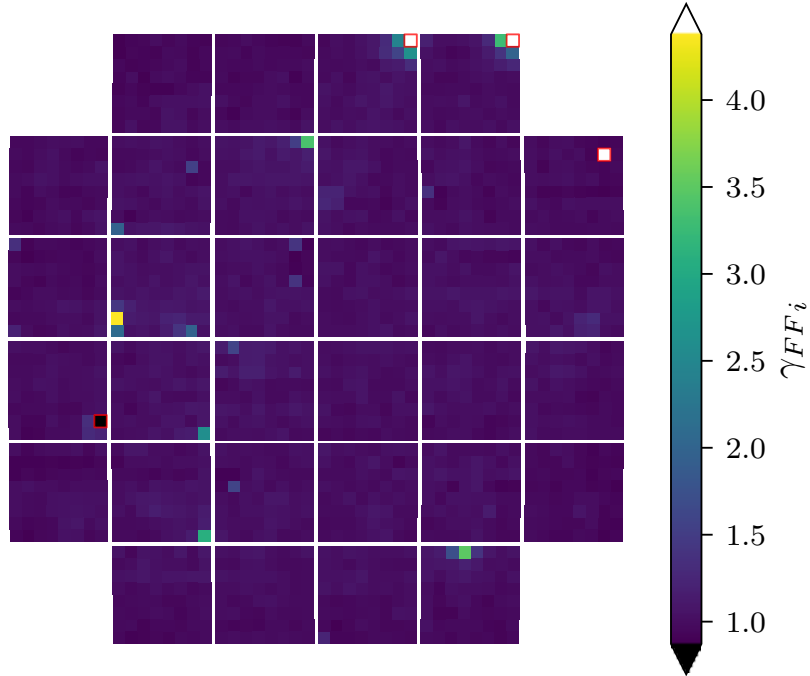


**Figure 5.12:** Camera image of the flat-field coefficient value,  $\gamma_{FF_i}$ , per pixel. Pixels that were designated “dead” or misbehaving are outlined in red, and exist beyond the colour-scale range.

To obtain  $\gamma_{M_i}$  per pixel  $i$  in the lab, datasets with around 50 p.e. average expected charge per pixel were produced. For each pixel, the average measured charge (in mVns) was linearly regressed, while forcing the fit through the origin. This regression is shown for a single pixel in Figure 5.11. The resulting gradient of the regression is equal to  $\gamma_{M_i}$ , which was combined with Equations 5.1 & 5.2 for the calibration of measured charge into photoelectrons. The nominal conversion value from mVns to photoelectrons for CHEC-S was calculated to be  $\gamma_Q = (35.555 \pm 3.041)$  mVns/p.e., and the spread of  $\gamma_{FF_i}$  across the camera is shown in Figure 5.12. The value for  $\gamma_Q$  can be converted into its equivalent single mV sample (i.e. peak-height) equivalent using the reference pulse from the *Cross Correlation* extraction method (Chapter 6), resulting in a conversion value of  $(4.373 \pm 0.374)$  mV/p.e..

The resulting residual spread in signal response between pixels at an average expected charge of  $(47.67 \pm 3.79)$  p.e. is shown in Figure 5.13. The final variation in signal response between pixels at this illumination was measured to be 0.5 %. Figures 5.14a and 5.14b show the improvement of the average charge spread between pixels for a higher and a lower illumination.

As the flat-field coefficients have been calculated in a manner in which they are unfolded from the illumination profile (by calculating the average expected

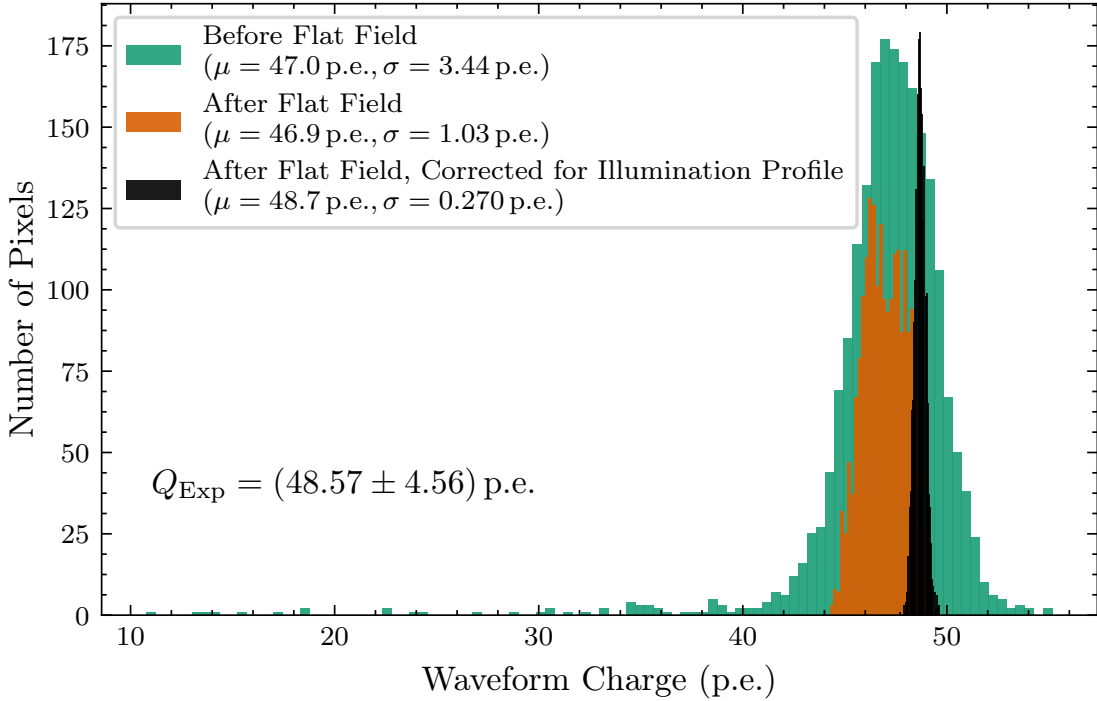


**Figure 5.13:** Comparison between the spread in the average signal amplitude per pixel before (blue) and after (orange) the flat-fielding calibration. The charges were extracted from a dataset where a theoretical pixel located at the centre of the camera would be expected to have a charge of  $Q_{\text{Exp}} \approx 50 \text{ p.e.}$ . The black histogram contains the charges after the difference in the illumination profile (Section B.3) between the pixels was considered, i.e. they contain the charge that would be measured if every pixel was located at the camera centre. Every pixel in the camera, excluding the “dead” pixels, was included in the histograms. The mean  $\mu$  and the standard deviation  $\sigma$  of each distribution are also shown.

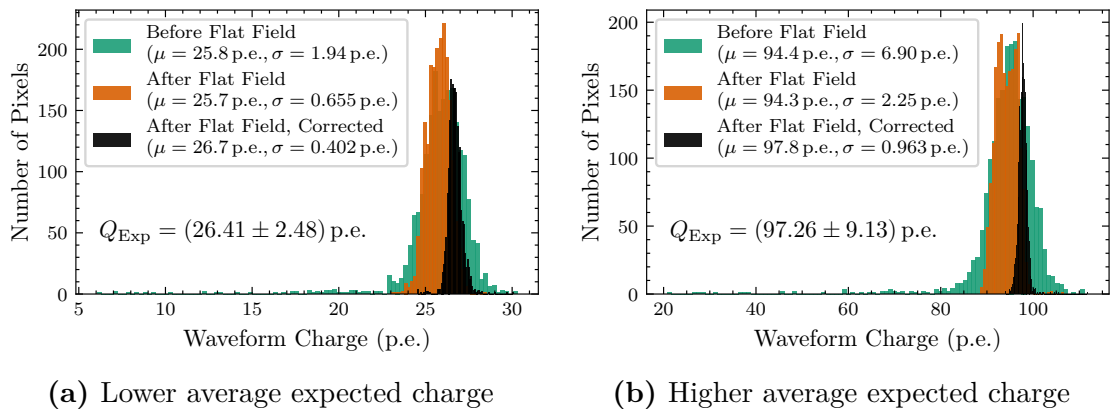


**Figure 5.14:** Same as Figure 5.13, but with a higher and lower average expected charge ( $Q_{\text{Exp}}$ ).

charge individually for each pixel), they are applicable to any environment the camera is used in. Any deviations that are measured in the signal between pixels are then due to the illumination profile present in the environment, and not due to the characteristics of the photosensor. Once the camera is on the telescope, the flat-field coefficients are intended to be routinely updated using the reflection of the LED flashers (Section ??) in the secondary mirror. This calibration will require an updated illumination profile in order to be performed.

### 1909 Consideration of Errors and Uncertainty

1910 The standard error on the estimate of the gradient per pixel,  $\sigma_{\gamma_{M_i}}$ , that arises from a  
 1911 standard linear regression can be calculated with the relation derived by Taylor [46]:

$$\sigma_{\gamma_{M_i}} = \sigma_r \sqrt{\frac{N}{N \sum Q_{\text{Exp}_i}^2 - (\sum Q_{\text{Exp}_i})^2}}, \quad i = 0, 1, 2, \dots, N, \quad (5.3)$$

$$\sigma_r = \sqrt{\frac{\sum (A_{Q_i} - A_{Q_f})^2}{N - 1}}, \quad (5.4)$$

1912 where  $N$  is the total number of regressed points  $i$ ,  $\sigma_r$  is the mean square error of the  
 1913 regression, the dependant variable  $A_{Q_i}$  is the average measured charge at the average  
 1914 expected charge  $Q_{\text{Exp}_i}$ , and  $A_{Q_f}$  is the value that results from the regression at that  
 1915 same value of  $Q_{\text{Exp}}$ . The denominator in Equation 5.4 is  $N - 1$  as we constrained  
 1916 the regression through the origin, therefore there was only one free parameter.  
 1917

1918 The error on  $\gamma_{M_i}$  is used as weights when calculating the average to obtain  $\gamma_Q$ .  
 1919 Therefore the uncertainty on  $\gamma_Q$  is quoted from the weighted standard deviation  
 1920 across the values of  $\gamma_{M_i}$  for each pixel.

#### 1921 5.3.4 Dead Pixels

1922 Figure 5.12 shows that some of the photosensor pixels contained either no signal or  
 1923 an odd signal, resulting in an extreme flat-field coefficient. This was likely due to  
 1924 damage to the pixel during handling, or due to water ingress. However, the four  
 1925 pixels constitute to 0.2 % of the camera, therefore the camera is still well within  
 1926 the **B-TEL-1295 Pixel Availability** CTA requirement (Section 3.2.3). These  
 1927 pixels were excluded from any calculations involving multiple pixels, including the  
 1928 expected-charge calibration and the charge-resolution across the camera.

## 1929 5.4 Saturation Recovery

1930 As evident in Figure 5.11, high illumination measurements (greater than  $\sim 200$  p.e.)  
 1931 are affected by saturation of the detector. The saturation shown is due to the  
 1932 TARGET ASIC, which saturates before the photosensor. However, while the height  
 1933 of the pulse increased no further, the excess charge caused the pulse to extend  
 1934 further (Figure 5.6b). Therefore, it could be possible to perform a simple correction  
 1935 for the saturation recovery by utilising this waveform behaviour. A simple, initial  
 1936 investigation into saturation recovery is shown in Figure 5.15, where the waveform  
 1937 was integrated in a window that started just before the pulse maximum, and  
 1938 extended to the end of the waveform. This resulted in an extracted charge that  
 1939 continued to increase with illumination, apart from in the region immediately after  
 1940 saturation. More investigation is required for this calibration.

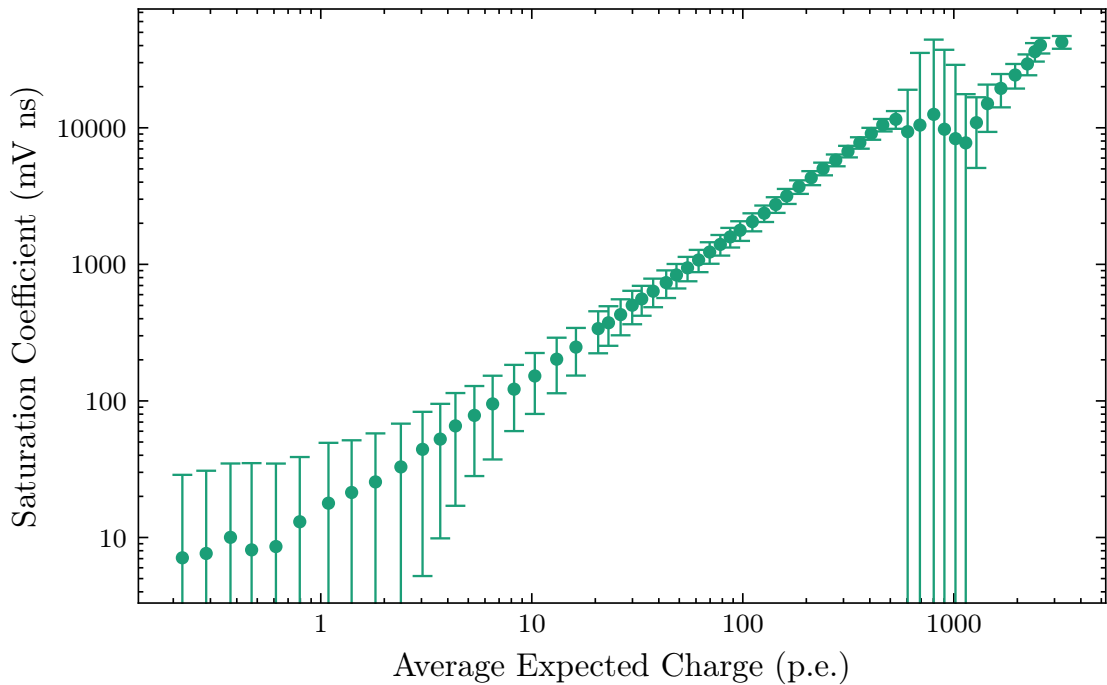


**Figure 5.15:** Initial investigation into recovering charge from a saturated waveform for the same pixel as shown in Figure 5.11. The saturation coefficient is the integral from just before the pulse maximum, to the end of the waveform readout.

## 1941 5.5 Timing Corrections

1942 Due to the routing of the electronics in the front-end, the electrical signal path is  
 1943 slightly different per channel, causing a small difference in apparent arrival of the  
 1944 pulse in the waveform. The relative arrival time per pixel for CHEC-S is shown

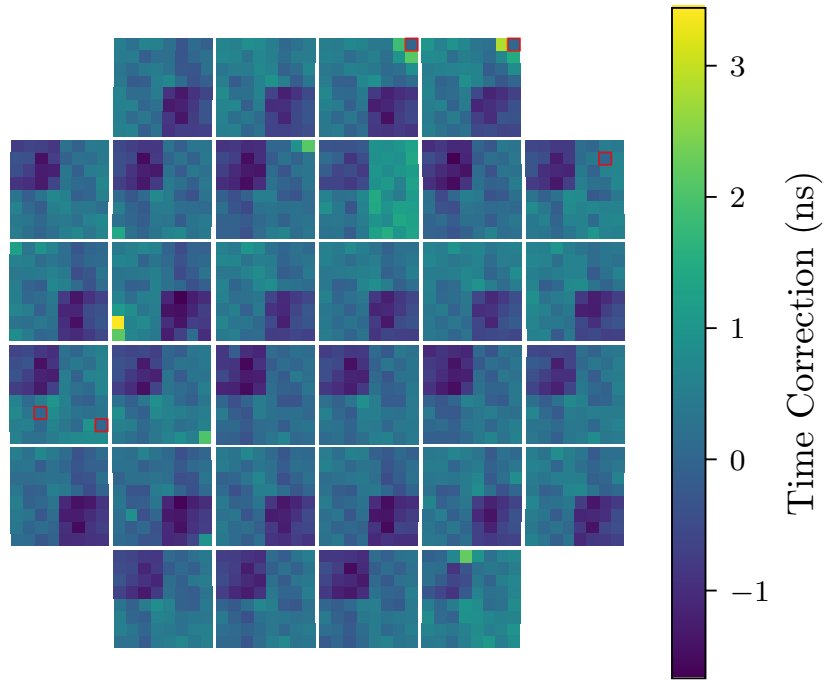


**Figure 5.16:** A camera image of CHEC-S showing the timing correction for each pixel. The “dead” pixels are outlined in red, and have a zero timing correction.

in Figure 5.16. This is measured by extracting the average arrival time per pixel over 1000 events at an average illumination of  $\sim 100$  p.e., and subtracting each pixels value by the average across the camera. It is clear that in every module, there is one particular ASIC slot, corresponding to a 16-pixel corner of the module, that has a longer electrical signal path.

Not only does the timing correction need to be taken into consideration when investigating the timing performance, it also can have a significant impact on the charge extraction performance. This is because the charge extraction approaches typically rely on other pixels (neighbouring or entire camera, see Chapter 6) sharing a compatible pulse time. A charge extraction routine that incorrectly extracts the charge by 1 ns can have a negative impact on the *Charge Resolution*. Discussions are ongoing on how to best include the timing corrections in the charge extraction.

## 5.6 Future

During the long development of CHEC, the calibration procedure has evolved significantly. Multiple iterations of the procedures have occurred to:

- Accommodate the changes required in the upgrades of hardware (such as from TARGET-5 to TARGET-C).

- 1962     • Simplify the calibration to save on computing resources.
  - 1963     • Account for additional factors, thereby improving the calibration (such as the
  - 1964       AC contribution to the Transfer Functions).
- 1965 Therefore, while each iteration improves in one aspect, it may be at the expense  
1966 of the others. As a result, the TARGET calibration procedure described in this  
1967 chapter appears quite complicated compared to the approaches detailed by Bechtol  
1968 et al. [44] and Albert et al. [25]. The next step in the calibration development for  
1969 CHEC is therefore to review the procedure used, with the aim of producing an  
1970 approach that is simpler, includes aspects such as temperature dependence, and  
1971 meets the requirements and processing rates required by CTA.

---

# 6

1972

1973

## Waveform Processing

1974

### Contents

---

1975

1976	<b>6.1 Introduction</b>	72
1977	<b>6.2 Charge Extraction Methods</b>	73
1978	6.2.1 Peak Finding	74
1979	6.2.2 Integration	76
1980	6.2.3 Approaches Adopted by Other IACTs	78
1981	6.2.4 Performance Assessment	80
1982	<b>6.3 Shower Reconstruction</b>	80
1983	6.3.1 Image Parametrisation	81
1984	6.3.2 Direction Reconstruction	82
1985	6.3.3 Energy Reconstruction	83
1986	6.3.4 $\gamma$ -Hadron Discrimination	83

1987

1989

1990

### 6.1 Introduction

1991 Methods for retrieving information about the Cherenkov shower have been a primary  
1992 component of the Imaging Atmospheric Cherenkov Technique since its inception.  
1993 Early techniques such as those used in the first observation of TeV Gamma rays  
1994 from the Crab nebula [47] are still utilised in modern IACTs. These techniques are  
1995 also applicable to CTA telescopes, and as CTA is a large consortium which consists  
1996 of the worldwide IACT community, the developers of advanced waveform reduction  
1997 and shower reconstruction approaches used by previous IACTs have prepared them  
1998 for use within CTA (for example, the ImPACT shower reconstruction technique  
1999 developed by [40]. However, as:

2000 (a) CTA will consist of the most advanced IACTs to date, with higher shower  
 2001 imaging resolution and telescope multiplicity than has previously been available,  
 2002  
 2003 (b) the capabilities of digital signal processing have significantly increased in the  
 2004 past decade,  
 2005 the opportunity for more advanced and more successful algorithms exists for CTA.  
 2006 Some efforts have already been made to develop novel approaches, for example, the  
 2007 utilisation of convolutional neural networks to reconstruct the shower's direction [48].  
 2008 However, it is an aspect that is expected to constantly evolve and improve during  
 2009 the lifetime of CTA. In this chapter I will provide insight into the existing and  
 2010 in-development reduction techniques utilised to extract the Cherenkov shower signal  
 2011 from the waveforms, and my involvement in designing a charge-extraction technique  
 2012 for CHEC-S. I will also provide a brief overview of the shower reconstruction methods  
 2013 typically used with IACTs. With regards to the CTA data levels (Figure 3.3), this  
 2014 chapter is mostly concerned with the steps from *DL0* to *DL2*.

## 2015 6.2 Charge Extraction Methods

2016 The immediate step after the waveform calibration is the extraction of signal (also  
 2017 sometimes referred to as charge) from the waveforms provided by the individual  
 2018 cameras. As a result of the low-level calibration detailed in Chapter 5, the waveforms  
 2019 from each CTA camera exist in a common state, with no remaining dependencies  
 2020 on the electronics they were produced by. Therefore, the extraction techniques  
 2021 are typically applicable to all CTA cameras.

2022 The extraction of signal from a waveform is a very generic problem, allowing  
 2023 for the utilisation of common signal processing techniques that are not unique to  
 2024 Cherenkov shower analysis. The goal is to extract the majority of signal from the  
 2025 pulse created by the Cherenkov shower light, while simultaneously limiting the  
 2026 inclusion of noise factors. Figure 6.1 shows a CHEC-S waveform which contains  
 2027 both signal and noise. Two quantities are extracted in this stage: the signal charge  
 2028 in each pixel, and the signal arrival time per pixel.

2029 The total signal charge in a pixel, i.e. the total number of photo-electrons released  
 2030 from the PMT's photocathode, is proportional to the total area below the pulse  
 2031 corresponding to the Cherenkov photons (blue area of Figure 6.1). If the waveforms  
 2032 were completely free of noise, and the readout window was large enough to capture  
 2033 the full Cherenkov signal, a simple integration of the entire readout would be a

reference  
where  
noise  
talked  
about,  
talk about  
all the  
contributing  
factors  
(noise  
etc.) to  
waveforms  
in ch2

Check all  
i.e. and  
e.g. for  
spaces

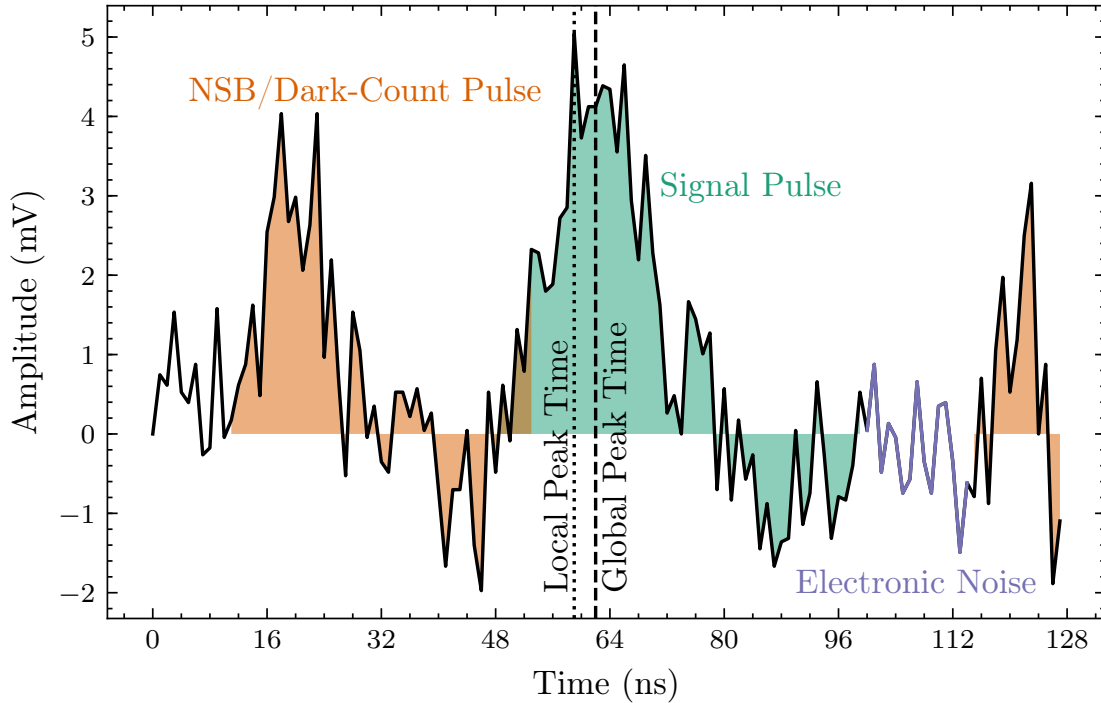


**Figure 6.1:** A waveform from CHEC-S lab data, illuminated by the laser with the filter wheel set to give an average expected charge of 3 p.e.. The waveform is annotated with the different components that contribute to the charge extraction. Although the electronic noise is only highlighted at one section, it affects every sample. Further information about the different contributors to the waveform can be found in Section ??

2034 satisfactory approach for obtaining the signal charge. However, as we do not have  
 2035 the luxury of perfect waveforms, more complex methods are required. Charge  
 2036 extraction algorithms typically consist of two aspects: how the signal pulse is  
 2037 found, and how the pulse is integrated.

### 2038 6.2.1 Peak Finding

2039 Two factors must be considered when finding the signal pulse of a Cherenkov shower.  
 2040 Firstly, the majority of camera pixels will not contain any Cherenkov signal while  
 2041 still containing noise. A peak finding technique that assumes a signal exists in the  
 2042 readout will be biased, as it will mistake the noise for a signal. Secondly, due to the  
 2043 nature of Cherenkov showers (Chapter ), the Cherenkov signal will have different  
 2044 arrival times between pixels due to the time evolution of the Cherenkov image. This  
 2045 time gradient across the image is especially apparent for high-energy showers at a  
 2046 large core distance from the telescope. The most successful peak-finding technique  
 2047 is one that best accounts for those two factors. Some simple techniques used to  
 2048 define a peak time from a waveform include:

reference  
where the  
time gra-  
dient of  
Cherenkov  
showers  
are  
described

- 
- 2049     • **Local Peak Finding:** Each waveform is treated independently from the  
 2050       others. The maximum point in the waveform is treated as the peak/arrival  
 2051       time. This approach is intrinsically biased to assume every waveform contains  
 2052       a signal; therefore, in the absence of a Cherenkov signal, the largest noise  
 2053       pulse will be extracted, resulting in a higher total charge than should be  
 2054       obtained.
- 2055     • **Global Peak Finding:** The waveforms from each pixel are combined into  
 2056       an average waveform, from which the maximum sample is treated as the peak  
 2057       time for every pixel. This technique is only useful if a large portion of the  
 2058       camera is simultaneously illuminated, such as by a laser in the case of lab  
 2059       commissioning and calibration runs.
- 2060     • **Neighbour Peak Finding:** The waveforms from neighbouring pixels to  
 2061       the pixel-of-interest are combined into an average waveform. The maximum  
 2062       sample in the average waveform is treated as the peak time for the pixel-  
 2063       of-interest. This technique is often preferred for Cherenkov images as it  
 2064       has a reduced charge bias (especially if the pixel-of-interest's waveform is  
 2065       not included in the average); pixels with Cherenkov signal typically have  
 2066       neighbours that also contain Cherenkov signal at a correlated time, while the  
 2067       neighbours of empty pixels only contain random noise, and therefore a peak  
 2068       time that is uncorrelated to the noise is chosen.
- 2069     • **Fixed Peak Value:** Due to a reliable definition of the camera trigger and  
 2070       subsequent electronic chain, the position of the pulse in the waveform could  
 2071       consistently be known a priori, allowing for a fixed peak time. However, this  
 2072       method requires a larger integration window size in order to capture the full  
 2073       pulse in the tail of the Cherenkov shower, which occur at a later time than  
 2074       the initial photons which trigger the camera. As a result, a larger amount  
 2075       of noise will be included in the integration window. However, this technique  
 2076       usually contains the least bias, as no signal is assumed to exist.

2077       A more complex peak-finding technique is the *Gradient Peak Finding* approach.  
 2078       This approach was designed for the VERITAS telescope [49][1][50], but is applicable  
 2079       to any IACT telescope that allows the dynamic specification of an integration window.  
 2080       *Gradient Peak Finding* utilises the gradient profile of the photon arrival time for  
 2081       gamma-induced Cherenkov showers, described in Section 1.3.2 and illustrated in  
 2082       Figure . This peak-finding technique is a two-pass approach performed by first  
 2083       extracting the signal using one of the other methods. The pulse-timing information

chec-m  
pulse time  
figure

2084 contained within the pixels that survive the image cleaning (Section 6.3.1) can  
 2085 then be used to obtain a relation between “distance along primary image axis”,  
 2086  $D_{ax}$ , and the pulse time,  $T_0$ . Figure [illustrates the geometry of  \$D\_{ax}\$  with respect to](#)  
 2087 the pixel position. Using the obtained relation between  $D_{ax}$  and  $T_0$ , an example  
 2088 of which is shown in Figure [, an unbiased pulse time is obtained for each pixel](#)  
 2089 depending on its position along the image axis.

figure  
with  
geometry

figure  
of  $D_{ax}$   
versus  $T_0$   
for checm  
figure

2090 These peak-finding methods have been described in relation to the maximum  
 2091 of the signal pulse, however they may instead use other characteristic positions  
 2092 of the pulse, such as the half-maximum time on the rising edge, or the centre  
 2093 of gravity of the pulse. Additionally, more advanced peak-finding techniques  
 2094 may up-sample (possibly by zero-padding in the frequency domain via a Fourier  
 2095 transform) or interpolate the signal to obtain a more precise peak time [1, 50],  
 2096 or even apply low-pass filters in order to remove low frequency baseline noise.  
 2097 The peak finding should be done in conjunction with any timing corrections  
 2098 (Section 5.5) that may be required.

### 2099 6.2.2 Integration

2100 Once the peak time has been obtained, the simplest approach to extract the  
 2101 signal is to define an integration window centred about this time. The size of  
 2102 the window needs to be large enough to capture sufficient signal from the pulse,  
 2103 but small enough that not too much noise (NSB, dark counts, afterpulsing) is  
 2104 included within the window, thereby maximising the signal-to-noise. Additionally,  
 2105 the camera’s pulse shape may not be symmetric, so a better signal-to-noise may  
 2106 be achieved by shifting the window a few samples with respect to the peak time.  
 2107 The optimal integration window size and shift for the CHEC-S waveforms is found  
 2108 to be 5 samples and 2 samples (i.e. 5 ns and 2 ns), [respectively, according to the](#)  
 2109 investigations performed in ??.

mention  
1 sample  
== 1 ns  
in ch2

2110 Beyond the simple “boxcar” integrator method (where every sample integrated  
 2111 has a weight of 1), other more advanced strategies may be used to extract the  
 2112 charge. One example is the fitting of the waveform in order to extract the signal  
 2113 pulse, either with an analytical description of the expected pulse or with a more  
 2114 unconstrained description, such as a cubic spline. A second advanced approach is  
 2115 the use of digital filters, which can be used in combination with knowledge of the  
 2116 pulse shape to robustly extract the signal even in the presence of high frequency  
 2117 noise with a large amplitude. Such a technique has been designed and adopted  
 2118 for GCT, referred to as the *Cross-Correlation* method.

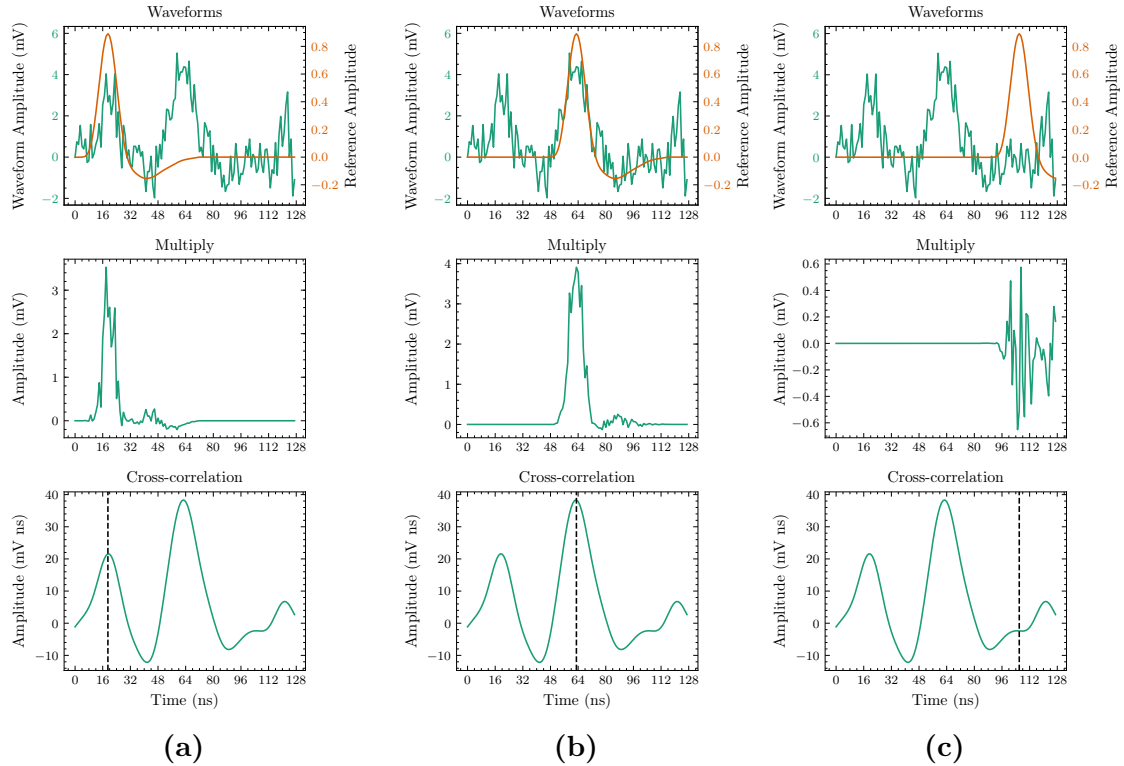


**Figure 6.2:** The three stages involved in obtaining the cross Correlation of a waveform with the reference pulse. The waveform investigated is the same one shown in Figure 6.1. The stages are shown for three time displacements (Equation 6.1): on an NSB/dark-count pulse before the signal (a), at the time of the signal (b), and at a time where there is only the baseline (c). The top panels show the waveform and the reference pulse shifted by the time displacement. The middle panels show the multiplication of the two traces in the first panel. The bottom panel shows the cross correlation for all time displacements. The value of the cross correlation at the time displacement shown by the red line is obtained by summing all the samples from the trace in the middle panel.

## 2119 Cross Correlation

2120 Cross-correlation is a common signal processing technique used as a measure  
 2121 of the similarity between two signals as a function of the displacement in time  
 2122 applied to one of the signals. Given a continuous function  $f(t)$  defined between  
 2123  $0 \leq t \leq T$  and a second continuous function  $g(t)$ , the cross-correlation between  
 2124 the two functions ( $f \star g$ ) is defined as

$$(f \star g)(\tau) = \int_0^T \bar{f}(t)g(t + \tau)dt, \quad (6.1)$$

2125 where  $\bar{f}(t)$  is the complex conjugate of  $f(t)$  and  $\tau$  is the time displacement (also  
 2126 referred to as the “lag”) between the two functions [51]. In descriptive terms, as  
 2127  $\tau$  increases,  $g(t + \tau)$  will slide past  $f(t)$ . The cross-correlation for a value of  $\tau_1$   
 2128 is then the integral across  $t$  of the product between  $f(t)$  and  $g(t + \tau_1)$ . For a

2129 discrete function that is real-valued, such as a sampled waveform, Equation 6.1  
2130 can instead be defined as

$$(f \star g)[n] = \sum_{m=0}^N f[m]g[m+n], \quad (6.2)$$

2131 where  $N$  is the total number of samples in the waveform and  $n$  is the sample  
2132 displacement from sample  $m$ .

2133 Through utilising a template of the expected pulse shape in the absence of noise  
2134 (hereafter referred to as the “reference pulse”), features inside the waveform that are  
2135 correlated with the reference pulse shape are emphasized, while features that are  
2136 not, such as the electronic noise, are suppressed. Therefore, the peaks in the cross  
2137 correlation correspond to the displacements where the signals match best, and the  
2138 values of the peaks correspond to an weighted integral of the entire waveform, and  
2139 can be used as an extracted charge value. An illustration of the *cross-correlation*  
2140 technique being applied on a CHEC-S waveform is shown in Figure 6.2.

2141 The reference pulse we use for the cross correlation was obtained via probing  
2142 the input analogue signal on the TARGET module and averaged on an oscilloscope.  
2143 It was then normalised such that cross-correlation between it, and the reference  
2144 pulse normalised to have an integral of 1, has a maximum value of 1. This  
2145 normalisation ensures that the cross-correlation result of a 1 p.e. signal, contained  
2146 in a waveform with units of mV, gives the conversion value from mVns to p.e..  
2147 The relative conversion into mV for “peak-height” investigations is also possible  
2148 using the reference pulse. An optimised implementation of cross-correlation exists  
2149 in `scipy.ndimage.correlate1d` [52], where the waveforms for every pixel are  
2150 processed in parallel.

2151

mention  
negatives  
of the cc  
approach,  
like the  
emphasis  
of nsb  
and cc,  
here or in  
appendix?

### 2152 6.2.3 Approaches Adopted by Other IACTs

2153 Some examples of charge-extraction approaches adopted by other IACTs are  
2154 outlined below.

#### 2155 MAGIC

2156 Members of the MAGIC telescope, Albert et al. [53], performed a study comparing  
2157 the techniques proposed for their signal reconstruction. Four approaches were  
2158 compared: *fixed-window*, *sliding-window* with amplitude-weighted time, *cubic spline*  
2159 *fit* with integral or amplitude extraction, and *digital filter*. It was concluded that  
2160 the digital filter, which relies on knowledge of the signal shape to minimise the

2161 noise contributions, provided a charge reconstruction with acceptable bias and  
2162 minimal variance, while remaining stable in the occurrence of small variations  
2163 in pulse shape and position.

2164 **VERITAS**

2165 Similar to the aforementioned study for the MAGIC telescope, comparisons of charge  
2166 extraction approaches were also performed for VERITAS [1, 49, 50]. Specifically,  
2167 the extraction methods compared included:

- 2168 • a *simple-window* integration using a priori knowledge of the Cherenkov pulse  
2169 time in the trace,
- 2170 • a *dynamic-window* integration which slides across the trace to find the  
2171 Cherenkov pulse,
- 2172 • a *trace-fit* evaluator with fits the trace with two exponential functions which  
2173 respectively describe the rise and fall time of the pulse,
- 2174 • a *matched-filter* which “uses a digital filter based on the assumed shape of  
2175 the FADC pulse to integrate the charge” [50, p. 2],
- 2176 • and finally an implementation of the *Gradient Peak Finding* approach de-  
2177 scribed earlier in this chapter.

2178 At first glance, some of these approaches bear resemblance to those used by MAGIC,  
2179 however there are slight differences:

- 2180 • In the VERITAS pulse fitting technique, an attempt to describe the pulse  
2181 analytically was made whereas the MAGIC approach used a more loosely  
2182 defined spline.
- 2183 • The filter used by VERITAS is a cross-correlation in Fourier space, whereas  
2184 the filter used by MAGIC is generated using their knowledge of the noise  
2185 auto-correlation matrix.

2186 Either as a result of these differences, or due to the difference in the instruments  
2187 themselves, the VERITAS *matched-filter* appears to result in a worse reconstruction  
2188 than one would expect from the conclusion reached by MAGIC. The study performed  
2189 by Cogan [50] for VERITAS concludes that the *matched-filter* ”holds promise“  
2190 for reconstructing low-amplitude signals, whereas while the *trace-fit* performs  
2191 extremely poorly for the low-amplitude signals (as expected), it performs the  
2192 best for amplitudes greater than 4 photoelectrons.

---

2193 **H.E.S.S.**

2194 The standard mode of charge extraction for the H.E.S.S. telescopes is to integrate  
2195  $N$  samples with respect to a fixed, but regularly verified, signal time [45]. H.E.S.S.  
2196 camera electronics underwent an upgrade in 2015/2016, subsequently allowing for  
2197 the update of the standard extraction mode to also output time-of-maximum and  
2198 time-over-threshold, and also allowed for full sample readout enabling the utilisation  
2199 of more complex charge extraction techniques [54][55].

2200 **ASTRI**

2201 Contrary to the other techniques described in this section, ASTRI (Astrofisica  
2202 con Specchi a Tecnologia Replicante Italiana) took the alternative direction of  
2203 a hardware-implemented charge extraction, utilising their CITIROC (Cherenkov  
2204 Imaging Telescope Integrated Read Out Chip) ASIC. The pulse from their SiPM is  
2205 amplified and shaped (with both a high-gain and low-gain channel) with a constant  
2206 shaping time of 37.5 ns. The maximum of the shaped peak-height is then converted  
2207 into an integrated charge, achieving no more than 1% introduced systematic error  
2208 [56]. The *DL0* and *DL1* formats are therefore identical in ASTRI's case as the  
2209 charge-extracted value is provided in place of waveforms. However, while this charge-  
2210 extraction technique is optimised for the ASTRI electronics, it removes the flexibility  
2211 of being able to dynamically select a charge-extraction technique within the software,  
2212 and adopting new software-based techniques that may be designed in the future.

2213 **6.2.4 Performance Assessment**

2214 Deciding on which charge extraction method to use is not trivial - as shown in the  
2215 above discussion, different cameras may perform better with different algorithms.  
2216 This is anticipated in `ctapipe` (4), where different ChargeExtractors can easily  
2217 be selected at runtime depending on the camera source.

2218 The assessment technique typically used for charge extractors in the context of  
2219 CTA is the *Charge Resolution* (Section 3.2.1). A performance assessment of charge  
2220 extraction techniques for CHEC-S can be found in Appendix ??.

2221 **6.3 Shower Reconstruction**

2222 The resulting images of the extracted signal per triggered telescope is only the first  
2223 stage of many to retrieve the properties of the Cherenkov-shower progenitor particle:  
2224 direction, energy, and class. The direction is necessary to retrieve in order to obtain

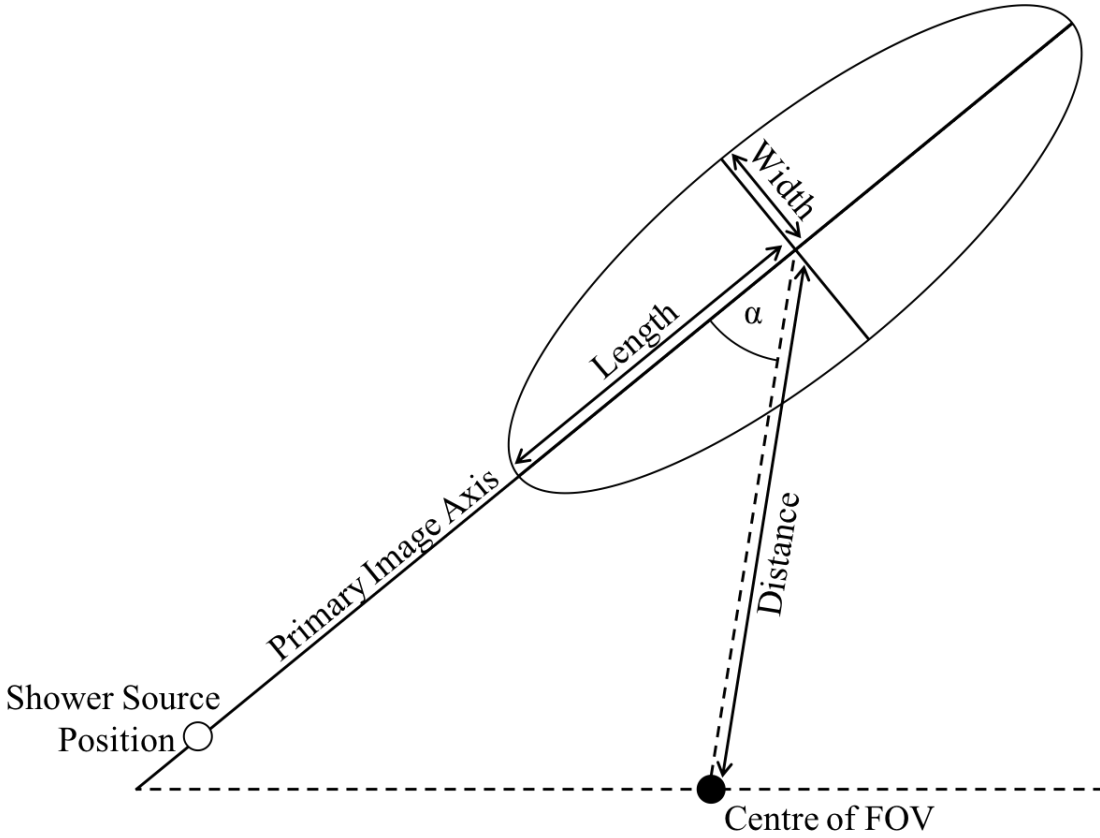


**Figure 6.3:** Schematic of the *Hillas Parameters* used to describe the Cherenkov shower image ellipse.

the source's position and spatial morphology. The energy is desired for studies of the source's spectrum. The class of the progenitor particle (gamma-ray, electron, or cosmic-ray hadron) is required in order to identify the gamma-rays among the hadronic background. All the information required to obtain these progenitor particle properties is contained within the image of extracted charge. As the focus of this thesis is on the low-level performance of the GCT cameras, this section will only include a brief overview of the simplest methods used in shower reconstruction. This information is supplied as context for the results described in ??.

### 6.3.1 Image Parametrisation

Pixels containing signal from the Cherenkov shower are identified by an image cleaning method such as the tailcuts approach: any pixels above a certain signal threshold are kept, and any neighbouring pixels (to those that survive the first threshold) that are above a lower signal threshold are also kept. The thresholds are optimised per telescope using Monte Carlo simulations. The resulting pixels are then parametrised in terms of their second moments. This parametrisation

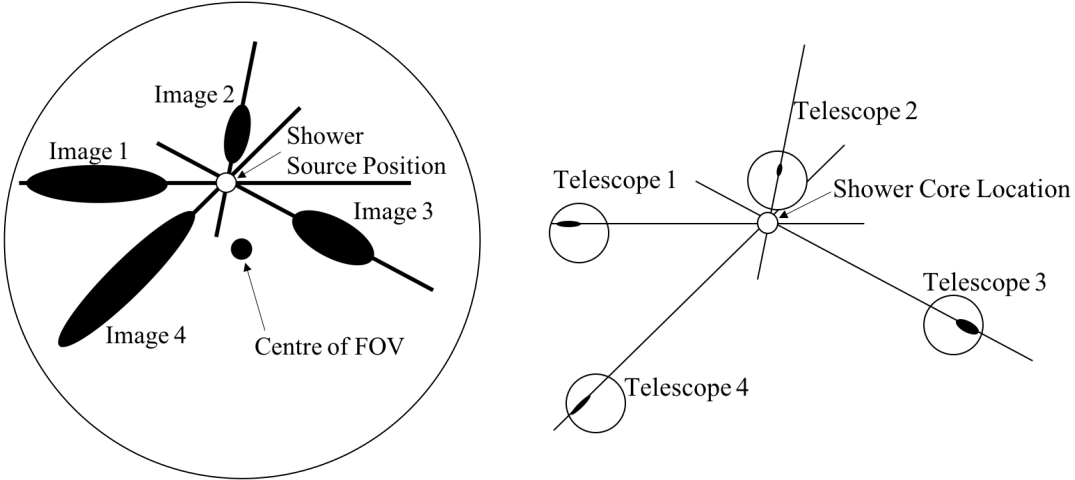


**Figure 6.4:** Reconstruction of the source location on the sky for the shower, achieved by superimposing the different views of the showers from different telescopes.

**Figure 6.5:** Reconstruction of the location of the shower core on the ground, achieved by combining the primary image axes at the relative telescope separations.

is a predominant IACT analysis technique that has been utilised in the majority of IACT experiments. It was first formalised by Hillas [57] and has subsequently been known as the *Hillas Parametrisation*. This technique exploits the elliptical shape of the gamma-induced shower images, and provides values for the centre of gravity of the ellipse, its primary axis position and orientation, its width, and its length (Figures 6.3). The `ctapipe` implementation of the *Hillas Parametrisation* is defined by Reynolds et al. [58].

### 6.3.2 Direction Reconstruction

Through utilising the primary image axis that results from the *Hillas Parametrisation*, the positional information about the shower can be obtained [1, 59, 60]. By superimposing the ellipses from different telescopes onto a single image (Figure ??), the stereoscopic combination allows for the source position of the shower to be retrieved with simple geometry. As explained in Chapter , this precisely resolves the astrophysical-source position on the sky for a gamma-ray shower. If, instead, the primary image axes are combined with the relative positional view of the telescopes (Figure 6.5), the core location of the shower in terms of ground coordinates may be obtained. For obtaining the intersections of the axes in both applications, the weighted-mean-direction of the intersections is typically calculated [61, 62]. While the extraction of the directional information is much more reliable through the use of the stereoscopic combination of the images, it is not impossible to estimate

refer to where it is explained that the two are the same, from introduction...

check wording in book

the direction of the source when only a single telescope is available. The primary challenge when performing this operation with a single telescope is the degeneracy in determining which direction along the primary image axis the source exists in. This is overcome with the *disp* method developed by Lessard et al. [63].

### 6.3.3 Energy Reconstruction

As aptly described by Dickinson [60, p. 16], “determining of the energy of the progenitor of a particular air shower relies on a form of electromagnetic calorimetry”. Once the distance from the telescopes to the shower is known (from the core position), it can be coupled with the *image size* (the total amount of integrated signal obtained from the Cherenkov shower) to obtain total energy released as Cherenkov light [1, 62]. This is a proportional measure of the energy of the shower progenitor particle (Section ).

section in introduction where it is shown that the majority of energy of the gamma-ray is released as Cherenkov light

### 6.3.4 $\gamma$ -Hadron Discrimination

One of the primary disadvantages of the Imaging Atmospheric Cherenkov Technique is the extremely large hadronic shower background. The sensitivity of an IACT is heavily influenced by its ability to exclude this background. A property that is traditionally relied upon in this background rejection process is the differences in morphology between gamma-ray and hadronic shower images. This is further described in Chapter 1. In traditional IACT analysis, the morphology of the showers are quantified by the *Hillas Parameters*. Gamma-ray showers typically exist within a narrow range of the parameters, while hadronic showers typically exhibit a broader spectrum of parameter values, as illustrated in Figure 6.6. By creating an acceptance range for the *Hillas Parameters*, the hadronic background can be excluded in a very simple way [60, 64, 65]. However, the higher the energy of the hadron shower is, the more it begins to resemble a gamma-ray shower, making it harder to discriminate using simple cuts on the *Hillas Parameters*. This is especially a problem for the Small Size Telescopes (SSTs), which are designed to operate within the gamma-ray energy range of 1-300 TeV. The distributions of the *Hillas* width and length from simulations of CHEC-S on the ASTRI telescope structure are shown in Figure 6.7. More advanced techniques, such as the use of *Boosted Decision Trees* [66], provide a much more effective background reduction, and therefore can considerably improve the sensitivity.

describe differences in images in intro, and show perfect examples with MC of CHECS. Lessard gives precise information about the differences

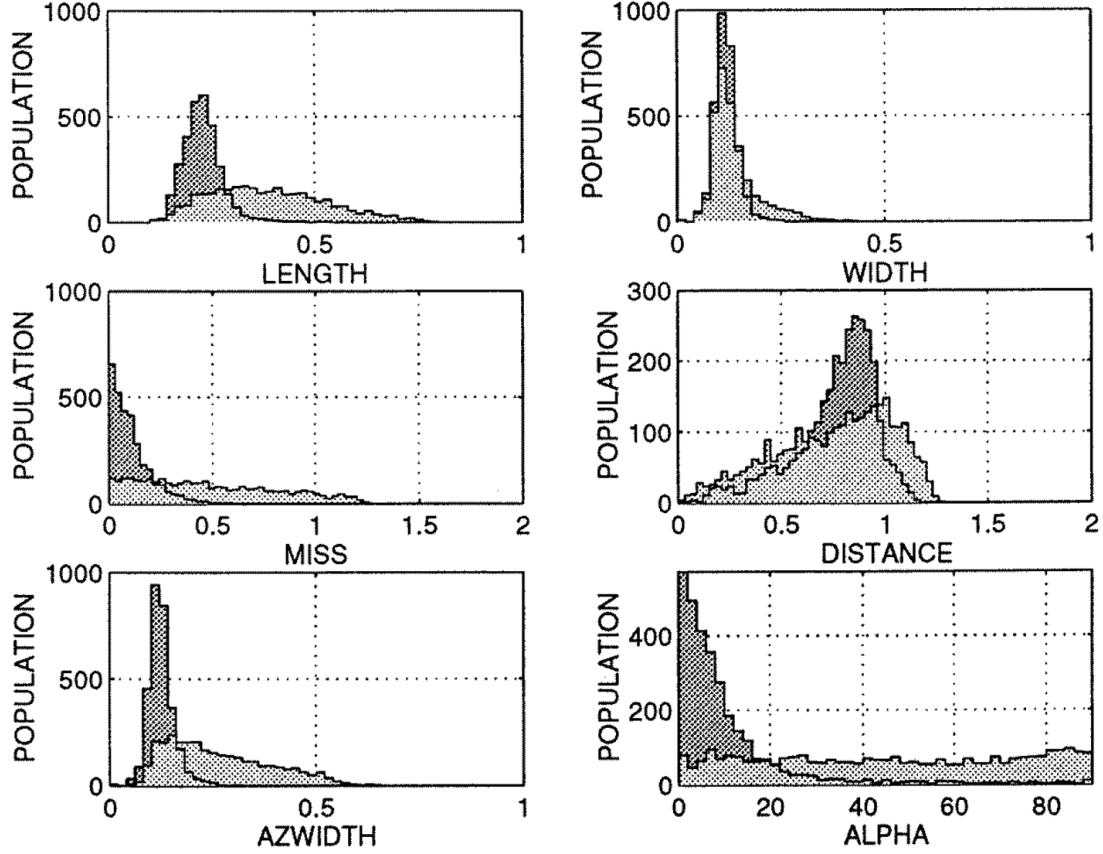


**Figure 6.6:** Example of the differences in the distributions of *Hillas Parameters* between simulated  $\gamma$ -ray-induced showers (dark) and real hadronic-induced showers (light) for the Whipple 10 m reflector [64].

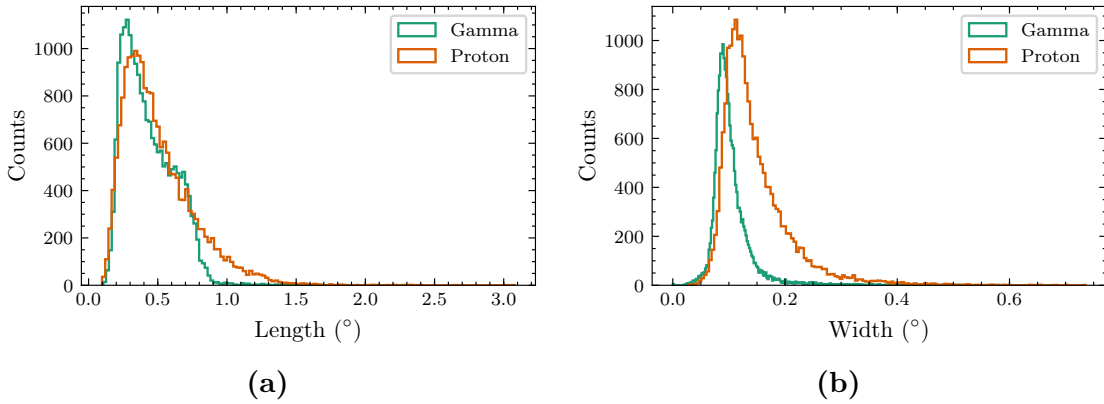


**Figure 6.7:** The *Hillas* width and length parameters extracted from Monte Carlo simulations of CHEC-S on the ASTRI telescope structure, for both gamma-ray and proton induced showers. The energy ranges simulated were 2-330 TeV for the gamma rays and 6-600 TeV for the protons. Each histogram contains approximately 20,000 shower images.

---

# 7

2292

2293

## Camera Performance

2294

### Contents

---

2295

2296	<b>7.1 Introduction</b>	85
2297	<b>7.2 CHEC-S Monte Carlo Model</b>	86
2298	<b>7.3 CHEC-S Charge Resolution</b>	88
2299	7.3.1 Procedure and Datasets	88
2300	7.3.2 Lab Results	92
2301	7.3.3 Lab versus Monte Carlo	92
2302	7.3.4 Night Sky Background	95
2303	7.3.5 Optical Crosstalk	97
2304	7.3.6 Analytical Description	99
2305	7.3.7 Conclusion	101
2306	<b>7.4 CHEC-S Pulse Shape</b>	101
2307	<b>7.5 CHEC-S Time Resolution</b>	102
2308	<b>7.6 CHEC-M</b>	104

2309

2311

---

2312

### 7.1 Introduction

2313 As discussed in Chapter 3, it is important that the CHEC camera meets certain  
2314 criteria in order for it to be accepted as an in-kind contribution to CTA. One  
2315 important subset of the criteria is the camera’s performance. The requirements  
2316 that must be fulfilled are driven by the science goals of CTA. If a camera does not  
2317 meet the requirements laid out by the CTA observatory, then it will be refused as a  
2318 contribution in its current state, lest the science goals of CTA are not achieved.

2319 This chapter will cover many of the primary standards used to assess a CTA  
2320 camera’s performance. The results shown in this chapter are all my own, and are  
2321 obtained using the procedures defined in the preceding chapters. Two important  
2322 aspects of the camera’s performance which are not included in this chapter are

2323 the trigger efficiency and absolute photon detection efficiency. The investigations  
 2324 into these parameters are ongoing, and I have not had direct involvement with  
 2325 these as part of my DPhil.

2326 **7.2 CHEC-S Monte Carlo Model**

2327 An important preface to reporting on the performance of CHEC is the description  
 2328 of the efforts in generating an accurate model of the camera for use inside the Monte  
 2329 Carlo simulations performed by `sim_telarray` (Chapter 4). These simulations allow  
 2330 us to explore the parameter space related to our camera performance more widely,  
 2331 and identify potential issues that cause the real camera to drift away from ideal  
 2332 operation. It is also a necessary step in investigating the on-sky performance  
 2333 of the telescope, as:

- 2334 • One does not have prior knowledge of the properties of the light incident on  
   2335 the pixels in the real world.
- 2336 • The camera is still being tested in the lab. An on-sky campaign for CHEC-S  
   2337 on the ASTRI telescope structure is planned for later this year.

2338 Contained within the lab data are the parameters required for the Monte Carlo  
 2339 validation process. Important parameters include:

- 2340 • Pixel position on the focal surface,
- 2341 • Pulse shape of a single photoelectron,
- 2342 • Trigger discrimination behaviour,
- 2343 • Quantum efficiency (or PDE),
- 2344 • Variation of quantum efficiency between pixels,
- 2345 • Electronic baseline variation,
- 2346 • Photosensor gain,
- 2347 • Variation of gain between pixels,
- 2348 • Single photoelectron multiplication response (Figure 2.8).

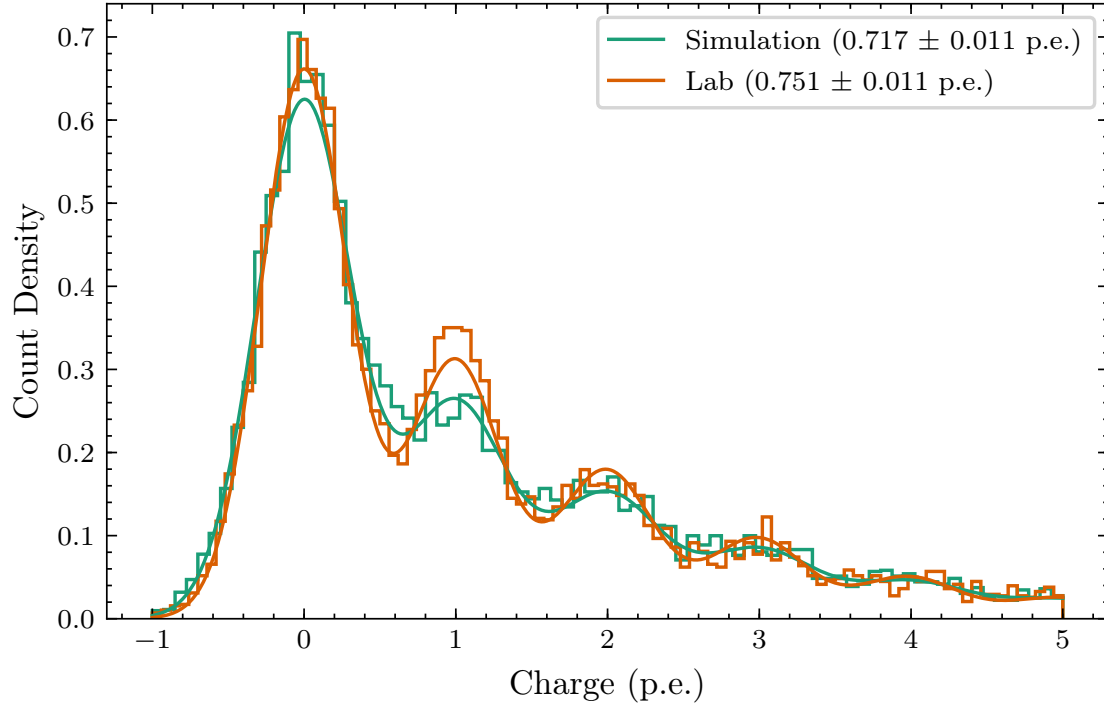


**Figure 7.1:** Comparison of the SPE spectra for a single pixel between lab measurements and simulations after an initial attempt towards a more accurate Monte Carlo model. The SPE spectra were identically constructed in both cases, using the *Cross Correlation* charge extraction method. Each spectra histogram was then fit using Equation ???. Three illuminations were simultaneously fit, however just a single illumination is displayed here. Both spectra are normalised in the x direction by their respective single-photoelectron value, and in the y direction such that their integral is 1.

Fit Parameter		Simulation	Lab
Average Illumination	[p.e.]	$0.717 \pm 0.011$	$0.751 \pm 0.011$
Pedestal Deviation	[p.e.]	$0.314 \pm 0.003$	$0.286 \pm 0.002$
Gain Deviation	[p.e.]	$0.109 \pm 0.009$	$0.078 \pm 0.007$
Optical Crosstalk		$0.387 \pm 0.007$	$0.350 \pm 0.006$

**Table 7.1:** Parameter values resulting from the fit to the spectra in Figure 7.1. The  $1\sigma$  parabolic errors obtained from the covariance matrix of the fit parameters are quoted.

2349

2350

2351

2352

2353

2354

2355

reference  
spe fitting  
equation

For the simulation results presented in this thesis, an updated value was obtained for as many of the relevant `sim_telarray` parameters as possible. Figure 7.1 displays the resulting differences in terms of the SPE spectra between lab and simulation. The discrepancies in parameters resulting from the fits to the SPE spectra are shown in Table 7.1, and are deemed to be close enough for the investigations in this thesis. Further details about the fit procedure for SPE spectra can be

2356 found in Appendix ???. The differences between lab and simulation in other factors  
2357 and at higher amplitudes are explored through *Charge Resolution* comparisons,  
2358 investigated later in this chapter.

## 2359 7.3 CHEC-S Charge Resolution

2360 The *Charge Resolution* is the principle criterion used within CTA to express how well  
2361 the camera can resolve a signal. The concept of *Charge Resolution* is introduced in  
2362 Section 3.2.1, alongside the CTA requirement **B-TEL-1010 Charge Resolution**.  
2363 It not only measures the quality of the camera's photosensor and electronics, but  
2364 also the aptitude of the calibration and signal extraction. Consequently, obtaining a  
2365 *Charge Resolution* of the camera that meets this requirement has been the underlying  
2366 driver behind my efforts in developing the techniques described in this thesis.

### 2367 7.3.1 Procedure and Datasets

2368 As directed in the **B-TEL-1010 Charge Resolution** requirement, one must  
2369 simulate the response of the camera to Cherenkov shower illumination to verify the  
2370 requirement is met. However, this result must be supported by evidence that the  
2371 *Charge Resolution* appropriately resembles the behaviour of the real camera. To  
2372 achieve this, I display the *Charge Resolution* with four different procedures. Each  
2373 procedure bridges the gap between the *Charge Resolution* I obtained with Cherenkov  
2374 shower simulations, and the *Charge Resolution* I obtained from lab measurements.  
2375 The procedures, and their associated names for the purpose of this thesis, are:

2376 **Lab** Utilises uniform illumination datasets taken in the lab that cover the full  
2377 dynamic range of the camera, with 1000 events at each illumination. The  
2378 average expected charge per pixel (in photoelectrons) for each illumination  
2379 is calibrated by the procedure detailed in Section ???. Using the calibration  
2380 procedures detailed in Chapter 5 and the *Cross Correlation* charge extraction  
2381 technique (Chapter 6), a value of measured charge in photoelectrons is obtained  
2382 for every waveform. As the average expected charge includes the Poisson  
2383 fluctuations, it is appropriate to use Equation 3.1 for calculating the *Charge*  
2384 *Resolution*, with the measured charge per waveform used for  $Q_{Mi}$  and the  
2385 average expected charge for  $Q_T$ . It is important to note that these datasets  
2386 are taken with no NSB contribution, and are therefore not a completely  
2387 appropriate measure against the CTA requirement (defined for an NSB photon  
2388 rate per pixel of 0.125 p.e./ns = 125 MHz). However, a DCR of  $\sim$ 5 MHz is  
2389 assumed to be present in the SiPM.

---

2390 **MCLab** Simulations of the dynamic range datasets from the lab are obtained  
 2391 with the updated `sim_telarray` camera model. Using the identical method  
 2392 used for the lab data (excluding the TARGET calibration) the charge is  
 2393 extracted and calibrated from the waveforms. The average expected charge  
 2394 for each illumination per pixel is also obtained in the same way as the previous  
 2395 procedure. However, the simulations contain perfect laser uniformity across  
 2396 the camera face (though the geometry corrections shown in Section B.3 are  
 2397 still applicable, as the simulations contain a point source  $\sim 1.5$  m from the  
 2398 camera). This dataset then fully represents the same measurements, but with  
 2399 the Monte Carlo model of the camera instead of the physical camera. With  
 2400 an accurate model of the camera, the *Charge Resolution* result should be  
 2401 the same as from the lab measurements. Equation 3.1 is also used in this  
 2402 procedure for calculating the *Charge Resolution*.

2403 **MCLabTrue** Utilises the same dataset as the previous procedure, but instead of  
 2404 using the average expected charge, the true number of photoelectrons that  
 2405 were incident on the pixel for each waveform are extracted from the simulation  
 2406 file. The linear fit between the average measured charge and the “true charge”  
 2407 is used to calibrate the extracted charge into corresponding units. As the  
 2408 unique value of “true charge” per waveform is now used as  $Q_T$ , Equation 3.4  
 2409 must be used to account for the lack of Poisson fluctuations in  $Q_T$ . The  
 2410 *Charge Resolution* resulting from this procedure demonstrates the change  
 2411 in transitioning from “average expected charge” to “true charge”, which is  
 2412 important for interpreting the results from the next procedure.

2413 **MCOnsky** Produced using a dataset containing Monte Carlo simulations of  
 2414 gamma-ray-induced air shower observations is created using `CORSIKA` and  
 2415 `sim_telarray`. A model of CHEC-S on the ASTRI telescope structure is  
 2416 used in the simulation. The *Charge Resolution* is then calculated with the  
 2417 same procedure as in *MCLabTrue*. As only a small section of the camera  
 2418 is illuminated by the Cherenkov shower, this procedure is dependant on  
 2419 the peak-finding methods described in Chapter 6. The *Local Peak Finding*  
 2420 technique is used for this investigation. This *Charge Resolution* procedure is  
 2421 the definitive approach for assessment of *Charge Resolution*, as defined in the  
 2422 requirement. The previous procedures exist to support the claim that this  
 2423 result is applicable to the real camera.

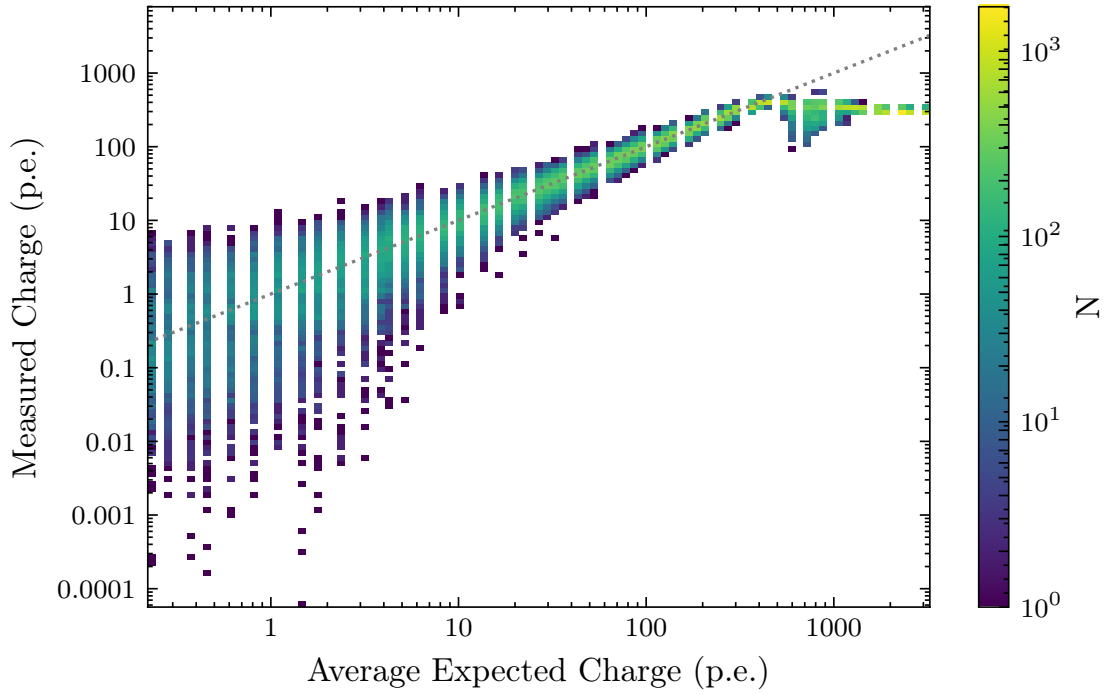


**Figure 7.2:** Two-dimensional histogram showing every measured charge for a single CHEC-S pixel, covering the full dynamic range. This dataset matches the one described in the *Lab* procedure in Section 7.3.1. The grey dotted line represents a one-to-one relation between the axes.

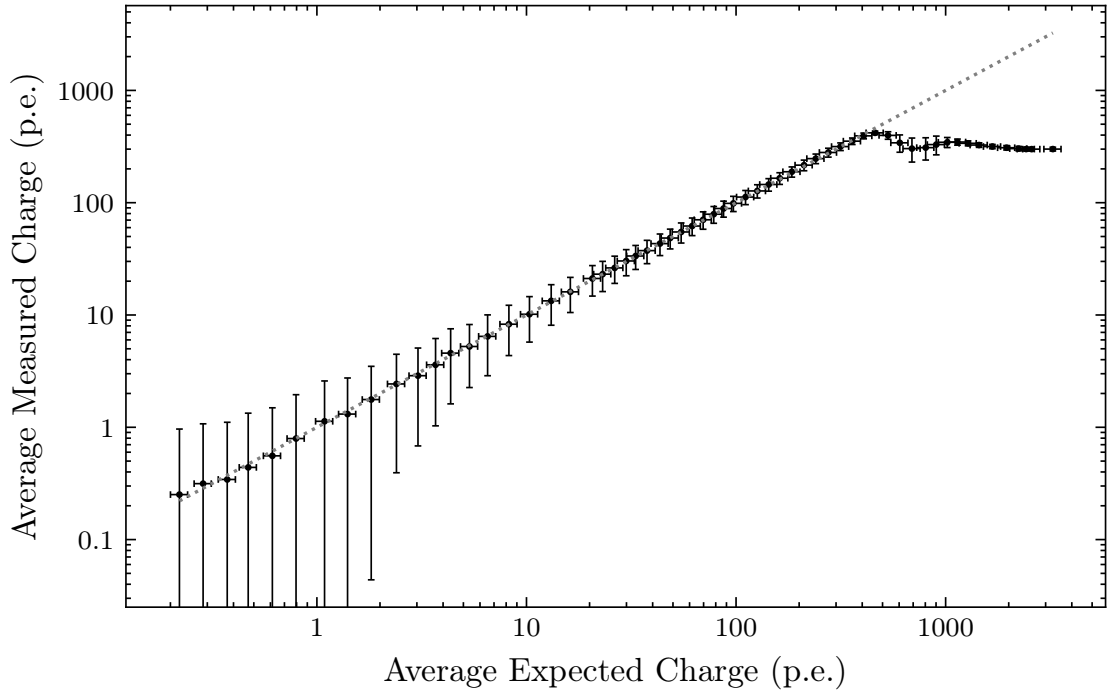


**Figure 7.3:** Similar to Figure 7.2, but summarising the entries in terms of their averages and standard deviation for each illumination. The X error bars represent the uncertainty in the filter-wheel calibration into units of p.e. (Section B.6).

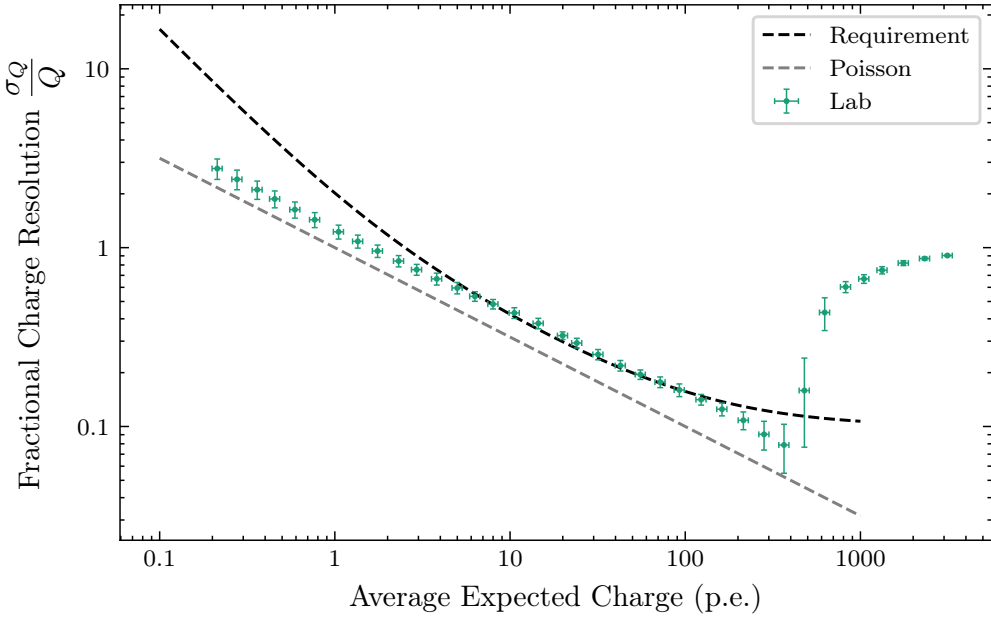


**Figure 7.4:** Average *Charge Resolution* across CHEC-S (excluding “dead” pixels) for the same Lab dynamic range dataset Figure 7.2 uses. The Y error bars represent the standard deviation of the *Charge Resolution* values across the camera. The X error bars represent the uncertainty in the filter-wheel calibration into units of p.e. (Section B.6). The points are binned to improve visibility. The presentation of the *Charge Resolution* in this form matches Figure 3.1.

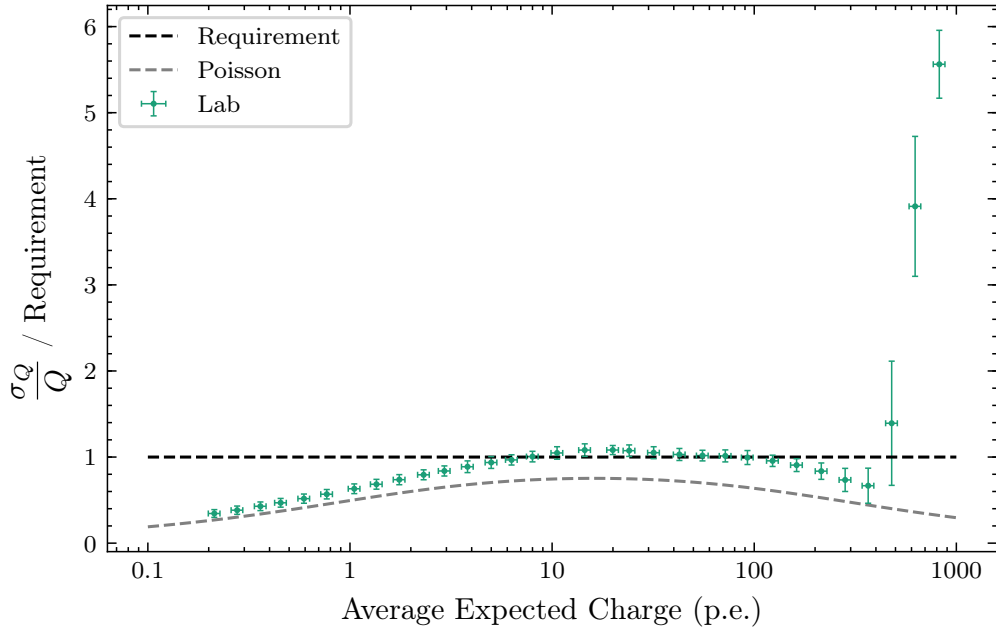


**Figure 7.5:** Same result shown in Figure 7.4, but with respect to the requirement curve to emphasise the separation between it and the points.

---

2424 **7.3.2 Lab Results**

2425 To begin, the different representations of the *Charge Resolution* are first explained  
2426 in terms of the *Lab* procedure and dataset. Figure 7.2 demonstrates the charge  
2427 extracted for the entire dynamic range dataset, post calibration. It is the purpose  
2428 of the *Charge Resolution* to consolidate the spread and bias of these measured  
2429 charges (from the average expected charge) into a single value per average expected  
2430 charge (or “true charge” where appropriate). The average measured charges in  
2431 Figure 7.3 seem to strongly follow a one-to-one relation with the average expected  
2432 charge (in the non-saturated region), attesting to the success of the extracted  
2433 charge calibration. However, to fully explore the performance of the camera, we  
2434 continue on to the *Charge Resolution* shown in Figure 7.4. It is immediately obvious  
2435 that in the saturated region ( $>300$  p.e.), the camera fails the *Charge Resolution*  
2436 requirement. This is expected, as we make no attempt to recover saturated signals  
2437 in this investigation. Methods to account for the saturation are briefly described  
2438 in Section 5.4, and will be fully explored in a future investigation.

2439 To investigate other less obvious features in the *Charge Resolution*, I display  
2440 the *Charge Resolution* in terms of its deviation from the requirement curve. This  
2441 is achieved by dividing the *Charge Resolution* curve by the requirement curve.  
2442 Figure 7.5 expresses the *Charge Resolution* from Figure 7.4 in this format. This is  
2443 how the *Charge Resolution* is visualised elsewhere in this thesis, as it shows how  
2444 close the points are to the requirement, and emphasises features that cause the  
2445 results to fail the requirement. In the region of  $10 < Q_{\text{Exp}} < 100$  p.e., the *Charge*  
2446 *Resolution* of the *Lab* dataset is above the requirement curve, and therefore fails the  
2447 requirement. By comparing this *Charge Resolution* to those resulting from different  
2448 Monte Carlo simulations that explore the contributing parameter space, we are able  
2449 to identify the primary factors resulting in a failure to meet the requirement.

2450 **7.3.3 Lab versus Monte Carlo**

2451 As a preface to the simulated *Charge Resolution* investigations, the differences in  
2452 the results of the procedures described in Section 7.3.1 are illustrated in Figure 7.6.  
2453 The earlier descriptions of each procedure indicate the following expected differences  
2454 between their *Charge Resolutions*:

- 2455 • With a perfect Monte Carlo model of the camera, there should be no differences  
2456 between the *Charge Resolution* of *Lab* and *MCLab*. Any deviations arise from  
2457 a misunderstanding in the camera’s behaviour, or from an unaccounted noise  
2458 contribution.

- 2459     • The difference between *MCLab* and *MCLabTrue* demonstrates the expected  
 2460       change when transitioning from the average expected charge, to the “true  
 2461       charge” that was detected in the pixel.
- 2462     • As they are the same camera model, and the same *Charge Resolution* calcu-  
 2463       lation approach, there should be very little difference between *MCLabTrue*  
 2464       and *MCOnsky*. The only factor to contribute to differences between the two  
 2465       procedures is the peak-finding that is necessary for the *MCOnsky* datasets.

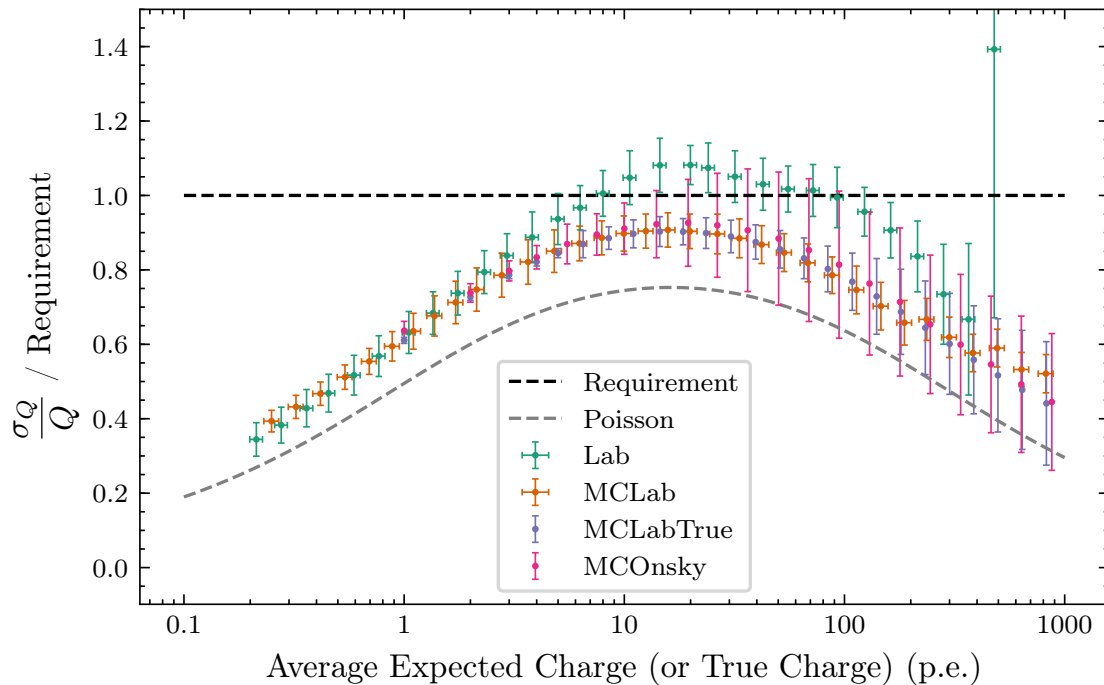


**Figure 7.6:** Comparison of the *Charge Resolutions* resulting from the different procedures described in Section 7.3.1. A background photon rate of 5 MHz is simulated in the Monte Carlo datasets to represent the DCR we expect inside the datasets produced from lab measurements. The saturated points from the *Lab* measurements are outside of the figure’s range.

2466     It is therefore apparent in Figure 7.6 that our simulation model is not a perfect  
 2467       representation of CHEC-S. The lack of saturation in the simulated datasets is  
 2468       expected, and that is a feature we will include in future investigations. However,  
 2469       from the simulated datasets we can conclude that in the absence of additional  
 2470       NSB photons, the *Charge Resolution* of our camera before the saturated region  
 2471       should be below the requirement. As we do not observe this in the non-simulated  
 2472       dataset, there must be a noise contribution we have not appropriately accounted  
 2473       for. The work required to fully diagnose this noise contribution is beyond the scope  
 2474       of this thesis; however, possible options include:

2475 **Transfer Functions** The simulations do not fully simulate the CHEC-S electronics.  
 2476 They contain no resemblance of the digitising behaviour of TARGET ASICs,  
 2477 and therefore no variations in amplitude response exists from sample-to-sample.  
 2478 Inaccuracies in the Transfer Function calibration (Chapter 5) could manifest  
 2479 themselves as differences between the *Charge Resolutions* of lab and simulated  
 2480 data.

2481 **Timing** As mentioned in Section 5.5, the variations in signal arrival time between  
 2482 pixels could degrade the *Charge Resolution*. This contribution is not included  
 2483 in the simulation.

2484 **Electrical Crosstalk** Inside the simulation, each pixel is considered independently.  
 2485 Due to electronic coupling, this is unfortunately not the case in reality.

2486 **Optical Crosstalk** A simplified form of optical crosstalk is used in the simulation,  
 2487 via the input SPE spectra shape. This may not fully characterise the full  
 2488 behaviour of the optical crosstalk.

Rich:  
better de-  
scription  
(technical)  
of how the  
electronic  
crosstalk  
happens,  
e.g. of  
ground  
bounce

2489 **Reference Pulse Shape** Another major difference between simulation and reality  
 2490 is the behaviour of the pulse shape. In simulations, the pulse shape at all  
 2491 illuminations is constructed by the superposition of the individual photo-  
 2492 electron pulses. If that description was appropriate for the real camera, the  
 2493 pulse shape dependency with amplitude would not be seen in Section 7.4.  
 2494 As we use the *Cross Correlation* charge extraction method, the measured  
 2495 charge is sensitive to changes in pulse shape. This could, in theory, result  
 2496 in discrepancies between the *Charge Resolutions* of lab and simulated data.  
 2497 However, the investigations in Appendix ?? seem to suggest this factor is not  
 2498 significant.

2499 Identifying the cause of this noise contribution is of paramount importance in the  
 2500 commissioning of CHEC-S. However, the remainder of this section will explore the  
 2501 possibility of meeting the *Charge Resolution* even in the presence of this unknown  
 2502 noise contribution. This procedure may give insight into the source of the noise.

2503 **7.3.4 Night Sky Background**

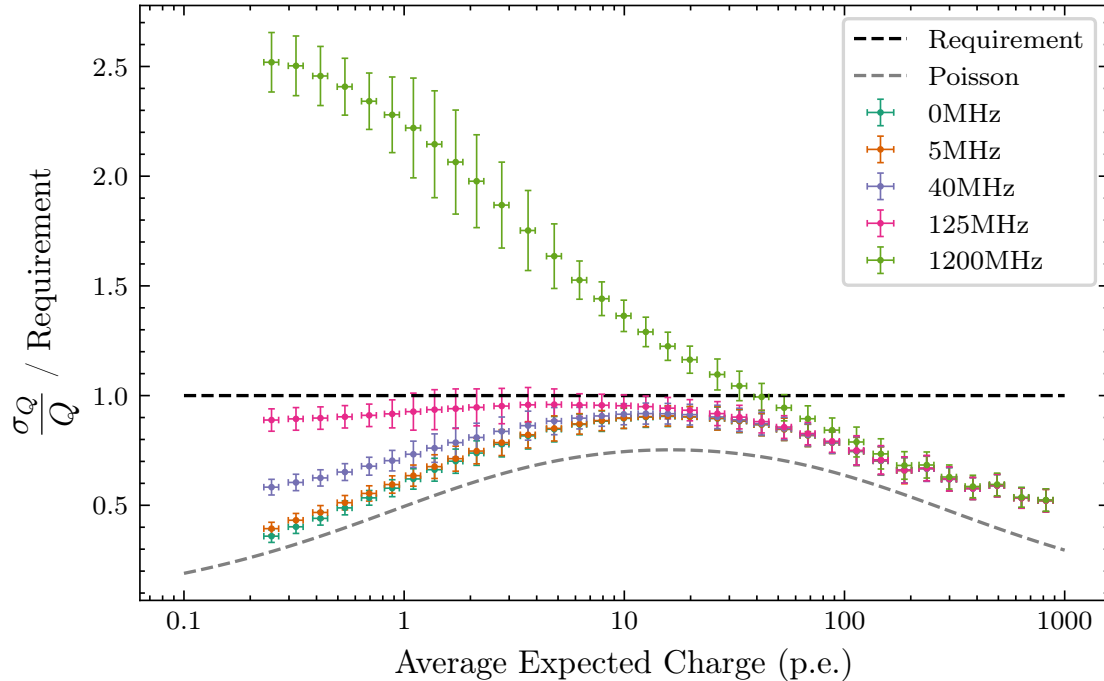


**Figure 7.7:** Comparison of the *Charge Resolutions* obtained from the *MCLab* procedure when simulating different Night Sky Background (NSB) photon rates.

2504 As the NSB photon rate increases, we expect more noise to be included in the  
 2505 charge extraction. This results in a higher charge than expected, and increases  
 2506 the variation in signal measured for the same average illumination. Figure 7.7  
 2507 illustrates the degradation in charge resolution caused by an increase in NSB rate.  
 2508 The effects are most pronounced at the lower values of average expected charge,  
 2509 where an increase in NSB has a larger impact on the signal-to-noise ratio. We can  
 2510 conclude from this figure that even if the unknown noise contribution in the *Lab*  
 2511 datasets is corrected for, the current design of CHEC-S could potentially fail to  
 2512 meet the CTA requirement at the specified NSB of 125 MHz.

2513 A similar dependence on NSB is observed with the *MCLabTrue* procedure  
 2514 in Figure 7.8, however the *Charge Resolutions* demonstrate an overall improved  
 2515 performance over the *MCLab* representation (Figure 7.7).

2516 Despite the improved performance achieved when using the “true charge”, a  
 2517 second consequence of higher NSB is the increased difficulty of finding the signal  
 2518 pulse among the noise pulses. As shown in Figure 7.9, this causes the current model  
 2519 of CHEC-S to fail the *Charge Resolution* requirement when observing Cherenkov  
 2520 showers. An alternative to the *Local Peak Finding* approach could improve on this  
 2521 bias to noise pulses, and therefore enable the requirement to be met.

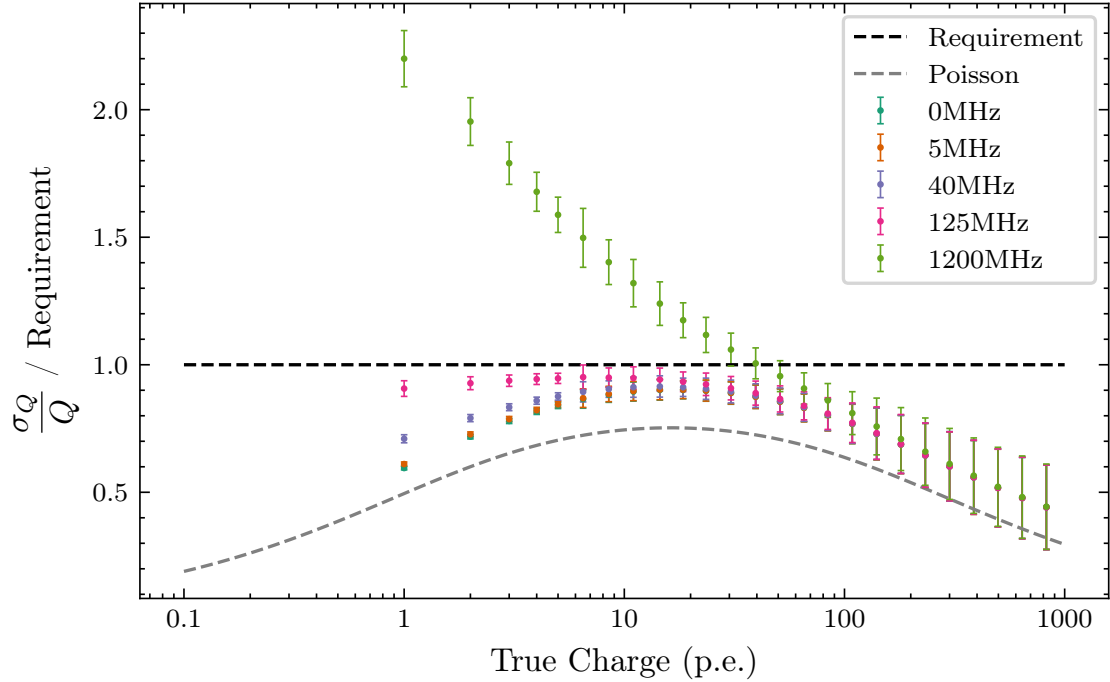


**Figure 7.8:** Comparison of the *Charge Resolutions* obtained from the *MCLabTrue* procedure when simulating different values of NSB.

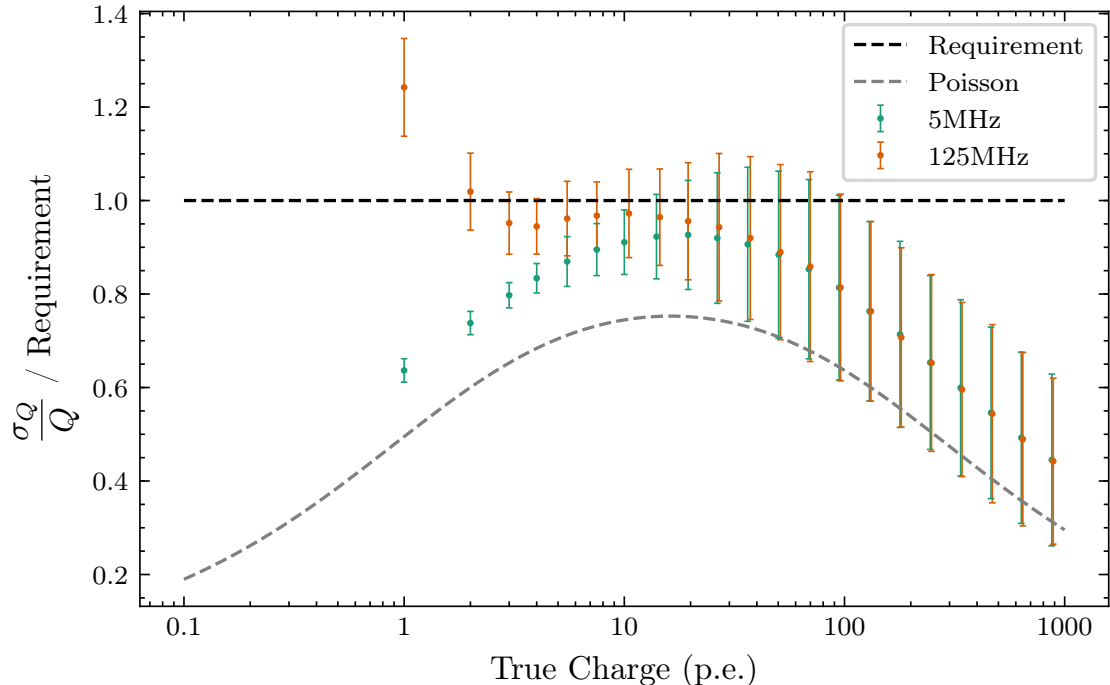


**Figure 7.9:** Comparison of the *Charge Resolutions* obtained from simulated observations of Cherenkov showers (via the *MCOnsky* procedure), when simulating different values of NSB. The signal inside each waveform is found with the *Local Peak Finding* approach.

2522 **7.3.5 Optical Crosstalk**

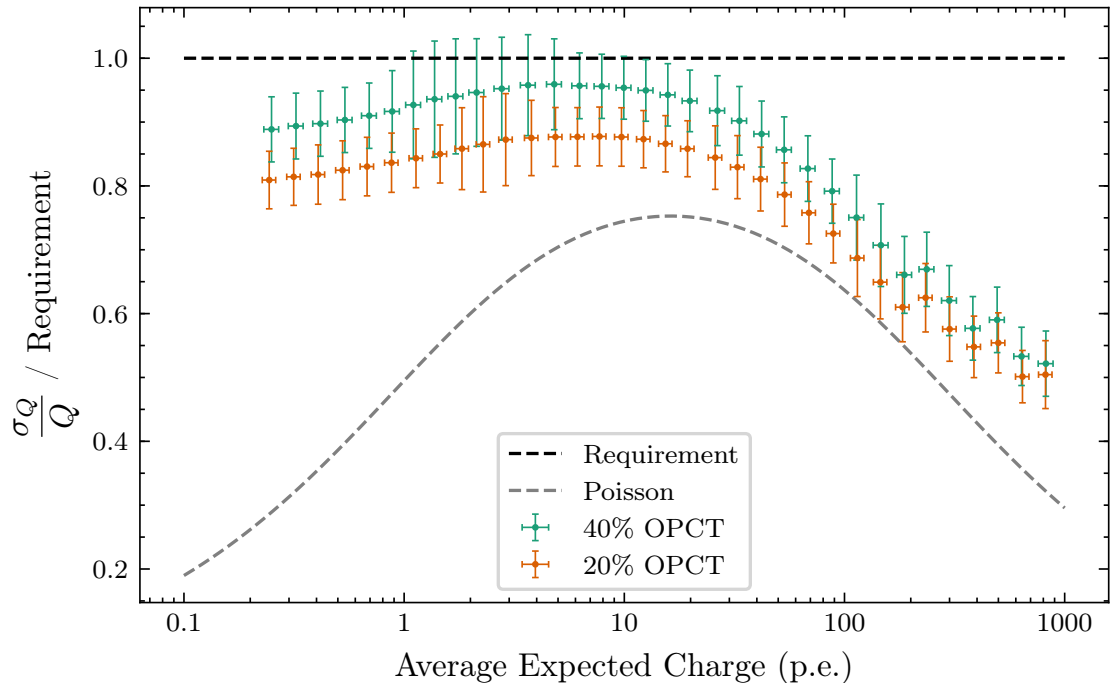


**Figure 7.10:** Comparison of the *Charge Resolutions* obtained from the *MCLab* procedure when simulating different values of optical crosstalk (abbreviated here as OPCT). An NSB rate of 125 MHz was included in these simulations.

2523 A prime suspect for the poor *Charge Resolution* is the very high (35-40 %) optical  
2524 crosstalk in the SiPMs currently used for the CHEC-S prototype. This value  
2525 range of optical crosstalk is obtained from the SPE fit parameters to the camera  
2526 pixels (the values for a single pixel are shown in Table 7.1). The optical crosstalk  
2527 contributes to the extracted charge in two ways:

- 2528 • The measured charge is consistently higher. This factor is accounted for in  
2529 the flat-fielding calibration (Section 5.3).
- 2530 • The spread in charge that results from a particular amount of photons is  
2531 larger. This is therefore expressed as an increase in the Excess Noise Factor  
2532 (ENF) (see Section 2.2.5).

2533 **Monte Carlo**

2534 Figure 7.10 demonstrates the *MCLab Charge Resolution* for a simulation of the  
2535 CHEC-S model, but with 20 % optical crosstalk. This is compared to the original

<sup>2536</sup> model with 40 % optical crosstalk. The effect of a reduced optical crosstalk in the  
<sup>2537</sup> simulation is an improvement in the *Charge Resolution* for all illuminations.

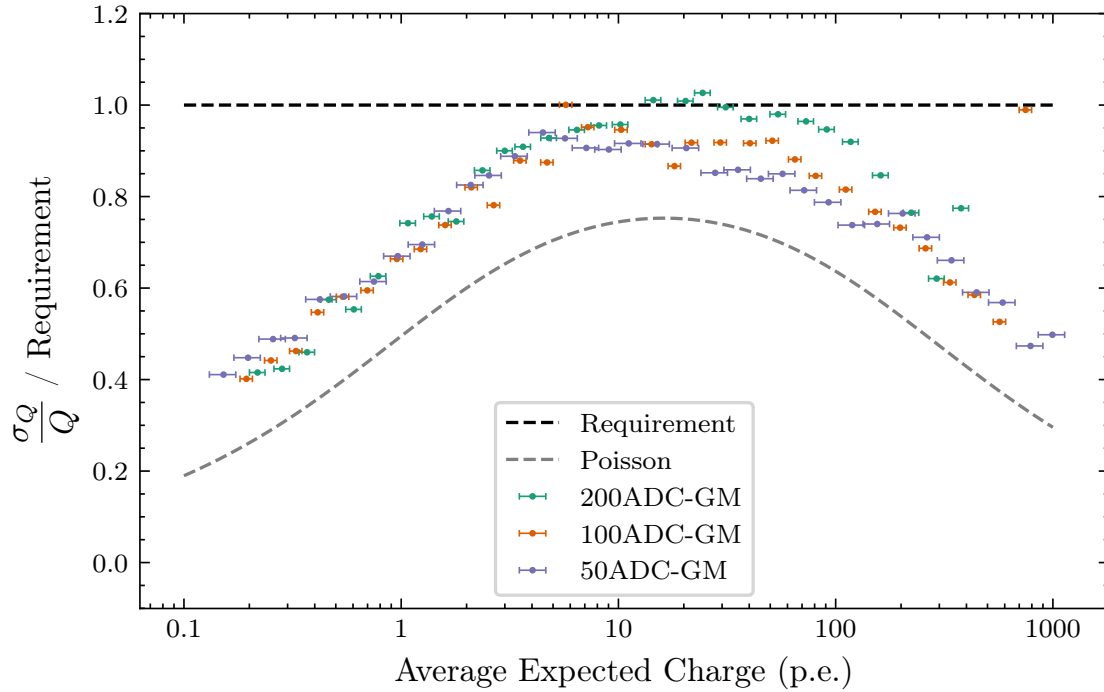


**Figure 7.11:** Comparison of the *Charge Resolutions* obtained from different *Lab* datasets. Each dataset is gain-matched to a different ADC value. By gain matching to different ADC values, a different bias voltage is applied to the SiPM pixel. As this dataset was gain-matched in units of ADC, the spread between pixels is large. Therefore, only a single pixel's *Charge Resolution* is shown.

Fit Parameter		200 ADC	100 ADC	50 ADC
Average Illumination 1	[p.e.]	$1.061 \pm 0.014$	$0.903 \pm 0.023$	$0.550 \pm 0.009$
Average Illumination 2	[p.e.]	$0.793 \pm 0.012$	$0.688 \pm 0.021$	$0.394 \pm 0.008$
Average Illumination 3	[p.e.]	$0.625 \pm 0.010$	$0.535 \pm 0.014$	$0.301 \pm 0.007$
Pedestal Deviation	[mVns]	$6.047 \pm 0.043$	$5.668 \pm 0.049$	$5.913 \pm 0.039$
Gain	[mVns]	$21.33 \pm 0.073$	$16.06 \pm 0.108$	$12.10 \pm 0.094$
Gain Deviation	[mVns]	$1.684 \pm 0.159$	$0.005 \pm 15.03$	$0.003 \pm 11.05$
Optical Crosstalk		$0.339 \pm 0.006$	$0.242 \pm 0.011$	$0.100 \pm 0.006$

**Table 7.2:** Parameter values resulting from the fit to the SPE spectra of the different gain-matched datasets for a single pixel. Three illuminations were simultaneously fit. These three illuminations are identical in terms of filter-wheel transmission (and therefore average photons) between the three gain-matched datasets.

---

2538 **Changing Bias Voltage**

2539 Due to the dependence of the optical crosstalk on the overvoltage across the SiPM  
 2540 (described in Section 2.2.4), it is possible to investigate the impact a reduced optical  
 2541 crosstalk has on *Charge Resolution* using *Lab* data that is taken with different bias  
 2542 voltages. Three datasets were generated, each gain-matched to a different ADC  
 2543 value (the Transfer Functions were not included in the gain matching procedure  
 2544 at the time). The 200 ADC gain-matched dataset is at a similar bias voltage to  
 2545 the the dataset in Figure 7.5. The 100 ADC and 50 ADC gain-matched datasets  
 2546 are produced by reducing the bias voltage. The effect of a reduced bias voltage on  
 2547 the SiPM characteristics is quantified in the parameters extracted from the fit to  
 2548 the SPE spectra, shown in Table 7.2. In total, the optical crosstalk is reduced by a  
 2549 factor of 3 to 10 % in going from a gain matching of 200 ADC to 50 ADC.

2550 Figure 7.11 shows the improvement in *Charge Resolution* with reduced bias  
 2551 voltage, bringing the result below the requirement. Additionally, by reducing the  
 2552 bias voltage, the unexplained noise component that was identified in the comparison  
 2553 between the *Lab* and *MCLab* datasets (Figure 7.6) appears to diminish, suggesting  
 2554 it is possibly related to the optical crosstalk.

2555 However, it is important to note that by reducing the bias voltage, we also  
 2556 decrease the Photon Detection Efficiency (PDE) of the SiPM (Figure 2.5). This  
 2557 effect is evident in the average illumination values quoted in Table 7.2. The result  
 2558 of a lower PDE is a reduction in the camera’s ability to detect Cherenkov shower  
 2559 photons. This contradiction between improving *Charge Resolution*, but reducing  
 2560 Cherenkov shower resolution, is one of the primary reasons the CTA requirements  
 2561 are being redefined to be in terms of photons, as described in Chapter 3.

2562 **7.3.6 Analytical Description**

2563 One further way to characterise the camera’s *Charge Resolution* is to use the analyti-  
 2564 cal description of the *Charge Resolution* provided by Equation 3.2. However, to fully  
 2565 interpret this function, we must understand the contribution of optical crosstalk to  
 2566 the  $\sigma_{ENF}$  parameter. If we assume that optical crosstalk is the dominant contributor  
 2567 to  $\sigma_{ENF}$  for an SiPM (a reasonable assumption due to the high photoelectron  
 2568 resolution, as shown in Figure 2.8), the following equations derived by Vinogradov  
 2569 [15] can be used to express the  $\sigma_{ENF}$  in terms of the optical crosstalk probability  $P_{\text{optc}}$ :

$$\sigma_{ENF} \approx 1 + P_{\text{optc}}, \quad (7.1)$$

$$\sigma_{ENF} \approx 1 + P_{\text{optc}} + \frac{3}{2} P_{\text{optc}}^2, \quad (7.2)$$

2570 where the former equation is applicable in a geometric chain model of the optical

2572 crosstalk behaviour (each single electron response is capable of only producing 1 or 0  
 2573 further electron responses) and the latter equation is applicable in a branching  
 2574 Poisson model (each single electron response produces a Poisson distributed random  
 2575 number of further electron responses). The  $P_{\text{optc}}^3$  term from the equation derived  
 2576 by Vinogradov [15] is assumed to be negligible.

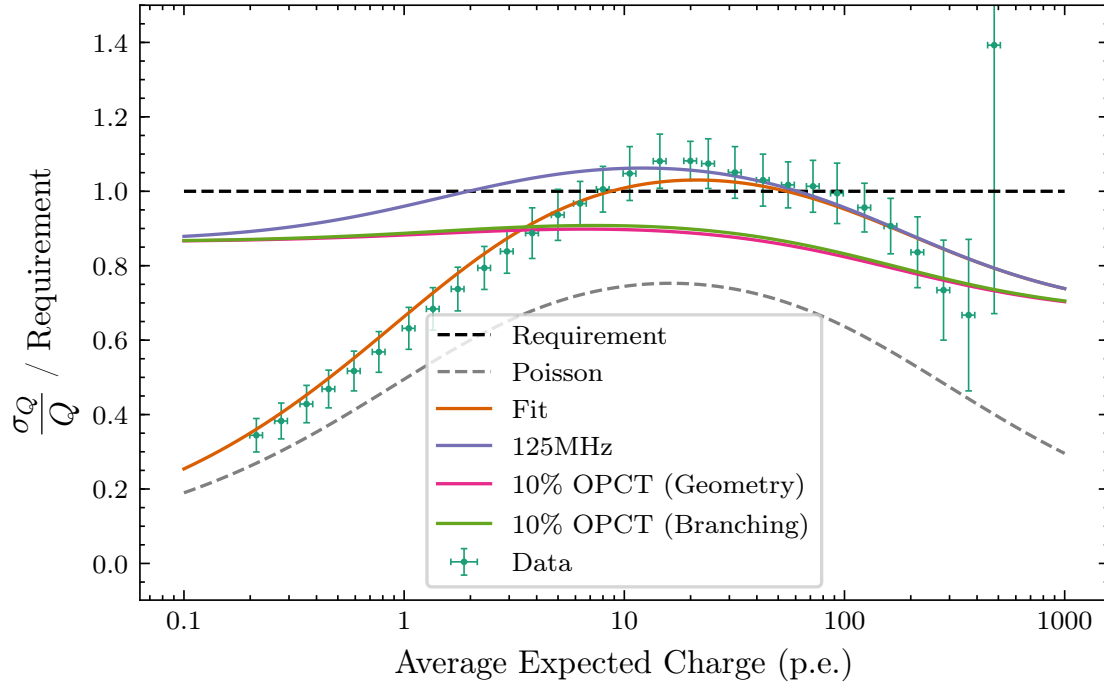


**Figure 7.12:** Analytical fit of the *Lab Charge Resolution* using Equation 3.2. All “non-dead” pixels are included in the fit to give an average characterisation of the whole camera. The fit result is used to predict the *Lab Charge Resolution* at 125 MHz NSB, and then with 10% optical crosstalk in the presence of 125 MHz NSB. The possible relationships between ENF and optical crosstalk are shown in Equations 7.1 and 7.2.

Fit Parameter	Values
Background Noise $\sigma_0$	$0.000 \pm 0.316$
Excess Noise Factor $\sigma_{\text{ENF}}$	$1.338 \pm 0.003$
Miscalibration $\sigma_g$	$0.067 \pm 0.001$

**Table 7.3:** Parameter values resulting from the fit to the *Lab Charge Resolution* (Figure 7.12) using Equation 3.2.

2577 Shown in Figure 7.12 is the result from fitting Equation 3.2 to the *Lab Charge*  
 2578 *Resolution* from Figure 7.5. The resulting parameters, shown in Table 7.3, indicate  
 2579 that  $\sigma_0$  was poorly constrained by the data points, however  $\sigma_{\text{ENF}}$  and  $\sigma_g$  are  
 2580 well characterised. The first conclusion provided by the fit is the miscalibration

is very low, and is potentially still overestimated due to the lack of high charge measurements (values above the saturation point were excluded). Secondly, the value extracted for  $\sigma_{ENF}$  in this fit is compatible with that obtained from the consideration of the single photoelectron multiplication response in Section 2.2.5. Thirdly, using Equations 7.1 and 7.2, the measured ENF suggests either an optical crosstalk of 34 % (geometric) or 25 % (branching Poisson) for the camera. If the same parameters are used in combination with a value for  $\sigma_0$  calculated using Equation 3.3 and values  $NSB = 125 \text{ MHz}$ ,  $t_w = 15 \text{ ns}$ , and  $n_e = 0.3$ , we can once again conclude that the *Charge Resolution* requirement is failed by the current CHEC-S design. The curve resulting from this extrapolation is shown in Figure 7.12 labelled as “125 MHz”.

### 7.3.7 Conclusion

The results of these *Charge Resolution* investigations seem to suggest the optical crosstalk is the dominating factor in the degradation of the *Charge Resolution* performance for CHEC-S. They also show that a reduction in optical crosstalk could allow CHEC-S to meet the *Charge Resolution* requirement. Such a reduction is possible with newer SiPMs, which use techniques such as “trenching” to reduce the optical crosstalk between microcells. This is discussed in more detail in Section ???. Within this year, a second CHEC-S prototype will be built using the latest SiPMs, which are reported to have an optical crosstalk of  $\sim 10\%$  (see Section 2.2.6). If we once again use the result of the fit from Figure 7.12, we can predict the *Charge Resolution* performance of this future camera under 125 MHz NSB. This is shown in the curves “10 % OPCT (Geometry)” and “10 % OPCT (Branching)”, and concludes that such a camera will safely meet the *Charge Resolution* requirement.

## 7.4 CHEC-S Pulse Shape

Although there is no CTA requirement attached directly to it, the pulse shape of the camera is important to understand. The pulse shape behaviour influences the performance of the charge extraction, especially when using methods that utilise the expected shape of the pulse, such as a fitting technique, or the *Cross Correlation* method. Figure 7.13 displays the average pulse shape of CHEC-S in terms of the pulse’s FWHM and rise time. The FWHM is defined as the width of the pulse at half of its maximum. The rise time is the time between 10 % of the pulse maximum, to 90 %. A perfect detector should have a consistent pulse shape at all illuminations, as shown with the simulation dataset in Figure 7.14. The only deviations from

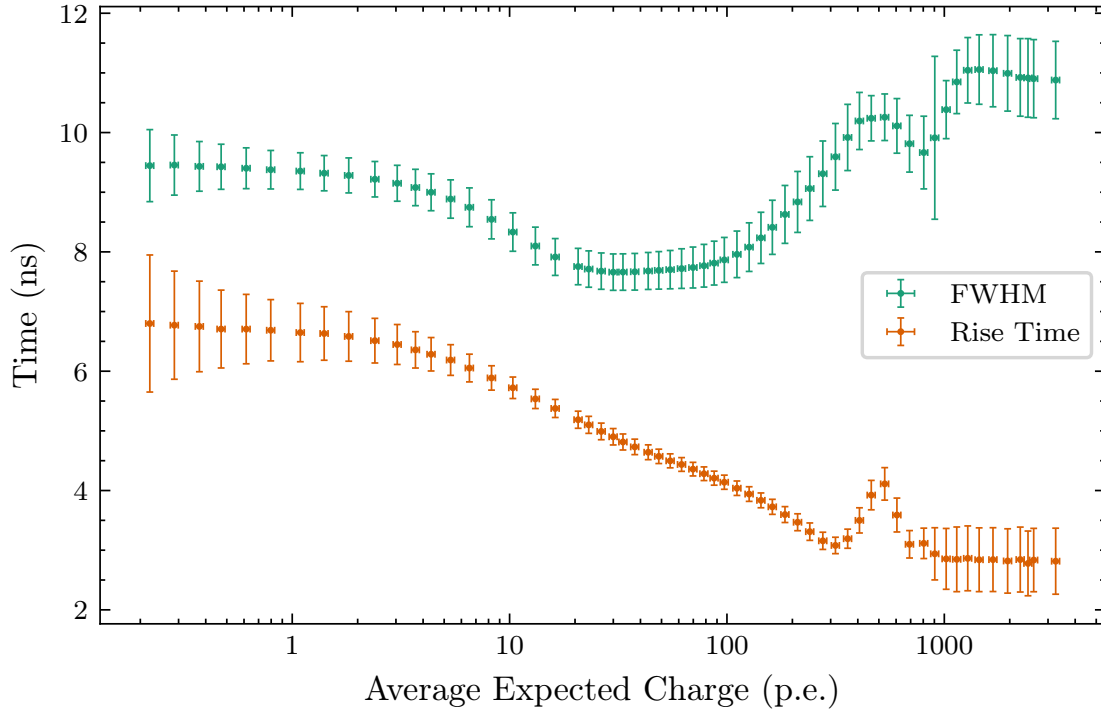


**Figure 7.13:** The average pulse shape across CHEC-S as a function of average expected charge (i.e. illumination). The Y errors are the standard deviation of the pulse shape parameters across the camera. The “dead” pixels are excluded from the calculation.

2614 a constant pulse shape in the simulation dataset is at low illuminations, where  
 2615 the noise makes it harder to characterise the pulse.

2616 It is suspect that the region in which the FWHM appears to drop in Figure 7.13  
 2617 ( $10 < Q_{\text{Exp}} < 100$  p.e.) coincides with the same region where we see the discrepancy  
 2618 between the *Lab* and *MCLab Charge Resolutions* (Figure 7.6). This suggests the two  
 2619 factors could be correlated. Further investigation into the pulse shape behaviour  
 2620 is required, possibly by probing at different points in the FEE to observe each  
 2621 components effect on the pulse shape.

## 2622 7.5 CHEC-S Time Resolution

2623 A further criterion for assessing a camera’s behaviour within CTA is the *Time*  
 2624 *Resolution*. Introduced in Section 3.2.2, the *Time Resolution* is a measure of how  
 2625 the pulse time varies between pixels. After applying the timing corrections for  
 2626 each pixel (Section 5.5), the *Time Resolution*  $\sigma_T$  for an event is calculated using  
 2627 Equation 3.5. Only pixels with a measured charge greater than 5 p.e. are included  
 2628 in the calculation. The mean and standard deviation of  $\sigma_T$  across multiple events  
 2629 is then expressed against the average expected charge as shown in Figure 7.15. In

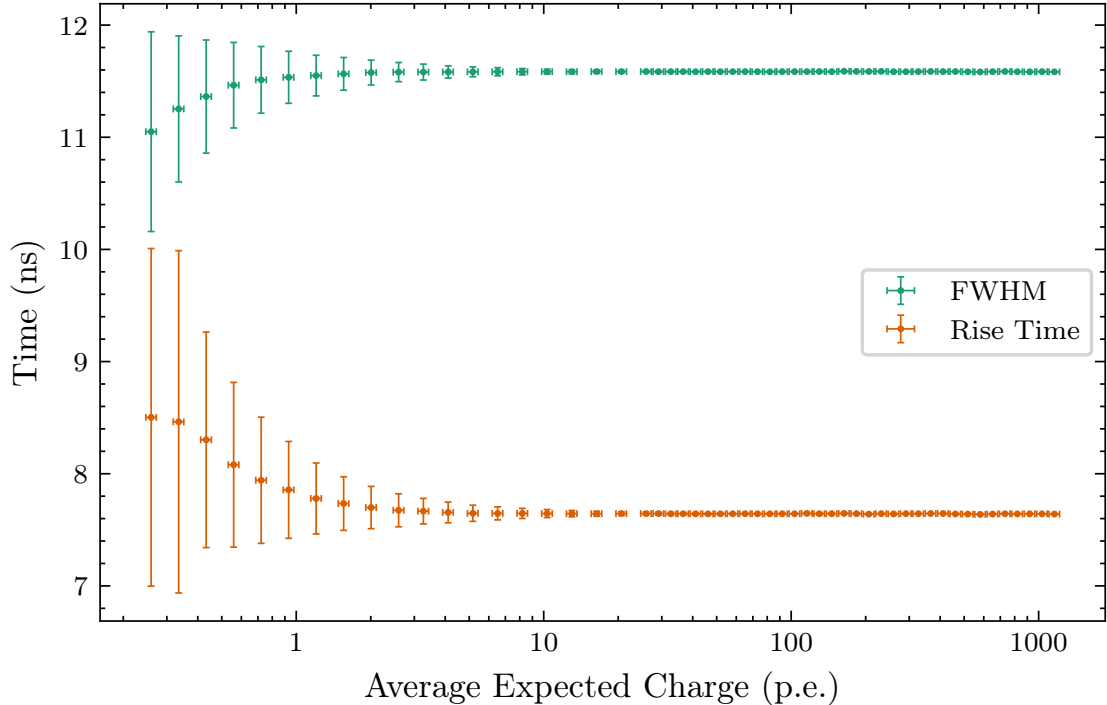


**Figure 7.14:** The average pulse shape extracted using data obtained from simulations of CHEC-S. The processing and representation is identical to those used in Figure 7.13. An NSB photon rate of 5 MHz is included to imitate the expected DCR contained in the measurements from the real camera.

order to meet the CTA requirement, the *Time Resolution* must remain below the requirement at all values of average expected charge.

While the curve for the real CHEC-S prototype appears to meet the requirement in Figure 7.15, the dataset used contained no NSB photons (only an assumed DCR of 5 MHz). Therefore, for extrapolation purposes, the *Time Resolution* extracted from a simulation at an NSB photon rate of 5 MHz, and a second simulation at a rate of 125 MHz, was included alongside the result from the real camera.

The pulse time extraction method used in this investigation was to select the maximum sample within a 14 ns window around the maximum of the average waveform across all pixels. This technique is very simple and highly influenced by to sample-to-sample variations. It is therefore no surprise that the camera appears to fail the *Time Resolution* requirement at high NSB photon rates. As outlined in the requirement, the method used to extract the pulse time for the calculation of *Time Resolution* does not need to be the same method used for charge extraction. Therefore a more advanced method, such as fitting the pulse, could be used to improve the resolution, and meet the requirement.

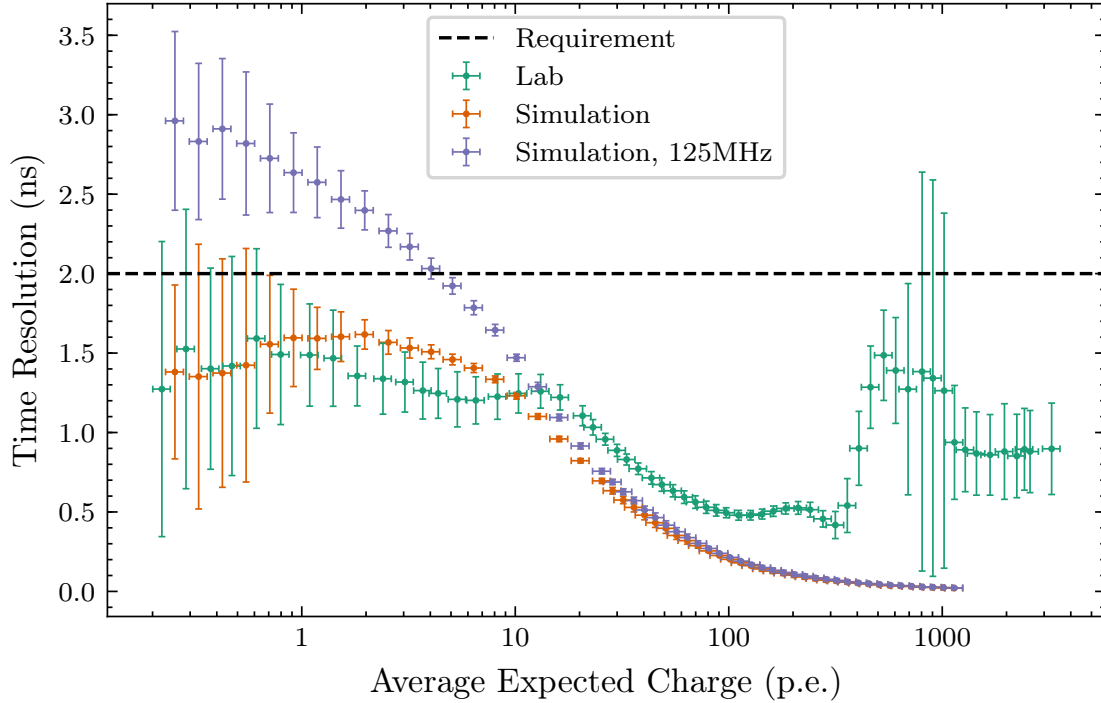


**Figure 7.15:** The *Time Resolution* of the CHEC-S prototype, compared against the *Time Resolution* from simulations of CHEC-S. The points represent the average *Time Resolution* across 100 events, while the Y error bars indicate the standard deviation across 100 events. The X error bars are the uncertainty in the average expected charge.

2646 A further conclusion that may be drawn from Figure 7.15 is that the real “Lab”  
 2647 camera does exhibit some additional time variations from pixel-to-pixel due to  
 2648 the electronics, which are not present in the simulation. This is the cause of the  
 2649 discrepancy between the “Lab” and “Simulation” curves at high illuminations. At  
 2650 lower illuminations however, the sample-to-sample noise is the dominating factor,  
 2651 resulting in a more similar behaviour between the two curves.

## 2652 7.6 CHEC-M

2653 Earlier studies of mine, that were concerned with the performance of CHEC-M, have  
 2654 previously been included in a publication on CHEC-M by Zorn et al. [21]. However,  
 2655 the calibration procedures have improved since that publication (hereafter referred  
 2656 to as the “CHEC-M paper”), and an investigation into the *Charge Resolution* was  
 2657 not previously performed. A brief update regarding the performance of CHEC-M is  
 2658 therefore included here, using the same techniques developed for CHEC-S, while  
 2659 relying on the same dataset used to produce the figures in the CHEC-M paper.

2660 Firstly, an updated version of the dynamic range plot (Figure 15 in the CHEC-M  
 2661 paper) is shown in Figure 7.16. By utilising similar techniques described in

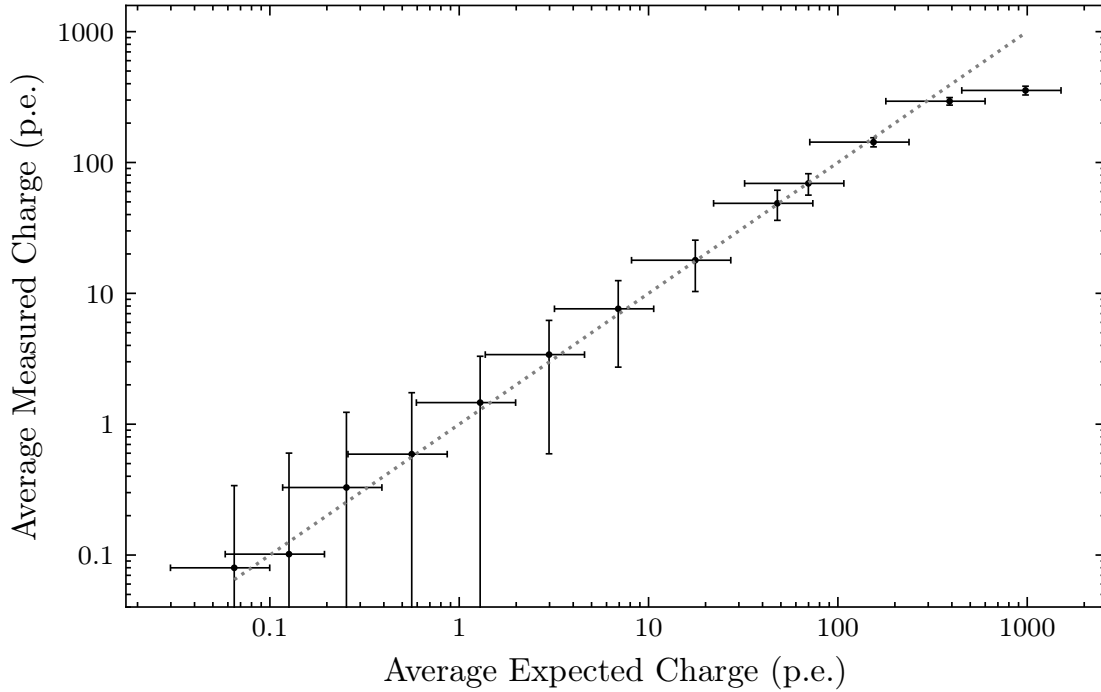


**Figure 7.16:** The dynamic range for a single CHEC-M pixel. Equivalent to Figure 7.3, but for CHEC-M.

2662 Section ??, the understanding of the filter wheel's behaviour (as it existed at  
 2663 the time this data was taken) was improved. This is reflected in the new positions  
 2664 of the points on the X axis, and the larger error bars which more appropriately  
 2665 represent the uncertainty in the calibration.

Fit Parameter	Values
Background Noise	$\sigma_0 = 0.814 \pm 0.007$
Excess Noise Factor	$\sigma_{ENF} = 1.642 \pm 0.008$
Miscalibration	$\sigma_g = 0.073 \pm 0.003$

**Table 7.4:** Parameter values resulting from the fit to the CHEC-M *Charge Resolution* (Figure 7.17) using Equation 3.2.

2666 Resulting from the dynamic range measurements, the *Charge Resolution* of  
 2667 CHEC-M can be constructed. This is shown in Figure 7.17, compared against the  
 2668 *Lab Charge Resolution* of CHEC-S, and the fit of Equation 3.2 to the CHEC-M  
 2669 points. The parameters resulting from the fit are shown in Table 7.4. While the  
 2670 MAPMTs of CHEC-M do not suffer from the large optical crosstalk found in the  
 2671 SiPMs of CHEC-S, CHEC-M does seem to still have a larger ENF. This is one  
 2672 justification for the choice of CHEC-S over CHEC-M.

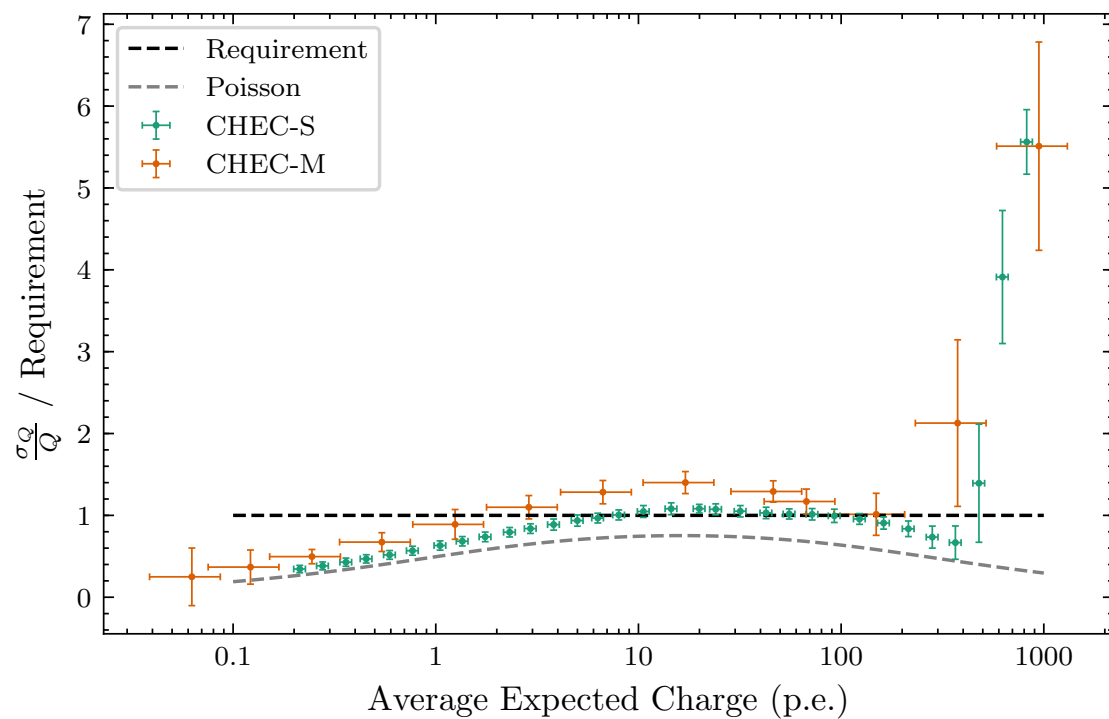


**Figure 7.17:** Charge Resolution of CHEC-M compared to the Charge Resolution of CHEC-S. The fit to the CHEC-M Charge Resolution using Equation 3.2 is also shown.

---

# 8

2673

2674

## On-Sky Observations

2675

### Contents

---

2676

2677	<b>8.1</b>	<b>Introduction</b>	.....	107
2678	<b>8.2</b>	<b>Cherenkov Shower Images</b>	.....	108
2679	<b>8.3</b>	<b>Jupiter Observations</b>	.....	112
2680	<b>8.4</b>	<b>Conclusion</b>	.....	114
2681	<b>8.5</b>	<b>Future</b>	.....	114

---

2683

2684

2685

### 8.1 Introduction

2686 Testing the operation of the camera on the telescope structure is a very important  
2687 part of the commissioning procedure. When on-telescope, the camera is in an  
2688 environment we have very little control over. It is exposed to factors such as  
2689 weather conditions and excessive NSB from various sources (including moonlight,  
2690 starlight, and artificial light pollution). The on-telescope campaigns are therefore  
2691 a useful measure of the robustness of the camera, and the procedures used to  
2692 operate the the telescope as a whole.

2693 The first on-telescope campaign took place during November 2015, at the location  
2694 of the GCT telescope structure (Observatoire de Paris-Meudon), just before the  
2695 inauguration of the GCT prototype. The primary intention of this campaign was  
2696 to test the integration and operation procedure for CHEC-M on the telescope  
2697 structure, however the first detection of Cherenkov light from atmospheric showers  
2698 by a CTA prototype camera was also achieved [4].

2699 After returning to the lab for further testing and characterisation, CHEC-M  
2700 was then re-installed on the GCT structure in March 2017 for a second on-telescope



**Figure 8.1:** Photo of CHEC-M installed on the GCT telescope structure, taken during the first on-telescope campaign [67].

campaign. During this second campaign the GCT telescope was pointed towards two VHE gamma-ray sources, Mrk421 and Mrk501. These two sources are blazar objects (Active Galactic Nuclei (AGN) with a relativistic jet directed towards Earth) and were the first extragalactic TeV sources to be discovered [Quinn1996, 69], testifying to their brightness. However, due to the high NSB background that is present at the Meudon site (20 to 100 times brighter than expected at the final CTA site), the camera had to be operated at a low gain and high trigger threshold [21]. The former setting was used as a precaution to avoid damage to the MAPMTs, and the latter to avoid triggering on the NSB photons. The combination of these operating conditions, and the limited observation time, meant an astrophysical detection was unlikely for this campaign. Nevertheless, Cherenkov showers were detected during the campaign. This chapter will describe the results I have obtained from the camera images taken during the campaign.

## 8.2 Cherenkov Shower Images

Utilising the calibration procedure defined in Chapter 5, and a simple integration window combined with the *Neighbour Peak Finding* technique described in Chapter 6, the signal in each pixel was extracted for every trigger event. The results shown in this section originate from a 30-minute-long observation of Mrk501, during which the camera received triggers at a rate of  $\sim 0.1$  Hz.



**Figure 8.2:** Photo of the reflection of CHEC-M in the GCT telescope's secondary mirror, taken during the first on-telescope campaign [68].

Figure 8.3 displays the distribution of *Hillas* width and length (Section 6.3.1) for the events that caused a camera trigger. Four events were chosen from the collection, and are marked with a cross on the figure. The images corresponding to each of the selected events are shown in Figure 8.4. These events were manually selected as they represent a range of possible event types:

- Figure 8.4a - A typical Cherenkov shower, most likely produced from a hadronic cosmic ray due to their abundance compared to gamma-ray showers. The majority of events fall under this category, and result in a cluster at low values of *Hillas* width and length.
- Figure 8.4b - A bright Cherenkov shower, from a high energy cosmic ray. These events are characterised by their large *Hillas* width and length.

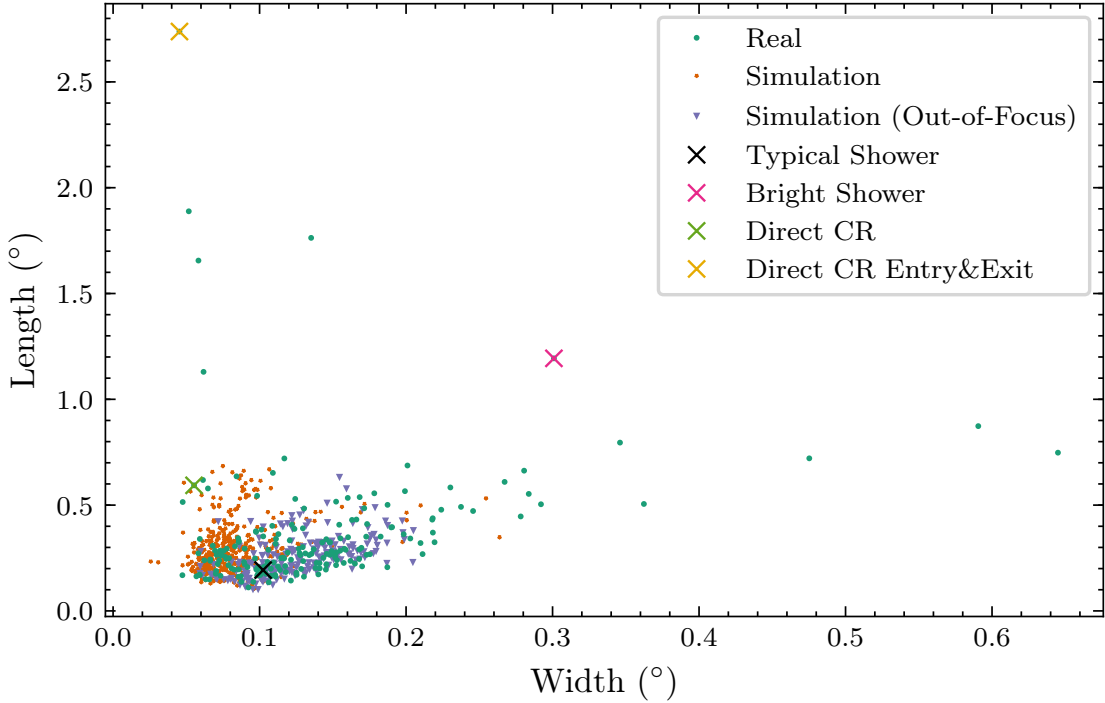


**Figure 8.3:** The *Hillas* length versus width of each image in a 30-minute-long observation of Mrk501 with CHEC-M on the GCT telescope structure (labelled as “Real”). Simulations of CHEC-M on the GCT telescope are also included for comparison. Four different types of events have been highlighted and assigned a category based on a manual examination of their camera image.

- 2731 • Figure 8.4c - A direct cosmic ray, grazing along the pixels on the focal surface
- 2732      and producing an electron avalanche in the MAPMTs. As the signal is located
- 2733      along the incident path of the cosmic ray, the ratio of *Hillas* length to width
- 2734      for these events is large. Due to their locality to a single telescope, these
- 2735      events are ignored in an IACT array, as only a single telescope triggers.
  
- 2736 • Figure 8.4d - Another cosmic ray. Due to the curved focal surface of CHEC-M,
- 2737      it is possible for a cosmic ray to enter and exit the focal surface at opposite
- 2738      sides. These events are characterised by very large ratios of *Hillas* length to
- 2739      width.

2740      A Monte Carlo simulation of proton-induced Cherenkov showers being detected

2741      by CHEC-M on the GCT telescope structure was produced to compare the real

2742      results to. The signal and *Hillas* parameters were extracted identically from

2743      the simulated waveforms. The distribution of *Hillas* width and length are also

2744      shown in Figure 8.3, under the label “Simulation”. It is immediately apparent

2745      that the distribution of *Hillas* width is a lot tighter in the simulation. This will

2746      be explained later in this chapter.

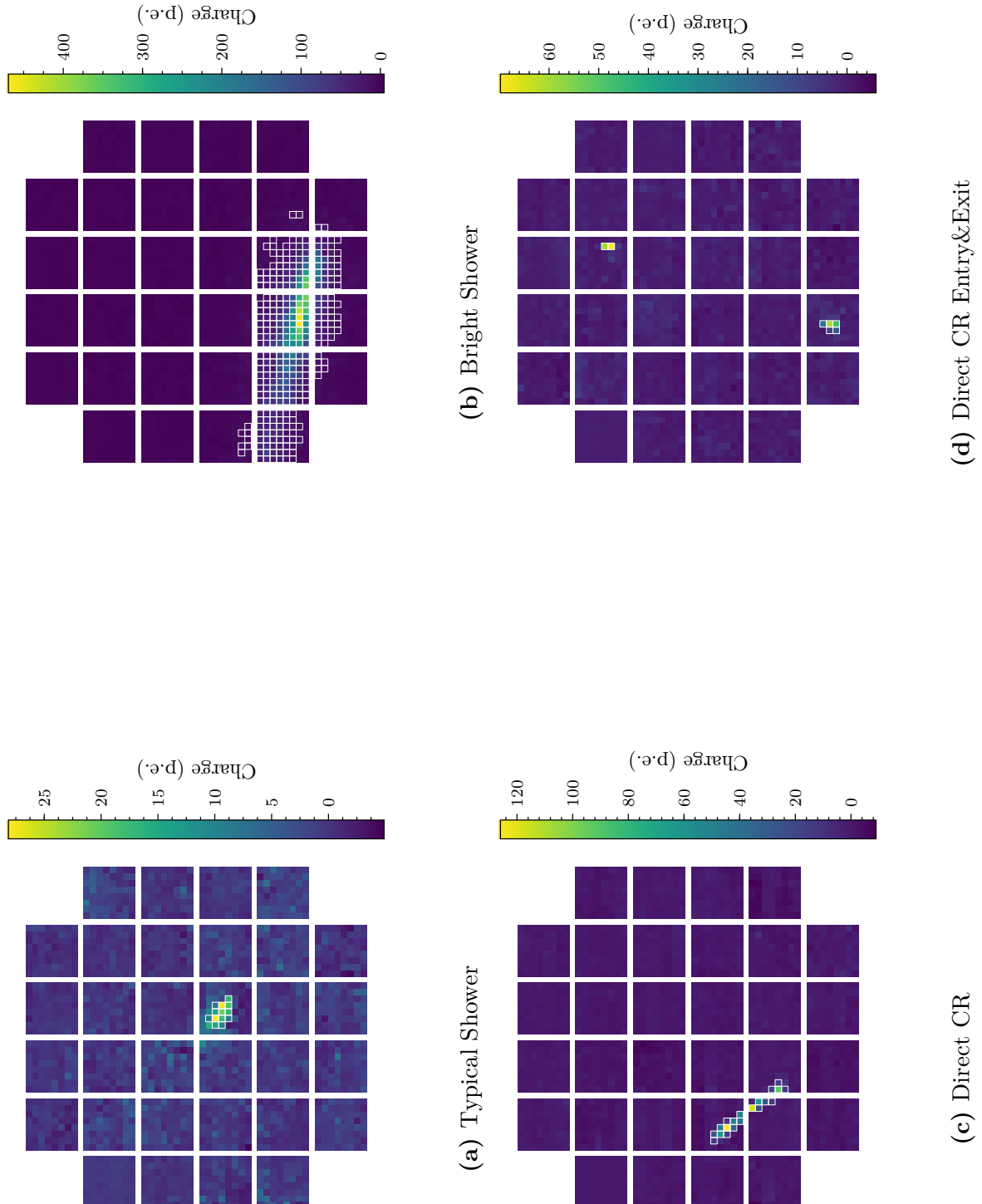


**Figure 8.4:** A selection of images taken by CHEC-M during its second on-telescope campaign. The images chosen correspond to the individually highlighted events in Figure 8.3.

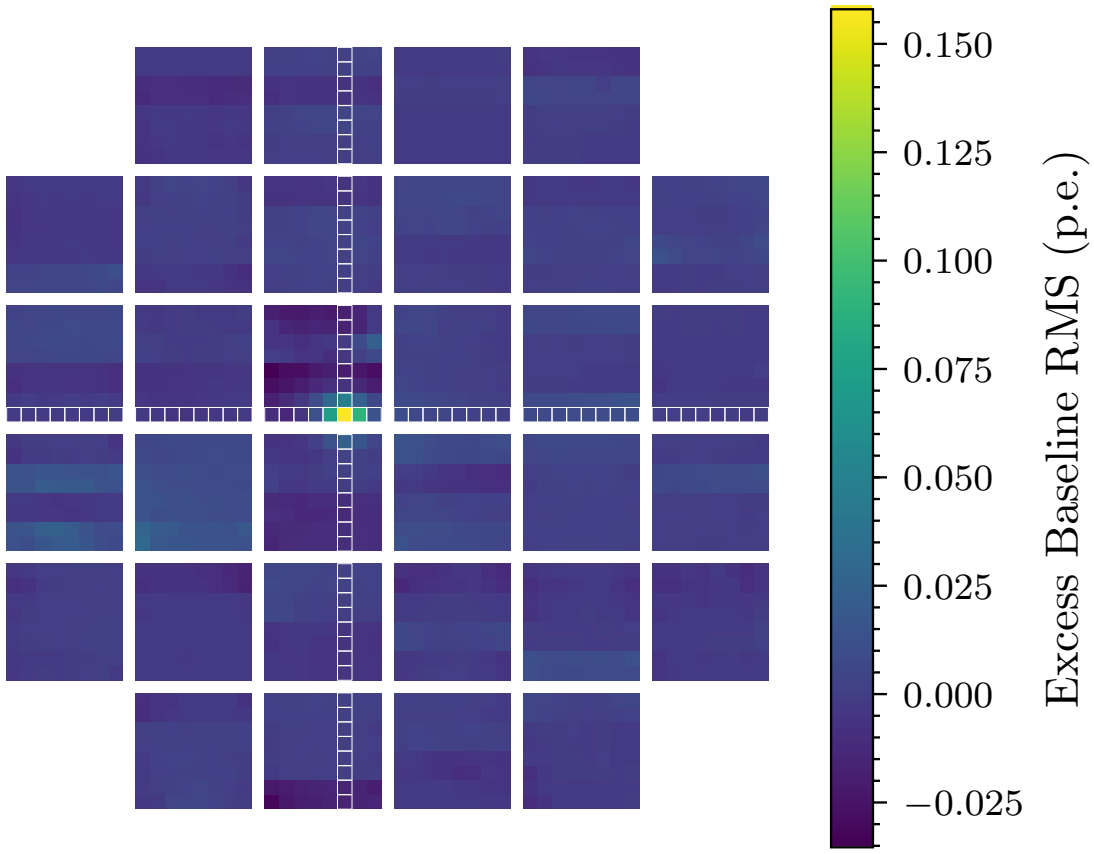


**Figure 8.5:** Camera image of the excess baseline RMS for observations of Jupiter taken during the second on-telescope campaign for CHEC-M.

### 2747 8.3 Jupiter Observations

2748 It has been considered within CTA that the pointing calibration for the telescopes  
 2749 may be performed using the change in pixel current as a star crosses a pixel's  
 2750 boundary [70]. As one of the primary effects of a higher NSB (such as that from  
 2751 starlight) is the increased variation of the waveform's baseline, it may be possible  
 2752 to achieve a pointing calibration using this information instead of the currents. An  
 2753 initial investigation into this possibility was explored during the second on-telescope  
 2754 campaign using Jupiter as a source.

2755 Two runs were taken: an “ON” axis observation, and an “OFF” axis observation.  
 2756 The ON observation was pointed at (and tracked) Jupiter, however intentionally  
 2757 slightly off axis to avoid it being located in the gap at the centre of the camera.  
 2758 The OFF observation was taken without Jupiter, or any other optically bright star  
 2759 in the FoV. The camera was triggered externally triggered at a rate of 300 Hz for  
 2760 approximately 5 minutes. This resulted in approximately 80,000 waveforms per

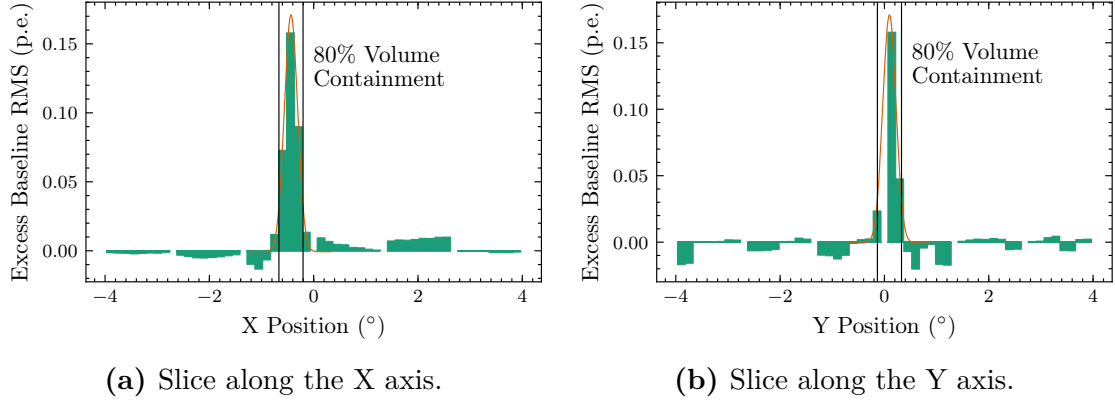


**Figure 8.6:** Slices of the camera image from Figure 8.5, along the white-highlighted pixels, showing the excess baseline RMS from each pixel in the slice. A slice of the 2D Gaussian fit to the PSF resulting from observing Jupiter is also shown, along with the corresponding 80 % volume containment radius.

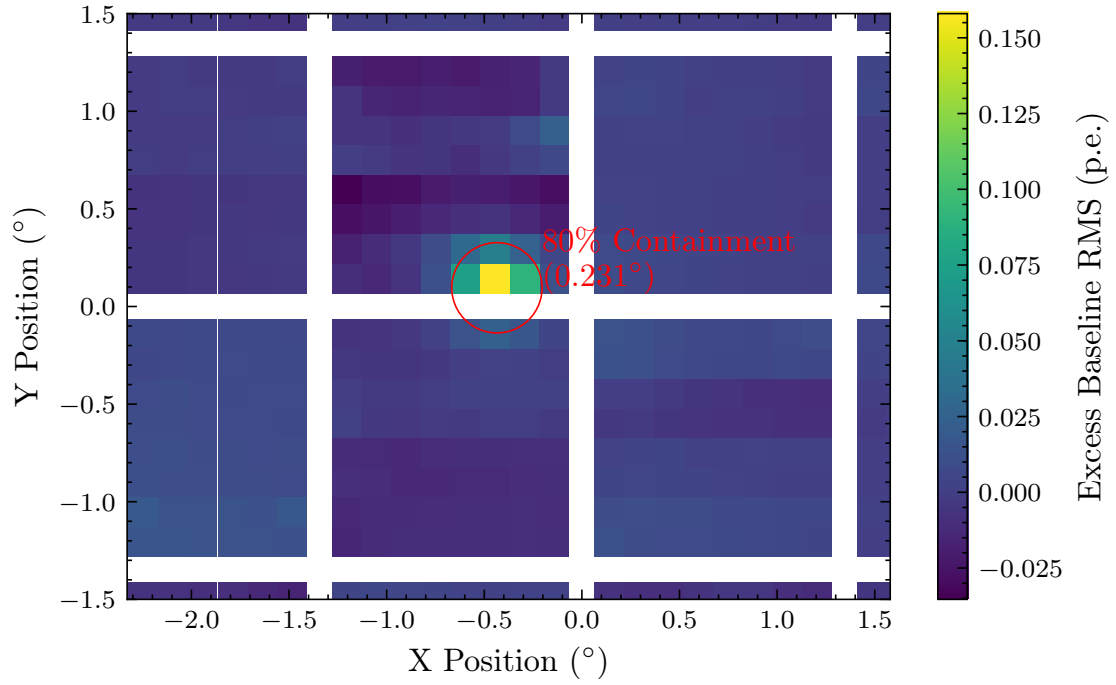


**Figure 8.7:** Zoom of Figure 8.5, showing the result of the 2D Gaussian fit to the PSF resulting from observing Jupiter, and the corresponding 80 % containment radius.

pixel for each of the observations. The Root-Mean-Square (RMS) of the waveforms was extracted for each waveform, and averaged over all events. The average RMS per pixel for the OFF observations were then subtracted from the ON observations. This removed any contributions from the camera electronics.

The resulting camera image of the excess RMS per pixel is shown in Figure 8.5. This profile of Jupiter in the camera is a measure of the Point Spread Function (PSF) of the telescope. The value that is used in CTA to characterise the PSF is the 80 % containment radius [2, 71]. To extract this value, a 2D Gaussian was fit to the camera image, using the X and Y coordinates of every pixel and their corresponding value of excess RMS baseline. In Figures 8.6a and 8.6b, a slice of the camera image for each axis is shown, intersecting at the pixel with the maximum excess RMS. Shown alongside the pixels distributions are the corresponding slices of the 2D Gaussian fit, demonstrating the fit’s successful representation of the profile, even with it being on the edge of a module. Figure 8.7 illustrates the 80 % containment radius on the camera image, resulting in a value of  $0.23^\circ$ .

## 8.4 Conclusion

The value extracted for the PSF is a magnitude larger than expected from Monte Carlo simulations, where a value of  $\sim 0.02^\circ$  was obtained [71]. As a discrepancy was also seen in the *Hillas* width between the real observations and simulations in Figure 8.3, it may suggest the camera was out-of-focus. As shown by Rulten et al. [2], an incorrect separation between the camera focal plane and the secondary mirror of just a few millimetres could account for a magnitude increase in the 80 % containment value. If a simulation is generated that represents the out-of-focus telescope, then we obtain the *Hillas* parameter distribution labelled as “Simulation (Out-of-Focus)” in Figure 8.3. This distribution is in much closer agreement with the *Hillas* parameters obtained during the on-telescope campaign.

## 8.5 Future

The next on-telescope campaign is planned for Autumn 2018, where CHEC-S will be placed on the ASTRI telescope structure which has been constructed on Mt. Etna, Sicily [Maccarone2017]. This will be the first on-telescope campaign for the CHEC-S prototype, and the first time a CHEC prototype has been installed on the ASTRI telescope structure.

---

# 9

2793

2794

## Summary

2795 Observations of the highest energy phenomena are facilitated by the SSTs

## Appendices

---

# A

2797

2798

## The Silicon Photomultiplier

2799

### Contents

---

2800

2801

A.1	Introduction	117
A.2	The P-N Junction	117
A.3	Avalanche PhotoDiode (APD)	120
A.4	Geiger-mode Avalanche PhotoDiode (G-APD)	120
A.5	Silicon Photomultiplier (SiPM)	121

2806

2808

---

2809

### A.1 Introduction

2810 Solid state photon detectors have been an active field of research since the 1960s [9],  
2811 however the development into a photosensor that is capable of both high resolution  
2812 photon counting, and a large dynamic range was only achieved in the 1990s [72].  
2813 Possibly as a result of their development process, the description of how an SiPM  
2814 operates can be subdivided into various solid state detectors, which provided the  
2815 building blocks towards the SiPM design. Due to their complexity compared to  
2816 PMTs, the full description of SiPMs are reserved for this appendix.

2817

### A.2 The P-N Junction

2818 As with all solid state devices, the building blocks of SiPMs are P-N Junctions. A p-  
2819 and n-type material are created by the addition of impurities to a semiconducting  
2820 material such as silicon. The impurities added to produce the n-type semiconductor  
2821 increases its number of freely moving electrons, while the impurities added to  
2822 produce the p-type semiconductor increases its number of freely moving holes.

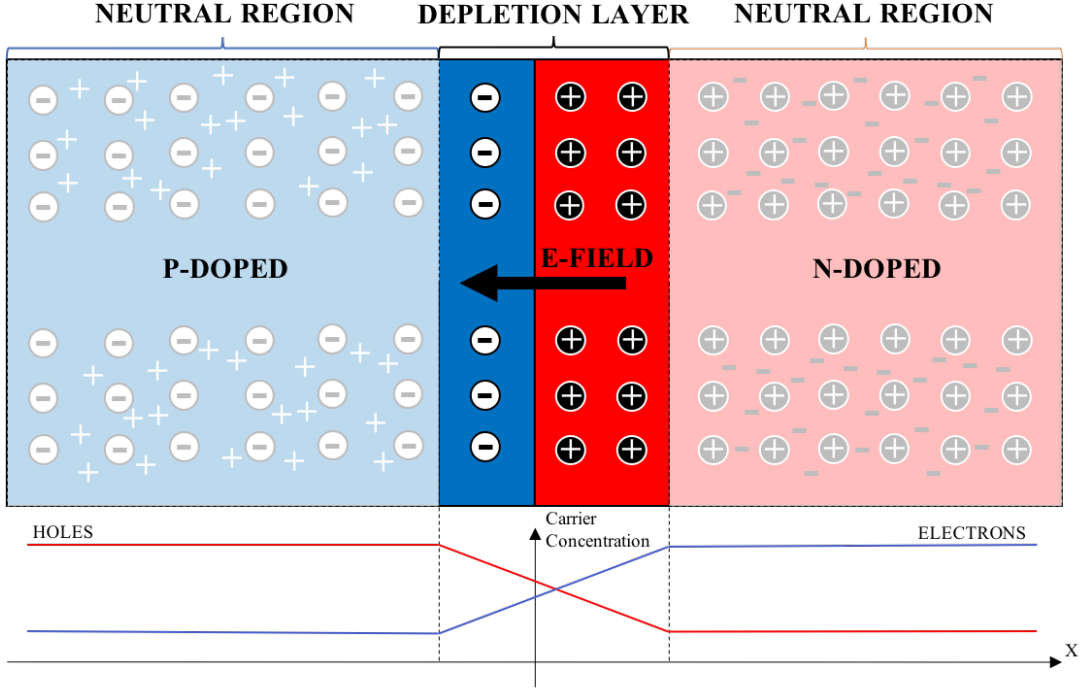


**Figure A.1:** My own illustration of a P-N Junction, inspired by Ghassemi, Sato, and Kobayashi [10].

When the two materials are joined, the P-N Junction is formed. As a result of the abundance of charges in each material, a diffusion current forms with electrons moving from the n-type material (leaving behind its immobile positive ions) to combine with the holes in the p-type material. The same occurs vice versa for the excess holes in the p-type material, leaving behind its immobile negative ions. The result is a region adjacent to the junction with no free charges remaining, known as the depletion layer (Figure A.1). The charge difference from the immobile ions produces an electric field inside the depletion layer, that points from its positively charged N side to its negatively charge P side. This electric field opposes the diffusion current and causes an equilibrium to be reached across the junction.

However, this equilibrium can be disturbed by the input of energy into the system, either by thermal excitation (producing what is known as *dark counts*) or by the photoelectric effect. If the energy provided to a bound electron is greater than the band gap energy (inherent to the semiconductor) then it becomes an excess charge carrier, leaving behind a hole. These excess charge carriers are known as an electron-hole pair. If these excess charge carrier are produced in the depletion layer, they will travel along the electric field in the direction according to its charge. For example, an excess electron charge carrier released in the P side of the depletion layer will travel in the opposite direction to the electric field, crossing the P-N Junction

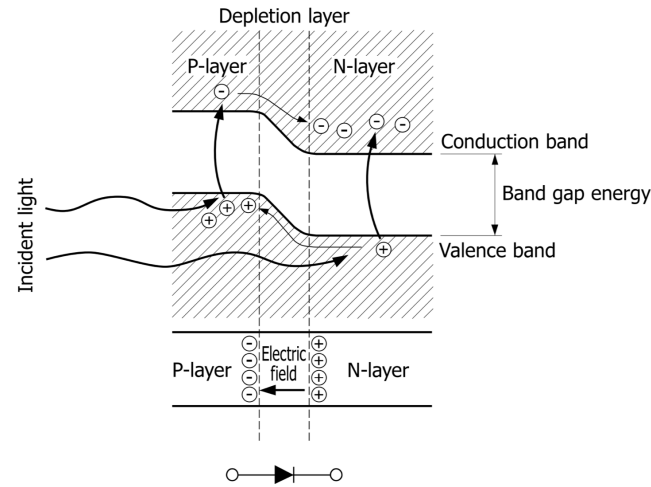


**Figure A.2:** Illustration of the silicon bandgap, demonstrating a bound electron being exited into an excess charge carrier via the photoelectric effect. The excess charge carrier is then accelerated in the opposite direction of the electric field, resulting in a current [10].

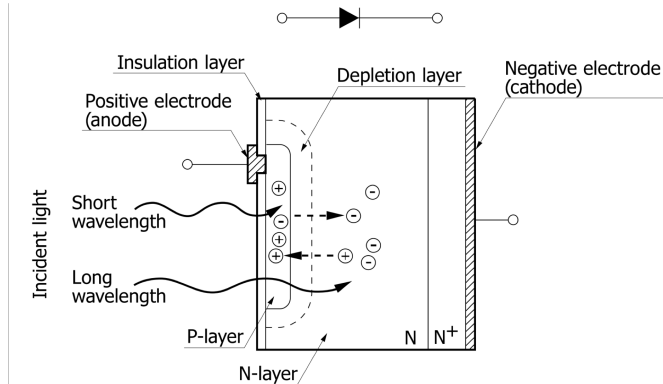


**Figure A.3:** Diagram of an Avalanche PhotoDiode with a reverse bias voltage applied. The N side of the semiconductor acts as the cathode. Traditionally the cathode is the “negative electrode”, however in reverse bias the N side is connected to the positive terminal. The P side of the semiconductor acts as the anode. Similarly to the N side, although the anode is the name traditionally given to the “positive electrode”, in reverse bias the P side is connected to the negative terminal. The result is the electrons are accelerated to the N side cathode, while holes are accelerated to the P side anode [10].

2842 to the N side. This is illustrated in Figure A.2. If a connection is formed between  
 2843 the P and N regions, this process will produce a current. If excess charge carriers  
 2844 are freed outside the depletion layer, they are generally short-lived, as there is no  
 2845 significant electric field to accelerate them, and therefore no net current is produced.

---

### 2846 A.3 Avalanche PhotoDiode (APD)

2847 In order to maximise the photosensitivity of the semiconductor, the depletion layer  
 2848 depth must be maximised. To achieve this, a reverse bias voltage is applied to  
 2849 the semiconductor. This means biasing the N side (cathode) to a higher electric  
 2850 potential than the P side (anode). The result of this is the freely-mobile holes on  
 2851 the P side, and the freely-mobile electrons on the N side, are pulled away from the  
 2852 junction. This leaves behind the charged ions and causes the depth of the depletion  
 2853 region to increase. The anode and cathode is illustrated in Figure A.3.

2854 In addition to an increased depletion layer depth, this reverse bias increases the  
 2855 electric field within the depletion region. Excess charge carriers achieve a higher  
 2856 kinetic energy as a result. If the mean kinetic energy attained between collisions  
 2857 with ions is greater than the band gap energy, additional charge carriers may be  
 2858 released. This impact ionisation effect results in a rapid multiplication of excess  
 2859 charge carriers, and is referred to as an avalanche. Such a device it therefore known  
 2860 as an APD. The ratio of final charge carrier signal that is read out to the initial  
 2861 photo-carriers produced is the gain of the APD, analogous to the gain of a PMT.

2862 The typical operation of a APD is to apply the bias voltage that optimally  
 2863 maintains relatively constant bandwidth and stable noise output, while achieving  
 2864 the highest gain level [10]. This voltage occurs before the *breakdown voltage*, where  
 2865 the gain approach infinity. This operation of the APD is known as “proportional” or  
 2866 “linear” mode [72], as the gain increases proportionally with bias voltage. However,  
 2867 APDs in this mode suffer from limited gain and large variations in their single  
 2868 amplification, and are therefore not useful in single photon counting. To better  
 2869 utilise APDs we must increase the bias voltage beyond the breakdown voltage,  
 2870 causing the APD to transition into Geiger mode.

### 2871 A.4 Geiger-mode Avalanche PhotoDiode (G-APD)

2872 In Geiger mode, a single photoelectron produces a self-perpetuating ionisation  
 2873 cascade. This effectively causes the silicon to become conductive, thereby amplifying  
 2874 the original electron-hole pair into a measurable current flow [13]. A “quenching  
 2875 resistor” is used in series with the diode to limit the current drawn during breakdown,  
 2876 thereby lowering the bias voltage across the diode and bringing it below the  
 2877 breakdown voltage. This halts the avalanche and results in a signal shape that  
 2878 can be read out from the voltage across the quenching resistor. The SiPM then  
 2879 undergoes a recovery back to the original “overvolatage” above the breakdown

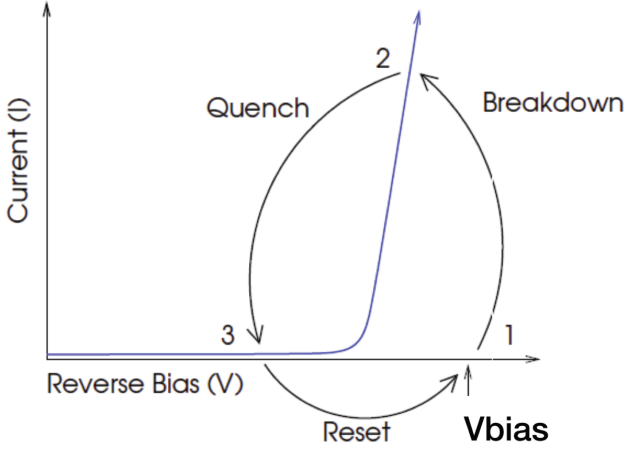


**Figure A.4:** Diagram of the current created by the avalanche versus reverse bias voltage [13]. The stages in the cycle of the G-APD operation are labelled. 1) The G-APD is set to a reverse bias voltage above the breakdown voltage. No current flows yet. 2) A excess charge carrier is produced by thermal excitation or the photoelectric effect. The carrier causes a Geiger discharge, creating a macroscopic current. 3) The current is quenched by a resistor in series with the diode. The bias voltage across the diode is reduced below the breakdown voltage, and the avalanche ceases. The G-APD then recharges ready for the next avalanche.

voltage, ready for the next photoelectron avalanche. This operation cycle of the Geiger-mode Avalanche PhotoDiode (G-APD) is shown in Figure A.4.

The disadvantage of this mode is that the G-APD is a binary device. All information about the number of generated photoelectrons in the semiconductor is lost. The only knowledge one can have is that there was at least one photoelectron. However, the response that results from this signal, completely independent of the number of initial photoelectrons, is extremely large and well defined, with a gain in the range  $10^5$ - $10^7$ . G-APDs are therefore very useful as single photon counting devices, but are not so useful in operations where a large dynamic range is desired.

## A.5 Silicon Photomultiplier (SiPM)

The final transition in this technology chain is to the concept of the SiPM. This device utilises a densely packed array of up to 10,000 G-APDs per  $\text{mm}^2$ . Each of these G-APD “microcells” has its own quenching resistor, and all the microcells are connected in parallel to a common bus [72]. Figure A.5 shows a simplification of the equivalent circuit diagram for an SiPM. The result is a detector that can count multiple photons, with a dynamic range that is essentially the number of microcells. Though, each microcell still operates as a binary sensor, therefore two

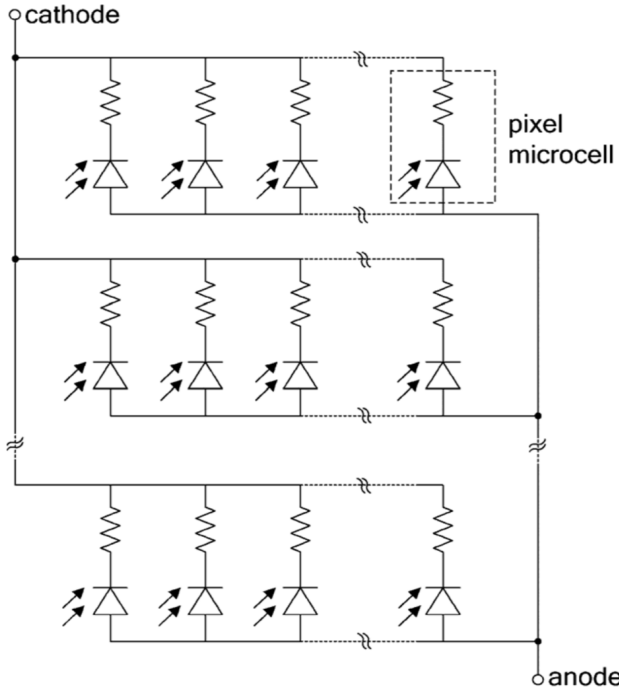


**Figure A.5:** Simplified equivalent circuit of an SiPM detector, demonstrating the individual microcells connected in parallel [73].

2897 photons incident on the same cell will only register as one. The superposition of  
 2898 the output current pulses from all the microcells results in the highly quantised  
 2899 measure of the number of photoelectrons produced.

---

# B

2900

2901

## Laboratory Characterisation

2902

### Contents

---

2903

2904	<b>B.1 Introduction</b>	123
2905	<b>B.2 Filter Wheel</b>	125
2906	B.2.1 Reference SiPMT	125
2907	B.2.2 Camera Correction	126
2908	<b>B.3 Illumination Profile</b>	126
2909	B.3.1 Laser Profile	127
2910	B.3.2 Camera Geometry	127
2911	B.3.3 Total Correction	129
2912	<b>B.4 Absolute Illumination</b>	130
2913	<b>B.5 Average Expected Charge</b>	131
2914	<b>B.6 Consideration of Errors and Uncertainty</b>	132

---

2915

2917

2918

### B.1 Introduction

2919 At the time of this writing, the CHEC-S prototype is being commissioned at the  
2920 Max-Planck-Institut für Kernphysik in Heidelberg, Germany. The camera is stored  
2921 in a dedicated dark room, which in this thesis I refer to as the lab. Figure ?? shows  
2922 a simple schematic of the CHEC-S test bench, which includes:

- 2923     • an enclosure to further limit the background light that enters the camera,  
2924     • a robot arm with an attached reference SiPM,  
2925     • a laser combined with a filter wheel containing a continuous neutral density  
2926       filter,  
2927     • and a diffuser to spread the light uniformly onto the camera focal surface.

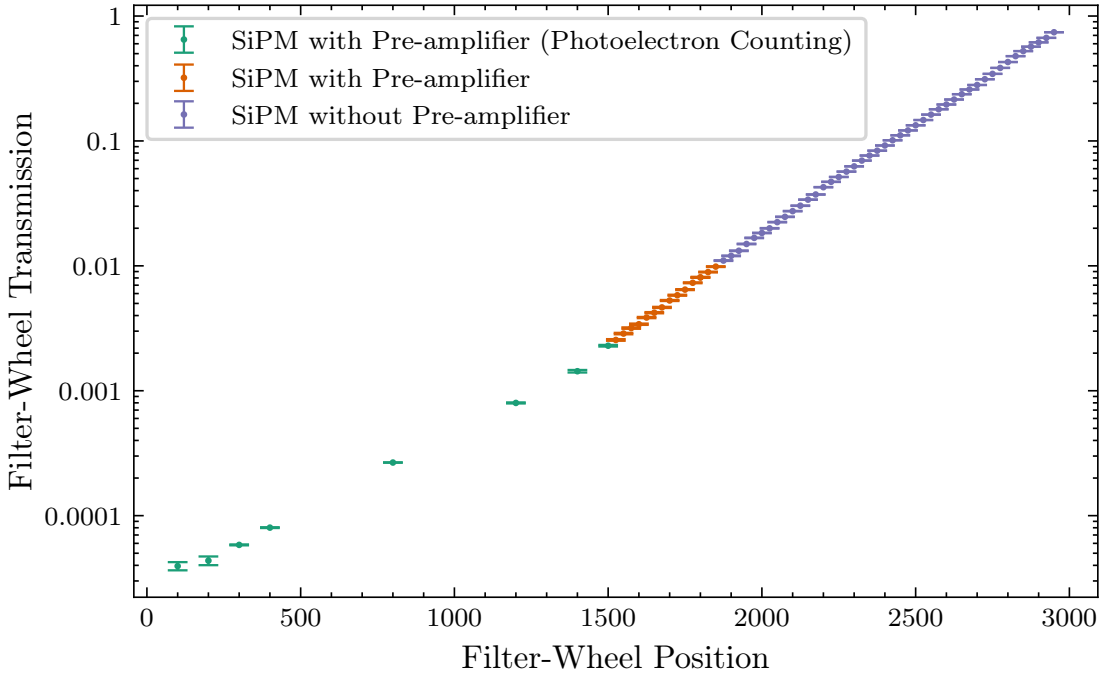


**Figure B.1:** Logarithm of transmission versus position for the filter wheel. The relationship is fit with a straight line.

2928 The latter two are contained with the smaller box attached to the camera enclosure.

2929 In order to fully commission the camera and understand its performance, we  
2930 must have accurate knowledge of average number of photoelectrons incident on  
2931 each pixel (i.e. the illumination), for each position setting of the filter wheel. It  
2932 was therefore necessary to characterise the lab set-up, via the calibration of the  
2933 laser and filter wheel combination. This was achieved via three stages:

2934 1. Measuring the relationship between filter-wheel position and light transmis-  
2935 sivity.

2936 2. Measuring the relative amount of light each pixel received due to its position  
2937 on the focal surface.

2938 3. Measuring an absolute illumination in photoelectrons for at least one filter-  
2939 wheel position.

2940 Through the combination of the results of these stages, a conversion from filter-wheel  
2941 position to expected number of photoelectrons in each pixel was obtained.

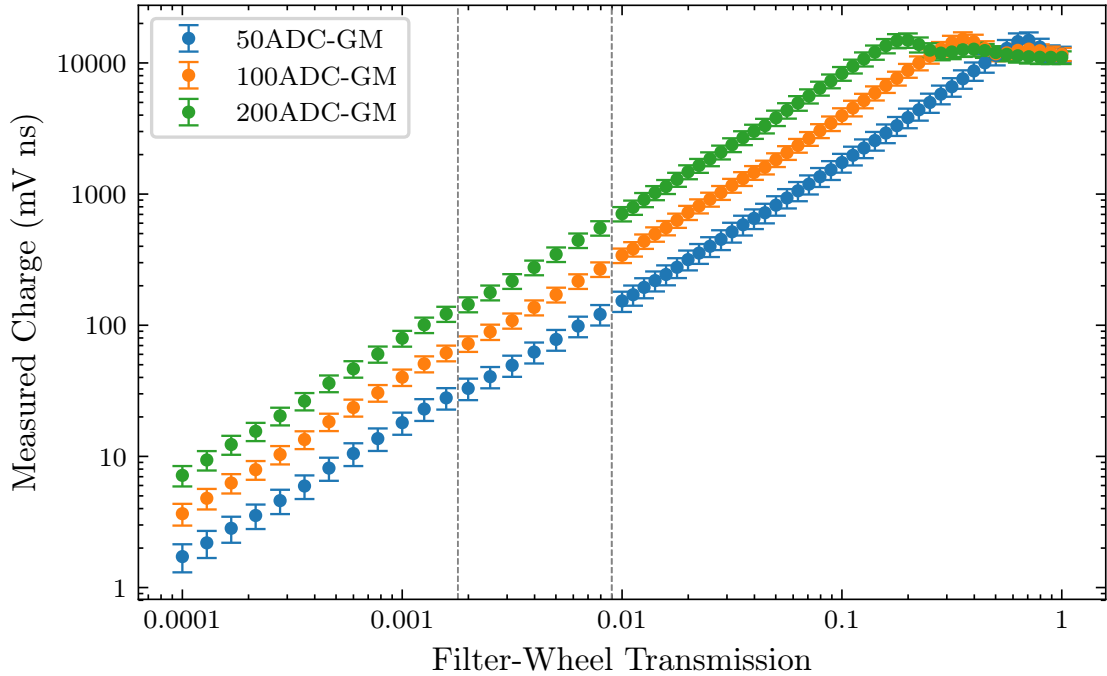


**Figure B.2:** Average charge across all CHEC-S pixels versus filter-wheel transmission. Three differently-gain-matched datasets are shown (50 ADC, 100 ADC, 200 ADC). Each gain matching results in a different bias voltage across the photosensor, and therefore a different gain, optical crosstalk, and PDE. Features shared between the datasets at a transmission value can only be due to errors in the filter-wheel calibration. Two clear features are highlighted by the vertical grey lines. Features shared at a measured charge value are due to shared properties in the Transfer Function (such as saturation).

## B.2 Filter Wheel

The calibration of the filter wheel was performed in two stages: an initial measurement with a reference SiPM in order to obtain an approximate handle on the relative illumination, and a secondary correction using the camera at different gain settings.

### B.2.1 Reference SiPMT

Using a single reference silicon photomultiplier pixel connected to an oscilloscope, centred on the camera focal plane, the ratio between the signal with and without the neutral-density filter was calculated for different filter-wheel positions (i.e. different attenuations). As the dynamic range of the reference SiPM was limited, in order to cover the full range of filters attenuations, three approaches were utilised:

1. **Low-range** - Average illumination obtained from SPE spectrum, with a pre-amplifier attached to the SiPM.
2. **Mid-range** - Average pulse area, with a pre-amplifier attached to the SiPM.

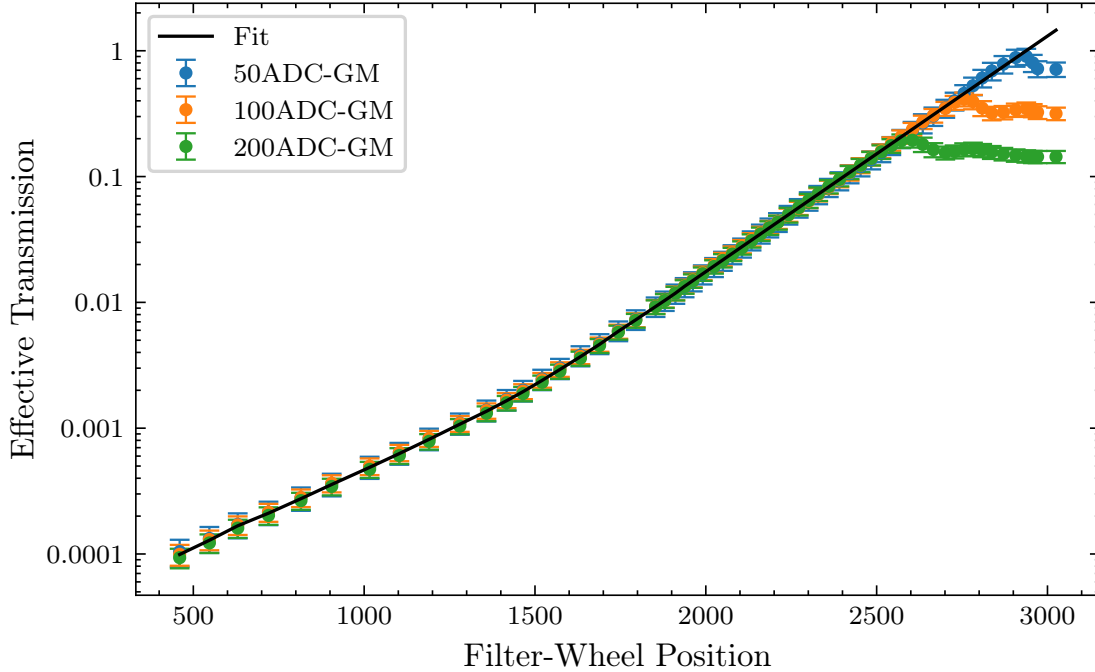


**Figure B.3:** The measured charges from Figure B.2 converted into an “effective transmission”, providing a filter-wheel calibration that is corrected for artefacts resulting from the first stage of calibration.

2955        3. **High-range** - Average pulse area, with no pre-amplifier attached.

2956        The overlapping values from each method were used to stitch the datasets together.

2957        The resulting points, shown in Figure B.1, were then used as a lookup table for

2958        the conversion from filter-wheel position to transmission.

### 2959        B.2.2 Camera Correction

2960        When looking at the average measured charge across the camera as a function  
 2961        of transmission, for three datasets where each has different bias voltages applied  
 2962        to the photosensors, features that share a position on the X axis can only occur  
 2963        from artefacts of the previous filter-wheel calibration. Figure B.2 indicates some  
 2964        of the artefacts which are easy to see. The measured charge was then converted  
 2965        into an “effective transmission” using the relation in Figure B.2. By plotting  
 2966        the “effective transmission” against filter-wheel position, a new conversion from  
 2967        filter-wheel position to transmission was obtained from the fit shown in Figure B.3.

## 2968        B.3 Illumination Profile

2969        Two contributions influence the relative amount of light each pixel receives, depend-  
 2970        ing on its position on the camera focal surface. The first is due to the laser uniformity

characteristics, the second is due to the curved focal surface of the camera.

### 2972 B.3.1 Laser Profile

2973 Despite attempts to homogenise the illumination from the laser-diffuser combination,  
 2974 non-uniformities were still present in the light received at the camera pixels.  
 2975 These non-uniformities needed to be accounted for in the calibration of the laser  
 2976 illumination. A trench in laser illumination across the Y coordinate that could be  
 2977 approximated with a linear gradient was found. This was discovered by attaching a  
 2978 single silicon photomultiplier pixel to a robot arm, and placing it at the camera  
 2979 position in front of the laser. Through the use of a single pixel, the amplitude  
 2980 measured is disentangled from the relative PDE. This pixel was then moved to  
 2981 each x-y position to calculate the ratio in signal amplitude, returning back to the  
 2982 origin to obtain a fresh value for comparison, thereby correcting for any deviations  
 2983 that may have occurred due to a change in temperature. The resulting linear  
 2984 gradient across the camera is shown in Figure B.5a.

### 2985 B.3.2 Camera Geometry

2986 Due to the spherical camera focal surface, each pixel is at a different distance  $d_z$   
 2987 from the light-source, and therefore receives a different amount of light depending on  
 2988 its distance  $x$  from the camera centre. Furthermore, at a “viewing angle”  $\beta$ , i.e. the  
 2989 angle between the normal to the pixel and the light-source, the amount of surface  
 2990 area of the pixel  $A_P$  visible to the light-source is reduced. The visible surface area  
 2991 is known as the “viewing area”  $A_V$ . The combined geometric correction to the light  
 2992 intensity required to compensate for these effects is almost circularly symmetric, and  
 2993 therefore can be analytically approximated by using a two dimensional description  
 2994 of the camera, with a circular focal surface:

$$2995 \quad d_1 = r - d_2 = r - \sqrt{r^2 - x^2}, \quad (\text{B.1})$$

$$2996 \quad d_z = \sqrt{x^2 + (d_c + d_1)^2} = \sqrt{x^2 + (d_c + r - \sqrt{r^2 - x^2})^2}. \quad (\text{B.2})$$

$$2997 \quad \beta = \theta + \alpha = \sin^{-1} \frac{x}{d_z} + \sin^{-1} \frac{x}{r}, \quad (\text{B.3})$$

$$2998 \quad \frac{A_V}{A_P} = \cos \beta, \quad (\text{B.4})$$

$$2999 \quad \frac{I_x}{I_c} = \frac{d_z^2}{d_c^2} \times \cos \beta, \quad (\text{B.5})$$

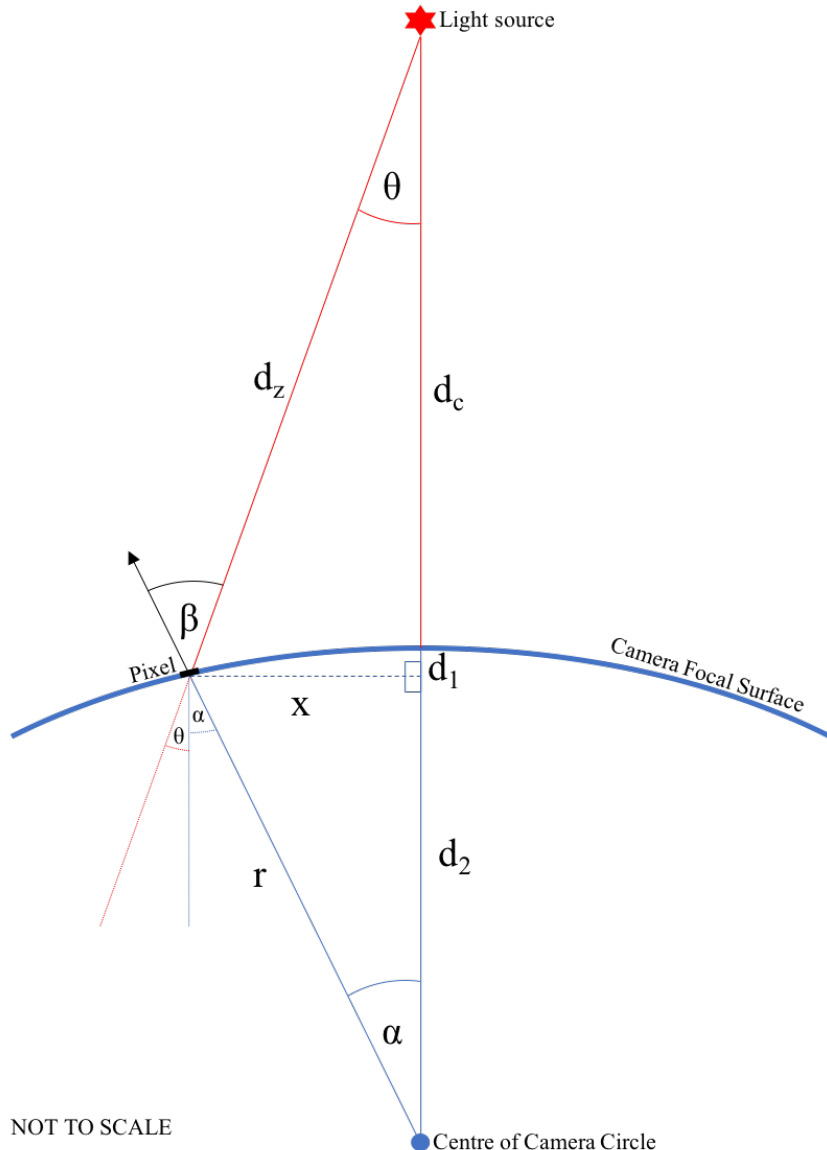


**Figure B.4:** Two-dimensional geometry schematic of the laboratory set-up for uniform camera illumination, used to calculate the reduction in light level for each pixel depending on its distance from the camera centre.

where  $A_P$  is the pixel area,  $I_x$  is the intensity measured at the position of the pixel,  $I_c$  is the intensity measured at the centre of the camera, and the remaining distances and angles are shown in Figure B.4.

The resulting geometry corrections to the intensity for each pixel, arising from Equation B.5, can be seen in Figure B.5b.

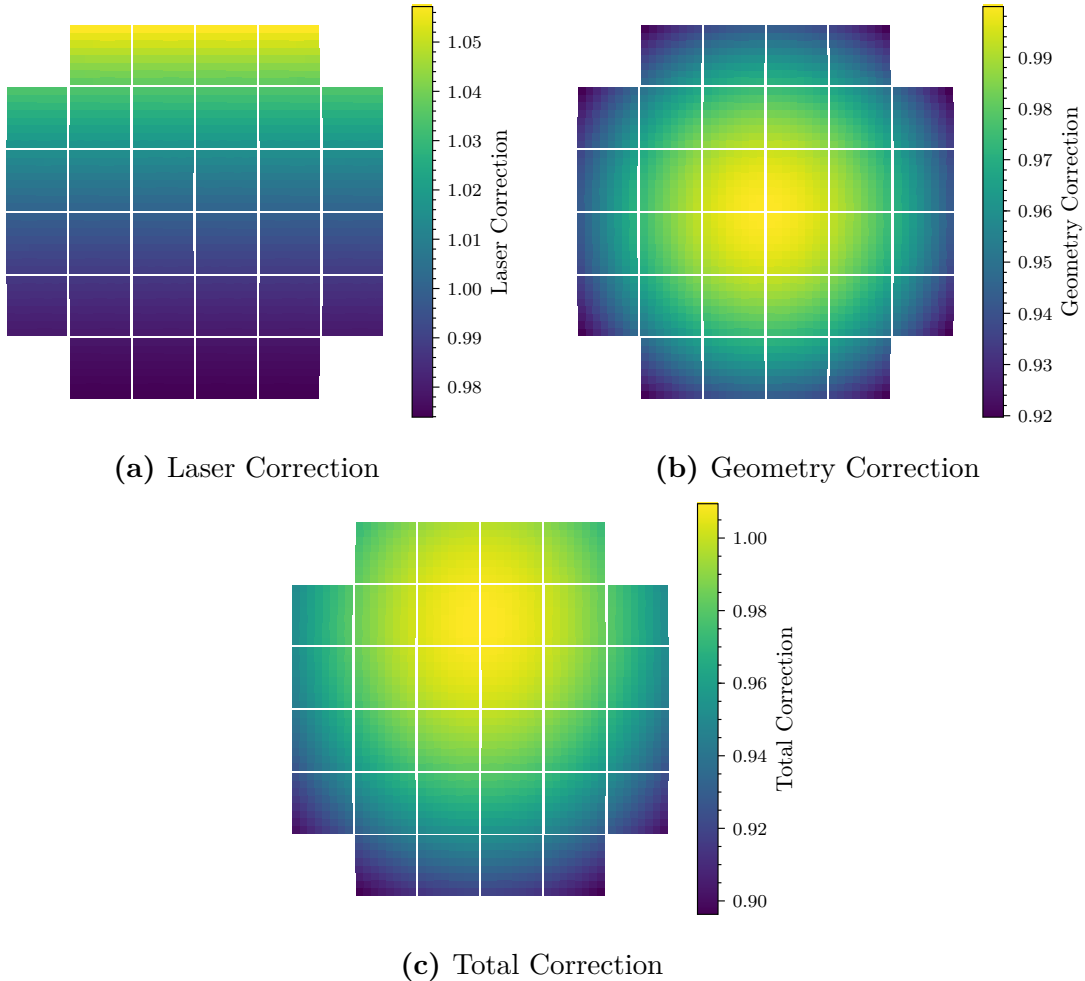


**Figure B.5:** The correction per pixel for the laser profile, camera geometry, and the combination of the two.

### B.3.3 Total Correction

The final illumination profile correction, combining both the laser profile and camera geometry, is shown in Figure B.5c. The description used for this calibration is only an approximation to the lab set-up. The following factors cause deviations from this model:

- The pixels are not precisely aligned on the spherical focal surface; the pixel angle is fixed to its module's angle. The modules are aligned on the spherical focal surface.
- The light source is not point-like. It produces a diffuse emission, which likely reflects along the walls of the box.

A future study could further improve on the models used for the illumination correction.

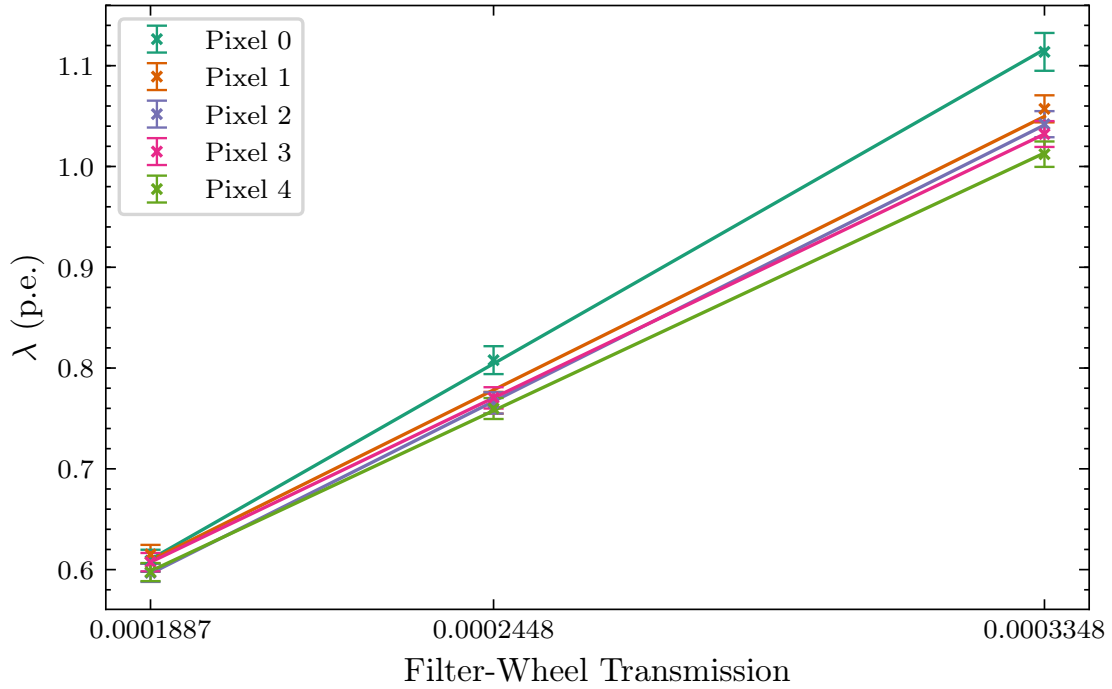


**Figure B.6:** Example of the linear regression to obtain the relationship between filter-wheel transmission and average illumination in photoelectrons ( $\lambda$ ), for 5 pixels. The values of  $\lambda$  are obtained from the simultaneous fits to the SPE spectra (Appendix ??). The error bars on the points are the  $1\sigma$  parabolic errors obtained from the covariance matrix of the fit)

## 3016 B.4 Absolute Illumination

3017 The method adopted to obtain a value for the absolute illumination was to use a  
 3018 fit to the SPE spectrum resulting from low-amplitude illumination of the pixels.  
 3019 Contained within this fit is the average illumination parameter,  $\lambda$ . The concept  
 3020 of the SPE fit is further covered in Chapter 5 and Appendix ??.

3021 By simultaneously fitting three illuminations, we obtained three values of  $\lambda$   
 3022 per pixel. With the three filter-wheel transmissions (corresponding to the three  
 3023 illuminations) on the x-axis, these values of  $\lambda$  were linearly regressed (weighted by  
 3024 the  $1\sigma$  parabolic error of the fit,  $\sigma_\lambda$ ) to obtain the gradient  $M_\lambda$  and y-intercept  $C_\lambda$   
 3025 per pixel. This linear regression is shown in Figure B.6. The y-intercept represents  
 3026 the value of  $\lambda$  one would get with zero filter-wheel transmission, and therefore  
 3027 indicates the NSB and DCR. The variation in  $M_\lambda$  across the pixels arises from the  
 3028 folding of the illumination profile and the relative PDE. Therefore, the next step  
 3029 was to correct for the illumination profile contribution to the gradient. The resulting  
 3030 spread of  $M_\lambda$  is solely from the relative PDE. The calibration from filter-wheel

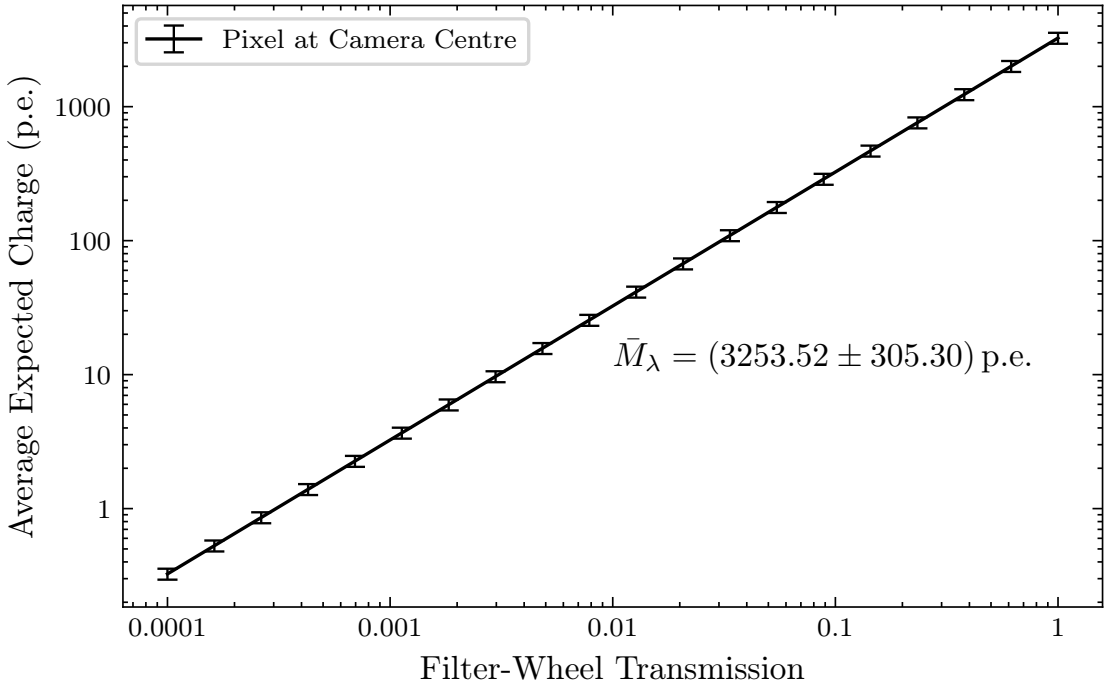


**Figure B.7:** Relationship between filter-wheel transmission and average expected charge in photoelectrons resulting from the filter-wheel calibration. The black line shows the conversion for a theoretical pixel positioned exactly at the camera centre. The error bars are calculated from the weighted standard deviation of the gradient estimates between the pixels, explained in Section B.6

3031 transmission  $T_{\text{FW}}$  to the average illumination across the whole camera  $\bar{I}_{\text{pe}}$  is then  
 3032 obtained by taking the averages of the linear regression coefficients:

$$\bar{I}_{\text{pe}} = \bar{M}_\lambda T_{\text{FW}} + \bar{C}_\lambda, \quad (\text{B.6})$$

## 3033 B.5 Average Expected Charge

3034 As we corrected for the NSB in the extracted signal value (Section 5.3), the NSB  
 3035 contribution to Equation B.6 ( $\bar{C}_\lambda$ ) is subtracted to give us the charge we expect  
 3036 when illuminating the camera with a filter-wheel transmission  $T_{\text{FW}}$ , for a theoretical  
 3037 pixel perfectly positioned at the camera centre. This relation is shown in Figure B.7.  
 3038 To obtain the average expected charge  $Q_{\text{Exp}}$  for each true camera pixel, this relation  
 3039 must be folded with the illumination profile correction factor  $F_{\text{pix}}$ :

$$Q_{\text{Exp}} = \bar{M}_\lambda T_{\text{FW}} F_{\text{pix}}. \quad (\text{B.7})$$

3040 This expression is important for the flat-fielding calibration (Chapter 5) and the  
 3041 calculation of the *Charge Resolution* for lab measurements (Chapter 7), as it

3042 tells us for a certain pixel and filter-wheel transmission, what charge we should  
3043 expect to measure on average.

## 3044 B.6 Consideration of Errors and Uncertainty

3045 When performing the weighted linear regression between  $\lambda_i$  and filter-wheel trans-  
3046 mission  $T_{FW_i}$  (with weights  $w_i = \frac{1}{\sigma_{\lambda_i}^2}$  accounting for the parabolic error in  $\lambda_i$ ), the  
3047 standard error on the estimate of the gradient per pixel,  $\sigma_{M_\lambda}$ , can be calculated  
3048 with the relation derived by Taylor [46]:

$$\sigma_{M_\lambda} = \sqrt{\frac{\sum w_i}{\sum w_i \sum w_i T_{FW_i}^2 - (\sum w_i T_{FW_i})^2}}, \quad i = 0, 1, 2, \dots, N. \quad (\text{B.8})$$

3049 During the correction for the illumination profile on the gradient estimates,  
3050 the illumination correction factors were also applied to the standard error on  
3051 the gradient estimate.

3052 While calculating the average gradient across the camera,  $\bar{M}_\lambda$ , the individual  
3053 gradient estimates were weighted by their corresponding standard error. To calculate  
3054 an uncertainty on the resulting value for  $\bar{M}_\lambda$ , the weighted standard deviation  
3055 between the gradient estimates were also calculated. This uncertainty is illustrated  
3056 in the error bars in Figure B.7. The resulting conversion value from filter wheel  
3057 transmission to expected charge for a theoretical pixel located at the centre of the  
3058 camera was calculated to be  $\bar{M}_\lambda = (3253.76 \pm 305.32)$  p.e..

check  
value

---

C

3059

3060

SPE Fitting

---

# D

3061

3062

## Transfer Function Investigations

3063

### Contents

---

3064

3065	<b>D.1 Plan</b> . . . . .	<b>134</b>
3066	D.1.1 Topics . . . . .	134
3067	D.1.2 Questions . . . . .	134
3068	<b>D.2 Introduction</b> . . . . .	<b>134</b>
3069	<b>D.3 TF Approaches</b> . . . . .	<b>135</b>
3070	D.3.1 No TF - Pedestal Subtraction Only . . . . .	135
3071	D.3.2 Raw TF Lookup with pedestal . . . . .	135
3072	D.3.3 PCHIP Interpolation . . . . .	135
3073	D.3.4 Polynomial Fit . . . . .	135
3074	<b>D.4 “Per Sampling Cell” or “Per Storage Cell”</b> . . . . .	<b>135</b>
3075	<b>D.5 Approach Comparison</b> . . . . .	<b>135</b>
3076	D.5.1 SPE Distribution . . . . .	135
3077	D.5.2 Charge Resolution . . . . .	135

3079  
3080

### D.1 Plan

#### D.1.1 Topics

- AC vs DC
- Charge resolution of different approaches
- SPE spectrum

#### D.1.2 Questions

- ?

3081

### D.2 Introduction

3083 limited data.....

3084 **D.3 TF Approaches**

3085 **D.3.1 No TF - Pedestal Subtraction Only**

3086 **D.3.2 Raw TF Lookup with pedestal**

3087 **D.3.3 PCHIP Interpolation**

3088 **D.3.4 Polynomial Fit**

3089 **D.4 “Per Sampling Cell” or “Per Storage Cell”**

3090 **D.5 Approach Comparison**

3091 **D.5.1 SPE Distribution**

3092 **D.5.2 Charge Resolution**

---

# E

3093

3094

## Charge Extractor Investigations

3095

### Contents

3096

3097	<b>E.1 Introduction</b> . . . . .	<b>136</b>
3098	<b>E.2 Integration Window</b> . . . . .	<b>136</b>
3099	E.2.1 Optimal Integration Window Parameters . . . . .	137
3100	E.2.2 Comparison with <i>Cross Correlation</i> . . . . .	139
3101	E.2.3 Conclusion . . . . .	141

3103

3104

---

### 3105 E.1 Introduction

3106 In Chapter 6, the different algorithms for extracting charge from a waveform are  
3107 extensively discussed, as well as the important considerations one must be vigilant  
3108 of when producing a charge-extraction algorithm. The purpose of this Appendix is  
3109 to inform about the performance of the chosen charge-extraction combination, *Cross*  
3110 *Correlation* and *Neighbour Peak Finding*, in comparison to typical charge-extraction  
3111 approaches, in the context of CHEC-S.

### 3112 E.2 Integration Window

3113 As an alternative to the *Cross Correlation* integration approach, one may instead use  
3114 a simple integration window, defined by the number of samples inside the “window  
3115 width”, and the number of samples the window is “shifted” from the peak time. In  
3116 order to investigate the performance of the integration-window approach fairly, one  
3117 must first optimise the values for the width and shift of the window when extracting  
3118 charge from a CHEC-S waveform. This exercise was performed using a Monte Carlo

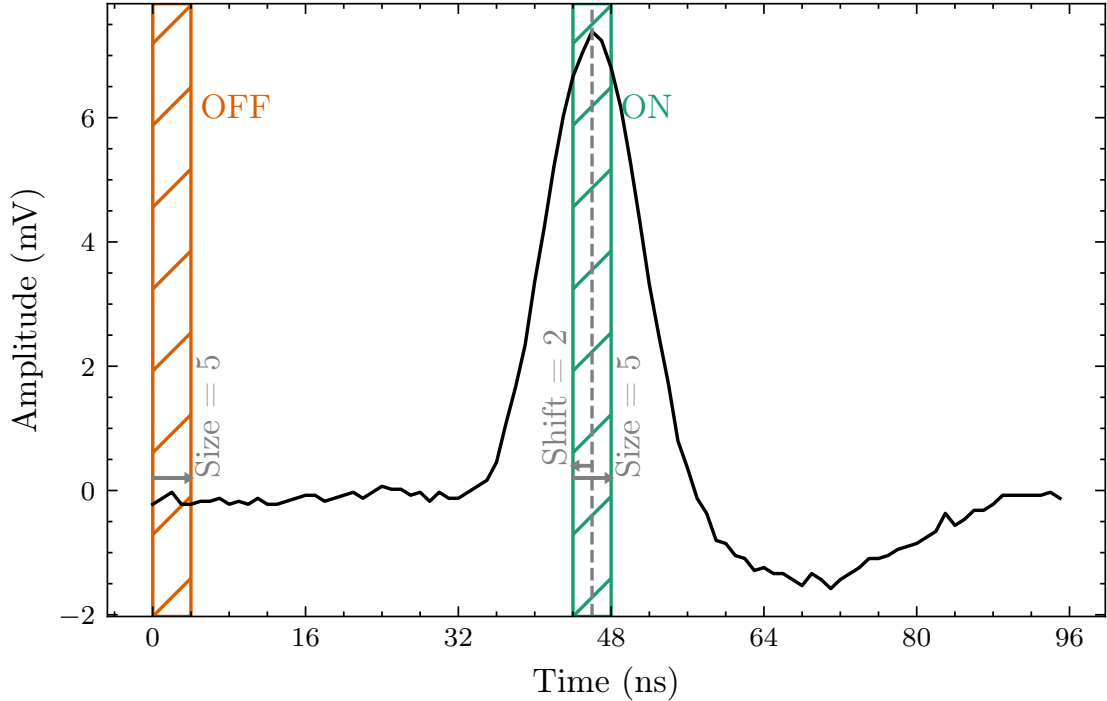


**Figure E.1:** Example waveform from a Monte Carlo simulation of CHEC-S, containing an approximately 50 p.e. signal. The “on” and “off” regions used to extract the signal-to-noise are illustrated. The window start position is defined as the peak position subtracted by the window shift. The window end position is defined as the window start plus the window size. A window size of 5 corresponds to 5 samples being included in the integration.

simulation of the lab set-up, where the camera was uniformly illuminated. The pulse time is consistent in simulations of this nature, therefore the same pulse time is manually chosen for every waveform. This allows the following investigation to be solely on the integration approach, avoiding any dependence on the peak finding.

### E.2.1 Optimal Integration Window Parameters

As explained in Chapter 6, the optimal integration window parameters are noise dependant; a larger integration window is likely to include more noise (NSB and DCR). However, a larger window size results in more of the signal being captured. In Figure E.2 the signal-to-noise (SNR) as a function of integration-window parameters is shown for different amplitude and noise values. The SNR investigation was performed as follows. Assume an “on” region of the waveform, where the extracted value contains the signal plus the noise, and an “off” region where the extracted value contains solely the noise contributions (Figure E.1). The optimal window for a constant signal on top of a fluctuating background is then found by:

$$\text{SNR} = \frac{\mu_{\text{on}}}{\sigma_{\text{off}}}, \quad (\text{E.1})$$

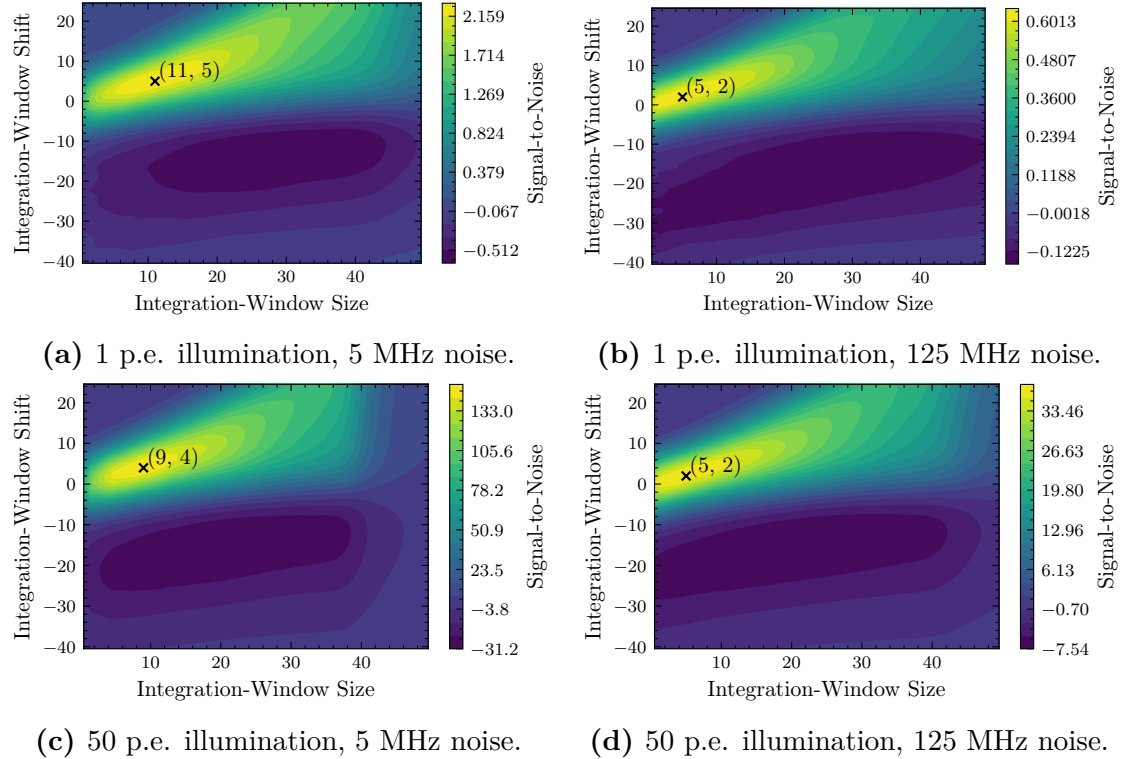


**Figure E.2:** Contour plot of signal-to-noise as a function of window width and shift, for different amplitudes and noise values. The maximum, annotated with the cross and position, indicates the optimal integration-window parameters when applied to a CHEC-S waveform. The definitions of window and shift are shown in Figure ???. The contours are split into percentiles of the range; the top 5 % of values are contained in the brightest yellow contour. Negative values correspond to an integration window concentrated on the undershoot of the pulse.

3133 where  $\mu_{\text{on}}$  is the average signal extracted from the “on” region, and  $\sigma_{\text{off}}$  is the  
 3134 standard deviation of the signal extracted from the “off” region. The approach of  
 3135 Equation E.1 is an alternative to looking for the optimal window for a fluctuating  
 3136 signal on top of a fluctuating background ( $\text{SNR} = \frac{\mu_{\text{on}}}{\sigma_{\text{on}}}$ ), which, due to the inclusion  
 3137 of the signal deviations from the “on” region, is much less sensitive to the noise  
 3138 fluctuations and has a strong dependence on the signal level, i.e. the Poisson  
 3139 fluctuations of the signal increases with amplitude.

3140 In Figure E.2 the conflict between a large window size to contain the full signal,  
 3141 and a small window to minimise noise is evident, resulting in a limited region in  
 3142 which a high signal-to-noise can be achieved. In conclusion, an integration window  
 3143 width of 5 samples and a shift of 2 samples appeared to be optimal for a noise of  
 3144 125 MHz, for both small and large amplitudes (Figures E.2b and E.2d respectively).  
 3145 This integration window is demonstrated in Figure E.1. As the *Charge Resolution*

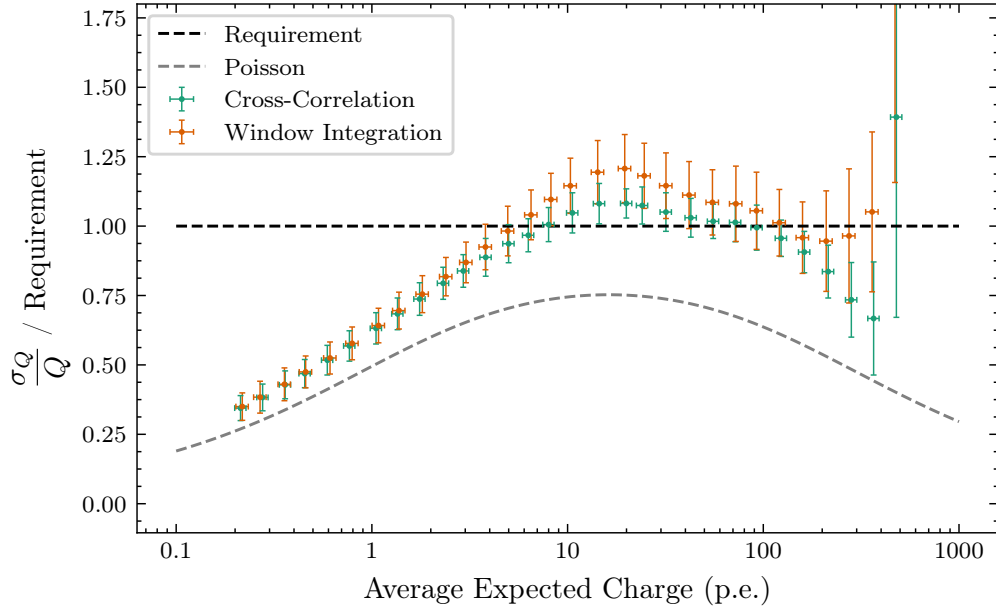


**Figure E.3:** *Charge Resolution* of the *Cross Correlation* charge extraction approach applied to uniformly illuminated lab data, compared to the *Charge Resolution* of the integration window approach for the same dataset. The Y axis is limited to exclude the high values that arise from saturation.

3146 requirements are defined at an NSB of 125 MHz, these window parameters are  
 3147 adopted for the following investigations.

### 3148 E.2.2 Comparison with *Cross Correlation*

3149 As described previously in the thesis, the most appropriate performance criterion  
 3150 for a charge extraction technique used for a CTA camera is the *Charge Resolution*.  
 3151 Outlined in Section 7.3.1 are the names I have defined to distinguish between different  
 3152 *Charge Resolution* procedures, each using different datasets and/or procedures. In  
 3153 order to evaluate the performance of the *Cross Correlation* technique with respect  
 3154 to a simple integration window, their resulting *Charge Resolutions* were compared  
 3155 in investigations that explore the relevant parameter space.

3156 The first comparison is shown in Figure E.3. It explores the comparative  
 3157 performance in the context of the measurements using the *Lab* dataset (i.e. using  
 3158 the real camera). A small performance improvement is observed with the cross-  
 3159 correlation technique for  $Q_{\text{Exp}} > 10$  p.e..

3160 In a comparison of the two extraction approaches when used in a simulation using  
 3161 the CHEC-S model, shown in Figure E.4, it is evident that the *Cross Correlation*  
 3162 approach performs worse than the *Window Integration*, especially at higher NSB.

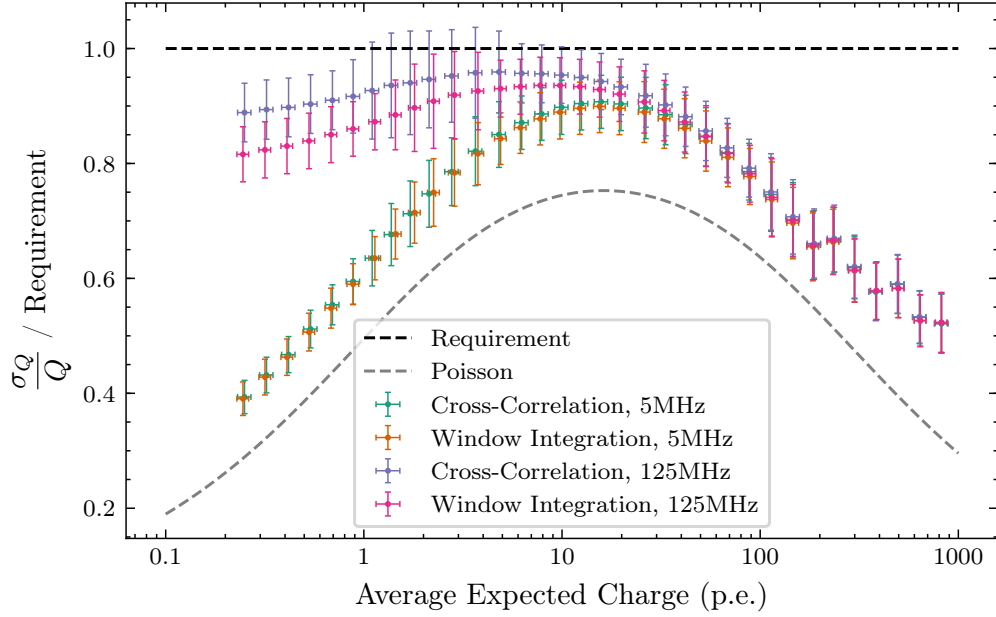


**Figure E.4:** Charge Resolution of the Cross Correlation charge extraction approach compared to the Charge Resolution of the integration window approach, for both 5 MHz and 125 MHz NSB noise. The dataset used is produced by Monte Carlo simulations of the camera uniformly illuminated, replicating the lab set-up (i.e. the *MCLab* procedure). The optical crosstalk of the photosensors in the simulation is 40 %.

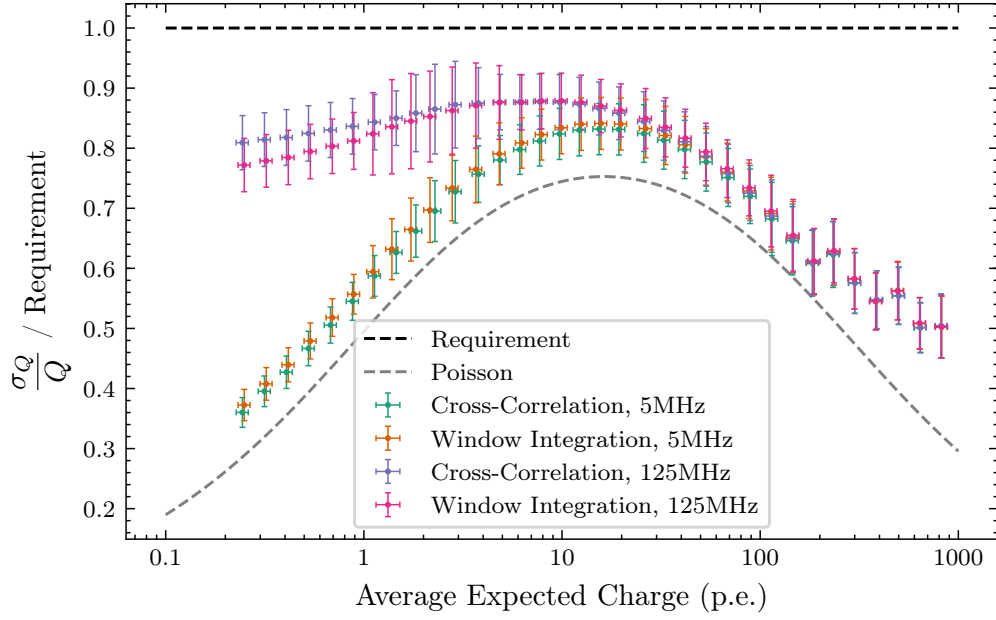


**Figure E.5:** Same as Figure E.4, but with a dataset containing an optical crosstalk value of 20 %.

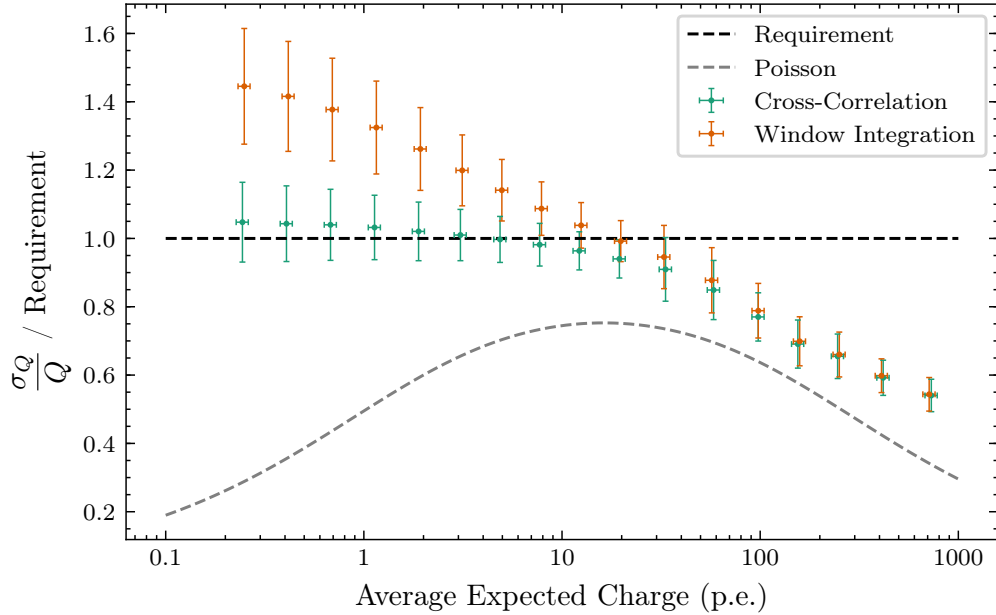


**Figure E.6:** Same as Figure E.4, but with a dataset containing a factor of 10 higher electronic noise.

3163     Figure E.5 shows a similar comparison to the previous one, however the optical  
 3164     crosstalk of the simulation model was reduced to 20 %. The result is an improved  
 3165     performance when using the *Cross Correlation* technique at low NSB rate. However,  
 3166     at high NSB, the *Window Integrator* performs slightly better.

3167     Finally, in Figure E.6 a simulation of CHEC-S is used, but with a factor of 10  
 3168     higher electronic noise. As a result, the *Cross Correlation* technique significantly  
 3169     improves the performance with respect to the *Window Integrator*.

### 3170     E.2.3 Conclusion

3171     The comparisons of *Charge Resolution* have confirmed our understanding of the  
 3172     *Cross Correlation* method:

- 3173         • The *Cross Correlation* method amplifies anything correlated with reference  
 3174         pulse shape. This includes NSB and optical crosstalk factors. Therefore, when  
 3175         these are the dominant noise factors in the waveforms, the *Window Integrator*  
 3176         performs slightly better.
- 3177         • When noise that is uncorrelated with the reference pulse shape is present in  
 3178         the waveform, such as a high amount of electronic noise, the *Cross Correlation*  
 3179         is an extremely useful tool to resolve the signal.

3180 It would appear that with the current simulation model of CHEC-S, the major noise  
3181 components are those correlated with the reference pulse shape. Therefore, not  
3182 much improvement is available through the *Cross Correlation* technique. However,  
3183 when the optical crosstalk of the SiPMs is lowered to 10% (see Section ??), the  
3184 other noise factors such as electronic noise could become a relatively significant  
3185 contribution to the total noise (as occurs in Figure E.5). This would therefore  
3186 justify the use of the *Cross Correlation* technique.

3187 Despite the conclusion obtained from the simulations, there does appear to be an  
3188 improvement when using the *Cross Correlation* method for measurements of the real  
3189 camera (Figure E.3). The only likely source of uncorrelated noise at  $Q_{\text{Exp}} > 10$  p.e.  
3190 is from the residuals in the Transfer Function calibration. It would appear that the  
3191 *Cross Correlation* method suppresses this additional noise component introduced  
3192 by the calibration. As the Transfer Functions are not present in the simulations,  
3193 this affect is not apparent in the *Charge Resolution* results obtained from them.

3194 A further investigation into the actual parameter regions of Equation 3.2 which  
3195 justify the use of the *Cross Correlation* approach is intended for the future.

## References

- 3197 [1] Peter Cogan and Sullivan Supervised by John Quinn. “Nanosecond Sampling of  
3198 Atmospheric Cherenkov Radiation Applied to TeV Gamma-Ray Observations of  
3199 Blazars with VERITAS”. In: December (2006).
- 3200 [2] Cameron Rulten et al. “Simulating the optical performance of a small-sized  
3201 telescope with secondary optics for the Cherenkov Telescope Array”. In:  
3202 *Astroparticle Physics* 82 (Sept. 2016), pp. 36–48. ISSN: 09276505. DOI:  
3203 10.1016/j.astropartphys.2016.05.002. URL:  
3204 <https://linkinghub.elsevier.com/retrieve/pii/S0927650516300652>.
- 3205 [3] V. Vassiliev, S. Fegan, and P. Brousseau. “Wide field aplanatic two-mirror  
3206 telescopes for ground-based  $\gamma$ -ray astronomy”. In: *Astroparticle Physics* 28.1 (Sept.  
3207 2007), pp. 10–27. ISSN: 09276505. DOI: 10.1016/j.astropartphys.2007.04.002.  
3208 arXiv: 0612718 [astro-ph]. URL:  
3209 <http://linkinghub.elsevier.com/retrieve/pii/S0927650507000527>.
- 3210 [4] J. J. Watson et al. “Inauguration and first light of the GCT-M prototype for the  
3211 Cherenkov telescope array”. In: *AIP Conference Proceedings* 1792 (2017), pp. 1–6.  
3212 ISSN: 15517616. DOI: 10.1063/1.4969027. arXiv: 1610.01452.
- 3213 [5] Hamamatsu. *Photomultiplier Tubes*. Technical Note, Accessed 20/09/2018. 2016,  
3214 p. 129. URL: [https://www.hamamatsu.com/resources/pdf/etd/PMT%7B%5C\\_%7DTPMZ0002E.pdf](https://www.hamamatsu.com/resources/pdf/etd/PMT%7B%5C_%7DTPMZ0002E.pdf).
- 3215 [6] T. C. Weekes. *Very High Energy Gamma-Ray Astronomy*. Bristol and Philadelphia:  
3216 Institute of Physics Publishing, 2003. ISBN: 0750306580.
- 3217 [7] Hamamatsu. *Photomultiplier Tubes: Basics and Applications*. Tech. rep. 2007. URL:  
3218 [https://www.hamamatsu.com/resources/pdf/etd/PMT%7B%5C\\_%7Dhandbook%7B%5C\\_%7Dv3aE.pdf](https://www.hamamatsu.com/resources/pdf/etd/PMT%7B%5C_%7Dhandbook%7B%5C_%7Dv3aE.pdf).
- 3219 [8] Hamamatsu. *Flat panel type multianode PMT assembly H8500 series / H10966*  
3220 *series*. Technical Document, Accessed 20/09/2018. 2011. URL:  
3221 [https://www.hamamatsu.com/resources/pdf/etd/H8500%7B%5C\\_%7DH10966%7B%5C\\_%7DTPMH1327E.pdf](https://www.hamamatsu.com/resources/pdf/etd/H8500%7B%5C_%7DH10966%7B%5C_%7DTPMH1327E.pdf).
- 3222 [9] D. Renker. “Geiger-mode avalanche photodiodes, history, properties and problems”.  
3223 In: *Nuclear Instruments and Methods in Physics Research Section A: Accelerators,*  
3224 *Spectrometers, Detectors and Associated Equipment* 567.1 (Nov. 2006), pp. 48–56.  
3225 ISSN: 01689002. DOI: 10.1016/j.nima.2006.05.060. URL:  
3226 <http://linkinghub.elsevier.com/retrieve/pii/S0168900206008680>.
- 3227 [10] A. Ghassemi, K. Sato, and K. Kobayashi. *MPPC*. Technical Note, Accessed  
3228 20/09/2018. 2017. URL: [https://www.hamamatsu.com/resources/pdf/ssd/mppc%7B%5C\\_%7Dkapd9005e.pdf](https://www.hamamatsu.com/resources/pdf/ssd/mppc%7B%5C_%7Dkapd9005e.pdf).
- 3229 [11] A. Biland et al. “FACT - Status and experience from three years operation of the  
3230 first SiPM camera”. In: *Proceedings of Science* 30-July-2015 (2015), pp. 1–8. ISSN:  
3231 18248039.

- 3236 [12] Hamamatsu. *S12642 DataSheet*. Data Sheet; Not publicly available. 2013.
- 3237 [13] SensL. *Introduction to SiPM*. Technical Note, Accessed 20/09/2018. 2011, pp. 1–16.
- 3238 [14] Ivan Rech et al. “Optical crosstalk in single photon avalanche diode arrays: a new  
3239 complete model”. In: *Optics Express* 16.12 (June 2008), p. 8381. ISSN: 1094-4087.  
3240 DOI: 10.1364/OE.16.008381. URL:  
3241 <https://www.osapublishing.org/oe/abstract.cfm?uri=oe-16-12-8381>.
- 3242 [15] S. Vinogradov. “Analytical models of probability distribution and excess noise  
3243 factor of solid state photomultiplier signals with crosstalk”. In: *Nuclear  
3244 Instruments and Methods in Physics Research Section A: Accelerators,  
3245 Spectrometers, Detectors and Associated Equipment* 695 (Dec. 2012), pp. 247–251.  
3246 ISSN: 01689002. DOI: 10.1016/j.nima.2011.11.086. arXiv: 1109.2014. URL:  
3247 <http://linkinghub.elsevier.com/retrieve/pii/S0168900211021565>.
- 3248 [16] M. Teich, Kuniaki Matsuo, and B. Saleh. “Excess noise factors for conventional  
3249 and superlattice avalanche photodiodes and photomultiplier tubes”. In: *IEEE  
3250 Journal of Quantum Electronics* 22.8 (Aug. 1986), pp. 1184–1193. ISSN: 0018-9197.  
3251 DOI: 10.1109/JQE.1986.1073137. URL:  
3252 <http://ieeexplore.ieee.org/document/1073137/>.
- 3253 [17] W. J. Kindt, H. W. van Zeijl, and S. Middelhoe. “Optical Cross Talk in Geiger  
3254 Mode Avalanche Photodiode Arrays: Modeling, Prevention and Measurement”. In:  
3255 *28th European Solid-State Device Research Conference*. Bordeaux, France, 1998,  
3256 pp. 192–195. URL: <http://ieeexplore.ieee.org/stamp/stamp.jsp?tp=%7B%5C%7Darnumber=1503521%7B%5C%7Disnumber=32252>.
- 3258 [18] R. Pagano et al. “Optimized silicon photomultipliers with optical trenches”. In:  
3259 *2011 Proceedings of the European Solid-State Device Research Conference  
(ESSDERC)*. IEEE, Sept. 2011, pp. 183–186. ISBN: 978-1-4577-0707-0. DOI:  
3260 10.1109/ESSDERC.2011.6044204. URL:  
3261 <http://ieeexplore.ieee.org/document/6044204/>.
- 3263 [19] Hamamatsu. *MPPC : S14521-8648 (bare type) Specification Sheet*. Data Sheet; Not  
3264 publicly available. 2018.
- 3265 [20] Hamamatsu. *MPPC : S14521-8649(resin type) Specification Sheet*. Data Sheet; Not  
3266 publicly available. 2018.
- 3267 [21] J. Zorn et al. “Characterisation and testing of CHEC-M—A camera prototype for  
3268 the small-sized telescopes of the Cherenkov telescope array”. In: *Nuclear  
3269 Instruments and Methods in Physics Research, Section A: Accelerators,  
3270 Spectrometers, Detectors and Associated Equipment* 904 (Oct. 2018), pp. 44–63.  
3271 ISSN: 01689002. DOI: 10.1016/j.nima.2018.06.078. arXiv: 1806.11308. URL:  
3272 <https://linkinghub.elsevier.com/retrieve/pii/S0168900218308143>.
- 3273 [22] Andrea De Franco. “The first GCT camera for the Cherenkov Telescope Array.” In:  
3274 *Proceedings of The 34th International Cosmic Ray Conference — PoS(ICRC2015)*.  
3275 Trieste, Italy: Sissa Medialab, Aug. 2016, p. 1015. DOI: 10.22323/1.236.1015.  
3276 URL: <https://pos.sissa.it/236/1015>.

- 3277 [23] Richard White. "CHEC: a Compact High Energy Camera for the Cherenkov  
 3278 Telescope Array". In: *Journal of Instrumentation* 12.12 (Dec. 2017),  
 3279 pp. C12059–C12059. ISSN: 1748-0221. DOI: 10.1088/1748-0221/12/12/C12059.  
 3280 arXiv: 1712.00354. URL:  
 3281 <http://arxiv.org/abs/1712.00354%20http://stacks.iop.org/1748-0221/12/i=12/a=C12059?key=crossref.c5160d771b5f8af8a5917164c6d2c0ae>.
- 3283 [24] S. Funk et al. "TARGET: A digitizing and trigger ASIC for the Cherenkov  
 3284 telescope array". In: *AIP Conference Proceedings*. Vol. 1792. 2017, p. 080012. ISBN:  
 3285 9780735414563. DOI: 10.1063/1.4969033. arXiv: 1610.01536. URL:  
 3286 <http://aip.scitation.org/doi/abs/10.1063/1.4969033>.
- 3287 [25] A. Albert et al. "TARGET 5: A new multi-channel digitizer with triggering  
 3288 capabilities for gamma-ray atmospheric Cherenkov telescopes". In: *Astroparticle  
 3289 Physics* 92 (June 2017), pp. 49–61. ISSN: 09276505. DOI:  
 3290 10.1016/j.astropartphys.2017.05.003. arXiv: 1607.02443. URL:  
 3291 <https://linkinghub.elsevier.com/retrieve/pii/S0927650517301524>.
- 3292 [26] Anthony Brown et al. "Flasher and muon-based calibration of the GCT telescopes  
 3293 proposed for the Cherenkov Telescope Array". In: *Proceedings of The 34th  
 3294 International Cosmic Ray Conference — PoS(ICRC2015)*. Vol. 30-July-20. Trieste,  
 3295 Italy: Sissa Medialab, Aug. 2016, p. 934. DOI: 10.22323/1.236.0934. arXiv:  
 3296 1509.00185. URL:  
 3297 <http://arxiv.org/abs/1509.00185%20https://pos.sissa.it/236/934>.
- 3298 [27] Francesco Dazzi et al. *CTA Architecture*. Internal Document (V1.0). CTA  
 3299 Observatory, 2018.
- 3300 [28] "*Countries and Institutes in CTA Consortium*". [Online; accessed 20-07-2018]. URL:  
 3301 <https://www.cta-observatory.org/about/cta-consortium/>.
- 3302 [29] "*Shareholders and Associate Members of CTAO gGmbH*". [Online; accessed  
 3303 20-07-2018]. URL: <https://www.cta-observatory.org/about/governance/>.
- 3304 [30] *CTA Requirements*. [Online; accessed 18-07-2018]. URL:  
 3305 <https://jama.cta-observatory.org>.
- 3306 [31] Alison Mitchell and Jim Hinton. *SYS-REQ/180326: Photoelectrons to Photons in  
 3307 Camera Performance Requirements*. Internal Document (Draft V1.0). CTA  
 3308 Observatory, 2018.
- 3309 [32] Stefan Ohm and Jim Hinton. *SCI-MC/121113: Impact of measurement errors on  
 3310 charge resolution and system performance*. Internal Document (V1.1). CTA  
 3311 Observatory, 2012.
- 3312 [33] Karl Kosack et al. *CTA High-Level Data Model Definitions*. Internal Document  
 3313 (Draft V0.3). CTA Observatory, 2017.
- 3314 [34] Konrad Bernlöhr. "Simulation of imaging atmospheric Cherenkov telescopes with  
 3315 CORSIKA and sim\_telarray". In: *Astroparticle Physics* 30.3 (Oct. 2008),  
 3316 pp. 149–158. ISSN: 09276505. DOI: 10.1016/j.astropartphys.2008.07.009.  
 3317 arXiv: 0808.2253. URL:  
 3318 <http://linkinghub.elsevier.com/retrieve/pii/S0927650508000972>.
- 3319 [35] D Heck et al. *CORSIKA: A Monte Carlo Code to Simulate Extensive Air Showers*.  
 3320 Vol. FZKA 6019. FZKA-6019. FZKA, 1998, pp. 1–90. URL: [http://www-ik.fzk.de/corsika/physics%7B%5C\\_%7Ddescription/corsika%7B%5C\\_%7Dphys.html](http://www-ik.fzk.de/corsika/physics%7B%5C_%7Ddescription/corsika%7B%5C_%7Dphys.html).

- 3322 [36] Stéfan van der Walt, S. Chris Colbert, and Gaël Varoquaux. “The NumPy Array:  
 3323 A Structure for Efficient Numerical Computation”. In: *Computing in Science &  
 3324 Engineering* 13.2 (Mar. 2011), pp. 22–30. ISSN: 1521-9615. DOI:  
 3325 10.1109/MCSE.2011.37. arXiv: 1102.1523. URL:  
 3326 <http://ieeexplore.ieee.org/document/5725236/>.
- 3327 [37] A. Balzer et al. “The H.E.S.S. central data acquisition system”. In: *Astroparticle  
 3328 Physics* 54 (Feb. 2014), pp. 67–80. ISSN: 09276505. DOI:  
 3329 10.1016/j.astropartphys.2013.11.007. arXiv: arXiv:1311.3486v1. URL:  
 3330 <http://dx.doi.org/10.1016/j.astropartphys.2013.11.007%20http://linkinghub.elsevier.com/retrieve/pii/S0927650513001655>.
- 3332 [38] A.U. Abeysekara et al. “Data acquisition architecture and online processing system  
 3333 for the HAWC gamma-ray observatory”. In: *Nuclear Instruments and Methods in  
 3334 Physics Research Section A: Accelerators, Spectrometers, Detectors and Associated  
 3335 Equipment* 888.January (Apr. 2018), pp. 138–146. ISSN: 01689002. DOI:  
 3336 10.1016/j.nima.2018.01.051. arXiv: 1709.03751. URL:  
 3337 <https://linkinghub.elsevier.com/retrieve/pii/S0168900218300688>.
- 3338 [39] E Gamma et al. *Design Patterns: Elements of Reusable Software*. Addison-Wesley  
 3339 professional computing series. Addison-Wesley, 1996, p. 395. ISBN: 020163361-2.  
 3340 DOI: 10.1093/carcin/bgs084. arXiv: dd. URL:  
 3341 <https://books.google.co.uk/books?id=vRfxugEACAAJ>.
- 3342 [40] R. D. Parsons and J. A. Hinton. “A Monte Carlo template based analysis for  
 3343 air-Cherenkov arrays”. In: *Astroparticle Physics* 56 (2014), pp. 26–34. ISSN:  
 3344 09276505. DOI: 10.1016/j.astropartphys.2014.03.002. arXiv: 1403.2993. URL:  
 3345 <http://dx.doi.org/10.1016/j.astropartphys.2014.03.002>.
- 3346 [41] Christoph Deil et al. “Gammapy - A prototype for the CTA science tools”. In:  
 3347 *Proceedings of 35th International Cosmic Ray Conference — PoS(ICRC2017)*.  
 3348 Trieste, Italy: Sissa Medialab, Aug. 2017, p. 766. DOI: 10.22323/1.301.0766.  
 3349 arXiv: 1709.01751. URL: <https://pos.sissa.it/301/766>.
- 3350 [42] D. Berge, S. Funk, and J. Hinton. “Background modelling in very-high-energy  $\gamma$   
 3351 -ray astronomy”. In: *Astronomy & Astrophysics* 466.3 (May 2007), pp. 1219–1229.  
 3352 ISSN: 0004-6361. DOI: 10.1051/0004-6361:20066674. arXiv: 0610959  
 3353 [astro-ph]. URL: <http://www.aanda.org/10.1051/0004-6361:20066674%20http://arxiv.org/abs/astro-ph/0610959%20http://dx.doi.org/10.1051/0004-6361:20066674>.
- 3356 [43] J. Knödlseder et al. “GammaLib and ctools: A software framework for the analysis  
 3357 of astronomical gamma-ray data”. In: *Astronomy & Astrophysics* 593 (June 2016),  
 3358 A1. ISSN: 0004-6361. DOI: 10.1051/0004-6361/201628822. arXiv: 1606.00393.  
 3359 URL: <http://dx.doi.org/10.1051/0004-6361/201628822%20http://www.aanda.org/10.1051/0004-6361/201628822%20http://arxiv.org/abs/1606.00393>.
- 3362 [44] K. Bechtol et al. “TARGET: A multi-channel digitizer chip for very-high-energy  
 3363 gamma-ray telescopes”. In: *Astroparticle Physics* 36.1 (Aug. 2012), pp. 156–165.  
 3364 ISSN: 09276505. DOI: 10.1016/j.astropartphys.2012.05.016. arXiv: 1105.1832.  
 3365 URL: <http://dx.doi.org/10.1016/j.astropartphys.2012.05.016%20http://linkinghub.elsevier.com/retrieve/pii/S0927650512001211>.

- 3367 [45] F. Aharonian et al. “Calibration of cameras of the H.E.S.S. detector”. In:  
 3368 *Astroparticle Physics* 22.2 (2004), pp. 109–125. ISSN: 09276505. DOI:  
 3369 10.1016/j.astropartphys.2004.06.006. arXiv: 0408145 [astro-ph].
- 3370 [46] J. R. Taylor. *An introduction to error analysis : the study of uncertainties in*  
 3371 *physical measurements*. 2nd. Sausalito, Calif. : University Science Books, 1997,  
 3372 pp. 181–199. ISBN: 978-0935702101.
- 3373 [47] T. C. Weekes et al. “Observation of TeV gamma rays from the Crab nebula using  
 3374 the atmospheric Cherenkov imaging technique”. In: *The Astrophysical Journal* 342  
 3375 (July 1989), p. 379. ISSN: 0004-637X. DOI: 10.1086/167599. URL:  
 3376 <http://adsabs.harvard.edu/doi/10.1086/167599>.
- 3377 [48] Idan Shilon et al. “Application of Deep Learning methods to analysis of Imaging  
 3378 Atmospheric Cherenkov Telescopes data”. In: March (2018). arXiv: 1803.10698.  
 3379 URL: <http://arxiv.org/abs/1803.10698>.
- 3380 [49] J. Holder. “Exploiting VERITAS Timing Information”. In: January (2005),  
 3381 pp. 383–386. arXiv: 0507450 [astro-ph]. URL:  
 3382 <http://arxiv.org/abs/astro-ph/0507450>.
- 3383 [50] P. Cogan. “Analysis of Flash ADC Data With VERITAS”. In: *Methods* 0.1 (2007),  
 3384 p. 4. arXiv: 0709.4208. URL: <http://arxiv.org/abs/0709.4208>.
- 3385 [51] Eric W. Weisstein. *"Cross-Correlation." From MathWorld—A Wolfram Web*  
 3386 *Resource*. [Online; accessed 20-07-2018]. URL:  
 3387 <http://mathworld.wolfram.com/Cross-Correlation.html>.
- 3388 [52] *SciPy: Open source scientific tools for Python: scipy.ndimage.correlate1d*. [Online;  
 3389 accessed 20-07-2018]. URL: <https://docs.scipy.org/doc/scipy/reference/generated/scipy.ndimage.correlate1d.html>.
- 3391 [53] J. Albert et al. “FADC signal reconstruction for the MAGIC telescope”. In:  
 3392 *Nuclear Instruments and Methods in Physics Research, Section A: Accelerators,*  
 3393 *Spectrometers, Detectors and Associated Equipment* 594.3 (2008), pp. 407–419.  
 3394 ISSN: 01689002. DOI: 10.1016/j.nima.2008.06.043. arXiv: 0612385 [astro-ph].
- 3395 [54] S. Klepser et al. “Hardware and software architecture of the upgraded H.E.S.S.  
 3396 cameras”. In: *Proceedings of Science* (2017), pp. 0–8. ISSN: 18248039. arXiv:  
 3397 1708.04550.
- 3398 [55] Raphaël Chalmé-Calvet et al. “Exploiting the time of arrival of Cherenkov photons  
 3399 at the 28 m H.E.S.S. telescope for background rejection: Methods and  
 3400 performance”. In: *Proceedings of Science* 30-July-20 (2015). ISSN: 18248039. arXiv:  
 3401 1509.03544.
- 3402 [56] D. Impiombato et al. “Procedures for the relative calibration of the SiPM gain on  
 3403 ASTRI SST-2M camera”. In: *Experimental Astronomy* 43.1 (2017). ISSN: 15729508.  
 3404 DOI: 10.1007/s10686-016-9516-z. arXiv: 1612.02186.
- 3405 [57] AM Hillas. “Cerenkov light images of EAS produced by primary gamma”. In:  
 3406 *International Cosmic Ray Conference* (1985). URL:  
 3407 <http://adsabs.harvard.edu/full/1985ICRC....3..445H>.

- 3408 [58] P. T. Reynolds et al. “Survey of candidate gamma-ray sources at TeV energies  
 3409 using a high-resolution Cerenkov imaging system - 1988-1991”. In: *The*  
 3410 *Astrophysical Journal* 404 (Feb. 1993), p. 206. ISSN: 0004-637X. DOI:  
 3411 10.1086/172269. URL: <http://adsabs.harvard.edu/doi/10.1086/172269>.
- 3412 [59] A. Daum et al. “First results on the performance of the HEGRA IACT array”. In:  
 3413 *Astroparticle Physics* 8.1-2 (Dec. 1997), pp. 1–11. ISSN: 09276505. DOI:  
 3414 10.1016/S0927-6505(97)00031-5. arXiv: 9704098 [astro-ph]. URL:  
 3415 <http://arxiv.org/abs/astro-ph/9704098%20http://linkinghub.elsevier.com/retrieve/pii/S0927650597000315>.
- 3417 [60] John Hugh Dickinson. “Very High Energy Gamma-Rays from Binary Systems”. In:  
 3418 (2010).
- 3419 [61] Stefan Eschbach et al. “Studies towards an understanding of global array pointing  
 3420 for the Cherenkov Telescope Array”. In: *Proceedings of The 34th International*  
 3421 *Cosmic Ray Conference — PoS(ICRC2015)*. Trieste, Italy: Sissa Medialab, Aug.  
 3422 2016, p. 1025. DOI: 10.22323/1.236.1025. URL:  
 3423 <https://pos.sissa.it/236/1025>.
- 3424 [62] K. Bernlöhr et al. “Monte Carlo design studies for the Cherenkov Telescope Array”.  
 3425 In: *Astroparticle Physics* 43 (Mar. 2013), pp. 171–188. ISSN: 09276505. DOI:  
 3426 10.1016/j.astropartphys.2012.10.002. arXiv: 1210.3503 [astro-ph.IM].  
 3427 URL: <http://dx.doi.org/10.1016/j.astropartphys.2012.10.002%20http://linkinghub.elsevier.com/retrieve/pii/S0927650512001867>.
- 3429 [63] R.W. Lessard et al. “A new analysis method for reconstructing the arrival direction  
 3430 of TeV gamma rays using a single imaging atmospheric Cherenkov telescope”. In:  
 3431 *Astroparticle Physics* 15.1 (Mar. 2001), pp. 1–18. ISSN: 09276505. DOI:  
 3432 10.1016/S0927-6505(00)00133-X. arXiv: 0005468 [astro-ph]. URL:  
 3433 [http://arxiv.org/abs/astro-ph/0005468%7B%5C%7D5Cnhttp://dx.doi.org/10.1016/S0927-6505\(00\)00133-X%20http://linkinghub.elsevier.com/retrieve/pii/S092765050000133X](http://arxiv.org/abs/astro-ph/0005468%7B%5C%7D5Cnhttp://dx.doi.org/10.1016/S0927-6505(00)00133-X%20http://linkinghub.elsevier.com/retrieve/pii/S092765050000133X).
- 3436 [64] David J. Fegan. “ $\gamma$ /hadron separation at TeV energies”. In: *Journal of Physics G: Nuclear and Particle Physics* 23.9 (Sept. 1997), pp. 1013–1060. ISSN: 09543899. DOI:  
 3437 10.1088/0954-3899/23/9/004. URL: <http://stacks.iop.org/0954-3899/23/i=9/a=004?key=crossref.6d9048310a121dd1ec40ab2f50efd418>.
- 3440 [65] A.M. Hillas. “Differences between gamma-ray and hadronic showers”. In: *Space Science Reviews* 75.1-2 (Jan. 1996), pp. 17–30. ISSN: 0038-6308. DOI:  
 3441 10.1007/BF00195021. URL: <http://link.springer.com/10.1007/BF00195021>.
- 3443 [66] S Ohm, C. van Eldik, and K Egberts. “ $\gamma$ /hadron separation in very-high-energy  
 3444  $\gamma$ -ray astronomy using a multivariate analysis method”. In: *Astroparticle Physics*  
 3445 31.5 (June 2009), pp. 383–391. ISSN: 09276505. DOI:  
 3446 10.1016/j.astropartphys.2009.04.001. arXiv: arXiv:0904.1136v1. URL:  
 3447 <http://linkinghub.elsevier.com/retrieve/pii/S0927650509000589>.
- 3448 [67] A. Okumura. *The Prototype of Gamma-ray Cherenkov Telescope (GCT) of the*  
 3449 *Cherenkov Telescope Array (CTA)*. [Online Image; accessed 16-09-2018]. Dec. 2015.  
 3450 URL: <https://www.flickr.com/photos/akiraokumura/23472763315>.

- 3451 [68] A. Okumura. *The Prototype of Gamma-ray Cherenkov Telescope (GCT) of the*  
3452 *Cherenkov Telescope Array (CTA)*. [Online Image; accessed 16-09-2018]. Dec. 2015.  
3453 URL: <https://www.flickr.com/photos/akiraokumura/23150523890>.
- 3454 [69] M. Punch et al. “Detection of TeV photons from the active galaxy Markarian 421”.  
3455 In: *Nature* 358.6386 (Aug. 1992), pp. 477–478. ISSN: 00280836. DOI:  
3456 10.1038/358477a0. URL:  
3457 <http://www.nature.com/doifinder/10.1038/358477a0>.
- 3458 [70] Markus Gaug et al. “Calibration strategies for the Cherenkov Telescope Array”. In:  
3459 ed. by Alison B. Peck, Chris R. Benn, and Robert L. Seaman. July. Aug. 2014,  
3460 p. 914919. ISBN: 9780819496171. DOI: 10.1111/12.2054536. URL:  
3461 <http://proceedings.spiedigitallibrary.org/proceeding.aspx?doi=10.1111/12.2054536>.
- 3462 [71] Thomas Armstrong et al. “Monte Carlo Studies of the GCT Telescope for the  
3463 Cherenkov Telescope Array”. In: (Aug. 2015). arXiv: 1508.06088. URL:  
3464 <http://arxiv.org/abs/1508.06088>.
- 3465 [72] N Otte. “The Silicon Photomultiplier-A new device for High Energy Physics,  
3466 Astroparticle Physics, Industrial and Medical Applications”. In: *Proceedings to*  
3467 *SNIC symposium (SLAC, Stanford, ... April (2006)*, pp. 1–9. URL:  
3468 <http://www.slac.stanford.edu/econf/C0604032/papers/0018.pdf>.
- 3469 [73] D. Marano et al. “Silicon Photomultipliers Electrical Model Extensive Analytical  
3470 Analysis”. In: *IEEE Transactions on Nuclear Science* 61.1 (Feb. 2014), pp. 23–34.  
3471 ISSN: 0018-9499. DOI: 10.1109/TNS.2013.2283231. URL:  
3472 <http://ieeexplore.ieee.org/document/6661445/>.